

Robust Sensor Fault Detection and Isolation of Gas Turbine Engines

Bahareh Pourbabae

A Thesis
in
The Department
of
Electrical and Computer Engineering

Presented in Partial Fulfillment of the Requirements
for the Degree of Doctor of Philosophy at
Concordia University
Montréal, Québec, Canada

December 2016

© Bahareh Pourbabae, 2016

CONCORDIA UNIVERSITY

School of Graduate Studies

This is to certify that the thesis proposal prepared

By: **Bahareh Pournabae**

Entitled: **Robust Sensor Fault Detection and Isolation of Gas Turbine Engines**

and submitted in partial fulfilment of the requirements for the degree of

Doctor of Philosophy

complies with the regulations of this University and meets the accepted standards with respect to originality and quality.

Signed by the final examining committee:

_____ Dr. C. Constantinides, Chair
_____ Dr. S. Habibi, External examiner
_____ Dr. F. Haghighat, External examiner
_____ Dr. S. Hashtrudi Zad, Examiner
_____ Dr. L. Rodrigues, Examiner
_____ Dr. K. Khorasani, Co-Supervisor
_____ Dr. N. Meskin, Co-Supervisor

Approved by _____

Chair of the ECE Department

Dean of Engineering

ABSTRACT

Robust Sensor Fault Detection and Isolation of Gas Turbine Engines

Bahareh Pourbabae, Ph.D.

Concordia University, 2016

An effective fault detection and isolation (FDI) technology can play a crucial role in improving the system availability, safety and reliability as well as reducing the risks of catastrophic failures. In this thesis, the robust sensor FDI problem of gas turbine engines is investigated and different novel techniques are developed to address the effects of parameter uncertainties, disturbances as well as process and measurement noise on the performance of FDI strategies. The efficiencies of proposed techniques are investigated through extensive simulation studies for the single spool gas turbine engine that is previously developed and validated using the GSP software. The gas turbine engine health degradation is considered in various forms in this thesis. First, it is considered as a part of the engine dynamics that is estimated off-line and updated periodically for the on-board engine model. Second, it is modeled as the time-varying norm-bounded parameter uncertainty that affects all the system state-space matrices and third as an unknown nonlinear dynamic that is approximated by the use of a dynamic recurrent neural network..

In the first part of the thesis, we propose a *hybrid Kalman filter* (HKF) scheme that consists of a single nonlinear on-board engine model (OBEM) augmented with piecewise linear (PWL) models constituting as the multiple model (MM) based estimators to cover the entire engine operating regime. We have integrated the generalized likelihood ratio (GLR)-based method with our MM-based scheme to estimate the sensor fault severity under various single and concurrent fault scenarios. In order to ensure the reliability of our proposed HKF-based FDI scheme during the

engine life cycle, it is assumed that the reference baselines are periodically updated for the OBEM health parameters.

In the second part of the thesis, a novel robust sensor FDI strategy using the MM-based approach is proposed that remains robust with respect to both time-varying parameter uncertainties and process and measurement noise. The scheme is composed of *robust Kalman filters* (RKF) that are constructed for multiple PWL models. The parameter uncertainty is modeled by using a time-varying norm bounded admissible structure that affects all the PWL state space matrices. The robust Kalman filter gain matrices are designed by solving two algebraic Riccati equations (ARE) that are expressed as two linear matrix inequality (LMI) feasibility conditions. The main objective is to propose a robust filter that satisfies the overall performance requirements and is not affected by system perturbations. The requirements include a quadratically stable filter that ensures bounded estimation error variances having predefined values.

In the third part of the thesis, a novel hybrid approach is proposed to improve the robustness of FDI scheme with respect to different sources of uncertainties. For this purpose, a *dynamic recurrent neural network* (DRNN) is designed to approximate the gas turbine engine uncertainty due to the health degradations. The proposed DRNN is trained offline by using the extended Kalman filter (EKF) algorithm for an engine with different levels of uncertainty, but with healthy sensors. The convergence of EKF-based DRNN training algorithm is also investigated. Then, the trained DRNN with the fixed parameters and topology is integrated with our online model-based FDI algorithm to approximate the uncertainty terms of the real engine. In this part, the previously proposed HKF and RKF are integrated with the trained DRNN to construct the hybrid FDI structure.

*To my parents,
Shokofeh and Ali
and my love,
Mehrsan*

ACKNOWLEDGEMENTS

First and foremost, I would like to extend my heartfelt gratitude and appreciation to my dissertation advisors, Prof. K. Khorasani and Dr. N. Meskin whose expertise, consistent guidance and advises as well as the ample time spent helped me bring this study in to success. I appreciate all your contributions of time, ideas, and funding to make my Ph.D. experience productive and stimulating.

I would like to thank my dissertation committee members, Prof. S. Habibi, Prof. F. Haghghat, Prof. L. Rodrigues and Dr. S. Hashtrudi Zad not only for their insightful comments and encouragement, but also for the hard questions which incented me to widen my research from various perspectives. My sincere thanks also goes to Prof. V. Ramachandran who provided me a great opportunity of teaching various undergraduate courses during my PhD study. In particular, I am grateful to him for all his support and valuable advices.

I will forever be thankful to my best and old friends Dr. Negar Ghourchian and Dr. Amin Haji-Abolhassani for all their help and support since the first day I came to Montreal. I will never forget their kindness and generosity for helping me get through the difficult times, and for all the emotional support, camaraderie, entertainment, and caring they provided.

Moreover, I wish to thank CS Communication and Systems Canada to provide me an opportunity to grow my career as an embedded control software specialist. I would specially like to thank our team leader, Dr. Mathieu Moze for all his support, flexibility and understanding throughout writing this thesis.

My time at Concordia was made enjoyable in a large part due to the many friends and that became a part of my life. I will never forget the sleepless nights we were working together before deadlines, the stimulating discussions, chatting and all good moments that we shared. I would like to thank my fellow lab mates Dr. Amir

Baniamerian, Dr. Najmeh Daroogheh, Dr. Zahra Gallehdari, Amin Salar, Maryam Abdollahi, Arefeh Amrollahi, Esmaeil Alizadeh and Mahsa Khoshab. I will really miss our amazing gatherings on Friday nights at EV12.401. Best wishes to all of you.

Last but not least, I would like to thank my family for all their love and encouragement. For my parents, who raised me with a love of science and supported me in all my pursuits. Determination, commitment and dedication would have remained fancy words without any meaning if you both did not implement them in your own life to show me what they really mean. Without the inspiration, drive, and support that you have given me, I might not be the person I am today. Besides my parents, I would like to thank my younger brother, Farzad, the little brilliant mathematician in our family. I can always count on you to cheer me up and to make things better. I am so proud to be your sister and cannot wait to see you become successful in life.

These past several years have not been an easy ride, both academically and personally without my true and forever love, Mehrsan. He has been non-judgmental of me and instrumental in instilling confidence. He has faith in me and my intellect even when I felt like digging hole and crawling into one because I did not have faith in myself. His faithful support during the final stages of this Ph.D. is so appreciated.

TABLE OF CONTENTS

List of Figures	xi
List of Tables	xvi
1 Introduction	1
1.1 Fault Detection, Isolation and Identification	1
1.2 Motivation	4
1.3 Literature Review	6
1.3.1 Model-Based Fault Diagnosis Approaches	7
1.3.2 Data-Based Fault Diagnosis Approaches	12
1.3.3 Hybrid Fault Diagnosis Approaches	16
1.3.4 Fault Diagnosis Techniques Applied to the Gas Turbine Engines	17
1.3.5 Piecewise Linear Models	21
1.4 General Problem Statement	22
1.5 Thesis Objectives	24
1.6 Thesis Contributions	26
1.7 Thesis Organization	30
2 Background Information	32
2.1 Gas Turbine Engine History	32
2.2 Principles of Jet Propulsions	33
2.3 Gas Turbine Engine Operation	35
2.4 Gas Turbine Engine Health Degradation	37
2.5 Gas Turbine Engine Mathematical Model	38
2.5.1 Rotor Dynamics	40
2.5.2 Volume Dynamics	40
2.6 Set of Nonlinear Equations	40

2.7	Background of Filtering Methods Formulations	42
2.7.1	Linear Kalman Filter (LKF)	42
2.7.2	Extended Kalman Filter (EKF)	44
2.7.3	Unscented Kalman Filter (UKF)	44
2.7.4	Cubature Kalman Filter (CKF)	47
2.8	Summary	49
3	Hybrid Kalman Filter Based Fault Detection, Isolation and Identification Scheme	51
3.1	Hybrid Kalman Filter (HKF) Design	52
3.1.1	Discrete-Time HKF Derivation Analysis	57
3.2	Piecewise Linear Models (PWL) Interpolation	60
3.3	Sensor FDI via Multiple-Model-Based Scheme	64
3.3.1	Single Fault Detection and Isolation (FDI) Scheme	65
3.3.2	Concurrent Fault Detection and Isolation (FDI) Scheme	66
3.4	Sensor Fault Identification	69
3.5	Simulation Results	72
3.5.1	Case 1: False Alarms Evaluation	75
3.5.2	Case 2: A 3% Sensor Bias Fault Detection and Isolation	76
3.5.3	Case 3: Sensor Fault Detection and Isolation for Different Fault Severities	80
3.5.4	Case 4: Sensor Fault Severity Identification	81
3.5.5	Case 5: Concurrent Fault Detection, Isolation and Identification	83
3.5.6	Case 6: Comparison	85
3.6	Summary	93
4	Robust Kalman Filter Based Fault Detection and Isolation	94
4.1	Problem Statement	95

4.2	Robust Kalman Filter Design	97
4.3	Piecewise Linear Models Integration Methodology	106
4.4	Robust Sensor FDI by Using a Multiple Model-Based Strategy	109
4.5	Simulation Studies	111
4.5.1	Case 1: False Alarms and Estimation Accuracy Evaluation	118
4.5.2	Case 2: Sensor FDI Using Single Layer of Multiple Models	122
4.5.3	Case 3: Sensor FDI by Using Two Layers of Multiple Models	129
4.6	Summary	132
5	Hybrid Fault Detection and Isolation Scheme	134
5.1	Proposed Hybrid Fault Detection and Isolation Structure	135
5.1.1	Dynamic Recurrent Neural Network (DRNN)	137
5.1.2	Bank of Hybrid/Robust Kalman Filters	140
5.2	DRNN Structure and the Training Process	142
5.3	Hybrid DRNN-based FDI Scheme	148
5.4	Convergence Analysis	151
5.5	Simulation Results	157
5.5.1	DRNN Training Process	158
5.5.2	DRNN Integration with Bank of Hybrid Kalman Filters	162
5.5.3	DRNN Integration with a Bank of Robust Kalman Filters	173
5.5.4	Comparison	183
5.6	Summary	186
6	Conclusions and Future Directions of Research	187
6.1	Multiple HKF-based Fault Detection, Isolation and Identification	188
6.2	Multiple RKF-based Fault Detection and Isolation	189
6.3	Hybrid DRNN-based Fault Detection and Isolation	191
	Bibliography	195

List of Figures

1.1	The concepts of hardware and analytical redundancies for FDI purposes.	2
1.2	Fault detection, isolation and reconfiguration scheme.	3
2.1	Different engine diagrams: (a) Turbojet, (b) Turbofan and (c) Turboprop [1].	34
2.2	Information flow diagram associated with several gas turbine engine physical problems [2].	37
2.3	Information flow diagram associated with single spool turbojet engine [3].	39
3.1	The MM-based FDI scheme based on the HKF corresponding to multiple operating regime.	67
3.2	Profiles of (a) the fuel flow rate, (b) altitude, and (c) the Mach number during a flight mission.	73
3.3	Mode probabilities for 3% bias fault applied at (a) $k_f = 50$ sec to the T_C sensor, (b) $k_f = 250$ sec to the P_C sensor, and (c) $k_f = 450$ sec to the N sensor in presence of the obtained maximum tolerable percentage of the estimation errors in Table 3.3 for the compressor health parameter reference baselines.	77
3.4	Estimated two concurrent sensor fault severities (a) a 6% bias fault that is applied to the T_C sensor at $k_f = 50$ sec, and (b) a 5% bias fault that is applied to the N sensor at $k_f = 250$ sec without considering any health parameter degradations.	84

3.5	Mode probabilities for a 3% bias fault that is applied at $k_f = 250$ sec to the T_C sensor by applying multiple (a) HKF, (b) LKF, (c) EKF, (d) UKF and (e) CKF based FDI approaches with 2.5% degradations applied to the compressor health parameters of the actual engine. . . .	86
3.6	Mode probabilities for a 3% bias fault applied at $k_f = 250$ sec to the T_C sensor using (a) the MHKF and (b) the EKF-based FDI methods, with $\alpha = 0.99$ and $\hat{\alpha} = 0.975$	89
3.7	Mode probabilities that are generated for the MM-based FDI method by utilizing (a-c) the HKF and (d-f) the LKF with one, three and five operating points.	92
4.1	The proposed MM-based FDI strategy that is based on the RKF corresponding to the entire operating region.	112
4.2	The profiles of (a) the fuel flow rate (\dot{m}_f), (b) altitude, and (c) the Mach number during a flight mission.	113
4.3	Mode probabilities for healthy sensors in presence of degradation of 5% when applied to the compressor mass flow rate and degradation of 2.5% when applied to the compressor efficiency by using (a) our proposed MRKF-based FDI, (b) the MRKF-based FDI according to [4] and (c) the standard MM-based FDI.	119
4.4	Real and estimated shaft rotational speed (N), during the (a) climbing and (b) landing flight conditions. These are generated by the healthy mode in the single-layer MM-based structures that utilize our proposed RKF and the one as proposed in [4] in presence of degradations of 5% and 2.5% applied to the compressor mass flow rate and the efficiency, respectively.	119

4.5	Mode probabilities by the first layer of MM-based FDI scheme for a single 3% bias fault when applied to the compressor exit temperature sensor using (a) our proposed RKF and (b) the RKF as proposed in [4] with degradations of 5% and 2.5% applied to the compressor mass flow rate and the efficiency, respectively.	123
4.6	Mode probabilities by the first layer of MM-based FDI scheme for a single 3% bias fault when applied to the compressor exit pressure sensor using (a) our proposed RKF and (b) the RKF as proposed in [4] with degradations of 5% and 2.5% applied to the compressor mass flow rate and the efficiency, respectively.	124
4.7	Mode probabilities by the first layer of MM-based FDI scheme for a single 3% bias fault when applied to the shaft rotational speed sensor using (a) our proposed RKF and (b) the RKF as proposed in [4] with degradations of 5% and 2.5% applied to the compressor mass flow rate and the efficiency, respectively.	124
4.8	Mode probabilities by the first layer of MM-based FDI scheme for a single 3% bias fault when applied to the turbine exit temperature sensor using (a) our proposed RKF and (b) the RKF as proposed in [4] with degradations of 5% and 2.5% applied to the compressor mass flow rate and the efficiency, respectively.	125
4.9	Mode probabilities by the first layer of MM-based FDI scheme for a single 3% bias fault when applied to the turbine exit pressure sensor using (a) our proposed RKF and (b) the RKF as proposed in [4] with degradations of 5% and 2.5% applied to the compressor mass flow rate and the efficiency, respectively.	125

4.10	Fault detection time delays by using our proposed two layer robust MM-based FDI approach for a single bias fault when injected at $k_{fs} = 250$ sec to the sensors (a) T_C , (b) N and (c) P_T as a function of the fault severity and the compressor health parameters degradation levels.	131
5.1	Overall structure of our proposed hybrid FDI scheme.	137
5.2	Offline training procedure of the DRNN for the hybrid engine modeling.	139
5.3	State-space model of the DRNN.	140
5.4	EKF-based training of the DRNN weights.	149
5.5	(a-c) FP1 fuel flow rate, altitude and Mach number, (d-f) FP2 fuel flow rate, altitude and Mach number.	158
5.6	DRNN structure	159
5.7	(a) Average of MSEs for five clusters of training and validation data, for (a) FP1 under $\alpha_{\dot{m}_C} = 0.93$ and $\alpha_{\eta_C} = 0.965$, and (b) FP2, under $\alpha_{\dot{m}_C} = 0.82$ and $\alpha_{\eta_C} = 0.91$, versus the number of hidden neurons. . .	161
5.8	(a) Average of MSEs for five clusters of training and validation data, for (a) FP1 under $\alpha_{\dot{m}_C} = 0.93$ and $\alpha_{\eta_C} = 0.965$, and (b) FP2 under $\alpha_{\dot{m}_C} = 0.82$ and $\alpha_{\eta_C} = 0.91$ versus the number of epochs.	162
5.9	Mode probabilities for healthy sensors for the engine with $\alpha_{\dot{m}_C} = 0.93$ and $\alpha_{\eta_C} = 0.965$ during FP1 using the (a) hybrid DRNN-HKF-based FDI scheme, and (b) multiple HKF-based FDI scheme.	164
5.10	Mode probabilities generated by (a) our proposed hybrid DRNN-HKF-based FDI scheme and (b) multiple HKF-based FDI scheme, for 3% bias fault applied at $k_f = 50$ sec to the N sensor with $\alpha_{\dot{m}_C} = 0.93$ and $\alpha_{\eta_C} = 0.965$	169

5.11	Mode probabilities generated by (a) our proposed hybrid DRNN-HKF-based FDI scheme and (b) multiple HKF-based FDI scheme, for 3% bias fault applied at $k_f = 250$ sec to the T_C sensor with $\alpha_{\dot{m}_C} = 0.93$ and $\alpha_{\eta_C} = 0.965$	169
5.12	Mode probabilities generated by (a) our proposed hybrid DRNN-HKF-based FDI scheme and (b) multiple HKF-based FDI scheme, for 3% bias fault applied at $k_f = 450$ sec to the P_C sensor with $\alpha_{\dot{m}_C} = 0.93$ and $\alpha_{\eta_C} = 0.965$	171
5.13	Mode probabilities for healthy sensors for the engine with $\alpha_{\dot{m}_C} = 0.82$ and $\alpha_{\eta_C} = 0.91$ during FP2 using the (a) hybrid DRNN-RKF-based FDI scheme, and (b) multiple RKF-based FDI scheme.	175
5.14	Mode probabilities generated by (a) our proposed hybrid DRNN-RKF-based FDI scheme and (b) multiple RKF-based FDI scheme, for 3% bias fault applied at $k_f = 50$ sec to the P_C sensor with $\alpha_{\dot{m}_C} = 0.82$ and $\alpha_{\eta_C} = 0.91$	180
5.15	Mode probabilities generated by (a) our proposed hybrid DRNN-RKF-based FDI scheme and (b) multiple RKF-based FDI scheme, for 3% bias fault applied at $k_f = 250$ sec to the T_C sensor with $\alpha_{\dot{m}_C} = 0.82$ and $\alpha_{\eta_C} = 0.91$	180
5.16	Mode probabilities generated by (a) our proposed hybrid DRNN-RKF-based FDI scheme and (b) multiple RKF-based FDI scheme, for 3% bias fault applied at $k_f = 450$ sec to the P_T sensor with $\alpha_{\dot{m}_C} = 0.82$ and $\alpha_{\eta_C} = 0.91$	182

List of Tables

3.1	Operational modes corresponding to various possible two concurrent sensor faults.	68
3.2	The operating point specifications corresponding to the designed PWL models, where \dot{m}_f and Alt are measured in Kg/m ² and ft, respectively.	74
3.3	Fault detection time (FDT) corresponding to the maximum tolerable percentage of the RBEE ($\overline{\Delta\alpha}$) at different stages of the flight profile.	77
3.4	The confusion matrix for 3% RBEE of the compressor health parameters.	78
3.5	The confusion matrix for 3% RBEE of the turbine health parameters.	78
3.6	The confusion matrix for the measurement noise signals where the SDs are multiplied by a factor of 20.	79
3.7	Sensor FDI algorithm performance indices corresponding to different levels of uncertainties.	80
3.8	The average sensor fault detection times for all fault modes as a function of the fault severity at different stages of the flight profile, under the maximum tolerable RBEE% for the compressor health parameters.	81
3.9	The average of the maximum detectable sensor bias fault (as percentage of the engine steady-state outputs) over the entire flight profile by using our FDI scheme when the corresponding maximum tolerable RBEE% reported in Table 3.3 are applied to the compressor and turbine health parameters.	81
3.10	The average WMSNE% for all flight modes as a function of the bias fault severity applied to various sensors without considering any estimation error for the health parameter reference baselines.	82

3.11	Absolute mean of residual signals associated with various types of nonlinear filters corresponding to the healthy mode in the MM-based scheme for the healthy engine sensors without health degradation. . . .	87
3.12	Sensor fault detection times using multiple non-interacting HKF, LKF, EKF, UKF and CKF based FDI approaches without considering health parameter degradation.	89
3.13	Sensor fault detection times using multiple interacting HKF, LKF, EKF, UKF and CKF based FDI approaches without considering any health parameter degradation.	90
3.14	Computational time as measured in seconds for different filtering methods.	90
3.15	Mean of the combined residual signals ($\bar{\gamma}_c^1$) associated with the healthy mode for both the HKF and LKF methods in terms of the number of the operating points.	92
4.1	The operating point specifications corresponding to multiple PWL models.	114
4.2	Comparison of the WMAPE% by using the MM-based FDI schemes using our proposed RKF (PRKF) and RKF in [4] in presence of different compressor health degradation levels for the engine healthy sensors scenario.	121
4.3	True positive (TP), false positive (FP) and false alarm rate (FAR) that are obtained for both robust methods if either the SD_w for the process noise is multiplied by a factor of 5 and degradations of 7% and 3.5% applied to the compressor mass flow rate and the efficiency, respectively.	122
4.4	The confusion matrix when the process noise standard deviations are multiplied by a factor of 5.	126

4.5	The confusion matrix when degradations of 7% and 3.5% are applied to the compressor mass flow rate and the efficiency, respectively. . . .	126
4.6	Our proposed robust sensor FDI scheme performance indices for different uncertainty levels.	127
4.7	Fault detection delay times for all sensor fault modes as a function of the fault severity for the single-layer MM-based FDI scheme by using the proposed RKF and the one designed in [4] when degradations of 5% and 2.5% are applied to the compressor mass flow rate and the efficiency, respectively. (×) denotes incorrect fault detection cases. . .	128
4.8	The maximum detectable sensor bias fault achievable in less than 10 seconds of delay by using the first layer of robust multiple models during the cruise flight condition when degradations of 5% and 2.5% are applied to the compressor mass flow rate and the efficiency, respectively.	128
4.9	Fault detection delay times for all sensor fault modes as a function of fault severity using the double-layer MM-based FDI scheme of the proposed RKF when degradations of 5% and 2.5% are injected to the compressor mass flow rate and the efficiency, respectively.	129
4.10	The maximum detectable sensor bias fault achievable in less than 10 seconds of delay by using double-layer robust multiple models during the cruise flight condition when degradations of 5% and 2.5% are injected to the compressor mass flow rate and the efficiency, respectively.	130
5.1	The network parameters that are determined during the DRNNs trainings associated with FP1 and FP2, respectively.	162
5.2	Comparison of the WMAPE% by using the HNNHKF and MHKF based FDI schemes in presence of different compressor health degradation levels and process and measurement noise factors for the engine healthy sensors scenario during the entire FP1.	166

5.3	True positives (TP), false positives (FP) and false alarm rates (FAR) that are obtained for HNNHKF and MHKF based FDI methods if either the K_w and K_v for the process and measurement noise or the compressor health degradation is increased.	167
5.4	Comparison of FDTs between the HNNHKF and MHKF based FDI schemes associated with a single 3% sensor bias fault that occurs at different stages of FP1 with $\alpha_{\dot{m}_C} = 0.93$ and $\alpha_{\eta_C} = 0.965$. (\times) denotes incorrect fault detection cases and ($*$) denotes false alarms and/or incorrect fault detections besides the correctly detected fault.	168
5.5	The confusion matrix that is obtained for hybrid DRNN-HKF-based FDI scheme for 3% single sensor bias fault that is applied to the engine under $\alpha_{\dot{m}_C} = 0.90$ and $\alpha_{\eta_C} = 0.95$	170
5.6	The confusion matrix that is obtained for hybrid DRNN-HKF-based FDI scheme for 3% single sensor bias fault that is applied to the engine under $K_w = 0.5$ and $K_v = 1.5$	170
5.7	Hybrid DRNN-HKF-based Sensor FDI algorithm performance indices corresponding to different levels of uncertainties.	171
5.8	The sensor fault detection times for all fault modes as a function of the fault severity during the cruise of FP1, with $\alpha_{\dot{m}_C} = 0.93$ and $\alpha_{\eta_C} = 0.965$	172
5.9	The maximum sensor bias fault (as percentage of the engine steady-state outputs) that can be detected in less than 20 seconds during the cruise mode of FP1 by using our proposed hybrid DRNN-HKF-based FDI scheme under $\alpha_{\dot{m}_C} = 0.93$ and $\alpha_{\eta_C} = 0.965$	173

5.10	Comparison of the WMAPE% by using the HNNRKF and MRKF based FDI schemes in presence of different compressor health degradation levels and process and measurement noise factors for the engine healthy sensors scenario.	177
5.11	TP, FP and FAR that are obtained for HNNRKF and MRKF based FDI methods if either the K_w and K_v for the process and measurement noise or the compressor health degradation is increased.	178
5.12	Comparison of FDTs between the HNNRKF and MRKF based FDI schemes associated with a single 3% sensor bias fault that occurs at different stages of FP2 with $\alpha_{\dot{m}_C} = 0.82$ and $\alpha_{\eta_C} = 0.91$. (\times) denotes not detectable fault and ($*$) denotes false alarms and/or incorrect fault detections besides the correct fault detection.	179
5.13	The confusion matrix that is obtained for hybrid DRNN-RKF-based FDI scheme for 3% single sensor bias fault that is applied to the engine under $\alpha_{\dot{m}_C} = 0.80$ and $\alpha_{\eta_C} = 0.90$	181
5.14	The confusion matrix that is obtained for hybrid DRNN-RKF-based FDI scheme for 3% single sensor bias fault that is applied to the engine under $K_w = 0.5$ and $K_v = 1.5$	181
5.15	Hybrid DRNN-RKF-based Sensor FDI algorithm performance indices corresponding to different levels of uncertainties.	181
5.16	The sensor fault detection times for all fault modes as a function of the fault severity during the cruise of FP2, with $\alpha_{\dot{m}_C} = 0.82$ and $\alpha_{\eta_C} = 0.91$. (\times) denotes a non-detectable fault, and ($*$) denotes the incorrect fault detection besides the correctly detected fault.	183

5.17 The maximum sensor bias fault (as percentage of the engine steady-state outputs) that are detected in less than 20 seconds during the cruise mode of FP2 by using our proposed hybrid DRNN-RKF-based FDI scheme under $\alpha_{\dot{m}_C} = 0.82$ and $\alpha_{\eta_C} = 0.91$. (\times) denotes non-detectable fault. 183

5.18 Comparison of FDT for 3% sensor faults during the cruise mode, maximum detectable faults in less than 20 seconds, WMAPE, FAR, ACC, and IFDR corresponding to hybrid DRNN-HKR and DRNN-RKF based FDI schemes, under $\alpha_{\dot{m}_C} = 0.93$ and $\alpha_{\eta_C} = 0.965$ for FP1 that is used for DRNN-HKF and $\alpha_{\dot{m}_C} = 0.82$ and $\alpha_{\eta_C} = 0.91$ for FP2 that is used for DRNN-RKF methods. (\times) denotes the non-detected fault, and ($*$) denotes incorrect fault detection cases besides the correctly detected fault. 185

List of Symbols and Abbreviation

α	Health Parameters Degradation Factors Vector
\dot{m}_n	Nozzle mass flow rate
\dot{m}_f	Fuel Flow Rate
η_{mech}	Mechanical efficiency
γ	Innovation Sequence
γ	Learning rate
$\hat{\alpha}$	Estimated Health Parameters Reference Baselines Vector
\hat{Y}_{un}	Actual engine measurements uncertainty terms estimated by DRNN
\hat{Y}_{un}	Estimated DRNN Output
λ	Health parameters degradation (reference baseline) factors vector
\mathcal{U}	DRNN augmented input vector
\mathcal{X}	DRNN internal state variable vector
$\phi(\cdot)$	Sigmoidal activation function
A	State (system) matrix
Alt	Altitude

C	Output matrix
c_p	Specific heat at constant pressure
c_v	Specific heat at constant volume
E	Rotor energy
H	Engine health parameters vector
H_u	Fuel specific heat
H_{OBEM}	OBEM health parameters vector
J	Rotor moment inertia
K	Kalman gain matrix
K_v	Measurement Noise Factor
K_w	Process Noise Factor
Mn	Mach Number
N	Spool Rotational Speed
$O(k)$	Induced local field of neuron potential at time k
P_C	Compressor Pressure
P_T	Turbine Exit Pressure
P_{CC}	Combustion Chamber Pressure
S	Covariance Matrix
SD_v	Measurement Noise Standard Deviations Vector
SD_w	Process Noise Standard Deviations Vector

T_C	Compressor Temperature
T_d	Intake temperature
T_M	Mixer temperature
T_T	Turbine Exit Temperature
T_{CC}	Combustion Chamber Temperature
U	Engine control input
v	Measurement noise vector
V_M	Mixer volume
w	Process noise vector
W_C	Power consumed by compressor
W_T	Power consumed by turbine
w_{ji}	Synaptic weight from the i^{th} neuron to the j^{th} neuron
X	Engine state variables vector
X_{OBEM}	OBEM state variables vector
Y	Engine sensor measurements vector
Y_m	Modified Sensor Measurements
Y_{OBEM}	OBEM outputs vector
\dot{m}_{CC}	Combustion chamber mass flow rate
\dot{m}_C	Compressor Mass Flow Rate
\dot{m}_T	Turbine Mass Flow Rate

η_C Compressor Efficiency

η_T Turbine Efficiency

BPTT Back Propagation Through Time

CM Confusion Matrix

DRNN Dynamic Recurrent Neural Network

FDT Fault Detection Time

GLR Generalized Likelihood Ratio

HNNHKF Hybrid DRNN-HKF

PWL Piecewise Linear Model

RBEE Reference baseline estimation error

RTRL Real-Time Recurrent Learning

WMAPE Weighted Mean Absolute Percentage Error

Chapter 1

Introduction

An effective fault detection, isolation and identification (FDII) technology can play a critical role in improving the system availability, safety and reliability as well as reducing the maintenance costs and risks of catastrophic failures. Over the past few years, many researchers have focused on developing sophisticated fault detection and isolation (FDI) schemes constituting as a significant component of an FDII solution [5,6]. There are many challenging problems regarding the FDII problem namely as the fault detection promptness, FDII accuracy, rates of false alarms, incorrect fault detections and robustness with respect to different sources of uncertainties.

1.1 Fault Detection, Isolation and Identification

There is an ever-increasing demand on reliability and safety of many engineering systems, such as aero-engines, chemical processes, manufacturing systems, electrical machines, power networks, vehicle dynamics and industrial electronic equipments that are subjected to multiple faults and abnormalities. As a result, it is paramount to detect, isolate and identify any kind of sensor, actuator and component faults as early as possible to implement different fault tolerant control (FTC) mechanisms to minimize the performance degradation and to avoid any dangerous situations. A

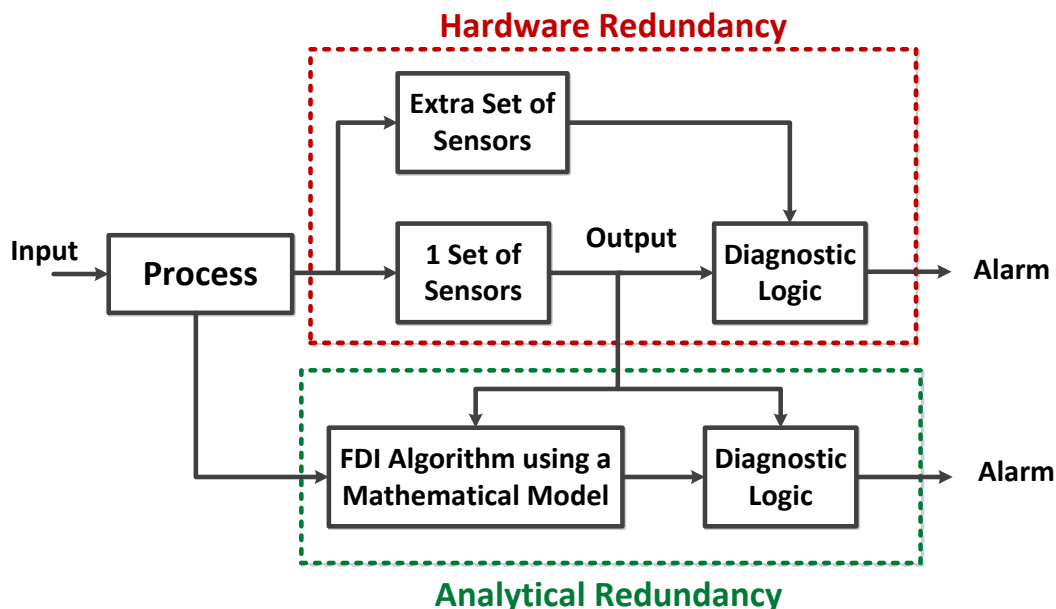


Figure 1.1: The concepts of hardware and analytical redundancies for FDI purposes.

fault is defined as a non-allowed sudden or gradual deviation of at least one parameter of the system from its normal and acceptable condition. In order to monitor, locate and detect the type and severity of various faults in safety critical systems the concept of redundancy, either hardware redundancy or analytical redundancy is utilized. The basic idea of hardware redundancy is to have two or more identical components with the same inputs whose corresponding output signals are compared using different approaches, such as limit checking or majority voting to report a fault within that component. However, the hardware redundancy cannot be applied to the whole system due to the cost, weight and the essential space for hardware installation. As a result, the analytical redundancy has become the main stream in fault detection and isolation (FDI) research since the 1980s [7], although it is a more challenging approach since the robustness should be always maintained against model uncertainties, noise and unknown disturbances. The analytical redundancy makes use of a mathematical model of the system. The hardware and analytical redundancy concepts are illustrated in Figure 1.1.

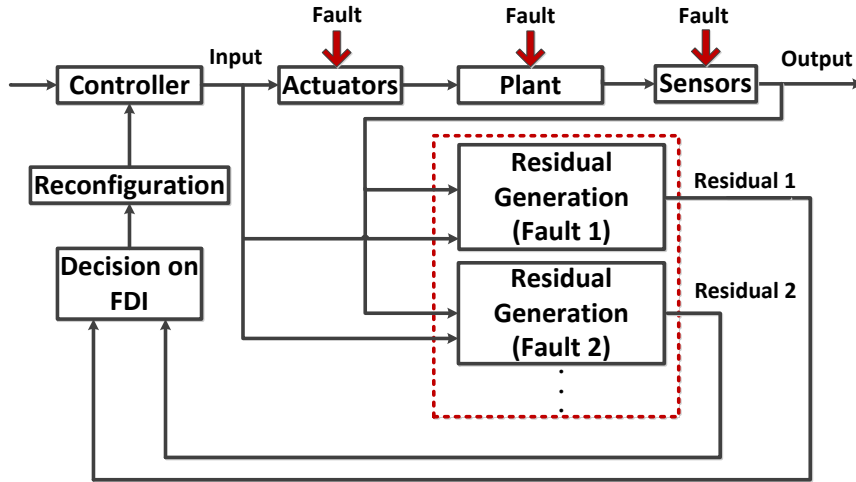


Figure 1.2: Fault detection, isolation and reconfiguration scheme.

The general analytical redundancy methodology for an FDII strategy consists of several important steps including: (a) the generation of residuals as indicators of faults, (b) the isolation of the faulty actuator, or sensor, or component element, and (c) the identification and estimation of the fault severity. The residual generation is a very important and challenging step in which the residual signal is supposed to be ideally zero under no-fault conditions. It should also be minimally sensitive to noise and disturbances and maximally sensitive to faults. In some FDII schemes, multiple residuals are generated for the purpose of fault isolation. In such schemes, each residual is sensitive to only one or a set of selected faults. Using statistical tools, the residuals are tested to determine any kind of deviation from zero. Finally, a fault tolerant controller is reconfigured to respond to any detected, isolated and identified fault and to yield the closed-loop system efficiency in presence of faults. The effectiveness of any fault tolerant control mechanism highly depends on the accuracy of the information that is provided by the fault diagnosis strategy. The overall structure of a fault tolerant control system as well as the fault detection and isolation structure is illustrated in Figure 1.2.

Generally, fault diagnosis approaches can be categorized into three distinct

groups including model-based, process history data-based and hybrid methods. The model-based methods are usually developed based on the governing physics rules that represent the behavior of the system. In contrast to the data-based approaches which usually face a problem in finding a generalized model that works for a wide range of operating conditions, the model-based methods can be the more accurate class of fault diagnosis methodologies if the comprehensive model of the system is available. These two methods' drawbacks can be solved by applying a hybrid method of fault diagnosis through integrating the model-based and data-based approaches. More details will be given in this chapter regarding different popular and available approaches corresponding to the aforementioned FDI categories. Multiple surveys are also available in the literature in which the history of FDI approaches and ongoing challenges are explained [6–13].

1.2 Motivation

An effective fault diagnosis, prognosis and health monitoring (DPHM) solution is an important and challenging problem in many disciplines in order to ensure the safe and acceptable operation of a system and to reduce the maintenance cost and the risks of catastrophic failures. Over the past few years, many researchers have focused on proposing different fault detection and isolation (FDI) schemes constituting as a significant component of the DPHM system. Since early research on FDI, gas turbines have been one of the challenging application areas which have received much attention. The main theme of research in gas turbines FDI is based on the Gas Path Analysis (GPA) which enables actuators, sensors and components fault diagnosis by observing engine's parameters such as the rotor speed, temperature and pressure at each stage and the fuel flow rates [14,15]. Fault diagnosis problems include detection, isolation and identification of different kinds of sensor, actuator

and component faults. The component faults are categorized into two groups of slow variations of engine parameters due to the turbine blade erosion and corrosion, worn seals, excess of clearance or a sudden effect due to the foreign or domestic object damage. All these faults have an effect on engine health parameters including the compressor and the turbine efficiencies and mass flow rates. The sensor faults include different kinds of bias, drift and accuracy changes, while the actuator faults are usually the loss of effectiveness and perhaps saturation.

In addition to the faults and the failures, the system is always influenced by noise, disturbances and various sources of uncertainties. Therefore, an effective FDI strategy should be capable of detecting and isolating different types of faults while keeping its robustness with respect to noise, disturbances and the uncertainties. This will avoid the risk of the false alarm generation. One of the important sources of uncertainty is the system's parameters variations like the health parameters degradations due to the gas turbine engine aging and deterioration. Therefore, the designed FDI strategy should be robust with respect to the health parameters degradations or be capable of being updated for the recent values of the health parameters in case the percentages of their degradations are available by the use of a certain health monitoring method.

Despite the dedication of a large body of works to study FDI problem for the gas turbine engines, there are still some challenging problems in this area among them are designing an applicable strategy to detect and isolate different faults in presence of health parameters degradation, noise and disturbances. Most of the available FDI approaches in the literature that are applied for gas turbine engine does not consider the health parameters degradation due to the gradual aging process of the engine. Also, the proposed approaches are mainly applied to the cruise condition rather than the entire engine operating regime. There are also complicated FDI methods in the literature that cannot be easily applied to real-time applications due

to the essential computational time and cost.

The main motivation for this thesis is to design and propose a sensor FDI scheme applied to the gas turbine engine considering all the aforementioned limitations and challenges. Our objective is to construct an FDI methodology that is not only able to detect and isolate different types of faults with different severities faster than the available methods, but also perform robustly with respect to various sources of uncertainties, such as the engine health degradation, noise and disturbances. To demonstrate the superiority of our proposed methodologies as compared to the examined methods in the literature, different performance indices are defined that are computed for our proposed methods and are compared with the other approaches.

In this thesis, the model-based and hybrid FDI methodologies are used to address the same sensor FDI problem and are applied to the single spool turbojet engine. The Chapters 3 and 4 of this thesis are on model-based methodology in which two filters namely as the hybrid Kalman filter (HKF) and robust Kalman filter (RKF) are designed to be applied as the detection filter in multiple-model structure and to be utilized for solving sensor FDI problem in presence of engine compressor and turbine health degradation. Moreover, in Chapter 5, our main motivation is to improve the sensor FDI algorithm efficiency by integrating the previously designed filters with the dynamic recurrent neural network structure to improve the robustness. The details regarding the problem statements and the main objectives of this thesis will be given in the following sections.

1.3 Literature Review

During the last four decades, fruitful results have been reported on fault detection and isolation methods as well as their applications in various industrial processes

and systems. A number of survey papers were written on three distinct categories of FDI approaches including the model-based, data-based and hybrid methods. In this section, we review the literature on available FDI approaches.

1.3.1 Model-Based Fault Diagnosis Approaches

In model-based methods, the system models are required to be available, which can be obtained by using either physical principles or system identification techniques. Based on the model, FDI algorithms are developed to monitor the consistency between the measured outputs of the practical systems and the model-predicted outputs. The model-based FDI approaches have been introduced in multiple survey papers [5, 6, 10, 16, 17] and can be grouped into basic approaches, namely as the (i) Kalman filter or observer based approaches, (ii) parity relations, (iii) optimization-based algorithms, (iv) parameter estimation and identification techniques, and (v) geometric approach.

The Kalman filter is capable of generating the residual signal whose statistical features determine the occurrence of a fault [18]. The common statistical tools for testing the Kalman filter residuals are the maximum likelihood method, or the generalized likelihood ratio (GLR). The concept of the parity relation-based FDI approach is to form residuals as the difference between the system and model outputs. These residuals are then subjected to a linear transformation. These two steps together constitute the residual generator that provides the desired FDI properties [19, 20]. The optimization based techniques are also capable of minimizing the sensitivity of residual signal towards different sources of uncertainty and maximizing the residual fault sensitivity [21]. The parameter estimation is another FDI technique in which the identification approaches are used to identify the faults that are reflected in system parameters. The estimated parameters are compared with the reference parameters obtained initially under healthy conditions [22]. The FDI

problem can also be formulated using the geometric techniques such as invariant subspaces [23, 24]. Multiple model approach is also a popular structure for FDI purposes in which different models are constructed for different healthy and faulty scenarios working in parallel with certain switching mechanism among the available modes. It enables one not only to detect and isolate different faults but it also provides one with information on the magnitude of the fault and its identification information [3, 25–28].

The efficiency of approaches that are used to perform different types of fault diagnosis can be measured by computing various factors such as the promptness of the fault detection, sensitivity to incipient fault, low false alarms and missed fault detections rates, and accuracy of the fault identification. The compromises among these criteria require extensive knowledge of the monitored system as well as the operating system conditions [29]. The above factors can also be affected by the accuracy of the system model used and a fault diagnosis method, the severity of the injected fault and also the current health condition of the operational system.

Another important criterion of the FDI strategy is its robustness with respect to the un-modeled or uncertain dynamics, disturbances and noise, and the parameter variations. Therefore, a number of approaches have been proposed in the literature to improve the FDI strategy robustness, by applying different methods like the adaptive threshold that is varied by the control activity [30], generating complete decoupling between different fault effects and unknown inputs that are independent of the fault modes by using methods such as the detection filter approach [31], the parity space approach [32, 33], the Eigen structure assignment [34, 35], the H_∞ optimization in the frequency domain [36] and the unknown input observer (UIO) approaches [6, 37–39]. Moreover, the robust observers are another active area within the robust model-based FDI techniques.

As per available discussions and comparisons for FDI methods in the literature,

it is shown that various observer-based methods, such as eigenstructure assignment, fault detection filters, and unknown input observers give identical residuals with that of an equivalent parity relation method. Similar as the observer-based methods, the parity relation method is capable of yielding directional or structural residual vectors using the system input-output transfer function or state-space model. Note that the observer-based and the parity relation approaches generally do not consider model uncertainties. In most cases, they are also limited to linear time-invariant (LTI) systems. Therefore, in the presence of model uncertainties, the fault detection algorithm would fail to yield zero-mean residual in the absence of faults. This problem can almost be rectified by selecting a higher threshold for statistical decision making. However, this normally leads to the longer fault detection delay [10, 40].

Conceptually, the modeling uncertainties are categorized into two distinct groups, namely the structured and unstructured uncertainties [41]. The structured uncertainty is normally denoted as a product of a known signature matrix by an unknown linear/nonlinear function. The unstructured uncertainty is defined using the upper bound which may be a constant value or a function of the state variables, inputs and the time. In order to make the FDI strategy robust with respect to the unstructured uncertainty, an adaptive threshold can be defined based on the upper bound of the uncertainty which is used for a fault detection. The structured type of uncertainty is a kind of unknown input for the system and its effects can be decoupled from the residual signal by the use of unknown input observers [42, 43]. The authors of [29, 39] found a transformed system with a reduced order which is disturbance decoupled while it is still affected by a fault. Their system is linear with respect to the fault and the uncertainty but it is nonlinear with respect to the state variables and inputs. However, the drawback of their approach is that convergence of the error dynamics is not proven or discussed.

In UIO-based robust FDI approaches, the structured modeling uncertainty is

added as an unknown input to the system dynamic equation, then an observer is designed whose estimation error converges to zero regardless of the uncertainty effect and the remaining design degree of freedom is used for a fault detection and isolation. This approach has been mostly used for linear systems, while the necessary and sufficient conditions for the existence of UIO has been found by Kudva in 1980 [44]. Recently, in [45] the unknown input observer problem is addressed without satisfying the sufficient condition through utilizing the double-model adaptive estimation approach. In [46], it has been shown that there are two possible equivalent approaches to make the estimation procedure robust with respect to the disturbance including the design of a disturbance decoupled observer for a disturbed system or design a standard observer for a disturbance decoupled system. The linear UIO-based FDI approaches have been also extended to nonlinear systems by linearizing them at different operating points and considering them as multiple model systems [47]. Some other nonlinear systems have also been expressed in terms of linear parts and a Lipschitz nonlinear state dependent part [48]. Unlike the UIO approaches, in H_∞ optimization process the sensitivity of the residual signal is maintained less than a predefined bound whereas the sensitivity to the faults is increased over the frequency range of them [36, 49]. Therefore, the effect of the modeling uncertainty on a residual signal can be fully decoupled by the use of the UIO procedure; however it can be attenuated by applying the H_∞ optimization approach. Keep in mind that the solvability conditions for the UIO method is more restrictive than the H_∞ approach.

The modeling uncertainty can also be represented as polytopic-type structure parameter uncertainty affecting the system matrices and time-varying norm-bounded matrices [50, 51]. Neglected nonlinearities, un-modeled dynamics, and modeling inaccuracies, including physical component faults can also be represented as sources of parameter uncertainties [10]. Two main robust observer methodologies,

that is algebraic Riccati equation (ARE) [52] and linear matrix inequality (LMI) approaches have been pursued in the literature to address systems with above uncertainties. Through the use of parametric Lyapunov functions, the LMI approach is capable of dealing with these uncertainties by designing less conservative filters [53]. It can also be used to solve multi-objective optimization problems by adjusting the sensitivity of the residual with respect to faults and different uncertainties. One of the advantages of the ARE approach is that the structure and gain of a designed estimator can incorporate and represent effects of parameter uncertainties. By utilizing the aforementioned two approaches, various filtering solutions have been proposed to compensate for the effects of parameter uncertainties, namely as robust H_∞ and H_2 filters [53–55], robust Kalman filters (RKF) [56] and set-valued filters. The robust H_∞ filter is constructed such that the H_∞ norm from the disturbance inputs to the filter error output is minimized. It makes no assumption on the spectral properties of the disturbance signal and is only designed for the worst case signal conditions.

To address fault isolation problem in the literature, normally a bank of filters can be used with one of two possible configurations namely as the generalized and the dedicated observer schemes. In generalized observer configurations, the i^{th} filter is sensitive to all faults except the i^{th} fault and also the uncertainty. In dedicated observer configurations, the i^{th} observer is only sensitive to the i^{th} fault and it is insensitive to all the other faults and the uncertainty. The second configuration is better for multiple simultaneous faults isolation [6].

Most of the model-based fault diagnosis approaches are based on the system linear model, extracted by linearizing the nonlinear model of the system. These models are applicable only around the operating point. In order to cover the entire operating range of the system, a certain number of linear models are designed at different operating points and are interpolated by the use of some techniques mentioned in the literature including Takagi-Sugeno fuzzy models [57], the functional

state approach using a discrete representation like automaton for describing the transitions between regions and multi-layer perceptron neural networks to recognize transitions between states [58], and also Markov mixtures of experts to define the transitions [59].

In some other works, the linear approaches are extended to be applied for fully nonlinear models of the system which leads to the nonlinear extension forms of the Kalman filter like the extended Kalman filter (EKF) [60], the unscented Kalman filter (UKF) [61] and the cubature Kalman filter (CKF) [62]. They are all suboptimal state estimators approximating the nonlinear system through linearization and assuming that the noise is Gaussian. Particle filter is another nonlinear state estimator that is widely used to solve FDI problems using the sequential Monte Carlo method without performing any linearization or restricting the noise to be Gaussian. In [63], the particle filters are used to generate a sequence of hidden states which are then used in a log-likelihood ratio to detect and isolate the faults. The general particle filter always suffers from the particle impoverishment problem, which can lead to the misleading state estimation results. In [64] an intelligent particle filter is proposed using the genetic algorithm to improve the particle diversity.

1.3.2 Data-Based Fault Diagnosis Approaches

In contrast to the model-based FDI approaches, the process history data-based approaches need a large amount of system history data in different healthy and faulty conditions. The data is presented as a priori knowledge to the diagnostic system. The procedure is known as the feature extraction that can be conducted in time or frequency domain. This extraction can be either qualitative or quantitative in nature [16]. The expert systems [65] and trend monitoring methods [66] are two major qualitative methods. The expert system FDI approach was initialized in 1980s and is based on a set of rules that are designed by the human expert using the

past experience. The quantitative methods are also categorized into two statistical and non-statistical methods. For instance, the neural networks (NN) are the non-statistical methods whereas the principal component analysis (PCA) [67,68], partial least square (PLS) [69,70] and support vector machine (SVM) [71,72] methods are the major statistical feature extraction methods. Generally, the quantitative methods are similar to pattern recognition problems in which different types of features are extracted and then classified. The feature extraction process normally needs sufficient domain knowledge and is an application-dependent procedure. Different signal processing techniques and classification methods are developed in the literature to extract informative features and to classify them for various purposes [73–76].

Neural networks (NN) are promising tools for fault diagnosis due to their proven success in system identification and strong capability in learning nonlinear transformations that map a set of inputs to a set of outputs [77,78]. In terms of topology, the NN can be classified into radial basis function networks, dynamic recurrent networks, self organizing maps and back-propagation networks. According to the learning strategy, NN-based fault diagnosis can be categorized into supervised-learning-based fault diagnosis and unsupervised-learning-based fault diagnosis [12].

In recent years in addition to the static multi-layer perceptron neural networks, the dynamic neural networks have been extensively used in fault diagnosis problems in order to incorporate dynamics to artificial neural networks [79]. Some of the other most applied neural networks which have been used for dynamic systems are the recurrent [80,81] and time-delay [82] neural networks. In recurrent or time-delay network, the network is fed with current or delayed values of the system inputs and outputs whereas the structure of the network is still static. On the other hand, the dynamic NN have dynamic neurons within their structure which makes them highly flexible and capable to be used for dynamic complex nonlinear systems as an approximator.

In general, the design, training and application of neural networks are case dependent, particularly for complex dynamic system, an inappropriate neural network structure can memorize the noise and become insensitive to the real variations in the signal of interest. One of the challenging problems for the NN-based FDI approach is the design of a proper learning algorithm. The researchers have to train the NN for all the original data representing the entire operational regime. In [83], the authors have tried to use a sequential training called Bootstrap method based on the stored pseudo-data which has the same statistical and parametric dependencies as the original data. The sequential NN training is helpful when there is not sufficient memory for storing all the original data for the entire operational regime and the data is also collected in a piecewise manner. Although, the pseudo-data does not generate the same original data, it has the same statistical information leading to similar estimated residuals.

One of the common forms of the neural network learning algorithms is the back propagation (BP) algorithm which trains and updates the neural network parameters by minimizing the sum of squared error and calculating the gradient of error. The BP algorithm is a supervised learning procedure whose normalized inputs are generated by the real system simulation. The number of hidden layer neurons is defined based on the convergence criterion. The BP approach has some limitations such as it converges very slow and the convergence is not guaranteed and it may converge to any local minimum on the error surface. In addition to the BP algorithm, the hybrid NN is another approach which uses the mixture of BP and variable structure surface. The convergence and the stability of this network has been proved using the Lyapunov function. It is also much faster and more accurate than the BP algorithm [15, 84]. Comparing with the first-order NN learning algorithm like BP which has a low speed of convergence and constant learning rate, the second-order methods like the quasi-Newton and Levenberg-Marquardt have better performance

but still with the problem of local minima [85].

The EKF-based NN is another form of the second-order learning algorithm which does not have any convergence problem since it encodes the information in terms of the state estimation error covariance matrix [86]. This method can be applied for both feed forward and recurrent networks in the forms of general EKF and decoupled EKF-based learning algorithms. The smooth variable structure filter (SVSF) is another NN learning approach as a kind of recursive sliding mode state and parameter estimator which forces the NN weights to the existing sub-space around a true system state trajectory [87]. Then, the states are forced to switch along the true state trajectory and the saturation term is used in this region to reduce the magnitude of chattering and to smooth the results [86, 88].

There are multiple work in the literature addressing the convergence and stability of various feed forward and recurrent neural networks training mechanisms. In [89], the stability of a discrete-time recurrent high-order neural network (RHONN) that is trained by the EKF algorithm is proved based on the Lyapunov approach. In [90], an effective EKF-based RNN training approach with the controllable training convergence is developed. Using the Lyapunov and the maximum likelihood methods, two adaptation laws are developed for the covariance matrices of the process and measurement noise. Moreover, the convergence of an EKF-based RNN training is investigated in [91] in which the dead-zone Kalman filter algorithm is utilized to improve the training robustness. The Lyapunov method is also used to show the stability of the proposed training approach for the RHONN.

In some practical applications, the statistical and non-statistical data-driven approaches are combined to improve the FDI performance. For instance, in [92] the Bayesian network is integrated with a recurrent NN in which the network is trained for the system under normal and known faulty conditions, whereas the Bayesian network is employed to generate random residuals. Moreover, in [93] a dynamic PCA

and feed-forward back-propagation network are combined to detect stator insulation failures, broken rotor bars, and bearing faults. The PCA is used to extract different features that are then applied to the NN to finally detect potential faults.

1.3.3 Hybrid Fault Diagnosis Approaches

Model-based and data-based fault diagnosis approaches have their distinctive advantages and various constraints. The model-based approaches can detect and isolate different types of faults with small amount of real-time data. However, its performance highly depends on the accuracy of the mathematical model that has been derived based on the physics principles or input-output identification techniques. On the other hand, the data-based approaches do not need any particular model and so they are more suitable to be applied for complicated industrial applications in which a comprehensive model is not available or it is challenging to be derived. However, the data-based approaches hardly consider the system dynamics which may lead to their degraded performance in presence of disturbances and system uncertainties. Therefore, in order to leverage the strength of various fault diagnosis approaches the hybrid structures are proposed in which two or more approaches are integrated.

In [94], the signal-based method and data-based methods are integrated to detect the plastic bearing faults, where a statistical approach is also used to isolate the outer race fault from other types of faults using the frequency-domain features that are extracted by the fast Fourier transform. The other types of faults are diagnosed using the K nearest neighbors (KNN) which is a data-based fault classifier on the basis of time-domain features. The vibration based analysis fault diagnosis is developed in [95] in which the wavelet transform is used to extract the features from the vibration signals and the PCA plus the probabilistic NN are then used to classify the extracted features. In [75], a wavelet transform is used to extract the features from stator currents, the PCA method is employed to reduce the dimension

and to eliminate the linear dependency among the features and the fuzzy SVM is then used to classify the features in order to detect the type and degree of a fault in a permanent-magnet synchronous generator motor. In [96], an SVM is used to detect a fault in chemical reactors that are subjected to high nonlinearities and variability of dynamic, however it is not capable of locating the fault due to highly transitional dynamics. Therefore, to improve fault isolation an observer is combined with the SVM, where the model is corrected using the information provided by the SVM in non-faulty conditions. Moreover, different hybrid approaches are presented in [97] to address the transmission line fault detection and isolation problem.

1.3.4 Fault Diagnosis Techniques Applied to the Gas Turbine Engines

Since early research on FDII, gas turbines have been one of the challenging application areas which have received much attention. The main approach in gas turbines FDII is based on the GPA, which enables one to accomplish the actuator, sensor and component diagnosis by observing the engine's parameters such as the rotor speed, temperature and pressure at different stages and the fuel flow rates [15]. Various fault diagnosis techniques have been developed for gas turbines based on GPA ranging from Kalman filters [98–101], neural networks [102], fuzzy logic [103], genetic algorithms [104], sliding mode observers [105], component adaptation approach [106,107], particle filters [108–110], H_∞ filter for linear parameter varying engine models [111] and hybrid diagnosis [112]. Some of the linear approaches have been extended to fully nonlinear models of the engine that have led to nonlinear extensions of the Kalman filters to extended Kalman filters (EKF) and unscented Kalman filters (UKF) [3,113].

Most of the proposed approaches for different types of fault diagnosis applied to

the gas turbines are based on the nominal engine modeling, while the engine performance deteriorates during its life cycle. The gas turbine engine health deterioration influences the fuel economy, and impact emissions, component life consumption, and thrust response of the engine. Therefore, in many applications the operational data is collected and used to evaluate the system parameters in order to improve the safety and reduce the operating costs. There are also various methods to estimate the health parameters, such as the weighted least squares [114], expert systems [115], Kalman filters [99, 116, 117], neural networks [118], and genetic algorithms [119].

In Kalman filter based parameter estimation algorithms, the parameters are augmented to the state vector and are simultaneously estimated with the state variables. This method has some numerical problem; therefore, the dual estimation procedure for estimating the parameters and state variables by the use of two parallel observers has been proposed to overcome the aforementioned numerical problem [85, 120]. Moreover, in [121] a Kalman filter and a maximum a posteriori (MAP) estimator are used to estimate the engine performance parameters, whereas a sensor selection procedure is also proposed to minimize health parameters estimation errors. The proposed method is finally applied to the linear turbofan engine model.

Generally, the engine health deterioration can be considered as one of non-fault related factors which may influence the rate of false alarms and/or incorrect fault detections. To address this issue, there are multiple model-based and data-based approaches are proposed in the literature that are robust with respect to different modeling uncertainties such as engine health degradation, noise and disturbances. For instance, in [122] a multiple model-based robust fault detection and isolation approach is proposed and tested on single-shaft industrial gas turbine working on different operating points. The MLP is also employed to perform FDI task and is combined with the locally linear neuro-fuzzy model to improve the robustness and fault detection accuracy particularly for incipient faults. In [123], a novel unknown

input observer is designed to estimate the faults of the system subjected to process disturbances. In this study, the disturbance is not decoupled completely by the use of the UIO, however it is attenuated by combining the UIO technique with linear matrix inequality (LMI). In [124] a dual robust Kalman filter is developed to estimate engine state state variables and health parameters to improve the FDI robustness for the turbofan engine. A fault detection estimator is developed in [112] that is combined with a bank of nonlinear adaptive fault isolation estimators to determine the type and location of a fault. The proposed FDI architecture is applied to a realistic nonlinear aircraft engine model recently developed by NASA researchers, whereas the robustness with respect to the normal engine health degradation is also maintained by means of an adaptive threshold.

The neural networks have been also extensively used for the gas turbine engines fault diagnosis. In [125] multiple neural networks are proposed for single shaft gas turbine fault diagnosis. The authors of [126] have extended the multiple neural networks to a cascaded network in order to isolate sensor and component faults. Probabilistic and hybrid neural networks are the other two important kinds of networks that have been used for gas turbine fault diagnosis [118, 127]. In [128], an ensemble of dynamic neural networks are designed for gas turbine health monitoring purposes in which various dynamic networks namely as, multi-layer perceptron (MLP), radial basis function (RBF) and dynamic SVM are individually trained to represent gas turbine dynamics. Next, three different ensemble homogeneous and heterogeneous configurations are constructed that are more accurate in engine dynamic identification. The jet engine component fault detection and isolation problem is also addressed by the use of multiple dynamic neural networks corresponding to various operating healthy and faulty modes of the engine in [129]. The FDI effectiveness is also investigated in presence of un-modeled dynamic, noise and disturbances. In [130], multiple auto-associative neural networks are used to solve sensor and

component FDI problem for an aircraft engine. The sensor data validation is also conducted in this study for the purpose of engine health monitoring. The multi sensor health diagnosis methodology is also proposed in [131] in which a hierarchical structure of deep belief network with multiple stacked restricted Boltzmann machines is employed to address aircraft engine health diagnosis using the sensor measurements.

Unlike the adaptive neural-network-based fault diagnosis approaches which need the upper bound of the uncertainty as an a priori knowledge, the hybrid framework is capable of working with any unknown uncertainty. In this framework, the empirical-based method like the NN is applied for different types of uncertainty approximation. In [132, 133], the NN is applied to approximate the linearization error as a source of modeling error for adjusting the linear observer. The authors have linearized the aircraft engine model for designing a linear Kalman Filter (LKF) to estimate the unmeasured performance parameters like the high pressure turbine inlet temperature, compressor stall margin and the thrust. For this purpose, the LKF is integrated with an RBF network with the growing and pruning learning algorithm which adds or deletes neurons to the hidden layer based on the RBF inputs [134]. The network is trained at different percentages of health degradations for a certain range of operational regime. Therefore, it is essential to have a large training data to cover the entire operational regime and the levels of health degradations which leads to increasing the size of the network as well as the computational complexity. Hence, it seems better to have different smaller networks each designed for a particular range of the operational regime and then have a method for scheduling among different networks.

The fusion of different processing techniques enables us to have a more reliable engine modeling and a fault diagnosis strategy. In [135, 136] the authors have worked on the hybrid engine model building for tracking the engine outputs.

They have proposed an Enhanced Self Tuning On-Board Real-Time Engine model (eSTORM). The eSTORM is the improved version of STORM. The STORM consists of two parts: the nominal state variable model (SVM) and a tuner which uses the residual between the real engine and the SVM outputs to adapt the SVM by estimating a set of health parameters representing the health deterioration of the engine. In eSTORM, a data-based approach such as a neural network is integrated with STORM while receiving the residuals (differences between the real engine and STORM outputs) and engine inputs to capture the un-modeled dynamics and uncertainties which influence the diagnostic information in STORM tuner. For training the neural network, first the tuner module is disabled and the engine input is applied just to the SVM to find the residual between the real engine and the SVM. Then, the engine inputs and the residuals are stored for training the NN. The network output is the estimated residual and the SVM is the piecewise linear (PWL) models being interpolated in terms of one of the variables. The tuner module is a linear Kalman filter which augments the health parameters to the state vector while its estimated outputs are used to adjust the SVM to the off-nominal performance condition. For capturing the modeling uncertainties and errors, the authors have used the non-linear autoregressive moving average method to find the transfer function between the input and the estimated residual vector. This approach has been mainly used for engine performance tracking, but not for the FDI applications. Also, the NN training is conducted using the back-propagation technique which converges slowly and may stuck in local optimum.

1.3.5 Piecewise Linear Models

Piecewise linear (PWL) systems have been extensively used in multiple control system applications to approximate a nonlinear system. In practical control systems, there are many components such as the dead-zone, saturation, relays and hysteresis

that can be modeled by the use of piecewise linear systems. Deriving the necessary and sufficient conditions for the stability of PWL models is an active field of research. There are many work in the literature in which the stability of switched PWL models is investigated for different switching mechanisms. In [137], the PWL model stability is studied based on a piecewise smooth Lyapunov function. It is shown that the system stability can be established if the Lyapunov function is obtained by solving a set of linear matrix inequalities. In [138], the stability and optimal performance are investigated for the PWL models based on the continuous Lyapunov function. The authors in [139] discussed stability analysis and controller design of PWL systems which may involve multiple equilibrium points based on a common quadratic Lyapunov function and a piecewise quadratic Lyapunov function. Moreover, piecewise affine system is a class of PWL models that is utilized in several papers including [140–142]. It is a broad modeling class that has been extensively used in hybrid and nonlinear system modeling.

1.4 General Problem Statement

One of the main challenges in the area of gas turbine engine health monitoring is the design of a robust FDI strategy to be applied for the entire engine life cycle. In other words, the FDI strategy should be not only robust with respect to different modeling uncertainties to avoid the false alarm generations, but it should be also capable of maintaining its performance during the entire engine life cycle. For this purpose, three different FDI approaches including multiple hybrid Kalman filters, multiple robust Kalman filters and the hybrid dynamic recurrent neural network based structures are proposed in this thesis to address the sensor fault detection and isolation problem in presence of engine health degradations, noise and disturbances for the single spool turbojet engine. In all the proposed FDI schemes, the engine health

parameters degradation is assumed as a major source of the time-varying modeling uncertainty. The other uncertainty effects such as process and measurement noise as well as the modeling errors due to the linearization process will also be investigated in our work.

In most of the available work in the literature, the aircraft engine FDI problem is addressed without considering the robustness with respect to the engine aging process during the life cycle. Moreover, most of the FDI approaches are employed in the cruise condition, whereas there is a high risk of fault occurrence during the climbing and landing modes. Therefore, in this thesis the FDI robustness is the main goal that is addressed using different model-based and hybrid structures. In Chapters 3 and 4 of this thesis two model-based FDI approaches namely as *Hybrid Kalman Filter* and *Robust Kalman Filter* are developed to solve sensor FDI problem. In Chapter 5, the previously developed filters are integrated with a *Dynamic Recurrent Neural Network* that is trained offline using the *Extended Kalman Filter* to improve the robustness and FDI performance in presence of various uncertainty sources. Moreover, to investigate the performance of our proposed FDI approaches multiple simulation studies are conducted and the results are compared with different available methods in the FDI literature.

For simulation studies, a single-spool aircraft engine that was previously created and validated by the commercially available GSP software is utilized. This model was developed in Simulink based on the real engine rotor and volume dynamics with common sensors measuring the temperatures and pressures at the exits of compressor and turbine as well as the spool rotational speed. As per the Monte-Carlo simulation studies as well as the computed performance metrics, it can be claimed that our proposed methodologies in this thesis are applicable to the real engine and various gas turbine engine benchmarks in literature.

1.5 Thesis Objectives

As stated earlier, the robustness of FDI approaches towards different non-fault related factors including the modeling uncertainties, parameter variations, noise and disturbances is one the challenging topic in the area of fault diagnosis, particularly the safety critical systems as the aircraft engines. This problem is addressed in different ways in this thesis.

In the first part of the thesis, we propose a *hybrid Kalman filter* (HKF) scheme that consists of a single nonlinear on-board engine model (OBEM) augmented with piecewise linear (PWL) models constituting as the multiple model (MM) based estimators to cover the entire engine operating regime. Therefore, multiple HKFs are constructed to ensure that the FDI algorithm works effectively in a wide range of operating conditions by decomposing the engine operating range into sub-regions each represented by a PWL model. We then apply a Bayesian approach to generate a general combined model based on the PWL models normalized weights. This provides us with a soft transition or interpolation among the PWL models. Towards this end, we have integrated the generalized likelihood ratio (GLR)-based method with our MM-based scheme to estimate the sensor fault severity under various single and concurrent fault scenarios. In this part of the thesis, it is assumed that the reference baselines for the engine health parameters, namely the efficiencies and the mass flow rates of the turbine and the compressor, can be estimated after a certain number of flights by using an off-line health monitoring module for determining the percentages of degradations. Consequently, in order to ensure the reliability of our proposed FDI scheme during the engine life cycle, the reference baselines are periodically updated for the OBEM health parameters. This procedure will be useful in preventing occurrence of false alarms due to the engine health parameters degradations. Despite this updating process, there is always a mismatch between the values of the real engine health parameters and the ones that are used in the OBEM

due to the off-line estimation errors of the health monitoring method. Therefore, the robustness of our proposed FDI scheme with respect to various health parameters estimation errors is also investigated through performing extensive Monte Carlo simulations.

In the second part of the thesis, a robust sensor FDI strategy using the MM-based approach is proposed that remains robust with respect to both time-varying parameter uncertainties and process and measurement noise in all the channels. The scheme is composed of *robust Kalman filters* (RKF) that are constructed for multiple PWL models. The parameter uncertainty is modeled by using a time-varying norm bounded admissible structure that affects all the PWL state space matrices. The robust Kalman filter gain matrices are designed by solving two algebraic Riccati equations (ARE) that are expressed as two linear matrix inequality (LMI) feasibility conditions. The main objective is to propose a robust filter that satisfies the overall performance requirements and is not affected by system perturbations. The requirements include a quadratically stable filter that ensures bounded estimation error variances having predefined values. The proposed multiple RKF-based FDI scheme is simulated for an entire flight profile of a single spool turbojet engine to diagnose various sensor faults despite the presence of parameter uncertainties, process and measurement noise. Our comparative studies confirm the superiority of our proposed FDI method in terms of promptness of the fault detection, estimation accuracy, lower false alarms and missed detection rates, as well as robustness with respect to the engine health parameters degradations when compared to the methods that are available in the literature.

In the third part of the thesis, a hybrid approach is proposed to improve the robustness of FDI scheme with respect to different sources of uncertainties. For this purpose, a *dynamic recurrent neural network* (DRNN) is designed to approximate the turbojet engine uncertainty due to the health degradations. The proposed

DRNN is trained offline by using the extended Kalman filter (EKF) algorithm for an engine with different levels of uncertainty, but with healthy sensors. The trained DRNN with the fixed parameters and topology is integrated with our online model-based FDI algorithm to approximate the uncertainty terms of the real engine. The approximated uncertainty is then removed from the sensor measurements and the modified sensor measurements are then applied into our proposed bank of filters to detect and isolate the engine sensor faults. In this part, the previously proposed HKF and RKF are integrated with the trained DRNN to construct the hybrid FDI structure. Different properties such as the fault detection time, false alarm, missed and incorrect fault detection rates as well as the ranges of detectable sensor faults are determined for our proposed hybrid FDI approach. Finally, the efficiency of different proposed FDI schemes is compared in terms of the faults detection times, robustness with respect to the engine health degradation, FDI accuracy and applicability for the entire flight profile.

1.6 Thesis Contributions

The main contributions of this thesis are summarized as follows:

- Multiple HKF-based sensor FDI scheme
 - The explicit derivations of the discrete-time HKF scheme is formally provided in Chapter 3.
 - A modular and hierarchical non-interacting MM-based HKF structure is developed to detect and isolate single and concurrent sensor faults during the entire engine operating regime (flight profile) having lower fault detection time and better robustness towards the engine health parameters degradations as compared with the other linear and nonlinear filtering methods in the literature. Our method is capable of operating during

the entire engine life cycle through periodically updating the reference baselines of the engine health parameters for the nonlinear OBEM. In addition, the computational time of our proposed method is lower than the investigated linear and nonlinear methods.

- Through performing extensive simulation studies and measuring the mean of residual signals, it is shown that the HKF is capable of estimating the engine outputs more accurately with less number of operating points and false alarm rates as compared to the linear Kalman filter (LKF) method.
 - Our proposed MM-based HKF structure is integrated with the GLR scheme to estimate the fault severity. This is accomplished by specifically eliminating the estimation of the fault detection time which is a necessary step in the standard GLR scheme.
 - Our proposed multiple HKF-based FDI scheme is compared with the MM-based schemes that utilize various linear and nonlinear filtering approaches such as the linear Kalman filter (LKF), extended Kalman filter (EKF), unscented Kalman filter (UKF) and the cubature Kalman filter (CKF) in terms of the promptness of the fault detection, false alarm and incorrect fault detection rates, robustness with respect to the engine degradations and computational time.
- Multiple RKF-based sensor FDI scheme
 - An RKF is proposed and designed for a system with time-varying parametric uncertainties in all the process matrices. It is formally shown that the filtering process is quadratically stable and is guaranteed to satisfy the individually prescribed *a priori* bounds on the state estimation error variances.
 - Multiple RKFs are designed associated to different PWL models that are

created at various operating points. Afterwards, a Bayesian approach is applied to generate a general integrated model as well as the combined residuals and covariance matrices that are associated with the robust filters based on the normalized PWL models weights to address the robust estimation problem for the entire operating range of an uncertain nonlinear system.

- The proposed multiple RKF's with their corresponding combined residual vectors and covariance matrices are then applied to solve the sensor FDI problem by using the MM-based approach for detecting and isolating sensor bias faults corresponding to various severities. Consequently, a robust MM-based approach is proposed to solve the sensor FDI problem. Unlike some of the available work in the literature, our proposed robust FDI scheme does no longer need to design any static or adaptive threshold for the fault detection algorithms based upon the *a priori* assumption on the uncertainty level.
- Unlike the first part of the thesis, the RKF-based FDI scheme is formally designed to remain robust against time-varying norm bounded parameter uncertainties by utilizing our proposed RKF approach without requiring one to estimate and update the system health parameters.
- The proposed robust MM-based FDI scheme is used to solve sensor FDI problem for the single spool turbojet engine. For this purpose, the deviations of engine health parameters from their healthy reference baselines are considered as time-varying parameter uncertainties. Moreover, our proposed robust FDI structure is evaluated in terms of its (a) estimation accuracy, (b) promptness in sensor fault detection time, and (c) its low false alarms and low incorrect fault detection rates by performing extensive simulation studies. The results are also compared with available

methods in the literature.

- Hybrid sensor FDI scheme
 - A hybrid structure as an integration of the DRNN-based identifier with the mathematical model of the system is proposed to approximate different uncertainty sources due to the turbojet engine modeling errors, health parameter variations, process and measurement noise. The DRNN is trained offline by using the EKF method which has a higher convergence rate and fitting accuracy as compared to the first order conventional learning approaches namely as, back-propagation learning method.
 - The proposed hybrid engine modeling strategy is integrated with our previously developed Hybrid Kalman Filter (HKF) and Robust Kalman Filter (RKF). Invoking such this integration leads to the superior sensor FDI results which decreases the fault detection time in different engine operating regime, enhances the robustness level and improves the FDI accuracy and performance outcomes as compared to our previously proposed pure model-based FDI approaches.
 - The convergence of our proposed recurrent neural network that is trained by means of the EKF algorithm is also investigated in Chapter 5.
 - Using extensive simulation studies and comparing different performance indices, it is demonstrated that the fusion of multiple HKFs with our proposed DRNN scheme is the superior method that is highly recommended as compared to the other methods that are either developed in this thesis or in the literature to be applied for gas turbine engine fault diagnosis.

1.7 Thesis Organization

In Chapter 2, we briefly review the gas turbine engine modeling as well as the required formulations corresponding to popular available estimators in the literature to which our proposed FDI approaches are compared. Various engine parameters and degradation factors are also introduced in this chapter.

In Chapter 3, we propose the overall hybrid Kalman filter structure as well as the onboard engine model in Section 3.1, whereas Section 3.2 presents the integration process of piecewise linear models. The sensor FDI multiple-model-based scheme is explained in details in Section 3.3 as well as the corresponding MM structures that are utilized to detect and isolate single and concurrent sensor faults. Our proposed HKF-based FDI approach is also integrated with the GLR method to estimate the severity of sensor fault in Section 3.4. In Section 3.5 multiple simulation case studies are presented in details to investigate the effectiveness of our proposed multiple HKF-based FDI scheme for different healthy and faulty scenarios under various engine health degradation magnitudes. In this section, our proposed approach is also compared with multiple popular estimators in the literature namely as, the extended kalman filter, unscented Kalman filter and the cubature Kalman filter [60–62,143]. Finally, Section 3.6 concludes the chapter.

Chapter 4 focuses on robust multiple-model-based FDI scheme for the linearized system with time-varying norm-bounded parameter uncertainty affecting all the state-space matrices as presented in Section 4.1. A robust Kalman filter is designed for the introduced uncertain system in Section 4.2. In this section, it is also shown that the proposed RKF is quadratically stable and satisfies the performance requirements on state estimation error variances. The corresponding piecewise linear models interpolation is explained in Section 4.3. Section 4.4 gives information on the structure of robust multiple-model scheme to address sensor FDI problem.

Multiple simulation case studies are conducted in Section 4.5 to investigate the effectiveness of our proposed robust MM-based FDI scheme and to compare it with similar approaches in the literature [4]. Finally, Section 4.6 concludes the chapter.

Chapter 5 is devoted to the novel hybrid FDI approach in which the dynamic recurrent neural network (DRNN) is integrated with the engine mathematical model to improve the modeling accuracy and to finally combine with our previously pure model-based FDI approaches including the HKF and RKF. The elements of our proposed hybrid FDI scheme are presented in Section 5.1. The DRNN structure as well as the offline network learning process in which an extended Kalman filter is employed to train the network parameters are explained in Section 5.2. Afterwards, Section 5.3 presents the analytical investigations on the convergence behavior of our proposed DRNN. Multiple simulation case studies are presented in Section 5.4 in which the optimal network parameters are determined for different engine uncertainty magnitudes. The hybrid DRNN-HKF and DRNN-RKF based FDI schemes are also compared in Section 5.3 in terms of their corresponding fault detection times, estimation accuracy, false alarm and incorrect fault detection rates as well as the ranges of detectable faults. Finally, Section 5.5 concludes the chapter.

Chapter 6 concludes the thesis and provides suggestions for future work.

Chapter 2

Background Information

In this chapter, the thesis background information is given on two important topics namely, the gas turbine engine history, operation and health degradation as well as some background of various filtering methods in the literature that are compared with our proposed filtering methods in the following chapters of this thesis.

2.1 Gas Turbine Engine History

Since the end of World War II, the jet engines have become at the forefront of aviation development. The first jet engine with centrifugal compressor driven by the radial turbine was developed by a German physicist, Hans Von Ohain, who worked for Ernst Heinkel, specializing in advanced engines in 1939. Following Ohain, Frank Whittle, a British scientist, also designed a centrifugal compressor driven by an axial turbine completely on his own. The General Electric and Pratt & Whitney are the two American jet builders who added the German lessons to those of Whittle and other British designers to design different fuel efficient and high thrust engines in aerospace industry [144]. The aircraft engine produces the hydraulic power, electric power, propulsion force and bleed air for the pneumatic system in order to provide the movement of the aircraft in the atmosphere over a long distance. The turbojet,

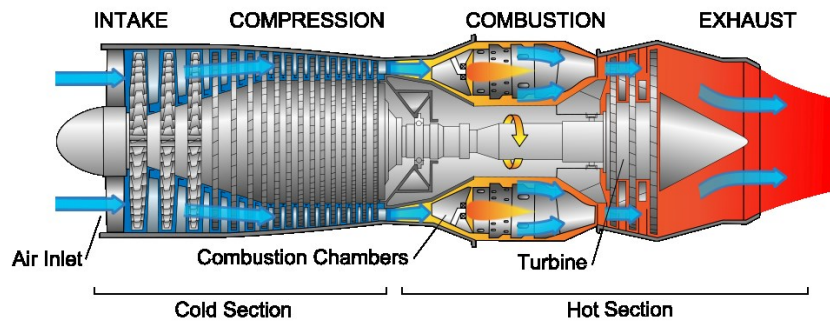
turbofan, turboprop and auxiliary power unit are the four important types of jet engines.

The turbojet engine is the first developed gas turbine engine that is used in less fuel efficient high-speed aircrafts generating substantial noise due to the extremely exhaust gas speed. The turbofan engines are also designed based on the turbojet engine fundamentals. They still provide high speed, but with better fuel efficiency which makes more efficient to be used in modern aircrafts. The turboprop engines are particularly designed to produce shaft horsepower that is used to drive the propeller. They provide us with the proper compromise between the high speed and fuel efficiency. The auxiliary power unit produces electric and pneumatic power for the aircrafts when the engines are not available. All of the above types of aircraft engines are the reaction engines that work similarly. They produce a propulsion force which is in the opposite direction of the mass flow through the jet nozzle and follows the Newton's laws of motion. Figure 2.1 illustrates different types of engines.

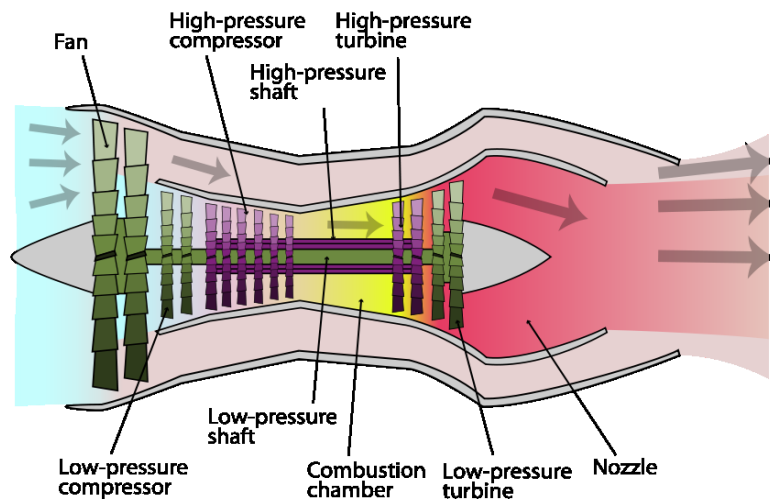
2.2 Principles of Jet Propulsions

In order to produce the propulsion force, the air has to be accelerated with pressure that can be increased by means of two methods: first it can be increased mechanically by the compressor, and second it can be increased thermally by increasing the volume of the air while the mixture of the fuel and air is heated in the combustion chamber. By the late of 1930's there has not been any efficient compressor which was able to yield the large continuous airflow to produce the suitable thrust. The combination of the above two methods did finally provide the aircraft with the suitable propulsion force.

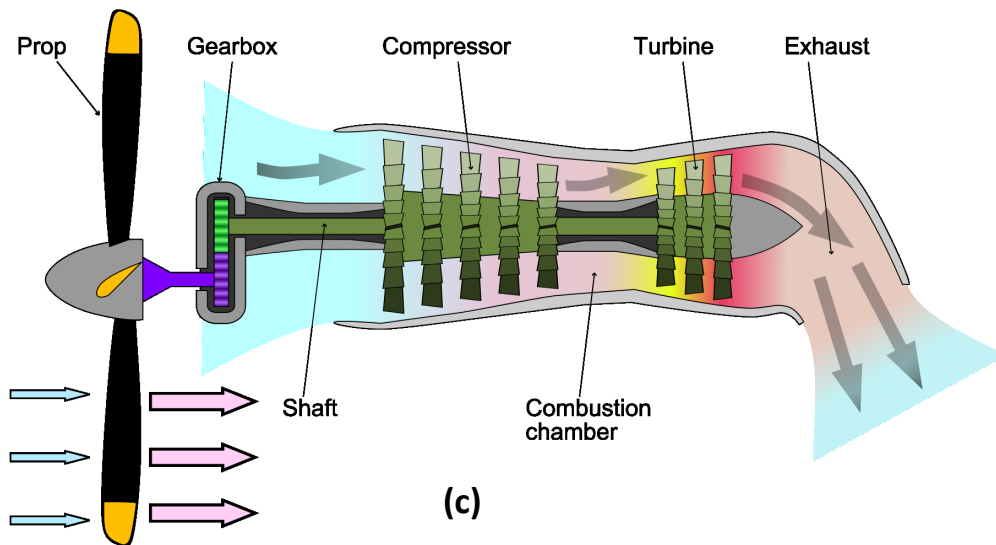
The gas turbine engines generate the thrust by accelerating the ambient air.



(a)



(b)



(c)

Figure 2.1: Different engine diagrams: (a) Turbojet, (b) Turbofan and (c) Turboprop [1].

The turbojet engines produce the high velocity gas, of which certain portion is used to drive the compressor or the accessories and is converted to the thrust. The high outlet gas velocity leads to the high aircraft speed as well as the loud noise sound. The turboprop engines produce small acceleration in a large quantity of the air with a propeller. The propeller is driven directly by means of the compressor shaft or the free turbine. There is also a reduction gear in turboprop engines that reduces the turbine rotation to the speeds that can be managed by the propeller. The turboprop engines are sufficiently efficient since all the air associated with them is converted to the torque. The turbofan engines use the advantages of both turbojet and turboprop engines. Their fan is enclosed in a casing instead of the propeller and is driven by the turbine shaft. They are mostly twin or triple spool engines, but without any reduction gear. In turbofan engines, a large portion of the air is converted to the torque that is applied to the fan and compressor, whereas its small portion is discharged by the engine core where it is converted to the thrust. Hence, the total thrust is produced by both fan and the core engine. The air portion value depends on the bypass ratio (the amount of air passes through fan duct comparing with the one passes through the core engine). The bypass ratio is usually between 4:1 to 9:1 [145].

2.3 Gas Turbine Engine Operation

The conversions between the mechanical and thermal energy are conducted according to thermodynamics laws, showing the relations between gas pressure, temperature and volume. A basic principle of physics called the law of conservation of energy governs the jet engine operation. A jet engine is designed to Hoover up huge amounts of air and to burn it with vast amounts of fuel. The air intake, compression, combustion, and exhaust are the four important operational stages of an

aircraft engine working cycle that happen simultaneously. Each stage is conducted in a particular engine element as follows [146].

First the ambient airflow is led to the engine through the gas inlet which provides sufficient air during different flight conditions. In this stage, the inlet air static pressure is increased. Then the air is led to the compressor which increases the pressure and provides continuous air for different subsystems namely, the combustion chamber, the pneumatic, cooling and anti-icing systems. Then a large quantity of air and fuel is mixed in the combustion chamber. In this section, the energy increase should be maximized, the pressure decrease and any damage to the combustion chamber materials should be minimized. The turbine provides torque for the compressor and also the gearbox. It also delivers the power to the fuel pump, oil pump, pneumatic pump, generator and other accessories. In turboprop engines the turbine deliver the power to the propeller. Finally, the exhausting duct lead the exhaust gas in to the atmosphere and prevents the contact of this gas from the below part of the wings. The jet nozzle increases the exhaust gas speed and sends it in to the correct direction [145].

Note that when the air passes through the turbine its temperature and pressure are decreased, whereas the volume is increased, and when it leaves the engine through the exhausting duct and the jet nozzle its temperature and pressure is continuously decreased and the velocity is increased. Moreover, the above working cycle is called the Brayton cycle which ideally has four important stages as below [147]:

- isentropic process: ambient air is drawn into the compressor, where it is pressurized,
- isobaric process: the compressed air moves towards the combustion chamber, where the fuel is burned, air is heated in a constant-pressure process,

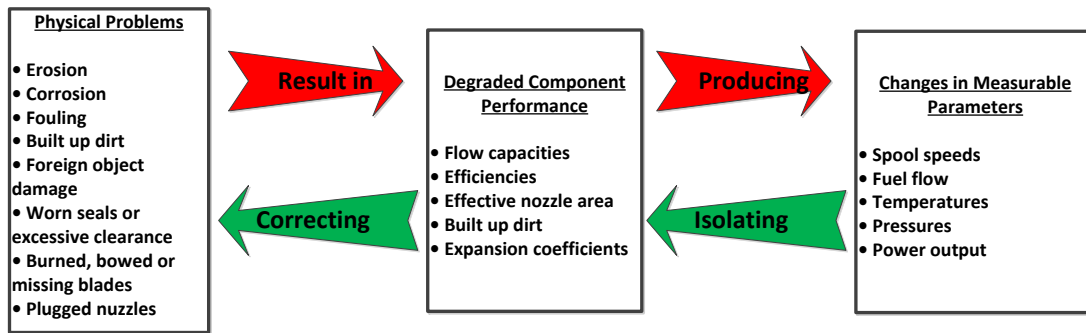


Figure 2.2: Information flow diagram associated with several gas turbine engine physical problems [2].

- isentropic process: the heated, pressurized air then gives up its energy, expanding through a turbine, where some of the extracted work is used to drive the compressor,
- isobaric process: heat rejection to the atmosphere.

2.4 Gas Turbine Engine Health Degradation

During the engine lifetime, the compressors and turbines undergo degradation due to various effects. The degradation level or the engine effective age determines the engine general health status. In the gas path, the health condition of each engine component is defined by its health parameters namely, the efficiency and mass flow rate that are slowly changed due to the engine aging process. These parameters cannot be measured directly, however their associated variations can be observed using the engine sensor measurements. Figure 2.2 displays different types of engine damages and physical problems as well as the information flow for the gas turbine engines [2].

In addition to the engine gas path sensors that are measuring the temperature, pressure and rotational speed at different stages of the engine, the vibration and oil monitoring sensors are also essential to complete the health monitoring process. The

aforementioned sensors can be used to detect degradation with bearings, gearing and other accessories as well as the lubrication system.

In this thesis, the robustness of our proposed fault detection and isolation approaches is investigated with respect to the engine health degradation, particularly the compressor degradation which is the major cause of output and efficiency loss in a gas turbine [148]. As per the information flow diagram in Figure 2.2, there are several factors affecting the compressor performance, whereas the most common cause is the compressor fouling. The compressor fouling is mostly caused by adherence of particles to the compressor surfaces. It increases the surface roughness and so decreases the compressor efficiency and mass flow rate. The compressor fouling is the recoverable deterioration that can be alleviated by online or offline compressor washing. During the fouling process, the reduction in compressor flow rate is almost twice as much as that in compressor efficiency. This in turn will lead to increase in fuel or electric demand driving the compressor [149, 150].

2.5 Gas Turbine Engine Mathematical Model

In this chapter, we review the main application details that is used in this thesis. All the developed approaches in this thesis are applied for a commercial single spool gas turbine engine that is previously developed in [3]. This model is generated based on the rotor and volume dynamics as defined below:

- Rotor dynamics: It shows the power imbalances between the compressor and turbine which causes the acceleration or deceleration of the rotor connecting the compressor and turbine shafts together.
- Volume dynamics: It shows any mass flow imbalance among the engine components that cause changes in pressure.

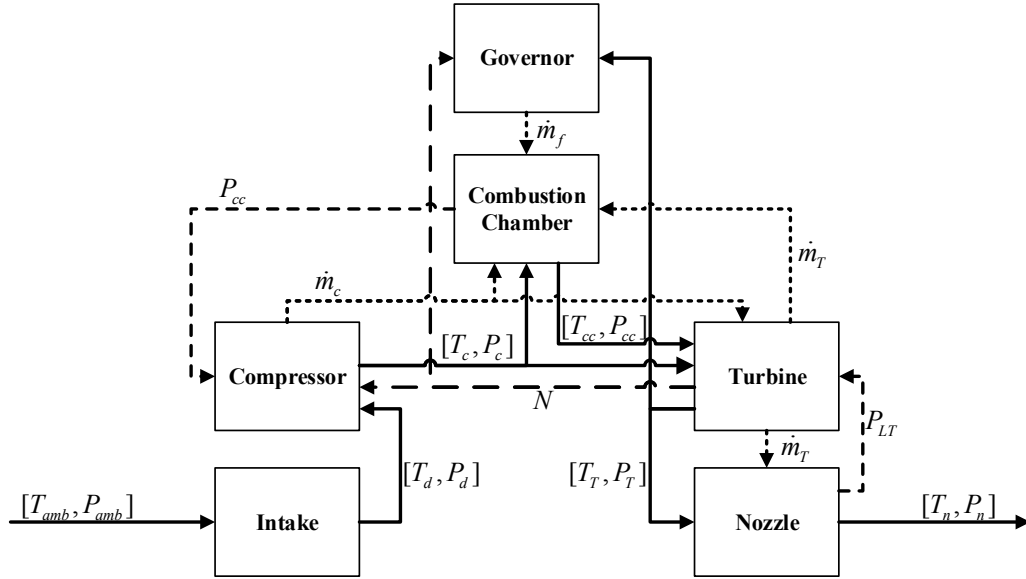


Figure 2.3: Information flow diagram associated with single spool turbojet engine [3].

Our model is validated by the commercially available standard software *GSP* 10 [151]. The responses corresponding to our mathematical model and the *GSP* match each other within an acceptable error tolerance (below 5%). The more detailed description of the model is given in [152, 153]. Figure 2.3 illustrates our single spool jet engine modular diagrams with the associated information flow in the SIMULINK model.

Note that in this model the heat transfer dynamics is not considered due to its negligible effects on engine behavior as compared to the rotor and volume dynamics. In the following, the detailed mathematical expressions corresponding to our engine dynamics are presented.

2.5.1 Rotor Dynamics

The following differential equation displays the energy balance among the compressor and turbine:

$$\frac{dE}{dt} = \eta_{\text{mech}} W_T - W_C, \quad (2.1)$$

where $E = \frac{J(\frac{N \cdot 2\pi}{60})^2}{2}$. Refer to the list of symbols for finding the descriptions corresponding to other different terms and variables.

2.5.2 Volume Dynamics

As explained in the previous section, the volume dynamics represents the mass flow rate imbalances among the engine components. This dynamics can be described as follows:

$$\dot{P} = \frac{\gamma RT}{V} (\sum \dot{m}_{\text{in}} - \sum \dot{m}_{\text{out}}). \quad (2.2)$$

where $R = 8.31447$ (Joul/mol.K), γ , \dot{m} (Kg/s), V (m^3), T (K) and P (Pascal) denotes the gas constant, heat capacity ratio, mass flow rate, volume, temperature and pressure corresponding to different engine components including the compressor and turbine.

2.6 Set of Nonlinear Equations

In this section, a set of nonlinear equations corresponding to a single spool jet engine is provide. In this thesis, our model is extended to the entire flight profile and is simulated in the SIMULINK to be used as both the actual engine and the on-board engine model(OBEM). Both the actual engine and the OBEM models operate in almost the same ambient conditions. The set of nonlinear state-space equations that

are used for the engine model are given as follows:

$$\begin{aligned}
\dot{P}_{CC}(t) &= \frac{P_{CC}(t)}{T_{CC}(t)c_v\dot{m}_{CC}(t)} [(c_p T_C(t)\alpha_{\dot{m}_C}\dot{m}_C(t) + \eta_{CC}(t)H_u\dot{m}_f(t) - c_p T_{CC}(t)\alpha_{\dot{m}_T}\dot{m}_T(t)) \\
&\quad - c_v T_{CC}(t)(\alpha_{\dot{m}_C}\dot{m}_C(t) + \dot{m}_f(t) - \alpha_{\dot{m}_T}\dot{m}_T(t))] \\
&\quad + \frac{\gamma RT_{CC}(t)}{V_{CC}(t)} (\alpha_{\dot{m}_C}\dot{m}_C(t) + \dot{m}_f(t) - \alpha_{\dot{m}_T}\dot{m}_T(t)), \\
\dot{N}(t) &= \frac{\eta_{\text{mech}(t)}\alpha_{\dot{m}_T}\dot{m}_T(t)c_p(T_{CC}(t) - T_T(t)) - \alpha_{\dot{m}_C}\dot{m}_C(t)c_p(T_C(t) - T_d(t))}{JN(t)(\frac{\pi}{30})^2}, \\
\dot{T}_{CC}(t) &= \frac{1}{c_v\dot{m}_{CC}(t)} [(c_p T_C(t)\alpha_{\dot{m}_C}\dot{m}_C(t) + \eta_{CC}(t)H_u\dot{m}_f(t) - c_p T_{CC}(t)\alpha_{\dot{m}_T}\dot{m}_T(t)) \\
&\quad - c_v T_{CC}(t)(\alpha_{\dot{m}_C}\dot{m}_C(t) + \dot{m}_f(t) - \alpha_{\dot{m}_T}\dot{m}_T(t))], \\
\dot{P}_T(t) &= \frac{RT_M(t)}{V_M(t)} (\alpha_{\dot{m}_T}\dot{m}_T(t) + \frac{\beta}{\beta + 1}\alpha_{\dot{m}_C}\dot{m}_C(t) - \dot{m}_n(t)), \tag{2.3}
\end{aligned}$$

where $X(t) = [P_{CC}(t), N(t), T_{CC}(t), P_T(t)]^T$ denotes the state variable vector that includes the combustion chamber pressure $P_{CC}(t)$ and temperature $T_{CC}(t)$, the rotational speed $N(t)$ and the turbine pressure $P_T(t)$. There is a single actuator that supplies the fuel flow ($U(t) = \dot{m}_f(t)$) as well as five sensors measuring $Y(t) = [T_C(t), P_C(t), N(t), T_T(t), P_T(t)]^T$, where $T_C(t) = T_d(t) \left[1 + \frac{1}{\alpha_{\eta_C}\eta_C(t)} \left[\left(\frac{P_{CC}(t)}{P_d(t)} \right)^{\frac{\gamma-1}{\gamma}} - 1 \right] \right]$ and $T_T(t) = T_{CC}(t) \left[1 - \alpha_{\eta_T}\eta_T(t) \left[1 - \left(\frac{P_T(t)}{P_{CC}(t)} \right)^{\frac{\gamma-1}{\gamma}} \right] \right]$ denote the compressor and the turbine temperatures, respectively. The variables $P_C(t)$ and $P_T(t)$ denote the pressures of the compressor and turbine, respectively.

Moreover, $H(t) = [\eta_C(t), \eta_T(t), \dot{m}_C(t), \dot{m}_T(t)]^T$ denotes the health parameter vector, where $\eta_C(t)$ and $\eta_T(t)$ denote the compressor and the turbine efficiencies, and $\dot{m}_C(t)$ and $\dot{m}_T(t)$ denote their mass flow rates, respectively. The health parameters are also multiplied by their corresponding fixed health parameter degradation factors or the reference baselines $\alpha = [\alpha_{\eta_C}, \alpha_{\eta_T}, \alpha_{\dot{m}_C}, \alpha_{\dot{m}_T}]^T$. The sensors are affected by the Gaussian measurement noise with the standard deviations of SD_v corresponding to the percentages of output vector at the cruise condition as defined in [3]. More details on other variables and constants in (2.1) are provided in [3].

The flight condition is defined by two environmental variables, namely the

altitude and the Mach number. The ambient temperature and pressure can be computed according to $T_{\text{amb}} = T_s - \frac{6.5 \text{Alt}}{1000}$ and $P_{\text{amb}} = P_s \exp\left(\frac{-g \text{Mn} \text{Alt}}{288R}\right)$, where $T_s = 288$ °K and $P_s = 1.01325$ bar are set to the standard condition, g is the gravitational acceleration, and Mn and Alt denote the Mach number and the altitude, respectively. Moreover, the ambient variables are affected by the Gaussian process noise with the standard deviations of SD_w corresponding to the percentages of standard conditions of ambient variables.

For our simulations, the noise factors associated with measurement and process noise are considered as K_v and K_w , respectively. It is assumed that the noise standard deviations that are defined above are multiplied by the noise factors. Different values are assigned to the noise factors for various simulation studies.

2.7 Background of Filtering Methods Formulations

In this thesis, our proposed filters are compared with the most common filtering methods in the literature, namely as the Linear Kalman Filter (LKF), Extended Kalman Filter (EKF), Unscented Kalman Filter (UKF) and Cubature Kalman Filter (CKF). Here, their brief formulations are given as an essential background. Meanwhile, more details can be found in [60–62, 143].

2.7.1 Linear Kalman Filter (LKF)

The linear Kalman filter is the linear quadratic estimation problem which has two steps namely, the prediction and correction. The state variables are estimated in the prediction step and are then corrected upon receiving the next measurement. The algorithm is recursive and no additional past information is required. The LKF

can be derived for the linear system as follows:

$$\begin{aligned} X(k+1) &= A(k)X(k) + B(k)U(k) + w(k), & X(0) &= X_0, \\ Y(k) &= C(k)X(k) + v(k), \end{aligned} \quad (2.4)$$

where $X(k)$, $Y(k)$, $w(k)$, $v(k)$ and X_0 display the system state variables, outputs, process and measurement noise and the initial values of the states, respectively. Moreover, $A(k)$, $B(k)$ and $C(k)$ are the time-varying state-space matrices. It is assumed that $w(k)$ and $v(k)$ are the zero mean Gaussian noise with the corresponding covariance matrices $W(k)$ and $V(k)$, respectively. Moreover, it is assumed that $p(X_0) = \mathcal{N}(\hat{X}(0|0), P(0|0))$, where $P(0|0)$ is the diagonal matrix with sufficiently small diagonal elements. Hence, the LKF prediction step is formulated as:

$$\begin{aligned} \hat{X}(k|k-1) &= A(k)\hat{X}(k-1|k-1) + B(k-1)U(k-1), \\ P(k|k-1) &= A(k)P(k-1|k-1)A^T(k) + W(k), \end{aligned} \quad (2.5)$$

where the $\hat{X}(k|k-1)$ and $P(k|k-1)$ are the predicted *a priori* state and covariance estimates. Finally, the correction step is formulated as:

$$\begin{aligned} \gamma(k) &= Y(k) - C(k)\hat{X}(k|k-1), \\ S(k) &= C(k)P(k|k-1)C^T(k) + V(k), \\ K(k) &= P(k|k-1)C^T(k)S^{-1}(k), \\ \hat{X}(k|k) &= \hat{X}(k|k-1) + K(k)\gamma(k), \\ P(k|k) &= (I - K(k)C(k))P(k|k-1), \end{aligned} \quad (2.6)$$

where $\gamma(k)$, $S(k)$ and $K(k)$ represent the innovation signal, residual covariance and Kalman gain matrix, respectively. Also, the $\hat{X}(k|k)$ and $P(k|k)$ are the *a posteriori* state and covariance estimates. It follows from the theory that the LKF is optimal in case the model perfectly matches the system, the noise signals are really Gaussian white noise and their corresponding covariances are exactly known. For more details regarding the LKF operation, refer to [143].

2.7.2 Extended Kalman Filter (EKF)

The Extended Kalman Filter is the nonlinear extension of the linear Kalman filter. Hence, the state transition and observation models do not need to be necessarily linear. Consider the following nonlinear dynamic system:

$$\begin{aligned} X(k) &= \mathcal{F}(X(k-1), u(k)) + w(k), \\ Y(k) &= \mathcal{G}(X(k)) + v(k). \end{aligned} \quad (2.7)$$

To design the EKF, at each time step the Jacobian matrix is evaluated with current predicted states and the nonlinear functions \mathcal{F} and \mathcal{G} are linearized at the current estimate. The EKF prediction step is formulated as:

$$\begin{aligned} \hat{X}(k|k-1) &= \mathcal{F}(\hat{X}(k-1|k-1), U(k)), \\ P(k|k-1) &= A(k-1)P(k-1|k-1)A^T(k) + W(k), \end{aligned} \quad (2.8)$$

where $A(k-1) = \frac{\partial \mathcal{F}}{\partial X} |_{\hat{X}(k-1|k-1), U(k)}$. Then, the EKF correction step is as follows:

$$\begin{aligned} \gamma(k) &= Y(k) - \mathcal{G}(\hat{X}(k|k-1)), \\ S(k) &= C(k)P(k|k-1)C^T(k) + V(k), \\ K(k) &= P(k|k-1)C^T(k)S^{-1}(k), \\ \hat{X}(k|k) &= \hat{X}(k|k-1) + K(k)\gamma(k), \\ P(k|k) &= (I - K(k)C(k))P(k|k-1), \end{aligned} \quad (2.9)$$

where $C(k) = \frac{\partial \mathcal{G}}{\partial X} |_{\hat{X}(k|k-1)}$. Unlike the LKF, the EKF is not optimal. Therefore, if there is any error in system modeling or initial estimation values the EKF may diverge. The EKF can be improved by employing the robust techniques. For more details regarding the EKF operation, refer to [60].

2.7.3 Unscented Kalman Filter (UKF)

The unscented Kalman filter is another filter that is utilized for nonlinear systems. The UKF approximates the probability density by deterministic sampling of points

(called sigma points) representing the underlying distribution as a Gaussian. The nonlinear transformation of these points are supposed to be the posterior distribution. The UKF tends to be more accurate and more robust than the EKF particularly for highly nonlinear systems. During the prediction step, the estimated state and covariance are augmented with the mean and covariance of the process noise as follows:

$$\begin{aligned} X^a(k-1|k-1) &= \begin{bmatrix} \hat{X}^T(k-1|k-1) & E(w^T(k)) \end{bmatrix}^T, \\ P^a(k-1|k-1) &= \begin{bmatrix} P(k-1|k-1) & 0 \\ 0 & W(k) \end{bmatrix}. \end{aligned} \quad (2.10)$$

Then, a set of $2n + 1$ sigma points is derived as follows from the augmented state and covariance where n is the dimension of the state:

$$\begin{aligned} \mathcal{X}^0(k-1|k-1) &= X^a(k-1|k-1), \\ \mathcal{X}^i(k-1|k-1) &= X^a(k-1|k-1) \\ &\quad + \left(\sqrt{(n+\lambda)P^a(k-1|k-1)} \right)_i, \quad i = 1, \dots, n \\ \mathcal{X}^i(k-1|k-1) &= X^a(k-1|k-1) \\ &\quad - \left(\sqrt{(n+\lambda)P^a(k-1|k-1)} \right)_{i-n}, \quad i = n+1, \dots, 2n \end{aligned} \quad (2.11)$$

where $\left(\sqrt{(n+\lambda)P^a(k-1|k-1)} \right)_i$ is the i^{th} column of the matrix square root of $(n+\lambda)P^a(k-1|k-1)$ that can be calculated using the Cholesky decomposition method [154]. Then, the sigma points are propagated through the transition function as $\mathcal{X}^i(k|k-1) = \mathcal{F}(\mathcal{X}^i(k-1|k-1))$, for $i = 0, \dots, 2n$. The weighted sigma points are recombined to produce the predicted state and covariance as follows:

$$\begin{aligned} \hat{X}(k|k-1) &= \sum_{i=0}^{2n} \mathcal{W}_s^i \mathcal{X}^i(k|k-1), \\ P(k|k-1) &= \sum_{i=0}^{2n} \mathcal{W}_c^i [\mathcal{X}^i(k|k-1) - \hat{X}(k|k-1)][\mathcal{X}^i(k|k-1) - \hat{X}(k|k-1)]^T, \end{aligned} \quad (2.12)$$

with the state and covariance weights are given by:

$$\begin{aligned}
\mathcal{W}_s^0 &= \frac{\lambda}{n + \lambda}, \\
\mathcal{W}_c^0 &= \frac{\lambda}{n + \lambda} + (1 - \alpha^2 + \beta), \\
\mathcal{W}_s^i &= W_c^i = \frac{1}{2(n + \lambda)}, \\
\lambda &= \alpha^2(n + \kappa) - n,
\end{aligned} \tag{2.13}$$

where α and κ control the spread of sigma points and β is related to the distribution of X . The normal values are $\alpha = 10^{-3}$, $\beta = 2$ and $\kappa = 0$.

Afterwards, during the correction step the predicted state and covariance are augmented again with the mean and covariance of the measurement noise as follows:

$$\begin{aligned}
X^a(k|k-1) &= \left[\hat{X}^T(k|k-1) \quad E(v^T(k)) \right]^T, \\
P^a(k|k-1) &= \begin{bmatrix} P(k|k-1) & 0 \\ 0 & V(k) \end{bmatrix}.
\end{aligned} \tag{2.14}$$

Similarly, a set of $2n + 1$ sigma points is derived from the augmented state and covariance as follows:

$$\begin{aligned}
\mathcal{X}^0(k|k-1) &= X^a(k|k-1), \\
\mathcal{X}^i(k|k-1) &= X^a(k|k-1) \\
&\quad + \left(\sqrt{(n + \lambda)P^a(k|k-1)} \right)_i, \quad i = 1, \dots, n \\
\mathcal{X}^i(k|k-1) &= X^a(k|k-1) \\
&\quad - \left(\sqrt{(n + \lambda)P^a(k|k-1)} \right)_{i-n}, \quad i = n + 1, \dots, 2n
\end{aligned} \tag{2.15}$$

Also,

$$\mathcal{X}(k|k-1) = \left[\mathcal{X}^T(k|k-1) \quad E(v^T(k)) \right]^T \pm \sqrt{(n + \lambda)V^a(k)}, \tag{2.16}$$

where $V^a(k) = \begin{bmatrix} 0 & 0 \\ 0 & V(k) \end{bmatrix}$. Then, the sigma points are predicted through the

observation function \mathcal{G} as follows:

$$\mathcal{Y}^i(k) = \mathcal{G}(\mathcal{X}^i(k|k-1)), \quad i = 0, \dots, 2n \quad (2.17)$$

and then, they are recombined to compute the predicted measurement and predicted measurement covariance as:

$$\begin{aligned} \hat{Y}(k|k-1) &= \sum_{i=0}^{2n} \mathcal{W}_s^i \gamma^i(k), \\ S(k|k-1) &= \sum_{i=0}^{2n} \mathcal{W}_c^i [\mathcal{Y}^i(k) - \hat{Y}(k|k-1)][\mathcal{Y}^i(k) - \hat{Y}(k|k-1)]^T. \end{aligned} \quad (2.18)$$

The state-measurement cross covariance matrix is given by:

$$P_{XY}(k|k-1) = \sum_{i=0}^{2n} \mathcal{W}_c^i [\mathcal{X}^i(k|k-1) - \hat{X}(k|k-1)][\mathcal{Y}^i(k) - \hat{Y}(k|k-1)]^T, \quad (2.19)$$

that is used to compute the Kalman gain as well as the updated state and covariance as follows:

$$\begin{aligned} K(k) &= P_{XY}(k|k-1)S^{-1}(k|k-1), \\ \hat{X}(k|k) &= \hat{X}(k|k-1) + K(k)(Y(k) - \hat{Y}(k|k-1)), \\ P(k|k) &= P(k|k-1) - K(k)S(k|k-1)K^T(k). \end{aligned} \quad (2.20)$$

According to the above procedure, it can be concluded that the UKF removes the requirement to explicitly calculate the Jacobian which is a complicated task for highly complex nonlinear systems. For more details regarding the UKF operation, refer to [61].

2.7.4 Cubature Kalman Filter (CKF)

The cubature Kalman filter which is the systematic solution for high-dimensional nonlinear filtering problems is so similar to the UKF. Similarly $2n$ certain points, called cubature points, ζ^i are computed through intersecting the unit sphere with

the xy axes and scaling by \sqrt{n} as follows:

$$\begin{aligned}\zeta_i &= \sqrt{n}e_i, & i &= 1, \dots, n \\ \zeta_i &= -\sqrt{n}e_{i-n}. & i &= n+1, \dots, 2n\end{aligned}\quad (2.21)$$

where e_i denotes a unit vector to the direction of coordinate axis i . The generated cubature points are then propagated as follows:

$$\mathcal{X}^i(k-1|k-1) = \hat{X}^a(k-1|k-1) + \sqrt{P^a(k-1|k-1)}\zeta_i, \quad (2.22)$$

where $X^a(k-1|k-1)$ and $P^a(k-1|k-1)$ are the augmented state and covariance that are computed in (2.10). The state and covariance prediction steps are derived as:

$$\begin{aligned}\mathcal{X}^i(k|k-1) &= \mathcal{F}(\mathcal{X}^i(k-1|k-1)), \\ \hat{X}(k|k-1) &= \frac{1}{2n} \sum_{i=1}^{2n} \mathcal{X}^i(k|k-1), \\ P(k|k-1) &= \frac{1}{2n} \sum_{i=1}^{2n} [\mathcal{X}^i(k|k-1) - \hat{X}(k|k-1)][\mathcal{X}^i(k|k-1) - \hat{X}(k|k-1)]^T,\end{aligned}\quad (2.23)$$

where all the weights associated to the state and covariance are equal to $\frac{1}{2n}$. Using the same augmentation in (2.14), the cubature points recomputed as:

$$\mathcal{X}^i(k|k-1) = \mathcal{X}^a(k|k-1) + \sqrt{V^a(k|k-1)}\zeta_i, \quad (2.24)$$

where $V^a(k) = \begin{bmatrix} 0 & 0 \\ 0 & V(k) \end{bmatrix}$. Then, the cubature points are projected through the observation function as:

$$\mathcal{Y}^i(k|k-1) = \mathcal{G}(\mathcal{X}^i(k|k-1)). \quad (2.25)$$

The weighted cubature points are recombined to compute the predicted measurement and its corresponding covariance as:

$$\begin{aligned}\hat{Y}(k|k-1) &= \frac{1}{2n} \sum_{i=1}^{2n} \mathcal{Y}^i(k|k-1), \\ S(k|k-1) &= \frac{1}{2n} \sum_{i=1}^{2n} [\mathcal{Y}^i(k|k-1) - \hat{Y}(k|k-1)][\mathcal{Y}^i(k|k-1) - \hat{Y}(k|k-1)]^T. \quad (2.26)\end{aligned}$$

The state-measurement cross-covariance matrix is also given by:

$$P_{XY}(k|k-1) = \frac{1}{2n} \sum_{i=1}^{2n} [\mathcal{X}^i(k|k-1) - \hat{X}(k|k-1)][\mathcal{Y}^i(k|k-1) - \hat{Y}(k|k-1)]^T, \quad (2.27)$$

that is used to compute the Kalman gain as well as the updated state and covariance as follows:

$$\begin{aligned}K(k) &= P_{XY}(k|k-1)S^{-1}(k|k-1), \\ \hat{X}(k|k) &= \hat{X}(k|k-1) + K(k)(Y(k) - \hat{Y}(k|k-1)), \\ P(k|k) &= P(k|k-1) - K(k)S(k|k-1)K^T(k).\end{aligned} \quad (2.28)$$

The CKF is the special case of UKF with $\alpha = 1$, $\kappa = 0$, and $\beta = 0$. It uses the spherical cubature rule for Gaussian filter approximation. For more details regarding the CKF operation, refer to [62].

2.8 Summary

In this chapter, a brief history of gas turbine engine as well as the basic principles of jet propulsion are explained. Different engine types namely, the turbojet, turbofan and turboprop engines with their corresponding operational cycles are also summarized. Then, four important stages of the Brayton cycle is explained in details.

This chapter also gives information on several engine physical problems besides their corresponding effects on engine health parameters. Afterwards, a set of

nonlinear equations of a single spool gas turbine engine that is used in this thesis is presented. The applied engine has four state variables representing the combustion chamber pressure and temperature, rotational speed and the turbine exit pressure. There are also five sensors measuring the temperatures and pressures at the exits of compressor and turbine as well as their connecting shaft rotational speed.

Finally, a brief background is also given for the most common filtering methods in the literature namely the LKF, EKF, UKF and CKF that are used in this thesis to be compared with our different proposed filtering schemes.

Chapter 3

Hybrid Kalman Filter Based Fault Detection, Isolation and Identification Scheme

In this chapter, a novel sensor fault detection, isolation and identification (FDII) strategy is proposed by using the multiple model (MM) approach. The scheme is based on multiple hybrid Kalman filters (HKF) which represents an integration of a nonlinear mathematical model of the system with a number of piecewise linear (PWL) models. The proposed fault detection and isolation (FDI) scheme is capable of detecting and isolating sensor faults during the entire operational regime of the system by interpolating the PWL models using a Bayesian approach. Moreover, the proposed multiple HKF-based FDI scheme is extended to identify the magnitude of a sensor fault by using a modified generalized likelihood ratio (GLR) method which relies on the healthy operational mode of the system.

To illustrate the capabilities of our proposed FDII methodology, extensive simulation studies are conducted for a nonlinear gas turbine engine. Various single and concurrent sensor fault scenarios are considered to demonstrate the effectiveness of

our proposed on-line hierarchical multiple HKF-based FDI scheme under different flight modes. Finally, our proposed HKF-based FDI approach is compared with various filtering methods such as the linear, extended, unscented and cubature Kalman filters (LKF, EKF, UKF and CKF, respectively) corresponding to both *interacting* and *non-interacting* multiple model (MM) based schemes. Our comparative studies confirm the superiority of our proposed HKF method in terms of promptness of the fault detection, lower false alarm rates, as well as robustness with respect to the engine health parameters degradations. It must be noted that the main achievements in this chapter are published in [155] and [156].

3.1 Hybrid Kalman Filter (HKF) Design

An actual aircraft gas turbine engine, used for deriving the on-board engine model (OBEM), and which is used for on-line diagnostic analysis can be described according to the following representation:

$$\begin{aligned}\dot{X}(t) &= \mathcal{F}_c(X(t), H(t), U(t), w(t)), \\ Y(t) &= \mathcal{G}_c(X(t), H(t)) + v(t),\end{aligned}\tag{3.1}$$

where $X(t) \in \mathbb{R}^n$, $H(t) \in \mathbb{R}^r$, $Y(t) \in \mathbb{R}^q$, $U(t) \in \mathbb{R}^p$, $w(t) \in \mathbb{R}^2$ and $v(t) \in \mathbb{R}^q$ denote the engine state variables, health parameters, sensor measurements, input signals, and Gaussian zero-mean process and measurement noise at time t , respectively. The engine dynamics is also an implicit function of the ambient condition parameters including the ambient temperature and pressure. The ambient parameters are defined in terms of the environmental parameters including the altitude and the Mach number. The engine health parameters in (3.1) will become degraded from their healthy reference baselines during the entire engine life cycle. Moreover, it is assumed that the inputs and outputs of an actual engine are discretized with sufficiently small sampling period for performing simulation and implementation of our

proposed on-line fault detection, isolation and identification (FDII) scheme. The discrete-time representation of the variables in (3.1) are denoted by $X(k)$, $Y(k)$, $H(k)$, $U(k)$, $w(k)$ and $v(k)$ with the discrete dynamic functions \mathcal{F} and \mathcal{G} replacing \mathcal{F}_c and \mathcal{G}_c , respectively.

The hybrid Kalman filter (HKF) consists of two main blocks that include a nonlinear on-board engine model (OBEM) and multiple piecewise linear (PWL) models derived at different operating points to cover the entire engine operating range. The continuous-time fault-free representation of the OBEM which can also be derived based on thermodynamics laws is now given as follows:

$$\begin{aligned}\dot{X}_{\text{OBEM}}(t) &= f_c(X_{\text{OBEM}}(t), H_{\text{OBEM}}(t), U(t)), \\ Y_{\text{OBEM}}(t) &= g_c(X_{\text{OBEM}}(t), H_{\text{OBEM}}(t)),\end{aligned}\tag{3.2}$$

where $X_{\text{OBEM}}(t) \in \mathbb{R}^n$ and $Y_{\text{OBEM}}(t) \in \mathbb{R}^q$ denote the OBEM state variables and outputs. Both the actual engine and the OBEM operate in parallel under the same flight conditions. Moreover, $H_{\text{OBEM}}(t) \in \mathbb{R}^r$ denotes the OBEM health parameters that can be represented by $H_{\text{OBEM}}(t) = \alpha^T h(X_{\text{OBEM}}(t))$, in which α defines the OBEM health parameters degradation factors (reference baselines). This parameter is an all-ones vector for the OBEM that represents a healthy or non-degraded engine. It is also assumed that the OBEM health parameters can be periodically updated and α is considered as fixed in between the updating intervals. In addition, $h(X_{\text{OBEM}}(t))$ denotes a state-dependent smooth function that corresponds to the compressor and the turbine performance maps and is modeled as a polynomial function for our developed gas turbine engine model. The updating process for the OBEM health parameters will be described below in detail. Moreover, for performing simulation and implementations, the continuous-time OBEM model is assumed to be discretized with sufficiently small sampling period. The discrete-time representation of the variables in (3.2) are denoted by $X_{\text{OBEM}}(k)$, $Y_{\text{OBEM}}(k)$, $H_{\text{OBEM}}(k)$ and $U(k)$ with the discrete dynamic functions f and g replacing f_c and g_c , respectively.

The continuous-time OBEM model is linearized and discretized at multiple operating points (corresponding to engine steady-state values) that are denoted by $(X_{ss_i}, U_{ss_i}, Y_{ss_i})$ with sufficiently small sampling period. The constructed multiple linear discrete-time state-space models is now given by:

$$\begin{aligned}\Delta X_i(k+1) &= A|_{X_{ss_i}} \Delta X_i(k) + B|_{U_{ss_i}} \Delta U_i(k), \\ \Delta Y_i(k) &= C|_{X_{ss_i}} \Delta X_i(k),\end{aligned}\tag{3.3}$$

where $i \in 1, \dots, L$ (L is the number of the operating points), $A|_{X_{ss_i}}$, $B|_{U_{ss_i}}$ and $C|_{X_{ss_i}}$ denote the state-space matrices associated with the i^{th} operating point, and $\Delta X_i(k) = X_{OBEM}(k) - X_{ss_i}$, $\Delta Y_i(k) = Y_{OBEM}(k) - Y_{ss_i}$ and $\Delta U_i(k) = U(k) - U_{ss_i}$. In the Subsection 3.1.1, the linearization and discretization process of the continuous-time OBEM model is described in more detail. In this chapter, it is assumed that the OBEM linearized models are obtained with the health parameters that are set to their healthy reference baselines. Also, the health parameter effects due to changes in the engine state variables have been implicitly incorporated into the matrices A and C , although the deviations from the healthy reference baselines are not incorporated in the linear models.

For each linearized model, an off-line linear Kalman filter is designed to estimate both the actual engine states and sensor outputs as follows:

$$\begin{aligned}\Delta \hat{X}_i(k+1) &= A|_{X_{ss_i}} \Delta \hat{X}_i(k) + B|_{U_{ss_i}} \Delta U_i(k) + K_{ss}^i (Y(k) - \hat{Y}_i(k)), \\ \Delta \hat{Y}_i(k) &= C|_{X_{ss_i}} \Delta \hat{X}_i(k),\end{aligned}\tag{3.4}$$

where $\Delta \hat{X}_i(k) = \hat{X}(k) - X_{ss_i}$, $\Delta \hat{Y}_i(k) = \hat{Y}(k) - Y_{ss_i}$ and K_{ss}^i denotes the steady-state Kalman filter gain matrix. For the purpose of constructing the multiple model HKFs, the steady-state Kalman gain matrices as well as the matrices $A|_{X_{ss_i}}$ and $C|_{X_{ss_i}}$ that are constructed associated with multiple operating points are stored in a look-up table. According to (3.4), the linear Kalman filter does not take into

account the effects of the health parameter degradations from their healthy reference baselines since the state-space matrices have already been determined for an all-ones α . Consequently, it does not have the required level of robustness for handling a vast number of health degradations that occur during the entire engine life cycle. Therefore, it is essential to update the health parameter reference baselines of the OBEM to maintain the reliability and accuracy of the state estimates and the performance of the FDII scheme through out the *entire engine life cycle* operation. For this purpose, the health parameter reference baselines can be estimated by an off-line health monitoring system and then periodically updated in the discrete-time OBEM model. Therefore, the on-line FDII scheme is integrated with an off-line health monitoring system.

The frequency of the health monitoring system updates is significantly lower than that of the on-line FDII algorithm, since the health degradation process is slow and gradual during one flight, although their accumulated effects after a number of flights may generate a large discrepancy between the OBEM and the actual engine. The off-line health monitoring module can either be a single augmented Kalman filter that estimates the health parameters based on the collected data during several flights or a nonlinear approximation method such as a neural network that receives the engine historical data. It must be noted that both the health monitoring and updating mechanism can be performed on-line having a sufficiently large sampling interval. However, the health parameter estimation process needs to be terminated whenever a fault occurs in the engine to avoid generating incorrect estimates of the health parameters.

The off-line health monitoring module uses the collected input and the measured output data to estimate the health parameter reference baselines, that is $\hat{\alpha}$. The estimated $\hat{\alpha}$ is updated periodically in the OBEM model within a determined

time interval \mathcal{T} that is usually a given number of flights or days. The update process feeds $\hat{\alpha}$ into the OBEM model so that the on-line FDII scheme can operate within the neighborhood of the degraded actual engine condition. Consequently, the OBEM model can now be re-written as follows:

$$\begin{aligned} X_{\text{OBEM}}(k+1) &= f(X_{\text{OBEM}}(k), \hat{\alpha}h(X_{\text{OBEM}}(k)), U(k)), \\ Y_{\text{OBEM}}(k) &= g(X_{\text{OBEM}}(k), \hat{\alpha}h(X_{\text{OBEM}}(k))). \end{aligned} \quad (3.5)$$

It must be noted that the OBEM model that is provided in (3.2) is used only once for performing the linearization process with α set to an all-ones vector, although the OBEM model in (3.5), with its reference baselines periodically updated, is the one that is utilized in our proposed HKF structure as well as in our on-line FDII scheme. For sake of notational simplicity, we use the same notations for the above two versions of the OBEM model.

To construct the HKF representation we modify (3.4) where the steady-state variables are replaced by the OBEM states and outputs that are obtained from (3.5) and also by using the previously stored steady-state Kalman filter gain and state-space matrices as follows:

$$\begin{aligned} \hat{X}_i(k+1) - X_{\text{OBEM}}(k+1) &= A|_{X_{\text{ss}_i}}(\hat{X}_i(k) - X_{\text{OBEM}}(k)) + K_{\text{ss}}^i(Y(k) - \hat{Y}_i(k)), \\ \hat{Y}_i(k) &= C|_{X_{\text{ss}_i}}(\hat{X}_i(k) - X_{\text{OBEM}}(k)) + Y_{\text{OBEM}}(k). \end{aligned} \quad (3.6)$$

In the above model the effects of the input and the B matrix are eliminated from the HKF formulation given the fact that these have already been accounted for by the OBEM model. The procedure for derivation of the discrete-time HKF is formally shown in Subsection 3.1.1.

Consequently, multiple HKFs are designed by using (3.6) for multiple operating points. After updating the OBEM health parameter reference baselines, there is no longer a need to recalculate the $A|_{X_{\text{ss}_i}}$, $C|_{X_{\text{ss}_i}}$ and K_{ss}^i matrices for each operating

point, since the effects of the health parameter degradations have been incorporated into the X_{OBEM} and Y_{OBEM} as given by (3.5).

One of the factors that can affect the efficiency of our proposed FDII algorithm is the estimation error of the off-line health monitoring module, that leads to mismatches between the actual engine and the OBEM outputs. Larger estimation errors may increase the fault detection time, and lead to occurrence of false alarms and incorrect fault detection rates. The acceptable ranges of the estimation errors that do not lead to false alarms and incorrect fault detection rates will be specified subsequently in Section 3.5 for different health parameters under various healthy and faulty scenarios. Moreover, the reliability of our proposed on-line FDII strategy as a function of different mismatching factors between the actual operational engine and the OBEM (as represented by the reference baseline estimation errors ($\text{RBEE} = \frac{|\alpha - \hat{\alpha}|}{\alpha}$)) and the magnitude of the process and measurement noise signals will be investigated subsequently in Section 3.5 by means of a confusion matrix analysis.

In order to develop our proposed HKF-based scheme as an FDII strategy, multiple piecewise linear (PWL) models need to be generated for each fault hypothesis at various operating points. Moreover, the PWL models will be integrated and fused to cover the entire operational regime of an engine. The detail description of this process is provided in Section 3.2.

3.1.1 Discrete-Time HKF Derivation Analysis

In Section 3.1, for the sake of notational simplicity the same notations were used for both versions of the OBEM. However, here we use X_{NOBEM} and Y_{NOBEM} to designate the nominal OBEM ($\alpha = 1$) that is equivalent to (3.2), and X_{OBEM} and Y_{OBEM} to designate the OBEM with the updated health parameters ($\hat{\alpha} \neq 1$) that is equivalent to (3.5).

Let the nominal continuous-time OBEM model (NOBEM) be represented by:

$$\begin{aligned}\dot{X}_{\text{NOBEM}}(t) &= f_c(X_{\text{NOBEM}}(t), H_{\text{NOBEM}}(t), U(t)), \\ Y_{\text{NOBEM}}(t) &= g_c(X_{\text{NOBEM}}(t), H_{\text{NOBEM}}(t)).\end{aligned}\quad (3.7)$$

To construct the HKF, the nominal continuous-time OBEM is initially linearized at a certain operating point $(X_{\text{ss}}, U_{\text{ss}}, Y_{\text{ss}})$ without considering degradations as follows:

$$\begin{aligned}\dot{X}_{\text{NOBEM}}(t) &= f_c(X_{\text{ss}}, U_{\text{ss}}) + \frac{\partial f_c}{\partial X_{\text{NOBEM}}}\bigg|_{X_{\text{ss}}}(X_{\text{NOBEM}}(t) - X_{\text{ss}}) + \frac{\partial f_c}{\partial U}\bigg|_{U_{\text{ss}}}(U(t) - U_{\text{ss}}) \\ &\quad + \Delta f_c, \\ Y_{\text{NOBEM}}(t) &= g_c(X_{\text{ss}}, U_{\text{ss}}) + \frac{\partial g_c}{\partial X_{\text{NOBEM}}}\bigg|_{X_{\text{ss}}}(X_{\text{NOBEM}}(t) - X_{\text{ss}}) + \Delta g_c,\end{aligned}\quad (3.8)$$

where $f_c(X_{\text{ss}}, U_{\text{ss}}) \equiv 0$ and $g_c(X_{\text{ss}}, U_{\text{ss}}) \equiv Y_{\text{ss}}$. The health parameters are the state-dependent functions whose effects are incorporated in the above partial derivatives. The linear continuous-time model is now discretized by using a sufficiently small sampling period to yield the corresponding discrete-time linear model:

$$\begin{aligned}X_{\text{NOBEM}}(k+1) - X_{\text{ss}} &= A|_{X_{\text{ss}}}(X_{\text{NOBEM}}(k) - X_{\text{ss}}) + B|_{U_{\text{ss}}}(U(k) - U_{\text{ss}}) + \Delta F, \\ Y_{\text{NOBEM}}(k) &= Y_{\text{ss}} + C|_{X_{\text{ss}}}(X_{\text{NOBEM}}(k) - X_{\text{ss}}) + \Delta G,\end{aligned}\quad (3.9)$$

where $A|_{X_{\text{ss}}} = \exp(A_c|_{X_{\text{ss}}} T_s)$, $B|_{U_{\text{ss}}} = (\int_0^{T_s} \exp(A_c|_{X_{\text{ss}}} \tau) d\tau) B_c|_{U_{\text{ss}}}$, and $C|_{X_{\text{ss}}} = C_c|_{X_{\text{ss}}}$ are obtained in terms of the state-space matrices that are associated with the continuous-time linear model $A_c|_{X_{\text{ss}}} = \frac{\partial f_c}{\partial X_{\text{NOBEM}}}\bigg|_{X_{\text{ss}}}$, $B_c|_{U_{\text{ss}}} = \frac{\partial f_c}{\partial U}\bigg|_{U_{\text{ss}}}$, and $C_c|_{X_{\text{ss}}} = \frac{\partial g_c}{\partial X_{\text{NOBEM}}}\bigg|_{X_{\text{ss}}}$, and the sampling period is denoted by T_s . Also, Δf_c , Δg_c , ΔF and ΔG represent the higher order terms in the linearization process. To construct the HKF, it is necessary to update the OBEM health parameters. Therefore, the nominal model is only used once to derive the state-space matrices and the steady-state values.

Assumption 3.1 The linearization of the nominal OBEM with $\alpha = 1$ and

the updated OBEM with $\hat{\alpha} \neq 1$ generate approximately the same matrices and steady-state values.

Therefore, given that Assumption 1 holds, the linearized version of the updated OBEM can be derived as follows:

$$\begin{aligned} X_{\text{OBEM}}(k+1) - X_{\text{ss}} &\approx A|_{X_{\text{ss}}}(X_{\text{OBEM}}(k) - X_{\text{ss}}) + B|_{U_{\text{ss}}}(U(k) - U_{\text{ss}}) + \Delta F, \\ Y_{\text{OBEM}}(k) &\approx Y_{\text{ss}} + C|_{X_{\text{ss}}}(X_{\text{OBEM}}(k) - X_{\text{ss}}) + \Delta G. \end{aligned} \quad (3.10)$$

Moreover, the relationship between the instantaneous values of $X_{\text{OBEM}}(k)$ and $Y_{\text{OBEM}}(k)$ and the steady-state values associated with each linearized model can be given by:

$$\begin{aligned} X_{\text{OBEM}}(k) &= X_{\text{ss}} + X_l(k), \\ Y_{\text{OBEM}}(k) &= Y_{\text{ss}} + Y_l(k), \end{aligned} \quad (3.11)$$

where $X_l(k)$ and $Y_l(k)$ represent the perturbations from the steady-state values as well as variations of the OBEM state variables and outputs due to updating the health parameters reference baselines. The linear Kalman filter can be designed as follows:

$$\begin{aligned} \hat{X}(k+1) - X_{\text{ss}} &= A|_{X_{\text{ss}}}(\hat{X}(k) - X_{\text{ss}}) + B|_{U_{\text{ss}}}(U(k) - U_{\text{ss}}) + K_{\text{ss}}(Y(k) - \hat{Y}(k)), \\ \hat{Y}(k) &= Y_{\text{ss}} + C|_{X_{\text{ss}}}(\hat{X}(k) - X_{\text{ss}}), \end{aligned} \quad (3.12)$$

which can be rewritten by using (3.11) as follows:

$$\begin{aligned} \hat{X}(k+1) - X_{\text{OBEM}}(k) + X_l(k) &= A|_{X_{\text{ss}}}(\hat{X}(k) - X_{\text{OBEM}}(k)) + K_{\text{ss}}(Y(k) - \hat{Y}(k)) \\ &\quad + A|_{X_{\text{ss}}}X_l(k) + B|_{U_{\text{ss}}}(U(k) - U_{\text{ss}}), \\ \hat{Y}(k) &= Y_{\text{OBEM}}(k) + C|_{X_{\text{ss}}}(\hat{X}(k) - X_{\text{OBEM}}(k)) + C|_{X_{\text{ss}}}X_l(k) - Y_l(k). \end{aligned} \quad (3.13)$$

Using (3.10), the last two terms in the R.H.S of (3.13) can be rewritten as

follows:

$$\begin{aligned}
A|_{X_{ss}}(X_{\text{OBEM}}(k) - X_{ss}) + B|_{U_{ss}}(U(k) - U_{ss}) &\approx X_{\text{OBEM}}(k+1) - X_{ss} - \Delta F, \\
C|_{X_{ss}}(X_{\text{OBEM}}(k) - X_{ss}) - Y_l(k) &\approx Y_{\text{OBEM}}(k) - Y_{ss} - Y_l(k) - \Delta G = -\Delta G. \quad (3.14)
\end{aligned}$$

Therefore, the discrete-time form of the HKF can be obtained as follows:

$$\begin{aligned}
\hat{X}(k+1) - X_{\text{OBEM}}(k+1) &\approx A|_{X_{ss}}(\hat{X}(k) - X_{\text{OBEM}}(k)) + K_{ss}(Y(k) - \hat{Y}(k)) - \Delta F, \\
\hat{Y}(k) &\approx Y_{\text{OBEM}}(k) + C|_{X_{ss}}(\hat{X}(k) - X_{\text{OBEM}}(k)) - \Delta G, \quad (3.15)
\end{aligned}$$

which will lead to (3.6) for the particular operating point if the higher order terms ΔF and ΔG as well as the approximation error due to Assumption 3.1 are neglected.

3.2 Piecewise Linear Models (PWL) Interpolation

Any given linear model of a nonlinear system has a limited operating range in which it remains valid. Nevertheless, our ultimate goal is to obtain a globally valid model which is valid for the entire operating regime. Therefore, the full operating range is divided into several sub-regions where each is defined around an operating point for which a piecewise linear (PWL) model can be derived [157]. The PWL models can then be integrated in order to construct a parameter-varying general model whose parameters are the PWL models weights that are obtained through an on-line Bayesian approach. This will provide one with a soft interpolation among the PWL models as opposed to a hard switching among them. In this thesis, the engine inputs including the fuel flow rate and ambient variables are used to partition the engine operational regime into multiple operating points for which the PWL models are constructed. These operating points are associated with different flight conditions such as climbing, cruise and landing modes. The selected number of operating

points depends on (a) the required HKF state estimation accuracy, (b) the FDII strategy reliability on correct decisions, and (c) false alarm rates within the range of the applied health parameter degradations. Hence, if there are no concerns on the memory utilization, the number of the operating points can be selected to be as high as possible to enhance the HKF estimation accuracy and the FDII scheme valid decision rates and also to decrease the false alarm rates.

One of the important advantages of our proposed HKF scheme is in requiring a smaller number of operating points as compared to standard linear Kalman filters for covering an entire operational regime of the engine. This is facilitated and made possible due to substitutions of the steady-state variables in (3.6) by the OBEM state and output variables. The operating range of a PWL model in (3.4) is only limited to the neighborhood of a corresponding operating point, although this can be extended to a larger range in (3.6) given that X_{OBEM} and Y_{OBEM} are changed according to the engine operating condition, which enable the PWL model to be valid in a wider range.

Since, the sensor fault is injected into the actual gas turbine engine and not the OBEM, we have for the faulty engine

$$\begin{aligned} X(k+1) &= \mathcal{F}(X(k), H(k), U(k), w(k)), \\ Y(k) &= \mathcal{G}(X(k), H(k)) + \sum_{s=1}^q b_s z_s \delta(k - k_{fs}) + v(k), \end{aligned} \quad (3.16)$$

where \mathcal{F} and \mathcal{G} represent the discrete-time dynamic equations of the actual gas turbine engine, q is the number of sensors, b_s represents the s^{th} sensor bias fault magnitude and z_s represents the fault location vector that has a unit value for the s^{th} element while the other elements are set to zero, and $\delta(k - k_{fs})$ denotes a unit step function that occurs at the sample k_{fs} corresponding to the s^{th} fault occurrence time. The bias is set to zero for the healthy sensor scenario. Therefore, there are a total of $q + 1$ sensor modes (corresponding to one healthy and q faulty sensor

modes).

The PWL models constructed for multiple operating points are now used to compute the corresponding K_{ss}^i for various sensor modes of the (3.16). The matrices $A|_{X_{ss_i}}$, $C|_{X_{ss_i}}$ and K_{ss}^i are finally stored in a look-up table and are used to construct multiple HKFs (MHKFs) as given by (3.6) for all the sensor modes.

Therefore, the HKF for the j^{th} sensor mode at the i^{th} operating point is designed as follows:

$$\begin{aligned}\hat{X}^{(i,j)}(k+1) - X_{\text{OBEM}}(k+1) &= A^i(\hat{X}^{(i,j)}(k) - X_{\text{OBEM}}(k)) + K_{ss}^i(Y(k) - \hat{Y}^{(i,j)}(k)), \\ \hat{Y}^{(i,j)}(k) &= C^i(\hat{X}^{(i,j)}(k) - X_{\text{OBEM}}(k)) + Y_{\text{OBEM}}(k) + b_{dj}a_j\delta_j(k),\end{aligned}\quad (3.17)$$

where $i = 1, \dots, L$, $j = 1, \dots, (q+1)$, b_{dj} denotes the pre-determined sensor bias fault that can be different from the actual sensor fault b_s that is injected into (3.16), a_j denotes the q -dimensional vector and is one of $q+1$ modes of a which is the fault parameter vector. For the healthy mode or $j = 1$, the fault parameter vector, a , is set to a zero vector whereas for $j = 2, \dots, q+1$, a_j has a unit value for the $(j-1)^{th}$ element and all the other elements are set to zero. Moreover, $A^i = A|_{X_{ss_i}}$, $C^i = C|_{X_{ss_i}}$ and K_{ss}^i are the previously stored state-space and Kalman gain matrices that depend on the i^{th} operating point. Therefore, $L \times (q+1)$ HKFs are constructed covering the entire engine operating range corresponding to different sensor modes. It must be noted that the state-space matrices depend only on the operating points but the Kalman gain matrices depend on both the operating points and the noise covariance matrices that are the same for all the sensor fault modes, given that the OBEM does not take into account the effects of sensor faults.

Although the operating range of a PWL model in the HKF scheme can be increased as compared to that of the one that uses the standard linear Kalman filters by replacing the steady-state values with the OBEM variables, still none of the PWL models are solely valid over the entire operating range of an engine. Therefore, corresponding to each PWL model one can associate a validity function

that is based on its normalized weight as obtained by means of the Bayes formula in (3.19). For this purpose, the residual vectors $\gamma^{(i,j)}$ and the covariance matrices $S^{(i,j)}$ that are generated by the multiple HKFs are used to compute the likelihood function $f^{(i,j)}$ for the j^{th} sensor mode at the i^{th} operating region as follows:

$$\begin{aligned}\gamma^{(i,j)}(k) &= Y(k) - \hat{Y}^{(i,j)}(k), & S^{(i,j)}(k) &= \text{cov}(\gamma^{(i,j)}(k)), \\ f^{(i,j)}(\gamma^{(i,j)}(k)) &= \frac{1}{(2\pi)^{q/2} \sqrt{|S^{(i,j)}(k)|}} \times \exp\left[\frac{-1}{2}(\gamma^{(i,j)}(k))^T (S^{(i,j)}(k))^{-1} (\gamma^{(i,j)}(k))\right],\end{aligned}\tag{3.18}$$

where it is assumed that the innovation sequence generated by the hybrid Kalman filter, $\gamma^{(i,j)}(k)$, is a Gaussian white noise process with zero mean and covariance matrix $S^{(i,j)}(k)$. The normalized weights for the j^{th} sensor mode are updated recursively by using the Bayes formula as follows:

$$\mu^{(i,j)}(k) = \frac{f^{(i,j)}(\gamma^{(i,j)}(k))\mu^{(i,j)}(k-1)}{\sum_{i=1}^L f^{(i,j)}(\gamma^{(i,j)}(k))\mu^{(i,j)}(k-1)}.\tag{3.19}$$

The weights computed above should also remain outside a narrow bound to avoid becoming close to zero as:

$$\begin{aligned}\text{if } \mu^{(i,j)}(k) > \rho &\text{ then } \mu^{(i,j)}(k) = \mu^{(i,j)}(k), \\ \text{if } \mu^{(i,j)}(k) \leq \rho &\text{ then } \mu^{(i,j)}(k) = \rho,\end{aligned}\tag{3.20}$$

where ρ is a design parameter that is determined by trial and error and it invokes the PWL models that have very small weights and it avoids them from being removed from the set of L models. It is also useful for numerical robustness of the recursive weight algorithm [158].

Following the computation of the normalized weights, multiple time-varying models are now constructed subject to various sensor modes. For each sensor mode, the corresponding model state-space matrices as well as the weighted innovation vector and the covariance matrix are obtained by using the PWL model state-space

matrices and their associated normalized weights as follows:

$$\begin{aligned}
A_c^j(k) &= \sum_{i=1}^L \mu^{(i,j)}(k) A^i, \\
C_c^j(k) &= \sum_{i=1}^L \mu^{(i,j)}(k) C^i, \\
\gamma_c^j(k) &= \sum_{i=1}^L \mu^{(i,j)}(k) \gamma^{(i,j)}(k), \\
S_c^j(k) &= \sum_{i=1}^L (\mu^{(i,j)}(k))^2 S^{(i,j)}(k),
\end{aligned} \tag{3.21}$$

where $A_c^j(k)$ and $C_c^j(k)$ denote the weighted state-space matrices of a linear time-varying model associated with the j^{th} sensor mode. Also, $\gamma_c^j(k)$ and $S_c^j(k)$ denote the weighted innovation vector and the covariance matrix of the j^{th} sensor mode, respectively. The above procedure is now designated as the *PWL models interpolation*. Consequently, $(q + 1)$ weighted innovation vectors and covariance matrices that operate through out the entire engine operational regime are used in the next two sections to develop our proposed FDI scheme.

3.3 Sensor FDI via Multiple-Model-Based Scheme

In this section, the overall structure of our proposed MM-based FDI scheme is presented. It is assumed that the fault parameter vector can take on only one of $(q + 1)$ sensor modes as a_j . Therefore, at each operating point there are $(q + 1)$ PWL models; one for the healthy sensors scenario and q corresponding to various faulty sensor scenarios, that have been designed and integrated with only one OBEM for constructing the multiple HKF (MHKF)-based scheme as formulated in (3.17). The innovation vectors and the covariance matrices that are generated by the MHKFs are fused and weighted as given by (3.21). Finally, there are $(q + 1)$ weighted innovation vectors and covariance matrices that are used in the MM-based FDI scheme, where

they are operating under different healthy and faulty sensor scenarios during the entire engine operational regime.

3.3.1 Single Fault Detection and Isolation (FDI) Scheme

In the MM-based approach [3, 27, 28], the hypothesis conditional probability $P_j(k)$ is defined as the probability that the fault parameter a assumes the mode a_j , $j = 1, \dots, q+1$, conditioned on the observed measurement history up to the k^{th} sample, that is:

$$P_j(k) = \Pr[a = a_j | \mathcal{Y}(k) = \mathcal{Y}_k], \quad (3.22)$$

where $\mathcal{Y}(k)$ is the random vector measurement history with $Y(1), Y(2), \dots, Y(k)$ partitions displaying the available measurements up to the k^{th} sample time. Similarly, \mathcal{Y}_k is the measurement history vector realization that has the partitions of Y_1, Y_2, \dots, Y_k . Therefore, the conditional probability can be computed recursively as follows:

$$P_j(k) = \frac{f_{Y(k)|a, \mathcal{Y}(k-1)}(Y_j | a_j, \mathcal{Y}_{k-1}) P_j(k-1)}{\sum_{h=1}^{q+1} f_{Y(k)|a, \mathcal{Y}(k-1)}(Y_j | a_h, \mathcal{Y}_{k-1}) P_h(k-1)}, \quad (3.23)$$

where $f_{Y(k)|a, \mathcal{Y}(k-1)}(Y_j | a_j, \mathcal{Y}_{k-1})$ denotes the Gaussian density function for the current measurement given by:

$$f_{Y(k)|a, \mathcal{Y}(k-1)}(Y_j | a_j, \mathcal{Y}_{k-1}) = \frac{1}{(2\pi)^{q/2} \sqrt{|S_c^j(k)|}} \times \exp\left[-\frac{1}{2}(\gamma_c^j(k))^T (S_c^j(k))^{(-1)} (\gamma_c^j(k))\right], \quad (3.24)$$

where $\gamma_c^j(k)$ and $S_c^j(k)$ are given by (3.21).

If the j^{th} sensor mode occurs, the probability associated with the j^{th} model will be larger than that of the others since its corresponding innovation vector and also the determinant of the covariance matrix will be much smaller than those that are predicted by the other filters and which are mismatched with the assumed fault scenario. Hence, the condition of the system and the location of a single faulty

sensor can be detected and isolated based on evaluating $P_j(k)$ and determining its maximum value. Consequently, our proposed MM-based approach is capable of detecting and isolating sensor faults. Figure 3.1 shows the structure of the MM-based FDI scheme that employs the MHKFs for the entire engine operational regime.

Our contribution here is the modification of our previously developed MM-based structure in [27] and [28] that utilizes only multiple standard linear Kalman filters and is designed for a single operating point into a general strategy that is applicable to the entire engine operational regime by means of the multiple HKF scheme and fusion and integration of the corresponding innovation vectors and covariance matrices.

As we will describe in more detail in Section 3.5, in this chapter five sensor faults are considered. Therefore, the total number of modes corresponding to each operating point of the jet engine is six, where mode #1 (P_1) corresponds to the healthy engine sensors and modes #2 to #6 (P_2 to P_6) correspond to a 3% sensor bias fault injected into sensors measuring the compressor exit temperature (P_2) and pressure (P_3), shaft rotational speed (P_4), the turbine exit temperature (P_5) and pressure (P_6), respectively.

3.3.2 Concurrent Fault Detection and Isolation (FDI) Scheme

For detection and isolation of two concurrent faults in the gas turbine engine, a hierarchical MM approach is proposed in [26] and [28] as shown in Table 3.1. In this scheme, it is assumed that the engine starts operating with healthy sensors when the first level of filters are active and the FDI scheme observes the sensors condition for occurrence of one of the five faulty modes. The active bank of filters operate based on the weighted innovation vectors and covariance matrices that are obtained in Section 3.2.

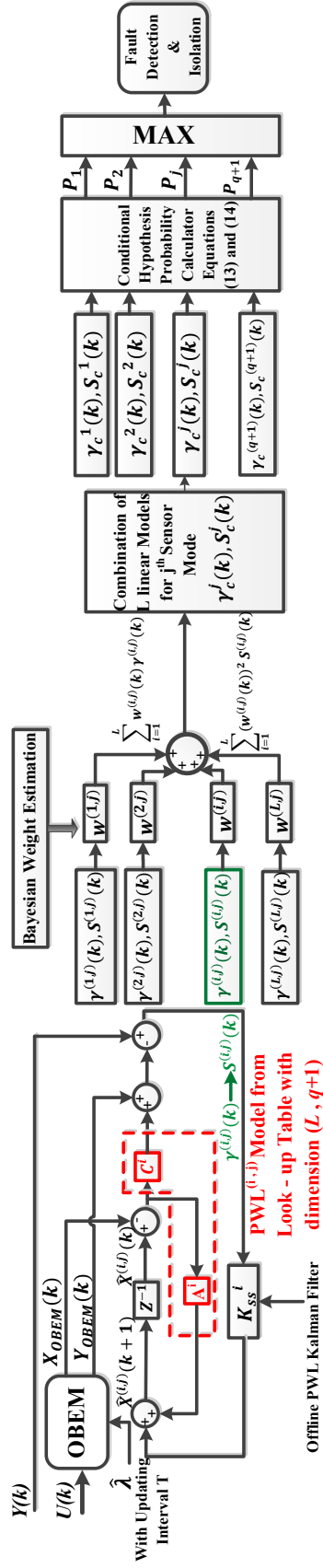


Figure 3.1: The MM-based FDI scheme based on the HKF corresponding to multiple operating regime.

Table 3.1: Operational modes corresponding to various possible two concurrent sensor faults.

Level	Operational Modes					
	#1	#2	#3	#4	#5	#6
First	Healthy	P_2	P_3	P_4	P_5	P_6
Second	P_2	P_2	P_2	P_2	P_2	P_2
		P_2	P_3	P_4	P_5	P_6
	P_3	P_3	P_3	P_3	P_3	P_3
		P_2	P_3	P_4	P_5	P_6
	P_4	P_4	P_4	P_4	P_4	P_4
		P_2	P_3	P_4	P_5	P_6
	P_5	P_5	P_5	P_5	P_5	P_5
		P_2	P_3	P_4	P_5	P_6
	P_6	P_6	P_6	P_6	P_6	P_6
		P_2	P_3	P_4	P_5	P_6

Once the first fault is detected and isolated according to the maximum probability criterion, the FDI scheme will activate the second level of the filters as shown in Table 3.1 for detection of the second concurrent faults. In our hierarchical MM scheme, it is assumed that the sensor faults do not occur simultaneously and there exists always a minimum time interval between the occurrence of two sensor faults that are called concurrent faults. Table 3.1 indicates all the possible configurations for the second bank of filters that are considered in the simulation results in Section 3.5. The first filter in the second level always corresponds to the detected faulty mode in the first level. For example, if the first filter detects a 3% bias in the compressor exit temperature sensor (P_2), then the first and the second filters in the second level respectively correspond to P_2 and the possibility of a larger bias fault within the compressor exit temperature sensor. Moreover, the third filter corresponds to the concurrent bias faults in the compressor exit temperature and pressure sensors (P_2 and P_3), the fourth filter corresponds to P_2 and P_4 , etc. This structure can easily be extended to the third and higher levels that correspond to occurrence of multiple concurrent sensor faults. It must be noted that when the new bank of filters is activated in the second level, the first bank will be disabled in order to avoid adding

any unnecessary computational burden. Therefore, at any given time only six filters are operating on-line.

Remark 3.1 In this chapter, the value of the pre-determined sensor bias fault severity, b_{dj} as given by (3.17), is considered to be the same for all the filters and only one level of fault severity is considered for the hierarchical MM scheme, although various pre-determined sensor bias faults can easily be incorporated into our strategy by correspondingly increasing the number of filters that are used in this scheme.

3.4 Sensor Fault Identification

One of the important requirements of a general control system is the capability to integrate the FDI scheme with a fault identification or estimation module in order to estimate the severity of a fault that has occurred in different components of the system such as sensors and actuators. In this chapter, a modified version of the generalized likelihood ratio (GLR) scheme is developed to estimate the severity of a sensor bias fault. The GLR was initially proposed by Willsky in [8] and was subsequently modified in [159–161] and [162]. This method is capable of estimating the time, location and severity of an occurred fault using a selected threshold. However, in this chapter the occurrence time and location of a fault have already been determined by means of our proposed MHKF-based approach as presented in Section 3.3. Hence, the fault severity will be estimated through the development of a modified version of the GLR scheme. The GLR method is a detection-estimation scheme in which the time of a fault is an *a priori* information input to the estimation stage. In this chapter, the GLR method is simplified by removing the detection process through integrating the GLR method with our proposed MM-based FDI scheme, and hence there is no longer a need to select a threshold for our FDII scheme.

Let us assume that a bias fault has occurred in the s^{th} sensor with the severity

b_s at the sample k_{fs} and it is detected and isolated at the sample k_{ds} when the $P_1(k)$ mode probability intersects with the $P_{(s+1)}(k)$ mode probability. Also, for $k \geq k_{ds}$, $P_{(s+1)}(k)$ has the highest value among the other mode probabilities as shown mathematically by $(s+1) = \arg_j \max P_j(k)$. Therefore, the effects of the s^{th} sensor fault still remain in the residual of the MHKF that is associated with the healthy mode. There are L PWL models corresponding to the healthy mode that will be used subsequently to estimate the fault severity as follows:

$$\begin{aligned}\hat{X}^{(i,1)}(k+1) - X_{\text{OBEM}}(k+1) &= A^i(\hat{X}^{(i,1)}(k) - X_{\text{OBEM}}(k)) + K_{ss}^i(Y(k) - \hat{Y}^{(i,1)}(k)), \\ \hat{Y}^{(i,1)}(k) &= C^i(\hat{X}^{(i,1)}(k) - X_{\text{OBEM}}(k)) + Y_{\text{OBEM}}(k),\end{aligned}\quad (3.25)$$

in which the j^{th} index and b_{dj} in (3.17) are equal to one and zero, respectively, that are designated to the healthy sensor mode. Therefore, the residual vector of the MHKF that is designed for the healthy sensor mode at any subsequent time can be expressed as follows:

$$\gamma^{(i,1)}(k) = b_s G_s^i(k, k_{ds}) z_s + v(k) \quad \text{for } k \geq k_{ds}, \quad (3.26)$$

where z_s is defined in (3.16) and $G_s^i(k, k_{ds})$ denotes the failure signature matrix that provides one with the information on the failure propagation through the filter, and which also depends on both k_{ds} and the sample time k at which the set of L innovation vectors are computed for the MHKFs associated with the healthy mode. The signature matrices for a sensor bias fault can be computed by using the recursive relations for the healthy mode MHKFs as follows [159]:

$$\begin{aligned}G_s^i(k, k_{ds}) &= I - C^i A^i J_s^i(k-1, k_{ds}), \\ J_s^i(k, k_{ds}) &= A^i J_s^i(k-1, k_{ds}) + K_{ss}^i G_s^i(k, k_{ds}),\end{aligned}\quad (3.27)$$

where $J_s^i(k, k_{ds})$ denotes the signature matrix for the state correction. The signature matrices $J_s^i(k, k_{ds})$ and $G_s^i(k, k_{ds})$ are defined separately for the L operating points over a window of duration $[k_{ds}, k_{ds} + \mathcal{N}]$, where \mathcal{N} denotes the data samples window

length. Also, it is assumed that $J_s^i(k_{ds}-1, k_{ds}) = 0$. The weighted signature matrices for a detected fault that cover the entire operating range of the gas turbine engine can be computed as follows:

$$\begin{aligned} G_s(k, k_{ds}) &= \sum_{i=1}^L \mu^{(i,1)}(k) G_s^i(k, k_{ds}), \\ J_s(k, k_{ds}) &= \sum_{i=1}^L \mu^{(i,1)}(k) J_s^i(k, k_{ds}), \end{aligned} \quad (3.28)$$

where $\mu^{(i,1)}(k)$ denotes the assigned weight to the i^{th} PWL model that is designed for the healthy sensor mode. Therefore, the modified GLR test which consists of a maximum likelihood estimation (MLE) of b_s when k_{ds} is known is used. For performing the maximization process, normally the log likelihood function is chosen as the GLR criterion as follows:

$$\begin{aligned} \mathcal{J} &= \sum_{k=k_{ds}}^{k_{ds}+\mathcal{N}} \gamma_c^{1T}(k) (S_c^1(k))^{(-1)} \gamma_c^1(k) - \sum_{k=k_{ds}}^{k_{ds}+\mathcal{N}} [\gamma_c^1(k) \\ &\quad - b_s G_s(k, k_{ds}) z_s]^T (S_c^1(k))^{(-1)} [\gamma_c^1(k) - b_s G_s(k, k_{ds}) z_s], \end{aligned} \quad (3.29)$$

where $\gamma_c^1(k)$ and $S_c^1(k)$ denote the weighted innovation vector and covariance matrix for the healthy sensor mode that are computed from (3.21). The maximization of the log likelihood function is associated with the minimization of the second summation in (3.29). It can easily be shown that the optimal solution to the MLE problem above is the estimated fault $\hat{b}_s = \frac{d_s}{c_s}$, that is the unbiased estimate of b_s having the minimum variance as follows:

$$\begin{aligned} d_s &= z_s^T \sum_{k=k_{ds}}^{k_{ds}+\mathcal{N}} G_s^T(k, k_{ds}) (S_c^1(k))^{(-1)} \gamma_c^1(k), \\ c_s &= z_s^T \sum_{k=k_{ds}}^{k_{ds}+\mathcal{N}} G_s^T(k, k_{ds}) (S_c^1(k))^{(-1)} G_s(k, k_{ds}) z_s. \end{aligned} \quad (3.30)$$

The above procedure can also be employed for estimating the severities of multiple concurrent faults that have already been detected and isolated by means of our proposed hierarchical MM-based FDI approach.

Remark 3.2 In this chapter, it is assumed that there is no feedback and information sent from the fault identification module to the FDI scheme; otherwise, the FDI scheme needs to have a variable structure for updating the pre-determined sensor bias faults based on the estimated faults severities.

3.5 Simulation Results

In this section, simulation results and performance evaluation of our proposed sensor FDI scheme as applied to several fault scenarios are presented for a nonlinear mathematical model of a commercial single spool jet engine that is described in Chapter 2. For this study, our model is extended to the entire flight profile and is simulated in the SIMULINK for use as both the actual engine and the OBEM model. The actual engine operates at a given health condition subject to the effects of process and measurement noise signals, whereas the OBEM health parameters reference baselines are periodically updated to their recently estimated values that are assumed to be generated by an off-line health monitoring module as described in Section 3.1.

Both the actual engine and the OBEM models operate in almost the same ambient conditions. The set of nonlinear state-space equations that are used for the engine model are given in (2.3). The ambient parameters are affected by the Gaussian process noise with the standard deviations of $SD_{\zeta} = [0.01, 0.01]^T$ corresponding to the percentages of standard conditions of ambient variables, and the sensors are affected by the Gaussian measurement noise with the standard deviations of $SD_v = [0.23, 0.164, 0.051, 0.097, 0.164]^T$ corresponding to the percentages of output vector at the cruise condition as defined in [3].

The noise free values of the ambient parameters are applied to the OBEM model. Also, the same control input is applied to both the actual engine and the

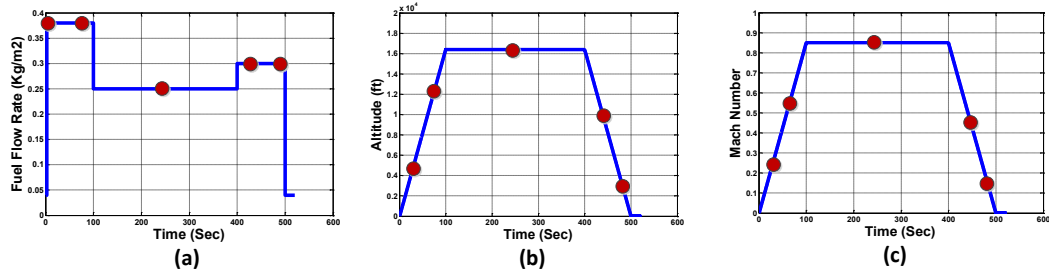


Figure 3.2: Profiles of (a) the fuel flow rate, (b) altitude, and (c) the Mach number during a flight mission.

OBEM models. The system is simulated for 520 sec with the sampling rate of 0.01 sec. The profiles of the altitude, Mach number and the fuel flow rate are shown in Figure 3.2.

According to the overall structure of our proposed scheme, as shown in Figure 3.1, six PWL models are constructed ($q = 5$) corresponding to each operating point for the five faulty sensor modes as well as the one healthy mode with the pre-determined sensor bias faults set to 3% of the engine steady-state outputs under the cruise condition. The states and sensor outputs are estimated by means of our proposed MHKFs. Finally, six weighted matrices are calculated according to (3.21) and are applied in the MM-based scheme for detecting and isolating the sensor bias faults that occur at different points of the flight profile.

For our simulations, the measurement and process noise covariance matrices are set to $0.01I$ and $0.1I$, respectively, where I denotes an identity matrix. In this chapter, the FDII scheme is implemented for the entire flight profile including the climbing, cruise and landing modes. Therefore, we assume and consider five operating points handling the entire flight profile ($L = 5$). This is the *minimum* number of the operating points that are obtained for each faulty mode that prevents the occurrence of a false alarm in the range of the applied health degradations. The number of the operating points depends on the dynamics of the engine as well as the

Table 3.2: The operating point specifications corresponding to the designed PWL models, where \dot{m}_f and Alt are measured in Kg/m² and ft, respectively.

Models Corresponding to Flight Conditions	\dot{m}_f	Mn	Alt
Operating Point 1 (Climbing)	0.38	0.2109	4070.538
Operating Point 2 (Climbing)	0.38	0.6585	12708.33
Operating Point 3 (Cruise)	0.25	0.85	16404.2
Operating Point 4 (Landing)	0.3	0.5402	10424.87
Operating Point 5 (Landing)	0.3	0.1203	2322.835

range of the applied fuel flow rate and the environmental parameters. We simulated our proposed FDII scheme with different number of operating points and also derived a confusion matrix for each case in order to analyze the false alarm rates and to decide on the minimum required number of the operating points that does not lead to any false alarms for the injected health degradations.

Table 3.2 shows the corresponding fuel flow rates as well as the flight conditions corresponding to all the applied PWL models that are designed for each sensor mode. The selected operating points are also displayed in Figure 3.2 using the red solid circles. In order to efficiently track the variations of the system input during the climbing and landing conditions, two operating points are selected for each of these two modes; whereas only one operating point is selected for the cruise condition given the presence of a constant input.

During the fault detection and isolation process, a mode probability $P_j(k)$ is generated for each weighted model using (3.23) and by determining the maximum $P_j(k)$, $j = 1, \dots, q + 1$, the sensor fault is detected and isolated.

The health parameter degradations due to the engine aging is one of the non-fault related factors that should be considered for a reliable and an accurate FDII strategy. Therefore, the performance of the FDII strategy is evaluated in presence of compressor or turbine health parameters degradations from their healthy reference baselines. Generally, there is a difference between the actual and the estimated

health parameter reference baselines due to off-line health monitoring estimation errors and also due to effects of noise and disturbances. Therefore, the robustness of our proposed FDII scheme will also be evaluated subsequently in this section with respect to the percentage of the reference baselines estimation errors.

3.5.1 Case 1: False Alarms Evaluation

Many factors such as (i) the dynamic mismatch between the OBEM model and the actual engine model, (ii) the large estimation errors for an off-line health monitoring module, and (iii) the process and measurement noise, may lead to false alarm flags. In order to evaluate the reliability and the efficiency of our proposed FDII scheme in terms of avoiding false alarms, our proposed scheme is simulated over the entire flight profile as shown in Figure 3.2. The estimated reference baselines ($\hat{\alpha}$) may differ from the actual degraded engine (α) and this can play a source of uncertainty in our FDII scheme in addition to the process and measurement noise. It should be noted that the dynamic mismatch between the actual engine and the OBEM models is also another source of uncertainty, but this is not investigated in this thesis. Therefore, the robustness of the FDII scheme against the percentage of the reference baselines estimation error RBEE ($\text{RBEE}\% = 100 \times \frac{\Delta\alpha}{\alpha}$, where $\Delta\alpha = |\alpha - \hat{\alpha}|$ and $\alpha \in [0, 1]$) is investigated in this section.

Based on our simulation studies for the healthy sensors scenario, the FDII algorithm is robust to the maximum percentage of reference baselines estimation error of 3% for the compressor health parameters and a maximum of 2% for the turbine health parameters. Our proposed FDII algorithm has declared no false alarms in the range of the above RBEEs, however the possibility of false alarms will increase if the RBEEs are increased beyond these upper limits. In case that one is within these limits, the mode probability of the healthy sensors is near one whereas the other probabilities corresponding to the faulty sensor scenarios are all almost

zero during the entire flight profile. The values for the probabilities depend on the design parameter ρ . In general the MM-based FDI is independent of ρ as long as it is selected as sufficiently small.

3.5.2 Case 2: A 3% Sensor Bias Fault Detection and Isolation

In this section, the performance of the sensor FDI scheme with respect to the fault detection time and the robustness of the algorithm with respect to the percentage of reference baselines estimation error (RBEE) are evaluated. This evaluation is performed during the entire flight profile which lasts for 520 sec, when a pre-determined bias fault with the severity of 3% of the engine steady-state output values under cruise condition occurs for a single sensor. Table 3.3 shows the fault detection times for each single sensor fault scenario at different stages of the flight profile including the climbing, cruise and landing modes. It also shows the maximum tolerable percentages of the RBEE of engine health parameters that is denoted by $\overline{\Delta\alpha}$. It is assumed that $\alpha = 0.99$. The limits are obtained through preserving two performance requirements for our proposed FDI scheme, namely: 1) the sensor fault detection time (FDT) should be less than 8 sec, and 2) no false alarms should be generated. This implies that our proposed FDI scheme can tolerate the reference baselines estimation error as long as the above performance requirements are fulfilled.

In addition, Figure 3.3 depicts the mode probabilities for three selected fault scenarios when the bias fault occurs at different instants of the flight profile. The value of the injected fault is set to 3% of the engine steady-state output values, while the percentage of the estimation errors for the compressor health parameters reference baselines (RBEE) are set at their maximum tolerable levels that are indicated in Table 3.3.

Table 3.3: Fault detection time (FDT) corresponding to the maximum tolerable percentage of the RBEE ($\overline{\Delta\alpha}$) at different stages of the flight profile.

Faulty Scenario	Maximum Tolerable RBEE%		Sensor FDT (sec)			
			$k_f = 50$	$k_f = 250$	$k_f = 450$	
Fault on T_C	Compressor	$\overline{\Delta\alpha_{\dot{m}_C}} = 2.52$	$\overline{\Delta\alpha_{\eta_C}} = 2.52$	3.7	4.1	6.3
	Turbine	$\overline{\Delta\alpha_{\dot{m}_T}} = 2.52$	$\overline{\Delta\alpha_{\eta_T}} = 1.51$	3.5	5.1	5.9
Fault on P_C	Compressor	$\overline{\Delta\alpha_{\dot{m}_C}} = 1.01$	$\overline{\Delta\alpha_{\eta_C}} = 1.01$	7.8	5.9	8
	Turbine	$\overline{\Delta\alpha_{\dot{m}_T}} = 1.01$	$\overline{\Delta\alpha_{\eta_T}} = 0.30$	3.4	2.7	2.5
Fault on N	Compressor	$\overline{\Delta\alpha_{\dot{m}_C}} = 1.21$	$\overline{\Delta\alpha_{\eta_C}} = 2.02$	6.5	2.6	3.5
	Turbine	$\overline{\Delta\alpha_{\dot{m}_T}} = 1.01$	$\overline{\Delta\alpha_{\eta_T}} = 0.81$	6.5	2.5	2.9
Fault on T_T	Compressor	$\overline{\Delta\alpha_{\dot{m}_C}} = 0.2$	$\overline{\Delta\alpha_{\eta_C}} = 0.2$	7.8	3	4.7
	Turbine	$\overline{\Delta\alpha_{\dot{m}_T}} = 0.1$	$\overline{\Delta\alpha_{\eta_T}} = 0.1$	6	2.2	2.3
Fault on P_T	Compressor	$\overline{\Delta\alpha_{\dot{m}_C}} = 0.3$	$\overline{\Delta\alpha_{\eta_C}} = 0.3$	7	2.6	3.4
	Turbine	$\overline{\Delta\alpha_{\dot{m}_T}} = 0.3$	$\overline{\Delta\alpha_{\eta_T}} = 0.1$	8	2.2	2.2

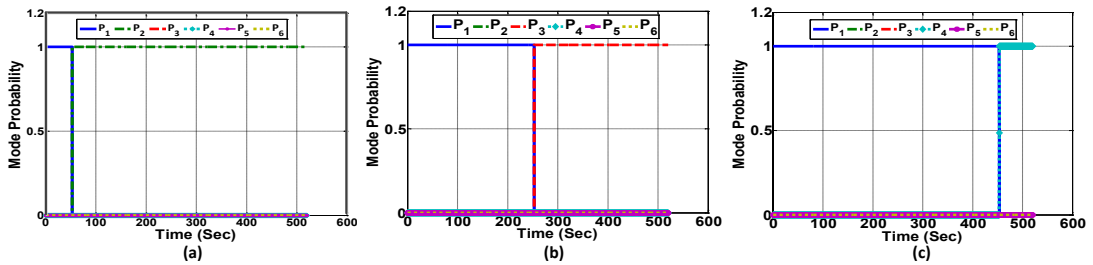


Figure 3.3: Mode probabilities for 3% bias fault applied at (a) $k_f = 50$ sec to the T_C sensor, (b) $k_f = 250$ sec to the P_C sensor, and (c) $k_f = 450$ sec to the N sensor in presence of the obtained maximum tolerable percentage of the estimation errors in Table 3.3 for the compressor health parameter reference baselines.

By comparing the results in Table 3.3, it can be concluded that the sensor fault detection times during the cruise mode are much less than that of the other flight modes since there is less variation of thrust and ambient conditions. In spite of a large input and ambient condition variations during the climbing and the landing modes, it is still possible to detect a sensor fault by applying our proposed FDI scheme. In order to show this capability, the sensor faults occur at $k_f = 50$ sec during the climbing mode, at $k_f = 250$ sec during the cruise mode and at $k_f = 450$ sec during the landing mode. The fault detection times are all indicated in Table 3.3 for various fault scenarios.

To quantify the effectiveness and reliability of our proposed FDI scheme in

Table 3.4: The confusion matrix for 3% RBEE of the compressor health parameters.

	T_C	P_C	N	T_T	P_T	No Fault
T_C	50	0	0	0	0	0
P_C	1	49	0	0	0	0
N	0	0	50	0	0	0
T_T	12	0	0	27	10	1
P_T	17	0	0	0	29	4
No Fault	0	0	0	0	0	50

Table 3.5: The confusion matrix for 3% RBEE of the turbine health parameters.

	T_C	P_C	N	T_T	P_T	No Fault
T_C	50	0	0	0	0	0
P_C	0	50	0	0	0	0
N	1	0	48	0	0	1
T_T	2	0	0	41	0	7
P_T	0	1	0	0	44	5
No Fault	0	1	0	0	0	49

presence of the mismatch between the OBEM model and the actual engine, confusion matrices are obtained for both the healthy and the faulty scenarios subject to different health parameter degradations and measurement noise. The rows in the confusion matrix are the fault conditions and the columns are the actual isolated faults. The element in the i^{th} row and j^{th} column (CM_{ij}) shows the rate that fault j is isolated when fault i occurs. Ideally, the confusion matrix should be a purely diagonal matrix. To obtain the confusion matrix for our sensor FDI scheme, 50 Monte Carlo simulations are performed in which the percentage of the RBEE exceeds the maximum tolerable limit that is reported in Table 3.3. Tables 3.4 and 3.5 show the confusion matrices for the healthy and 3% faulty scenarios as applied to the gas turbine engine sensors during the cruise mode subjected to 3% RBEE of both the compressor and the turbine health parameters, respectively.

In addition to the percentage of the RBEE, the measurement noise is another factor that can affect the performance of our proposed FDI scheme. Consequently, Table 3.6 depicts the confusion matrix that is obtained for investigating the effects

Table 3.6: The confusion matrix for the measurement noise signals where the SDs are multiplied by a factor of 20.

	T_C	P_C	N	T_T	P_T	No Fault
T_C	48	0	0	0	0	2
P_C	0	46	0	0	0	4
N	0	0	49	0	0	1
T_T	0	0	0	48	0	2
P_T	0	0	0	1	47	2
No Fault	0	0	0	0	1	49

of measurement noise signals, when their original standard deviations (SD_v) are multiplied by a factor of 20.

According to our simulations, the initial impact of any increase in either the standard deviation of the noise measurements or the percentage of the RBEE is to delay the fault detection time. Moreover, the occurrence of false alarms and incorrect fault detections are the other consequences due to increases in the above uncertainty sources. Different performance indices can be defined to quantify the robustness of our proposed sensor FDI algorithm with respect to the levels of uncertainty sources [163], namely:

$$\begin{aligned}
 \text{FPR} &= \frac{\sum_{j=1}^5 \text{CM}_{6j}}{\sum_{j=1}^6 \text{CM}_{6j}}, & \text{ACC} &= \frac{\sum_{i=1}^6 \text{CM}_{ii}}{\sum_{j=1}^6 \sum_{i=1}^6 \text{CM}_{ij}}, \\
 \text{IFDR} &= \frac{\sum_{j=1}^5 \sum_{i=1}^5 \text{CM}_{ij}(i \neq j)}{\sum_{j=1}^6 \sum_{i=1}^5 \text{CM}_{ij}}, & & (3.31)
 \end{aligned}$$

where FPR, ACC and IFDR denote the false positive (false alarm) rate, accuracy and incorrect fault detection rate, respectively, that are calculated in Table 3.7 to investigate the effects of various uncertainty sources.

According to Table 3.7, increasing the levels of the uncertainty sources results in decrease of ACC, but increase in FPR and IFDR. Notwithstanding these observations, our proposed sensor FDI scheme still works sufficiently robust against a high level of measurement noise as well as discrepancies between the OBEM model and the actual engine health parameters reference baselines.

Table 3.7: Sensor FDI algorithm performance indices corresponding to different levels of uncertainties.

Scenarios	FPR	ACC	IFDR
3% Compressor RBEE	0	0.85	0.16
4% Compressor RBEE	0.12	0.66	0.376
3% Turbine RBEE	0.02	0.94	0.016
4% Turbine RBEE	0.04	0.91	0.076
Noise $SD \times 20$	0.02	0.956	0.0004
Noise $SD \times 25$	0.02	0.91	0.012

3.5.3 Case 3: Sensor Fault Detection and Isolation for Different Fault Severities

In real applications, there is no guarantee that the sensor bias fault severity always matches the 3% pre-determined fault for which the MM structure is designed. Therefore, it is essential to investigate the performance of our proposed MM-based FDI scheme for an applied sensor bias fault having different severities starting from the minimum detectable bias. Table 3.8 shows the average detection times for all the faulty modes as a function of the fault severities, when the applied faults occur at different stages of the flight profile with also the maximum tolerable RBEE% for the compressor health parameters that are indicated in Table 3.3. It can be observed from Table 3.8 that the higher the fault severity with respect to the pre-determined 3% fault, the later the detection time, given that the actual fault becomes further different from the pre-determined bias fault. Note that the minimum detectable sensor bias fault is 2% that requires larger time to be detected as compared to the higher fault severities, especially during the climbing and landing flight modes.

It should be pointed out that our proposed MM-based structure is designed for a 3% sensor bias fault and is not capable of detecting and isolating sensor bias faults that have far greater severities. For this purpose, Table 3.9 shows the maximum detectable sensor bias faults by using our proposed FDI scheme by also considering

Table 3.8: The average sensor fault detection times for all fault modes as a function of the fault severity at different stages of the flight profile, under the maximum tolerable RBEE% for the compressor health parameters.

Fault Time	2%	3%	4%	5%	6%
$k_f = 50$ sec	14.18	6.56	6.74	7.42	8.6
$k_f = 250$ sec	8.34	3.64	3.98	4.76	5.7
$k_f = 450$ sec	17.66	5.18	5.32	6.66	7.52

Table 3.9: The average of the maximum detectable sensor bias fault (as percentage of the engine steady-state outputs) over the entire flight profile by using our FDI scheme when the corresponding maximum tolerable RBEE% reported in Table 3.3 are applied to the compressor and turbine health parameters.

Fault Modes	Max. Tolerable Compressor RBEE%	Max. Tolerable Turbine RBEE%
T_C	25%	70%
P_C	20%	50%
N	12%	100%
T_T	10%	14%
P_T	70%	75%

the maximum tolerable RBEE% for the compressor and the turbine health parameters. The reported detectable fault severities in Table 3.9 correspond to the average fault severities for all the flight modes. However, if an applied sensor bias fault increases beyond the corresponding maximum detectable fault as indicated in Table 3.9, an incorrect fault may be detected. Therefore, it is recommended that one incorporates more models within the MM-based structure corresponding to higher pre-determined sensor faults to become capable of detecting and isolating faults with higher magnitudes in shorter durations of time.

3.5.4 Case 4: Sensor Fault Severity Identification

One of the advantages of our proposed MM-based FDI scheme is its capability in providing information on the occurred fault severity. However, this method is not precise for fault severity estimation, since it provides one with only information on the level of an occurred fault instead of the exact fault severity. Therefore, the

modified GLR method introduced in Section 3.4 is integrated with our MM-based FDI scheme to estimate the sensor bias fault magnitude and severity. In order to investigate the performance of our proposed fault severity estimation method, the notion of the percentage of weighted mean square normalized residual errors (WMSNE) are obtained for various detected fault scenarios as follows:

$$\begin{aligned} \text{WMSNE}\% &= \frac{1}{L} \sum_{i=1}^L \frac{\sum_{k=k_{ds}}^{\mathcal{K}} w^{(i,s+1)}(k) \left(\frac{Y(k) - \hat{Y}^{(i,s+1)}(k)}{Y(k)} \right)^2}{\sum_{k=k_{ds}}^{\kappa} w^{(i,s+1)}(k)} \times 100, \\ \hat{Y}^{(i,s+1)}(k) &= C^i (\hat{X}^{(i,s+1)}(k) - X_{\text{OBEM}}(k)) + Y_{\text{OBEM}}(k) \\ &\quad + \hat{b}_s z_s \delta(k - k_{ds}), \quad s = 1, \dots, q \end{aligned} \quad (3.32)$$

where \mathcal{K} is the total simulation samples and $\hat{Y}^{(i,s+1)}(k)$ is the numerically constructed output associated with the $(s+1)^{th}$ operational mode corresponding to the s^{th} fault, in which the fault vector effect is generated based on the estimated fault magnitude \hat{b}_s and the fault occurrence detected time k_{ds} . It must be noted that there is no feedback and information sent from the fault estimation module to the filters for updating their pre-determined bias faults. Table 3.10 shows the average percentage of the WMSNE that is measured for different stages of the flight profile as a function of the bias fault severity as applied to various sensors.

Table 3.10: The average WMSNE% for all flight modes as a function of the bias fault severity applied to various sensors without considering any estimation error for the health parameter reference baselines.

Fault	2%	3%	4%	5%	6%
T_C	0.0085	0.0067	0.0073	0.0124	0.0195
P_C	0.1360	0.1106	0.1293	0.1689	0.2537
N	0.0111	0.0109	0.0107	0.0105	0.0104
T_T	0.0137	0.0066	0.0128	0.0312	0.0944
P_T	0.1313	0.1269	0.1359	0.1503	0.1615

According to Table 3.10, the average percentage of WMSNE is less than 0.5% for various faults that are limited within the operational range of our FDI scheme as was defined in the preceding case. It can also be observed that the percentage

of the WMSNE is lower for the cruise flight mode as compared to the climbing and landing modes due to the high variations of the engine thrust.

3.5.5 Case 5: Concurrent Fault Detection, Isolation and Identification

In previous simulations only a single sensor fault is applied to the gas turbine engine. In this case study, our proposed FDII scheme is used for concurrent fault scenarios that occur at different stages of the flight profile. For this purpose, the hierarchical scheme described in Section 3.3.2 is used to diagnose the concurrent sensor faults. The fault detection times and the percentages of the WMSNE as given by (3.32) are obtained for two selected scenarios with concurrent sensor faults. The first scenario simulates the effects of a 6% bias fault applied to the T_C sensor at $k_f = 50$ sec during the climbing mode and the concurrent 5% bias fault applied to the N sensor at $k_f = 250$ sec during the cruise mode. The estimated concurrent faults are depicted in Figure 3.4.

The concurrent faults for the first scenario are detected and isolated after 1.7 and 2.4 seconds, respectively from their occurrence instants, whereas the percentages of the WMSNEs are 0.0208% and 0.106%, respectively. The second scenario simulates the effects of a 4% bias fault that is applied to the T_T sensor at $k_f = 250$ sec during the cruise mode and the concurrent 6% bias fault that is applied to the P_T sensor at $k_f = 450$ sec during the landing mode. The concurrent faults for the second scenario are detected and isolated after 0.9 and 0.4 seconds, respectively from their occurrence instants, whereas the percentages of the WMSNEs are 0.0125% and 0.1702%, respectively.

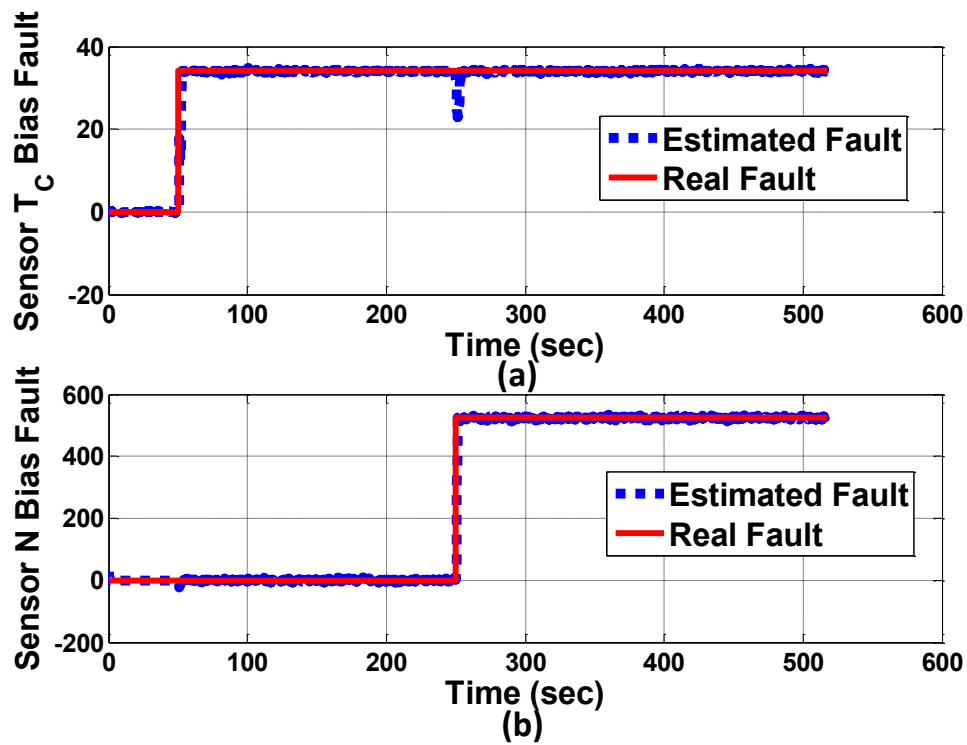


Figure 3.4: Estimated two concurrent sensor fault severities (a) a 6% bias fault that is applied to the T_C sensor at $k_f = 50$ sec, and (b) a 5% bias fault that is applied to the N sensor at $k_f = 250$ sec without considering any health parameter degradations.

3.5.6 Case 6: Comparison

In this section, the efficiency of our proposed MM-based sensor FDI scheme which utilizes the MHKF as a detection filter is compared with different filtering methods including the linear Kalman filter (LKF) [143], extended Kalman filter (EKF) [60], unscented Kalman filter (UKF) [61], and the cubature Kalman filter (CKF) [62]. It must be noted that in the following conducted experiments, multiple combined residual vectors and covariance matrices associated with multiple operating points are computed for both the HKF and LKF filtering methods to construct the multiple HKF (MHKF) and multiple LKF (MLKF)-based FDI schemes, respectively. Moreover, our MM-based FDI scheme is compared with the *interacting multiple model* (IMM) approach [164, 165]. Different experiments are conducted in this section to compare the promptness of the fault detection and isolation scheme as well as the degree of robustness towards the health parameters degradations among the above filtering methods. In all the experiments, similar process and measurement noise signals are applied to the gas turbine engine and similar noise covariance matrices are used to construct the above filters. The sampling rates for simulating the actual engine and the nonlinear filtering approaches are 0.01 sec and 0.1 sec, respectively. Also, $2n + 1$ sigma points, where n is the dimension of the state variable vector, are generated in the UKF method with the tuning parameters $\alpha = 10^{-3}$, $\beta = 2$ and $\kappa = 0$. For the CKF method, $2n$ cubature points are generated through intersecting the unit sphere with the Cartesian axes and are then scaled by \sqrt{n} . The details regarding the formulations of the above applied filtering methods are included in Chapter 2.

Experiment 1: The 3% single bias fault is applied to different sensors at $k_f = 250$ sec during the cruise mode with no health parameter degradations. All the filters are capable of detecting and isolating the injected fault correctly with

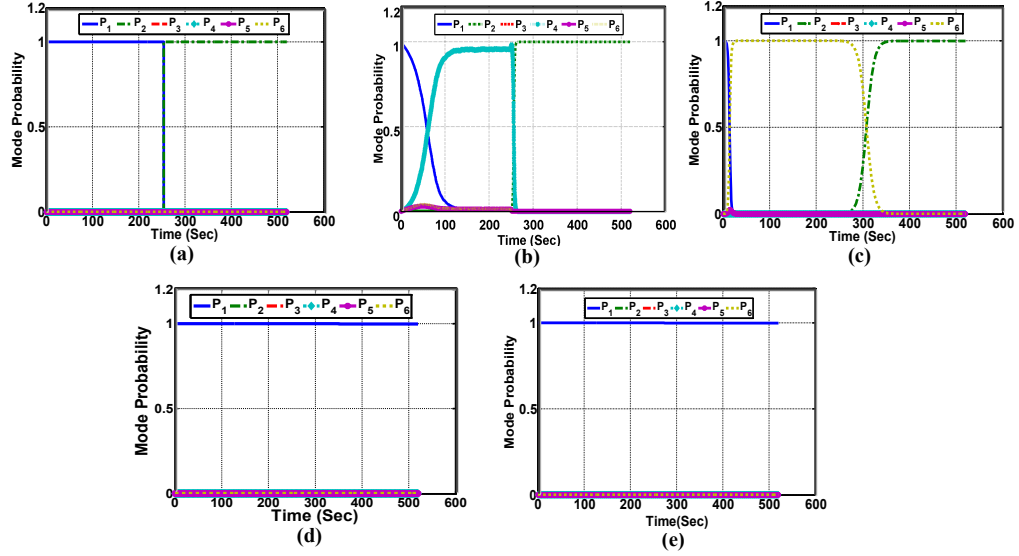


Figure 3.5: Mode probabilities for a 3% bias fault that is applied at $k_f = 250$ sec to the T_C sensor by applying multiple (a) HKF, (b) LKF, (c) EKF, (d) UKF and (e) CKF based FDI approaches with 2.5% degradations applied to the compressor health parameters of the actual engine.

different fault detection times. The sensor FDTs are shown in Table 3.12 for the detection filters that are utilized in the MM-based FDI scheme. It can be concluded from Table 3.12 that our proposed approach is capable of detecting and isolating the sensor faults faster than other methods, particularly the MLKF method, given that the OBEM can capture the nonlinear behavior of the engine more effectively than others. Although, the EKF, UKF, and CKF are well-known nonlinear filtering methods, however they detect and isolate the injected sensor faults with more delay than our proposed method. According to our observations that are included in Table 3.11, the HKF has smaller estimation error as compared to the EKF, UKF, and CKF, which leads to faster FDI performance. It is also expected that in case the OBEM is subjected to certain un-modeled dynamics with respect to a real engine, the FDTs that are obtained with multiple EKF, UKF, and CKF based FDI schemes are more comparable with our proposed MHKF-based FDI scheme.

Table 3.11: Absolute mean of residual signals associated with various types of non-linear filters corresponding to the healthy mode in the MM-based scheme for the healthy engine sensors without health degradation.

Sensor	Absolute Mean of Residual Signal			
	MHKF	EKF	UKF	CKF
T_C	8.8329×10^{-4}	0.00063	0.0058	0.0039
P_C	0.0044	0.0186	0.0127	0.0105
N	4.0454×10^{-4}	0.0032	0.0011	0.0009
T_T	8.1498×10^{-4}	0.0081	0.0085	0.0069
P_T	0.0014	0.0028	0.0082	0.0074

Experiment 2: The robustness of our developed MHKF-based FDI approach is compared with the other filtering methods here. The 3% bias fault is applied to the T_C sensor at $k_f = 250$ sec during the cruise mode with 2.5% degradations that are applied to the compressor health parameters. In this experiment, it is assumed that the OBEM health parameters are not updated and the 2.5% degradation is only applied to the compressor health parameters of the actual engine. Therefore, the reference baselines associated with the compressor health parameters are one for both the OBEM model and the nonlinear model that is used for deriving the other nonlinear filtering methods. The mode probabilities that are generated in this scenario are depicted in Figure 3.5. It can be concluded that our method outperforms the other approaches in terms of robustness with respect to the health parameters degradations. It is also shown in Figure 3.5 that the applied fault can be detected by using the EKF and MLKF methods in addition to our method, but false alarms are generated by these methods before the occurrence of the fault.

Experiment 3: Our proposed MHKF method is similar to the EKF in the sense of the linearization process at certain operating points instead of the entire flight profile. Therefore, one may expect that the EKF method can yield similar results to that of the MHKF method in case the health parameters are also updated for the nonlinear engine model used for deriving the EKF. In this experiment, the

same engine model where its health parameters are updated is used for the MM-based structures that utilize the MHKF and EKF schemes. The 3% bias fault is applied to the T_C sensor at $k_f = 250$ sec during the cruise mode with $\alpha = 0.99$ and $\hat{\alpha} = 0.975$. The estimated health parameters are updated similarly for both the EKF and MHKF schemes. Figure 3.6 shows the mode probabilities that are generated in this scenario. According to Figure 3.6, the EKF is also capable of correctly detecting and isolating the applied fault by using the health parameters updating mechanism. However, the fault detection time and the computational time of the EKF is far greater than that of the MHKF. The MM-based FDI method is capable of detecting and isolating the applied fault in 2.7 sec and 20.8 sec by using the MHKF and EKF methods, respectively. The same results are also obtained for the other fault scenarios.

Experiment 4: In this experiment, the performance of the FDI algorithm that utilizes our proposed MHKF as well as the other filtering methods are compared in the *interacting multiple model* (IMM) structure. For the IMM-based FDI structure, the sensor FDTs are computed for the 3% single bias fault that is applied to the sensors with no health parameter degradations as represented in the Table 3.13. According to the simulation results, the fault is detected sooner by using the IMM structure that utilizes all the detection filters except the MHKF. It appears that the interactions among the multiple models do not improve the MHKF-based FDI scheme performance. For simulating the IMM scheme which utilizes our proposed MHKF, the off-diagonal elements of the transition probability matrix should be selected less than 0.001; otherwise, the probability of the healthy mode monotonically decreases to reach almost 0.8 before the occurrence of a sensor fault which can enhance the risk of a false alarm. Therefore, it is not recommended to use the IMM scheme for the MHKF method.

Table 3.12: Sensor fault detection times using multiple non-interacting HKF, LKF, EKF, UKF and CKF based FDI approaches without considering health parameter degradation.

MM-Based FDI Approach	Fault Detection Time (FDT) (sec)				
	T_C	P_C	N	T_T	P_T
HKF	0.2	0.2	0.2	0.2	0.3
LKF	8.3	38.2	16.9	12.1	12.4
EKF	1	1	0.9	0.8	0.9
UKF	0.6	0.7	0.6	0.7	2.7
CKF	0.6	0.6	0.7	0.7	2.3

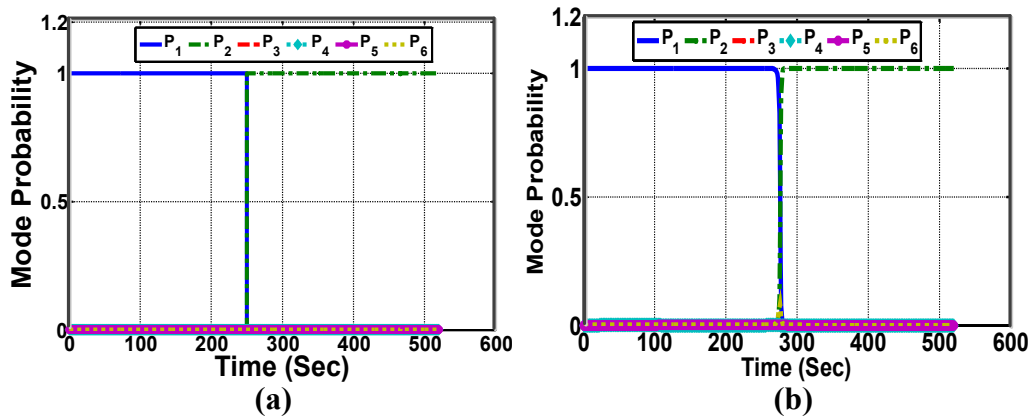


Figure 3.6: Mode probabilities for a 3% bias fault applied at $k_f = 250$ sec to the T_C sensor using (a) the MHKF and (b) the EKF-based FDI methods, with $\alpha = 0.99$ and $\hat{\alpha} = 0.975$.

Experiment 5: In this experiment, the computational time of all the above filtering methods are obtained and compared with our proposed MHKF approach in Table 3.14. This comparison confirms the advantages of implementing the MHKF approach in real-time applications. The computational time is measured for only the filters corresponding to the healthy mode by the use of “*tic-toc*” command in Matlab. It must be noted that the computational time of the MHKF includes the time for not only simulating the healthy mode but also for running the OBEM model. Therefore, based on the information provided in Table 3.14, the MHKF scheme is

Table 3.13: Sensor fault detection times using multiple interacting HKF, LKF, EKF, UKF and CKF based FDI approaches without considering any health parameter degradation.

MM-Based FDI Approach	Fault Detection Time (FDT) (sec)				
	T_C	P_C	N	T_T	P_T
HKF	0.3	0.4	0.3	0.3	0.5
LKF	6.3	35.8	15.7	11.6	11.8
EKF	0.9	0.9	0.7	0.8	0.8
UKF	0.5	0.5	0.5	0.6	2.3
CKF	0.5	0.5	0.5	0.5	1.9

Table 3.14: Computational time as measured in seconds for different filtering methods.

MHKF	MLKF	EKF	UKF	CKF
131.21	526.81	1184.2	2856.4	2673.44

faster and more suitable than the other filtering methods to be utilized during the entire flight profile. Computing the Jacobian functions in each time step for the EKF method and also the cubature and sigma points with their corresponding mean and covariance weight matrices for the CKF and UKF methods, respectively are time consuming operations that lead to the higher computational time compared to our proposed MHKF scheme. Moreover, the MLKF approach computes the Kalman gain matrices on-line, whereas the MHKF utilizes the previously stored gain matrices. However, if the same steady-state Kalman gain matrices are computed off-line and stored for use in the MLKF approach, the average computational time associated with the healthy mode filters in the MLKF scheme is about 80 seconds, which is less than that of the MHKF method. Under this situation, the extra computational time required by the MHKF is associated with the OBEM operations. Therefore, the only disadvantage of the MHKF method is the amount of memory that is needed for storing the look-up tables that include the matrices A^i , C^i and K_{ss}^i at different operating points.

Experiment 6: In this experiment, the number of the required operating points is investigated by measuring the mean of the combined residual signals in presence of the health parameter degradations for the LKF and HKF methods. To cover the entire flight profile, five operating points are generated for the HKF method as described in Table 3.2. Note that the LKF method still needs more operating points since it is not capable of tracking rapid variations of the thrust during the climbing and landing modes, and therefore it generates false alarms due to the higher estimation error as compared to the HKF scheme. Table 3.15 compares the mean of the HKF and LKF combined residual signals that are associated with the healthy mode as a function of the number of operating points. The Figure 3.7 displays the mode probabilities that are generated for the HKF and LKF methods for different numbers of operating points. In this experiment, the engine has no sensor fault, but a 3% degradation is applied to the actual engine compressor health parameters. As stated in Section 3.5.1, the HKF is robust with respect to the applied health degradations even without updating the OBEM model health parameters, although the HKF needs to be updated for larger degradation levels. Based on the results obtained, it can be concluded that the mean of the combined residual signal associated with the healthy mode can be reduced by increasing the number of the operating points. It is expected that the LKF estimation error decreases further by increasing the number of the operating points. However, we are not capable of perfectly avoiding generation of a false alarm by using the LKF method corresponding to our particular flight profile by increasing the number of operating points, since the LKF cannot track high variations of the thrust in our application. Therefore, it may be feasible to apply the LKF with the combined PWL models if the engine thrust increases with the slower speed than ours since the PWL model weights calculation is a time-consuming process which may diminish the ability of the LKF to track the rapid variations of the thrust.

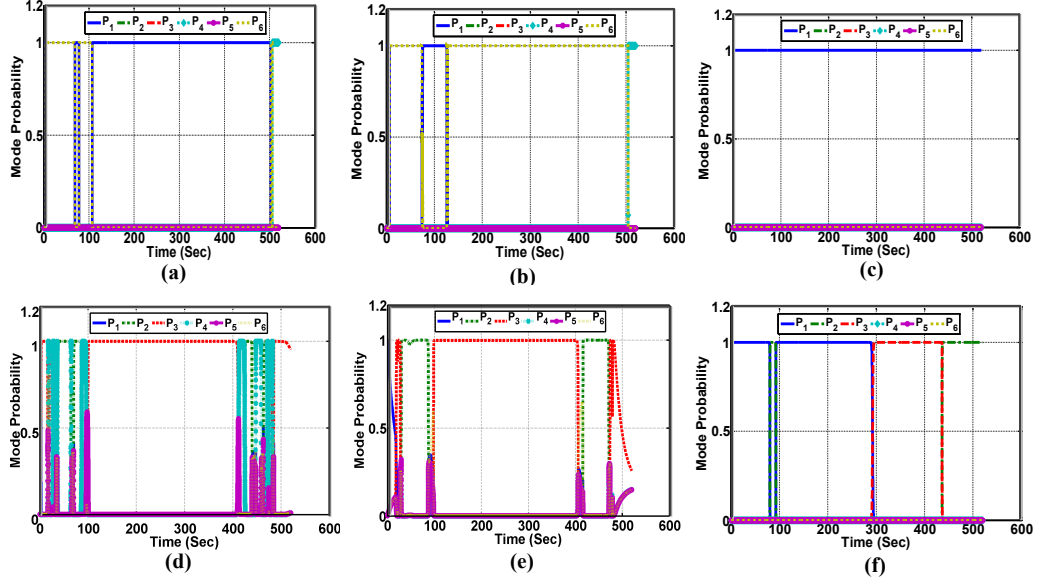


Figure 3.7: Mode probabilities that are generated for the MM-based FDI method by utilizing (a-c) the HKF and (d-f) the LKF with one, three and five operating points.

Table 3.15: Mean of the combined residual signals ($\bar{\gamma}_c^1$) associated with the healthy mode for both the HKF and LKF methods in terms of the number of the operating points.

$\bar{\gamma}_c^1$	1 operating point		3 operating points		5 operating points	
	HKF	LKF	HKF	LKF	HKF	LKF
Measurement 1	0.109	0.2305	0.077	0.1091	0.0119	0.0857
Measurement 2	0.2286	0.943	0.0771	0.1523	0.0216	0.1315
Measurement 3	0.0255	0.0123	0.0167	0.0053	0.0003	0.0014
Measurement 4	0.0813	0.3339	0.0745	0.2372	0.0197	0.1008
Measurement 5	0.0152	0.0477	0.0116	0.036	0.0006	0.0049

Therefore, it can be concluded that the MM-based FDI scheme which utilizes our proposed HKF approach is capable of promptly detecting and isolating various sensor bias faults during the *entire flight profile* by updating the OBEM health parameters reference baselines and even without updating the OBEM model for certain levels of health parameter degradations. Our scheme also estimates the engine state and output variables with more accuracy and smaller number of operating points as compared to that by the MLKF based FDI scheme.

3.6 Summary

In this chapter, a single and concurrent fault detection, isolation and identification method is proposed in which a novel hybrid Kalman filter (HKF) is constructed using a nonlinear on-board engine model (OBEM) as well as multiple piecewise linear models that are derived in different operating points to cover the entire operating regime. The proposed HKF is capable of capturing the system nonlinearities and can cover the entire operating regime of a nonlinear system with less number of operating points as compared to the linear Kalman filter. In this chapter, it is assumed that the engine health parameters are estimate offline using a health monitoring tool and will be updated periodically for the OBEM. Nevertheless, the robustness of our proposed multiple HKF-based FDI scheme is investigated with respect to different health parameters degradation magnitudes. Our proposed FDI scheme is also integrated with the GLR method to estimate the severity of a sensor fault at different stages of the flight profile for the single spool gas turbine engine. Finally, it is demonstrated through extensive simulation studies that the accuracy and the robustness of our multiple HKF-based FDI approach against the engine health parameters degradations are higher than those of generated by the LKF, EKF, UKF and CKF based multiple model FDI approaches.

Chapter 4

Robust Kalman Filter Based Fault Detection and Isolation

In this chapter, a novel robust sensor fault detection and isolation (FDI) strategy using the multiple model-based (MM) approach is proposed that remains robust with respect to both time-varying parameter uncertainties and process and measurement noise in all the channels. The scheme is composed of robust Kalman filters (RKF) that are constructed for multiple piecewise linear (PWL) models that are constructed at various operating points of an uncertain nonlinear system. The parameter uncertainty is modeled by using a time-varying norm bounded admissible structure that affects all the PWL state space matrices. The robust Kalman filter gain matrices are designed by solving two algebraic Riccati equations (ARE) that are expressed as two linear matrix inequality (LMI) feasibility conditions.

The main goal of the multi-objective formulation is to propose a robust filter that satisfies the overall performance requirements and is quadratically stable. The requirements include a quadratically stable filter that ensures bounded estimation error variances having predefined values. Moreover, our proposed fault detection and isolation (FDI) scheme is capable of detecting and isolating sensor faults during

the entire operational regime of the system by interpolating the PWL models using a Bayesian approach. The proposed multiple RKF-based FDI scheme is simulated for a single spool gas turbine engine to diagnose various sensor faults despite the presence of parameter uncertainties, process and measurement noise. Our comparative studies confirm the superiority of our proposed FDI method in terms of promptness of the fault detection, estimation accuracy, lower false alarms and missed detection rates, as well as robustness with respect to the engine health parameters degradations when compared to the methods that are available in the literature. It must be noted that the main achievements in this chapter are published in [166] and [167].

4.1 Problem Statement

Let us consider a nonlinear, discrete-time closed-loop system that is governed by:

$$\begin{aligned} X(k+1) &= \mathcal{F}(X(k), w(k)), \\ Y(k) &= \mathcal{G}(X(k), v(k)) + \sum_{s=1}^q b_s z_s \delta(k - k_{fs}), \end{aligned} \quad (4.1)$$

where $X(k) \in \mathbb{R}^n$ and $Y(k) \in \mathbb{R}^q$ denote the state and measured output variables, respectively, $w(k) \in \mathbb{R}^p$ and $v(k) \in \mathbb{R}^q$ denote uncorrelated zero-mean Gaussian white noise signals with respective covariances $W > 0$ and $V > 0$. Moreover, b_s denotes the s^{th} sensor bias fault severity and z_s denotes the fault location vector that has a unit value for the s^{th} sensor and zero for the other elements, and $\delta(k - k_{fs})$ represents a unit step function that is activated at the time k_{fs} corresponding to the occurrence of the s^{th} fault. For the healthy sensor the bias is set to a value of zero. Consequently, $q+1$ sensor modes, representing q faulty and one healthy sensor modes are considered.

To design multiple linear filters for accomplishing the sensor fault detection and isolation that operates during the entire operating range of the system, the *fault-free* form of the nonlinear system is linearized at multiple operating points. These points

are denoted by $(X_{ss_i}, Y_{ss_i}, w_{ss_i}, v_{ss_i})$, $i \in 1, \dots, L$ (L denotes the required number of operating points that cover the entire operating region of the nonlinear system). The constructed multiple PWL models associated with the healthy sensors are now given by:

$$\begin{aligned}\Delta X^i(k+1) &= A|_{X_{ss_i}} \Delta X^i(k) + B|_{w_{ss_i}} \Delta w^i(k), \\ \Delta Y^i(k) &= C|_{X_{ss_i}} \Delta X^i(k) + D|_{v_{ss_i}} \Delta v^i(k),\end{aligned}\tag{4.2}$$

where $A|_{X_{ss_i}}$, $B|_{w_{ss_i}}$, $C|_{X_{ss_i}}$ and $D|_{v_{ss_i}}$ denote the i^{th} operating point system matrices and $\Delta X^i(k) = X(k) - X_{ss_i}$, $\Delta Y^i(k) = Y(k) - Y_{ss_i}$, $\Delta w^i(k) = w(k) - w_{ss_i}$ and $\Delta v^i(k) = v(k) - v_{ss_i}$. In this chapter, it is assumed that w_{ss_i} and v_{ss_i} are zero without loss of any generality.

The system matrices can be influenced by norm-bounded time-varying parameter uncertainties, which correspond to subcategory of linear fractional norm-bounded uncertainties, due to either imperfect knowledge on some parameters, or system components degradation, or deviations from the operating point when the system is linearized or there are uncertainties in the noise variances. Hence, multiple PWL models that are constructed in (4.2) can represent the parametric uncertainties as follows:

$$\begin{aligned}\Delta X^i(k+1) &= (A^i + \Delta A^i(k)) \Delta X^i(k) + (B^i + \Delta B^i(k)) \Delta w^i(k) \\ \Delta Y^i(k) &= (C^i + \Delta C^i(k)) \Delta X^i(k) + (D^i + \Delta D^i(k)) \Delta v^i(k),\end{aligned}\tag{4.3}$$

where $A^i = A|_{X_{ss_i}}$, $B^i = B|_{w_{ss_i}}$, $C^i = C|_{X_{ss_i}}$ and $D^i = D|_{v_{ss_i}}$. Note that $\Delta A^i(k)$, $\Delta B^i(k)$, $\Delta C^i(k)$ and $\Delta D^i(k)$ denote *admissible* time-varying parameter uncertainties that are associated with the i^{th} operating point. Moreover, it is assumed that the uncertainties satisfy the following relationship:

$$\begin{aligned}\begin{bmatrix} \Delta A^i(k) & \Delta B^i(k) \\ \Delta C^i(k) & \Delta D^i(k) \end{bmatrix} &= \begin{bmatrix} M_1^i \\ M_2^i \end{bmatrix} F^i(k) \begin{bmatrix} N_1^i & N_2^i \end{bmatrix}, \\ F^i(k) F^{i\top}(k) &\leq I,\end{aligned}\tag{4.4}$$

where $F^i(k)$ represents an uncertain norm-bounded time-varying matrix that satisfies the above condition for the i^{th} operating point. The matrices M_1^i and M_2^i yield perturbed elements of the system matrices through the parameter uncertainties, whereas the matrices N_1^i and N_2^i are employed to represent the maximum possible uncertainties that may occur in the matrices that are associated with the i^{th} operating point. The parameter uncertainties are said to be *admissible* if they can satisfy the above condition. We now state our first definition.

Definition 1. *The linear uncertain system (4.3) is said to be quadratically stable if a positive definite matrix Q^i exists such that*

$$(A^i + \Delta A^i(k))Q^i(A^i + \Delta A^i(k))^T - Q^i < 0, \quad (4.5)$$

for all the admissible uncertainties $\Delta A^i(k)$ [168].

We are now in a position to state the *main objective* of this chapter. Specifically, our goal is to design multiple quadratically stable linear robust Kalman filters that are capable of detecting and isolating sensor faults having predefined upper bounds on the estimation error variances in presence of parameter uncertainties. To address the above problem, first a linear RKF is designed for a single operating point and then the methodology is extended to multiple operating points as well as for uncertain PWL models in the following sections.

4.2 Robust Kalman Filter Design

For the i^{th} uncertain PWL model that is given by (4.3) and satisfies the Definition 1, a linear RKF is designed with the parameters \bar{A}^i , \bar{C}^i and K^i as follows:

$$\begin{aligned} \Delta \hat{X}^i(k+1) &= \bar{A}^i \Delta \hat{X}^i(k) + K^i (\Delta Y^i(k) - \Delta \hat{Y}^i(k)) = G^i \Delta \hat{X}^i(k) + K^i \Delta Y^i(k), \\ \Delta \hat{Y}^i(k) &= \bar{C}^i \Delta \hat{X}^i(k), \quad i = 1; \dots, L, \end{aligned} \quad (4.6)$$

where $G^i = \bar{A}^i - K^i \bar{C}^i$ (\bar{A}^i , \bar{C}^i and K^i are the i^{th} filter gain matrices defined subsequently in this section), the estimated vectors are defined as $\Delta \hat{X}^i(k) = \hat{X}(k) - X_{\text{ss}_i}$ and $\Delta \hat{Y}^i(k) = \hat{Y}(k) - Y_{\text{ss}_i}$. The problem is to design the gain matrices G^i and K^i such that for all admissible uncertainties that satisfy the condition (4.4), the designed filter is ensured to be quadratically stable, and moreover it satisfies $\text{Var}(e_l^i(k)) < (\sigma_l^i)^2$ for $l = 1, \dots, n$, where $e_l^i(k)$ denotes the l^{th} element of the estimation error vector defined as $e_l^i(k) = \Delta X_l^i(k) - \Delta \hat{X}_l^i(k)$ associated with the i^{th} filter and $(\sigma_l^i)^2$ denotes the individually predefined upper bound for the l^{th} element of the estimation error variance associated with the i^{th} filter.

The state estimation error for the i^{th} filter that is denoted by $e^i(k) = \Delta X^i(k) - \Delta \hat{X}^i(k)$ has an associated covariance matrix $P^i(k)$, where its steady-state is denoted by P^i . For notational simplicity, the superscript letter i is removed for the filter design process in this section. Therefore, the error dynamics is governed by:

$$e(k+1) = Ge(k) + \left((A - G - KC) + (M_1 F(k) N_1 - K M_2 F(k) N_1) \right) \Delta x(k) \\ + (B + M_1 F(k) N_2) \Delta w(k) - (KD + K M_2 F(k) N_2) \Delta v(k). \quad (4.7)$$

By defining the matrices:

$$A_f = \begin{bmatrix} A & 0 \\ A - G - KC & G \end{bmatrix}, \quad B_f = \begin{bmatrix} B & 0 \\ B & -KD \end{bmatrix}, \\ M_{1f} = \begin{bmatrix} M_1 \\ M_1 - K M_2 \end{bmatrix}, \quad N_{1f} = \begin{bmatrix} N_1 & 0 \end{bmatrix}, \\ M_{2f} = \begin{bmatrix} M_1 & 0 \\ M_1 & -K M_2 \end{bmatrix}, \quad N_{2f} = \begin{bmatrix} N_2 & 0 \\ 0 & N_2 \end{bmatrix},$$

$$\Delta A_f(k) = M_{1f} F(k) N_{1f}, \quad \Delta B_f(k) = M_{2f} \begin{bmatrix} F(k) & 0 \\ 0 & F(k) \end{bmatrix} N_{2f}, \quad (4.8)$$

for the augmented state variable, and $X_f(k) = [\Delta X(k)^T \ e(k)^T]^T$, the dynamic model becomes:

$$X_f(k+1) = (A_f + \Delta A_f(k))X_f(k) + (B_f + \Delta B_f(k))w_f(k), \quad (4.9)$$

where $w_f(k) = [\Delta w(k)^T \ \Delta v(k)^T]^T$. Assuming a quadratically stable augmented system, $X(k)$ which is the covariance matrix of $X_f(k)$ satisfies the discrete-time Lyapunov equation:

$$\begin{aligned} X(k+1) &= (A_f + \Delta A_f(k))X(k)(A_f + \Delta A_f(k))^T \\ &\quad + (B_f + \Delta B_f(k))W_f(k)(B_f + \Delta B_f(k))^T, \end{aligned} \quad (4.10)$$

where $W_f = \begin{bmatrix} W & 0 \\ 0 & V \end{bmatrix}$ and $\mathcal{X} = \begin{bmatrix} \mathcal{X}_{xx} & \mathcal{X}_{xe} \\ \mathcal{X}_{xe}^T & P \end{bmatrix}$ represent the steady-state covariance matrices of $w_f(k)$ and $X_f(k)$, respectively.

Before presenting our main result for design of the RKF, we first present a useful preliminary result below.

Lemma 1. *Let ϵ be a positive scalar and P_f denotes a symmetric positive definite matrix such that $N_{1f}P_fN_{1f}^T < \epsilon I$. Then,*

$$(A_f + \Delta A_f(k))P_f(A_f + \Delta A_f(k))^T \leq A_f(P_f^{-1} - \epsilon^{-1}N_{1f}^T N_{1f})^{-1}A_f^T + \epsilon M_{1f}M_{1f}^T. \quad (4.11)$$

Proof: According to Lemma 2 in [169], let us define

$$Z(k) = A_f P_f N_{1f}^T (\epsilon I - N_{1f} P_f N_{1f}^T)^{-1/2} - M_{1f} F(k) (\epsilon I - N_{1f} P_f N_{1f}^T)^{1/2}, \quad (4.12)$$

In view of the fact that $F(k)F^T(k) \leq I$, and by invoking the matrix inversion lemma, it can be shown that $Z(k)Z^T(k) \geq 0$, and the inequality (4.11) holds as follows. Let us define:

$$Z(k) = A_f P_f N_{1f}^T (\epsilon I - N_{1f} P_f N_{1f}^T)^{-1/2} - M_{1f} F(k) (\epsilon I - N_{1f} P_f N_{1f}^T)^{1/2}. \quad (4.13)$$

It follows that, the positive semi-definite matrix $Z(k)Z^T(k)$ can be expressed as

$$\begin{aligned}
Z(k)Z^T(k) &= A_f P_f N_{1f}^T (\epsilon I - N_{1f} P_f N_{1f}^T)^{-1} N_{1f} P_f A_f^T - A_f P_f N_{1f}^T F^T(k) M_{1f}^T \\
&\quad - M_{1f} F(k) N_{1f} P_f A_f^T + M_{1f} F(k) (\epsilon I - N_{1f} P_f N_{1f}^T) F^T(k) M_{1f}^T \\
&= A_f P_f N_{1f}^T (\epsilon I - N_{1f} P_f N_{1f}^T)^{-1} N_{1f} P_f A_f^T - \left(A_f P_f \Delta A_f^T(k) \right. \\
&\quad \left. + \Delta A_f(k) P_f A_f^T + \Delta A_f(k) P_f \Delta A_f^T(k) \right) \\
&\quad + \epsilon M_{1f} F(k) F(k)^T M_{1f}^T. \tag{4.14}
\end{aligned}$$

Since $F(k)F^T(k) \leq I$, it can be concluded that

$$Z(k)Z^T(k) \leq \Sigma(k), \tag{4.15}$$

where

$$\begin{aligned}
\Sigma &= A_f P_f N_{1f}^T (\epsilon I - N_{1f} P_f N_{1f}^T)^{-1} N_{1f} P_f A_f^T \\
&\quad - \left((A_f + \Delta A_f(k)) P_f (A_f + \Delta A_f(k))^T \right) + A_f P_f A_f^T + \epsilon M_{1f} M_{1f}^T. \tag{4.16}
\end{aligned}$$

It follows from $Z(k)Z^T(k) \geq 0$ that $\Sigma \geq 0$. Hence,

$$\begin{aligned}
(A_f + \Delta A_f(k)) P_f (A_f + \Delta A_f(k))^T &\leq A_f \left(P_f + P_f N_{1f}^T (\epsilon I - N_{1f} P_f N_{1f}^T)^{-1} N_{1f} P_f \right) A_f^T \\
&\quad + \epsilon M_{1f} M_{1f}^T \tag{4.17}
\end{aligned}$$

and by using the matrix inversion lemma, the R.H.S of the above inequality is $A_f (\epsilon I - N_{1f} P_f N_{1f}^T)^{-1} A_f^T + \epsilon M_{1f} M_{1f}^T$. This completes the proof of the lemma. \square

Lemma 2. *Let λ denote a positive scalar and $N_{2f} W_f N_{2f}^T < \lambda I$, it then follows that*

$$\begin{aligned}
(B_f + \Delta B_f(k)) W_f (B_f + \Delta B_f(k))^T &\leq B_f (W_f^{-1} - \lambda^{-1} N_{2f}^T N_{2f})^{-1} B_f^T + \lambda M_{2f} M_{2f}^T. \tag{4.18}
\end{aligned}$$

Proof: Let us define

$$Z(k) = B_f W_f N_{2f}^T (\lambda I - N_{2f} W_f N_{2f}^T)^{-1/2} - M_{2f} F(k) (\lambda I - N_{2f} W_f N_{2f}^T)^{1/2}. \quad (4.19)$$

The result follows along the same lines as those used for the proof of the Lemma 1 above, and therefore the details are not included. This completes the proof of the lemma. \square

We now state the main result of this section.

Theorem 1. *Suppose the uncertain system (4.3) satisfies the Definition 1. Let us select $\beta_1 > 0$ and $\beta_2 > 0$ as sufficiently small constants and let $U_o \in \mathbb{R}^{q \times q}$ denote an arbitrary orthogonal matrix. Provided that the parameters $\epsilon > 0$ and $\lambda > 0$ and a matrix $H \in \mathbb{R}^{n \times q}$ exist where the following two conditions hold, namely:*

(a) *A positive definite matrix $P_1 > 0$ exists as the solution to the algebraic Riccati equation (ARE1):*

$$\begin{aligned} AP_1 A^T - P_1 + AP_1 N_1^T (\epsilon I - N_1 P_1 N_1^T)^{-1} N_1 P_1 A^T + (\epsilon + \lambda) M_1 M_1^T \\ + B(W^{-1} - \lambda^{-1} N_2^T N_2)^{-1} B^T + \beta_1 I = 0. \end{aligned} \quad (4.20)$$

(b) *There exists a positive definite solution $P_2 > 0$ for the algebraic Riccati equation (ARE2):*

$$\begin{aligned} \bar{A} P_2 \bar{A}^T - P_2 - \theta R^{-1} \theta^T + \left((\epsilon + \lambda) M_1 M_1^T + B(W^{-1} - \lambda^{-1} N_2^T N_2)^{-1} B^T \right) \Gamma \\ \left((\epsilon + \lambda) M_1 M_1^T + B(W^{-1} - \lambda^{-1} N_2^T N_2)^{-1} B^T \right)^T + H H^T \\ + (\epsilon + \lambda) M_1 M_1^T + B(W^{-1} - \lambda^{-1} N_2^T N_2)^{-1} B^T + \beta_2 I = 0, \end{aligned} \quad (4.21)$$

where

$$\begin{aligned} \phi &= (P_1^{-1} - \epsilon^{-1} N_1^T N_1)^{-1} A^T, \\ \Gamma &= \phi^{-1} (P_1^{-1} - \epsilon^{-1} N_1^T N_1)^{-1} (\phi^{-1})^T, \\ \bar{A} &= A + \left((\epsilon + \lambda) M_1 M_1^T + B(W^{-1} - \lambda^{-1} N_2^T N_2)^{-1} B^T \right) \phi^{-1}, \\ \bar{C} &= C + \epsilon M_2 M_1^T \phi^{-1}, \end{aligned}$$

$$\begin{aligned}
\theta &= \bar{A}P_2\bar{C}^T + \left((\epsilon + \lambda)M_1M_1^T + B(W^{-1} - \lambda^{-1}N_2^TN_2)^{-1}B^T \right) \Gamma(\epsilon M_1M_2^T) \\
&\quad + (\epsilon M_1M_2^T) \\
R &= \bar{C}P_2\bar{C}^T + (\epsilon M_2M_1^T)\Gamma(\epsilon M_1M_2^T) + (\epsilon + \lambda)M_2M_2^T \\
&\quad + D(V^{-1} - \lambda^{-1}N_2^TN_2)^{-1}D^T, \tag{4.22}
\end{aligned}$$

and with the inequality constraints that are given by

$$N_1P_1N_1 < \epsilon I, \quad N_{2f}W_fN_{2f}^T < \lambda I, \tag{4.23}$$

then the detection filter with the gains selected according to

$$K = \theta R^{-1} + HU_oR^{-\frac{1}{2}}, \tag{4.24}$$

$$G = \bar{A} - K\bar{C}, \tag{4.25}$$

can be designed such that the augmented system (4.9) is quadratically stable for all the admissible parameter uncertainties. Moreover, if there exists a positive definite solution $P_2 > 0$ for (4.21) which satisfies the condition $[P_2]_l \leq \sigma_l^2$ ($l = 1, 2, \dots, n$), then the filter with the gains designed according to (4.24) and (4.25) satisfies $\text{Var}[e_l(k)] = [P]_l \leq [P_2]_l \leq \sigma_l^2$ (where $[.]_l$ denotes the l^{th} diagonal element of a square matrix). This implies that the designed robust filter is a priori variance constrained.

Proof: First, it is shown that the augmented system (4.9) is quadratically stable. Define $P_f = \text{diag}(P_1, P_2)$, it then follows from (4.11) and (4.18) that

$$\begin{aligned}
&(A_f + \Delta A_f(k))P_f(A_f + \Delta A_f(k))^T - P_f \\
&\quad + (B_f + \Delta B_f(k))W_f(B_f + \Delta B_f(k))^T \leq \Psi \tag{4.26}
\end{aligned}$$

where $\Psi = A_f(P_f^{-1} - \epsilon^{-1}N_{1f}^TN_{1f})^{-1}A_f^T + \epsilon M_{1f}M_{1f}^T - P_f + B_f(W_f^{-1} - \lambda^{-1}N_{2f}^TN_{2f})^{-1}B_f^T +$

$\lambda M_{2f} M_{2f}^T$, and

$$\begin{aligned}
\Psi_{11} &= A(P_1^{-1} - \epsilon^{-1} N_1^T N_1)^{-1} A^T + \epsilon M_1 M_1^T - P_1 + B(W^{-1} - \lambda^{-1} N_2^T N_2)^{-1} B^T \\
&\quad + \lambda M_1 M_1^T \\
&= A(P_1 + P_1 N_1^T (\epsilon I - N_1 P_1 N_1^T)^{-1} N_1 P_1) A^T + (\epsilon + \lambda) M_1 M_1^T - P_1 \\
&\quad + B(W^{-1} - \lambda^{-1} N_2^T N_2)^{-1} B^T, \tag{4.27}
\end{aligned}$$

$$\begin{aligned}
\Psi_{12} &= A(P_1^{-1} - \epsilon^{-1} N_1^T N_1)^{-1} (A - G - KC)^T + (\epsilon + \lambda) M_1 M_1^T - \epsilon M_1 M_2^T K^T \\
&\quad + B(W^{-1} - \lambda^{-1} N_2^T N_2)^{-1} B^T, \tag{4.28}
\end{aligned}$$

$$\begin{aligned}
\Psi_{22} &= (A - G - KC)(P_1^{-1} - \epsilon^{-1} N_1^T N_1)^{-1} (A - G - KC)^T + G P_2 G^T \\
&\quad + \epsilon (M_1 - K M_2)(M_1 - K M_2)^T - P_2 + B(W^{-1} - \lambda^{-1} N_2^T N_2)^{-1} B^T \\
&\quad + K D (V^{-1} - \lambda^{-1} N_2^T N_2)^{-1} D^T K^T + \lambda M_1 M_1^T + \lambda K M_2 M_2^T K^T \\
&= \bar{A} P_2 \bar{A}^T - P_2 + \left((\epsilon + \lambda) M_1 M_1^T + B(W^{-1} - \lambda^{-1} N_2^T N_2)^{-1} B^T \right) \Gamma \\
&\quad \left((\epsilon + \lambda) M_1 M_1^T + B(W^{-1} - \lambda^{-1} N_2^T N_2)^{-1} B^T \right)^T + (\epsilon + \lambda) M_1 M_1^T \\
&\quad + B(W^{-1} - \lambda^{-1} N_2^T N_2)^{-1} B^T - \theta R^{-1} \theta^T \\
&\quad + (K R^{\frac{1}{2}} - \theta R^{-\frac{1}{2}})(K R^{\frac{1}{2}} - \theta R^{-\frac{1}{2}})^T. \tag{4.29}
\end{aligned}$$

It follows from (4.27) and the ARE1 that $\Psi_{11} = -\beta_1 I$. Also, $\Psi_{21} = \Psi_{12}^T$, which becomes zero by substituting (4.25) into (4.28). Furthermore, the ARE2 and (4.25) result in $\Psi_{22} = -\beta_2 I$, given that $U_o U_o^T = I$. Consequently, $\Psi < 0$, and from the Lyapunov stability theory it can be concluded that the augmented system is quadratically stable.

Finally, to show $\text{Var}[e_l(k)] = [P]u \leq [P_2]u \leq \sigma_l^2$, let us define Ω by invoking (4.26) as follows:

$$\begin{aligned}
\Omega &= \Psi - \left((A_f + \Delta A_f(k)) P_f (A_f + \Delta A_f(k))^T - P_f \right. \\
&\quad \left. + (B_f + \Delta B_f(k)) W_f (B_f + \Delta B_f(k))^T \right), \tag{4.30}
\end{aligned}$$

which is a positive definite matrix. Then, from (4.10) and (4.30), it follows that

$$(A_f + \Delta A_f(k))(P_f - X)(A_f + \Delta A_f(k))^T - (P_f - X) + \Omega - \Psi = 0, \quad (4.31)$$

where P_f and \mathcal{X} denote steady-state matrices that result in $(A_f + \Delta A_f(k))(P_f - \mathcal{X})(A_f + \Delta A_f(k))^T - (P_f - \mathcal{X}) \leq 0$. Given the quadratically stable augmented process, then $P_f - \mathcal{X} \geq 0$ and $[\mathcal{X}]_{22} \leq [P_f]_{22}$, which imply that $P \leq P_2$. Therefore, it can easily be shown that if $[P_2]_u \leq \sigma_l^2$ ($l = 1, 2, \dots, n$), where σ_l^2 s denote the predefined *a priori* upper bounds on the estimation error variances, then the designed filter satisfies $\text{Var}[e_l(k)] = [P]_u \leq [P_2]_u \leq \sigma_l^2$. This now completes the proof of the theorem. \square

In order to represent the *a priori* individually predefined state estimation error variances conditions as stated in Theorem 1 into the solution process for the AREs, equations (4.20) and (4.21) are expanded into two quadratic matrix inequalities (QMI) as follows:

$$\begin{aligned} AP_1A^T - P_1 + AP_1N_1^T(\epsilon I - N_1P_1N_1^T)^{-1}N_1P_1A^T + (\epsilon + \lambda)M_1M_1^T \\ + B(W^{-1} - \lambda^{-1}N_2^TN_2)^{-1}B^T < 0, \end{aligned} \quad (4.32)$$

$$\begin{aligned} \bar{A}P_2\bar{A}^T - P_2 - \theta R^{-1}\theta^T + \left((\epsilon + \lambda)M_1M_1^T + B(W^{-1} - \lambda^{-1}N_2^TN_2)^{-1}B^T \right) \Gamma \\ \left((\epsilon + \lambda)M_1M_1^T + B(W^{-1} - \lambda^{-1}N_2^TN_2)^{-1}B^T \right)^T + HH^T \\ + (\epsilon + \lambda)M_1M_1^T + B(W^{-1} - \lambda^{-1}N_2^TN_2)^{-1}B^T < 0. \end{aligned} \quad (4.33)$$

In order to simplify the process of solving the QMIs, they are converted into two feasibility linear matrix inequality (LMI) conditions. The first QMI can be re-arranged into $\bar{M} + \bar{L}^T\bar{Q}\bar{L} < 0$, where

$$\begin{aligned} \bar{M} &= AP_1A^T - P_1 + B(W^{-1} - \lambda^{-1}N_2^TN_2)^{-1}B^T + (\epsilon + \lambda)M_1M_1^T, \\ \bar{L} &= N_1P_1A^T, \quad \bar{Q} = (\epsilon I - N_1P_1N_1^T)^{-1}. \end{aligned} \quad (4.34)$$

According to the constraint $N_1 P_1 N_1^T < \epsilon I$, the matrix \bar{Q} is positive definite. The matrices \bar{M} and \bar{Q} are also symmetric. By using the Schur complement lemma, $\bar{M} + \bar{L}^T \bar{Q} \bar{L} < 0$ is satisfied if and only if the following LMI is feasible

$$\begin{bmatrix} \bar{M} & \bar{L}^T \\ \bar{L} & -\bar{Q}^{-1} \end{bmatrix} < 0. \quad (4.35)$$

Following along the same lines, the second QMI can be re-arranged into $\tilde{M} - \tilde{L}^T \tilde{Q} \tilde{L} < 0$, where

$$\begin{aligned} \tilde{M} &= \bar{A} P_2 \bar{A}^T - P_2 + \left((\epsilon + \lambda) M_1 M_1^T + B(W^{-1} - \lambda^{-1} N_2^T N_2)^{-1} B^T \right) \Gamma \\ &\quad \left((\epsilon + \lambda) M_1 M_1^T + B(W^{-1} - \lambda^{-1} N_2^T N_2)^{-1} B^T \right)^T + H H^T \\ &\quad + (\epsilon + \lambda) M_1 M_1^T + B(W^{-1} - \lambda^{-1} N_2^T N_2)^{-1} B^T, \\ \tilde{L} &= \theta^T, \quad \tilde{Q} = R^{-1}, \end{aligned} \quad (4.36)$$

and θ and R are defined in (4.22). The matrices \tilde{M} and \tilde{Q} represent symmetric matrices and \tilde{Q} is a positive definite matrix. Using the Schur complement lemma, $\tilde{M} - \tilde{L}^T \tilde{Q} \tilde{L} < 0$ is satisfied if and only if the following LMI is feasible

$$\begin{bmatrix} \tilde{M} & \tilde{L}^T \\ \tilde{L} & \tilde{Q}^{-1} \end{bmatrix} < 0. \quad (4.37)$$

To solve for $P_1 > 0$ and $P_2 > 0$, the predefined *a priori* upper bound conditions on the state estimation error variances ($[P_2]_{ll} \leq \sigma_l^2$ $l = 1, \dots, n$), should also be added to the above LMI feasibility conditions. To summarize, at each operating point the positive definite matrices P_1 and P_2 are obtained such that the LMI conditions in (4.35) and (4.37) are feasible, while ensuring that the conditions $[P_2]_{ll} \leq \sigma_l^2$ are also satisfied. These results are then used to determine the RKF gain matrices by using (4.24) and (4.25).

For each uncertain PWL model given by (4.3), the filter parameters are obtained off-line by satisfying the LMI feasibility conditions as well as the constraints

associated with the estimation error variances. Consequently, multiple RKF's corresponding to L PWL models are designed as follows:

$$\begin{aligned}\Delta\hat{x}^i(k) &= G^i\Delta\hat{x}^i(k) + K^i\Delta y(k), \\ \Delta\hat{y}^i(k) &= \bar{C}^i\Delta\hat{x}^i(k), \quad i = 1, \dots, L,\end{aligned}\tag{4.38}$$

that cover the entire operating region of the nonlinear system with healthy sensors. For developing our proposed multiple RKF-based scheme for accomplishing our proposed FDI strategy, multiple PWL models corresponding to various operating points are generated for each sensor fault hypothesis. Moreover, the PWL models need to be integrated together in order to cover the entire operating region of the nonlinear system in (4.1). The detailed description and development of this process is provided in the next section.

4.3 Piecewise Linear Models Integration Methodology

Similar to Chapter 3, the system operating region is partitioned into multiple subregions where each region is associated with a certain operating point for which a PWL model is derived. To construct a general model with varying parameters, the PWL models are then integrated. The PWL models normalized weights are calculated by utilizing an on-line Bayesian technique.

The PWL models that are previously constructed corresponding to multiple operating points in (4.3) are now used to obtain the RKF gains K^i and G^i for various sensor modes of equation (4.1). Therefore, multiple RKF's are designed for various sensor modes and multiple operating points. Associated with the j^{th} sensor mode

and corresponding to the i^{th} operating point the RKF is designed according to:

$$\begin{aligned}\Delta\hat{X}^{(i,j)}(k+1) &= G^i\Delta\hat{X}^{(i,j)}(k) + K^i\Delta Y^i(k), \\ \Delta\hat{Y}^{(i,j)}(k) &= \bar{C}^i\Delta\hat{X}^{(i,j)}(k) + b_{dj}a_j\delta_j(k),\end{aligned}\tag{4.39}$$

with $i = 1, \dots, L$, $j = 1, \dots, (q+1)$, b_{dj} is the pre-determined sensor bias fault that can be possibly nonidentical to the actual sensor fault b_s (injected and applied to the equation (4.1)), a_j denotes a q -dimensional vector and represents one of the $q+1$ modes of a representing the fault. For the healthy mode $j = 1$, the fault parameter a is assigned to $a_1 = 0$, which leads to a bank of filters that are denoted by (4.38). On the other hand for $j = 2, \dots, q+1$, a_j has a value of one for the $(j-1)^{th}$ element with the rest assigned to zero.

Therefore, a total of $L \times (q+1)$ RKF's are designed that cover and handle all the operating regions of the nonlinear system associated with the various sensor modes. It should be pointed out that the system matrices that depend on only the operating points will be identical corresponding to all the sensor fault modes associated with a particular operating point.

The normalized weights that are associated with the PWL models are determined by using the Bayes formula in (4.41). Specifically, the likelihood function $f^{(i,j)}(\gamma^{(i,j)}(k))$ for the j^{th} sensor mode corresponding to the i^{th} operating region is computed by using the residuals $\gamma^{(i,j)}(k)$ and covariance matrices $S^{(i,j)}(k)$ which are determined by using multiple RKF's as follows, respectively:

$$\begin{aligned}\gamma^{(i,j)}(k) &= \Delta Y^i(k) - \Delta\hat{Y}^{(i,j)}(k), \\ S^{(i,j)}(k) &= \text{cov}(\gamma^{(i,j)}(k)), \\ f^{(i,j)}(\gamma^{(i,j)}(k)) &= \frac{1}{(2\pi)^{q/2}\sqrt{|S^{(i,j)}(k)|}} \times \exp\left(\frac{-1}{2}(\gamma^{(i,j)}(k))^T(S^{(i,j)}(k))^{(-1)}(\gamma^{(i,j)}(k))\right),\end{aligned}\tag{4.40}$$

In the above expression the residual vector $\gamma^{(i,j)}(k)$ is assumed to be a Gaussian white noise process having a mean of zero and a covariance matrix $S^{(i,j)}(k)$. The

j^{th} sensor mode normalized weights are adjusted iteratively by utilizing the Bayes formula according to:

$$\mu^{(i,j)}(k) = \frac{f^{(i,j)}(\gamma^{(i,j)}(k))\mu^{(i,j)}(k-1)}{\sum_{i=1}^L f^{(i,j)}(\gamma^{(i,j)}(k))\mu^{(i,j)}(k-1)}. \quad (4.41)$$

To avoid the weights from becoming too close to zero we assume that they remain outside a narrow band according to:

$$\begin{aligned} \text{if } \mu^{(i,j)}(k) > \rho \text{ then } \mu^{(i,j)}(k) &= \mu^{(i,j)}(k), \\ \text{if } \mu^{(i,j)}(k) \leq \rho \text{ then } \mu^{(i,j)}(k) &= \rho, \end{aligned} \quad (4.42)$$

where ρ is a design parameter as defined in Chapter 3.

Once the normalized weights, multiple time-varying models corresponding to various sensor modes are constructed, the entire operating region of the nonlinear system is fully covered. Corresponding to each sensor mode, the original PWL model system matrices and their corresponding normalized weights are utilized so that the respective time-varying model matrices as well as the weighted residual vectors and the covariance matrices are computed as follows:

$$\begin{aligned} A_c^j(k) &= \sum_{i=1}^L \mu^{(i,j)}(k)A^i, & C_c^j(k) &= \sum_{i=1}^L \mu^{(i,j)}(k)C^i, \\ B_c^j(k) &= \sum_{i=1}^L \mu^{(i,j)}(k)B^i, & D_c^j(k) &= \sum_{i=1}^L \mu^{(i,j)}(k)D^i, \\ \gamma_c^j(k) &= \sum_{i=1}^L \mu^{(i,j)}(k)\gamma^{(i,j)}(k), & S_c^j(k) &= \sum_{i=1}^L (\mu^{(i,j)}(k))^2 S^{(i,j)}(k), \end{aligned} \quad (4.43)$$

where $A_c^j(k)$, $C_c^j(k)$, $B_c^j(k)$ and $D_c^j(k)$ represent the weighted linear time-varying system matrices associated with the sensor j^{th} mode. Furthermore, $\gamma_c^j(k)$ and $S_c^j(k)$ represent the weighted residuals and covariance matrix of the sensor j^{th} mode, respectively. The methodology that is outlined above will now be referred to as the *PWL models integration*. Therefore, a total of $(q + 1)$ weighted residuals and covariance matrices are monitored corresponding to all the operational region of the

system that will be utilized in the following section for developing our proposed *robust MM-based FDI scheme*.

4.4 Robust Sensor FDI by Using a Multiple Model-Based Strategy

In the preceding sections, multiple robust Kalman filters (MRKF) are designed to operate during the entire operating region of a nonlinear system in presence of time-varying parameter uncertainties. This was accomplished by means of solving two feasibility LMI conditions that are associated with each operating point for computing the filter gains independent of the uncertainty levels. The designed multiple RKF are now utilized in the MM-based structure to detect and isolate various sensor faults.

Similar to Chapter 3, it is assumed that the fault parameters can take on only one of $(q + 1)$ sensor modes that is denoted by a_j . In other words, corresponding to each operating point there will be $(q + 1)$ PWL models; one model associated with the healthy sensors case as well as q models associated with various faulty sensors cases in order to construct the multiple RKF-based scheme as represented in (4.39). Moreover, the residuals and covariance matrices as generated by the MRKFs will be fused as governed by (4.43). In other words, there will be $(q + 1)$ fused residuals and covariance matrices to be utilized in the MM-based FDI scheme. These quantities will operate under various healthy and faulty sensor cases corresponding to the full operating region of the nonlinear system.

In the multiple model scheme we define the hypothesis conditional probability $P_j(k)$ as the probability where a fault parameter a takes on the value a_j (for $j = 1, \dots, q + 1$) conditioned on the observed measurements up to the k^{th} sample time. In other words, $P_j(k) = \Pr[a = a_j | \mathcal{Y}(k) = \mathcal{Y}_k]$, where $\mathcal{Y}(k)$ denotes the random

measurement history with $Y(1), Y(2), \dots, Y(k)$ partitions displaying the available measurements up to the k^{th} sample time. Moreover, \mathcal{Y}_k represents the measurement history realization with the partitions Y_1, Y_2, \dots, Y_k . The conditional probability can therefore be computed iteratively according to:

$$P_j(k) = \frac{f_{Y(k)|a, \mathcal{Y}(k-1)}(Y_j|a_j, \mathcal{Y}_{k-1})P_j(k-1)}{\sum_{h=1}^{q+1} f_{Y(k)|a, \mathcal{Y}(k-1)}(Y_h|a_h, \mathcal{Y}_{k-1})P_h(k-1)}, \quad (4.44)$$

where $f_{Y(k)|a, \mathcal{Y}(k-1)}(Y_j|a_j, \mathcal{Y}_{k-1})$ represents the Gaussian density function for the current measurement that is given by

$$f_{Y(k)|a, \mathcal{Y}(k-1)}(Y_j|a_j, \mathcal{Y}_{k-1}) = \frac{1}{(2\pi)^{q/2} \sqrt{|S_c^j(k)|}} \times \exp\left(\frac{-1}{2}(\gamma_c^j(k))^T (S_j(k))^{(-1)} (\gamma_c^j(k))\right), \quad (4.45)$$

where $\gamma_c^j(k)$ and $S_c^j(k)$ are given by (4.43).

For a given fault parameter having the value a_j , the j^{th} model probability will have a larger value than all the others that are mismatched with the considered fault scenario. Consequently, the system condition and location of a faulty sensor can be detected and isolated by evaluating $P_j(k)$ and determining its maximum value.

Hence, our proposed MM-based scheme is capable of detecting and isolating different sensor faults. Figure 4.1 depicts the structure of the MM-based FDI scheme where the MRKFs corresponding to the entire operating range of an uncertain nonlinear system are utilized. It should be emphasized that the contribution that we have made above is related to the modification and extension of our previously developed standard MM-based structures in [28] and [27], where we have only utilized multiple standard linear Kalman filters that were designed for a single operating point now into a robust scheme that utilizes multiple robust Kalman filters for the entire operational region of a nonlinear system by means of their corresponding integrated residual vectors and covariance matrices as specified in (4.43) and (4.45). Moreover, a novel robust MM-based FDI structure is introduced in this chapter

that utilizes our proposed robust detection filters rather than standard filters that generally are not formally designed to be robust with respect to parameter uncertainties. The robustness and estimation accuracy of our proposed robust MM-based FDI method is subsequently compared with other standard available methods in the literature in Section 4.5.

Remark 4.1 The above MM structure can also be extended to detect and isolate multiple concurrent sensor faults by the use of a hierarchical MM-based structure as developed in Chapter 3. In the hierarchical structure, the original nonlinear system is assumed to start operating with healthy sensors so that the first level of filters are active and our proposed FDI scheme observes the sensor conditions for the first occurrence of only a faulty mode. Once the first fault is detected and isolated, by invoking the maximum probability criteria, the second level of RKF filters will be activated by the FDI scheme for detection and isolation of the second concurrent faults. Moreover, for avoiding any unnecessary computational burden, the first bank of filters will be disabled when the second bank of filters are activated in the second level. Therefore, at any given time only $(q + 1)$ filters are operating on-line. These details are rather straightforward to develop and therefore are not included here due to space limitations.

4.5 Simulation Studies

Below we provide simulation results corresponding to a nonlinear model of a single spool jet engine. Moreover, performance evaluations of our developed robust sensor FDI scheme when applied to various fault scenarios are also presented to demonstrate the capabilities and effectiveness of our proposed scheme. It should be noted that the gas turbine engine was previously introduced in Chapter 2.

For our study, the actual engine is simulated and developed in SIMULINK

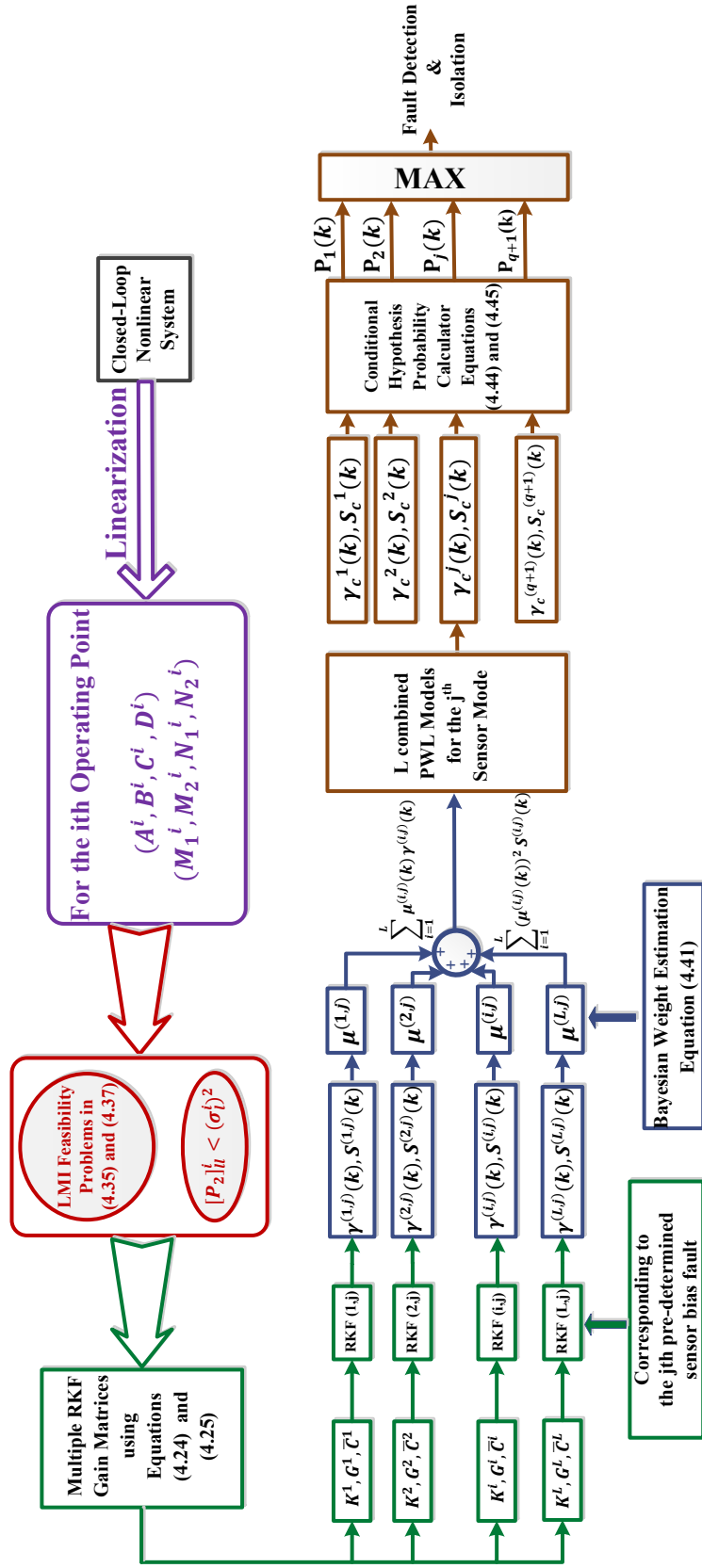


Figure 4.1: The proposed MM-based FDI strategy that is based on the RKF corresponding to the entire operating region.

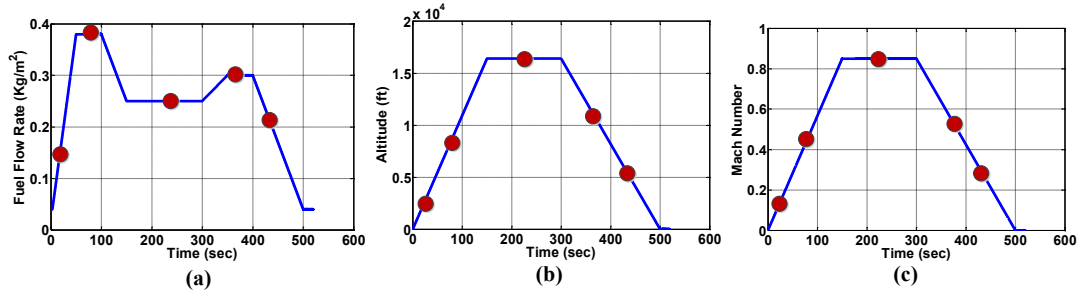


Figure 4.2: The profiles of (a) the fuel flow rate (\dot{m}_f), (b) altitude, and (c) the Mach number during a flight mission.

and the PWL models are obtained by linearizing the nonlinear model at multiple operating points during the entire engine flight profile. The residual vectors and covariance matrices are integrated by using the algorithm that is introduced in Section 4.3. These are then utilized in the robust MM-based structure to detect and isolate various sensor faults. Also, the RKF gain matrices are obtained individually for each operating point. Various uncertainty sources including the engine health parameters degradations due to normal aging process as well as process and measurement noise that influence the system operation are considered in this chapter. It should be pointed out that in this section no predefined upper bounds are considered for the state estimation error variances since these are more essential for tracking and fault tolerant control systems rather than fault detection and isolation problems.

The sensors are affected by measurement noise with the standard deviations of $SD_v = [0.23, 0.164, 0.051, 0.097, 0.164]$ that is associated with the output vector. The process noise has the standard deviations of $SD_w = [0.1, 0.1, 0.001]$, which is also applied to the ambient temperature and pressure as well as the Mach number, respectively.

The system is simulated for 520 sec and the profiles of the altitude, Mach number and the fuel flow rate during a designed flight mission are shown in Figure 4.2.

For simulations, it is assumed that there are five operating points to fully

Table 4.1: The operating point specifications corresponding to multiple PWL models.

Operating Points Corresponding to Flight Conditions	\dot{m}_f Kg/m ²	Mn	Alt ft
Operating Point 1 (Climbing)	0.1557	0.1077	2077.9
Operating Point 2 (Climbing)	0.38	0.4255	8211.9
Operating Point 3 (Cruise)	0.25	0.85	16404.2
Operating Point 4 (Landing)	0.3	0.5313	10253
Operating Point 5 (Landing)	0.2142	0.2847	5495.4

handle the entire flight profile ($L = 5$). It should be pointed out that five is the minimum number of operating points that can be obtained for each faulty mode to prevent occurrence of a false alarm corresponding to the selected compressor health parameters degradations. Generally speaking, the number of operating points depends on the engine dynamics as well as the range of the applied fuel flow rate and the environmental parameters. Table 4.1 shows the corresponding fuel flow rates as well as the flight conditions for which the PWL models associated to each sensor mode are designed. The selected operating points are also displayed in Figure 4.2 using the red solid circles. In order to efficiently follow system input variations corresponding to the climbing and landing situations, two operating points are designated corresponding to each mode; whereas only one operating point is designated corresponding to the cruise condition given that in this situation the input is taken as constant for the duration of the flight.

Moreover, it is assumed that the engine parameter uncertainties due to health parameters degradations satisfy the condition of equation (4.4) in which M_1 , M_2 , N_1 and N_2 are obtained by the use of a singular value decomposition method that is applied to the matrices ΔA , ΔB , ΔC and ΔD . For simulation studies, these matrices are determined at each operating point corresponding to degradations of 5% and 2.5% that are applied to the compressor mass flow rate and efficiency, respectively, due to the fouling effects that represent as the major compressor degradation factor

caused by adherence of particles to the compressor surfaces. Unlike other types of compressor degradation factors such as corrosion and erosion, fouling is recoverable through periodic online and/or offline compressor washing. The washing mechanism is capable of recovering the compressor to reach its maximum power and to maintain the gas turbine operating as new. According to [150], after almost 3000 hours of operation 7% degradation would occur in the compressor assuming no degraded parts are replaced and no washing process is applied. However, the washing process is normally performed sooner to reduce the cost of fuel or electricity demand driving the compressor. Also, a reliable FDI scheme needs to be robust with respect to the engine health degradation before performing any maintenance or washing process. It must also be noted that in this chapter only the compressor health parameters degradations are considered, however the same design procedure and case studies can be applied to the turbine health parameters degradation.

The filter gain matrices are obtained by solving two LMI feasibility conditions with the use of the YALMIP toolbox [170]. The effectiveness of our proposed robust MM-based FDI scheme is evaluated for various percentages of the compressor health parameters degradation. The arbitrary matrix H in the Theorem 1 is set to a zero matrix. The filter gain matrices associated with a certain operating point are fixed for all the sensor modes that are included in the MM-based scheme, however the residuals, covariance matrices and the associated pre-determined bias faults are different.

For simulations, different layers of multiple models associated with different ranges of the sensor bias faults are constructed, whereas each has the overall structure that is shown in Figure 4.1. The first layer of robust multiple models is composed of six linear models ($q = 5$). These modes correspond to the operating point that is constructed for one healthy and including five faulty sensor modes. They are specified based on the pre-determined sensor bias fault set to 3% of the engine

steady-state outputs.

In the first layer, mode #1 ($P_1(k)$) corresponds to the healthy engine sensors, modes #2 to #6 ($P_2(k)$ to $P_6(k)$) correspond to the sensor bias faults that are respectively applied to sensors measuring the compressor exit temperature and pressure, shaft rotational speed, and the turbine exit temperature and pressure. During the fault detection and isolation process, a mode probability $P_j(k)$ is generated for each linearized model by using the equation (4.44) as well as by determining the maximum of the $P_j(k)$, $j = 1, \dots, q + 1$, so that the sensor fault can be detected and isolated. In general, when the sensors are healthy, the first mode probability that is associated with the mode that is healthy reaches its maximum value. Upon the occurrence of a fault, the probability of the healthy mode is reduced and the probability mode corresponding to the occurred fault is increased to the point where it reaches the maximum among all the other mode probabilities.

However, a single layer of multiple models is only capable of detecting and isolating a sensor fault within a certain fault severity range; therefore, multiple layers corresponding to multiple models that all operate simultaneously will clearly enhance the range of the detectable sensor faults. The number of layers depends on the desired and acceptable fault detection delay time corresponding to various faulty modes as well as the range of applied sensor faults. In this chapter, two layers of multiple models are constructed to detect and isolate sensor faults within less than 10 seconds after the fault injection. The maximum detectable sensor bias fault is obtained individually for each sensor. It is obvious that one may need more number of layers to achieve either higher sensor bias faults or to obtain smaller acceptable fault detection delay times.

In the following subsections, various case studies are simulated to investigate and demonstrate the advantage of our proposed robust FDI scheme performance as compared to the standard MM-based FDI structure that uses linear Kalman filters

(LKF) as well as the robust MM-based FDI structure that uses the RKF designed in [4] in terms of fault promptness detection, fault estimation accuracy, false alarms and incorrect fault detection rates. In [4], the RKF is designed for time varying parameter uncertainties that only affect the state and measurement matrices but not the process and measurement noise distribution matrices.

Three simulation case studies are conducted in this chapter as summarized below:

- **Case 1:** To evaluate the robustness of our proposed robust MM-based FDI method, the engine model in (2.3) is simulated without a sensor fault but with various compressor health degradations during the entire flight profile. Our objective is to compare the false alarm rates and estimation accuracy between our proposed robust MM-based method and the MM-based structures that utilize the LKF and the RKF as designed in [4].
- **Case 2:** To evaluate the effectiveness of our proposed robust MM-based FDI method, the engine model in (2.3) is simulated with a single sensor bias fault that occurs during the flight cruise condition by using a *single layer of multiple models* that is developed for a pre-determined 3% sensor bias fault. Moreover, the compressor health parameters degradation is set to $\alpha_{m_C} = 0.95$ (5% degradation) and $\alpha_{\eta_C} = 0.975$ (2.5% degradation). Our objective is to compare the fault detection delay time, the FDI accuracy and the incorrect fault detection rates corresponding to our proposed robust MM-based method with the MM-based structure that utilizes the RKF as designed in [4]. Moreover, detection ranges corresponding to our single layer multiple models for various sensor faults are obtained given that the fault detection time delay should be less than 10 seconds.
- **Case 3:** To improve the performance of our proposed robust MM-based FDI

method, the engine model in (2.3) is simulated with a single sensor bias fault that occurs during the flight cruise condition by using two layers of the multiple models. These models are developed for various pre-determined sensor bias faults. Our objective is to investigate the fault detection delay times as a function of the sensor fault severities and different levels of the compressor health parameters degradation.

4.5.1 Case 1: False Alarms and Estimation Accuracy Evaluation

In this case study simulation, no fault is applied to the engine sensors. Therefore, the mode probability corresponding to healthy sensor mode should be approximately close to one and other probabilities associated with the faulty sensor modes should be all almost close to zero. In other words, it is required that the FDI system should declare no false alarms despite presence of parameter uncertainties. Figure 4.3 provides a comparison between the mode probabilities for healthy sensors that are generated by our proposed robust FDI method, the standard MM-based FDI scheme (which uses the LKF approach), and the robust MM-based FDI method that utilizes the RKF as designed in [4]. All the above FDI schemes are composed of a single layer of multiple models.

According to Figure 4.3 (c) the standard MM-based FDI method generates many false alarms for the healthy sensors due to the effects of compressor health degradation, however the other two robust MM-based structures do not generate any false alarms. Moreover, Figure 4.4 displays the real and estimated shaft rotational speed for the healthy sensors subjected to degradations of 5% and 2.5% applied to the compressor mass flow rate and efficiency, respectively. The results are displayed for almost 60 seconds of climbing and 100 seconds of landing conditions.

According to Figure 4.4 our proposed RKF yields lower estimation errors than

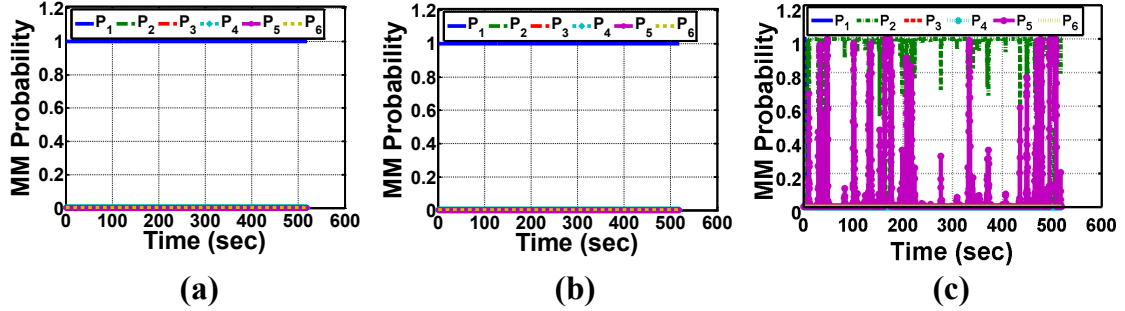


Figure 4.3: Mode probabilities for healthy sensors in presence of degradation of 5% when applied to the compressor mass flow rate and degradation of 2.5% when applied to the compressor efficiency by using (a) our proposed MRKF-based FDI, (b) the MRKF-based FDI according to [4] and (c) the standard MM-based FDI.

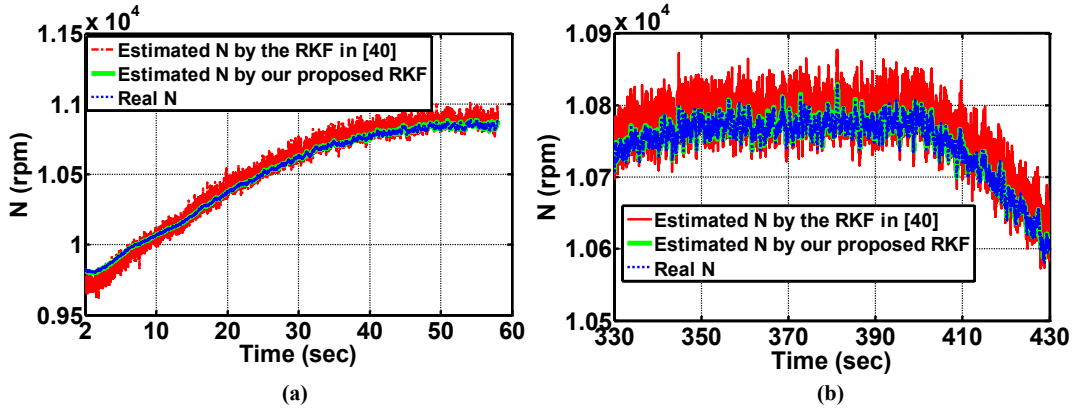


Figure 4.4: Real and estimated shaft rotational speed (N), during the (a) climbing and (b) landing flight conditions. These are generated by the healthy mode in the single-layer MM-based structures that utilize our proposed RKF and the one as proposed in [4] in presence of degradations of 5% and 2.5% applied to the compressor mass flow rate and the efficiency, respectively.

the one designed in [4]. Therefore, although both methods detect no fault in Figure 4.3 (a) and (b), our proposed RKF has less estimation error. In another experiment, the metric known as the weighted mean absolute percentage error (WMAPE) is calculated for all the engine outputs during the flight profile as follows:

$$\text{WMAPE}\% = \frac{1}{L} \sum_{i=1}^L \frac{\sum_{k=1}^{\kappa} \mu^{(i,1)}(k) \left(\left| \frac{\Delta y^i(k) - \Delta \hat{y}^{(i,1)}(k)}{y_{ss_i}} \right| \right)}{\sum_{k=1}^{\kappa} \mu^{(i,1)}(k)} \times 100, \quad (4.46)$$

where κ denotes the total number of simulation samples and $\Delta \hat{y}^{(i,1)}(k)$ denotes the estimated output vectors generated by the RKF's as constructed for the i^{th} operating point and are associated with the healthy mode in the MM-based structure.

To evaluate the estimation accuracy of our proposed robust FDI method, the WMAPE% is calculated for the engine healthy sensor measurements in presence of various percentages of the compressor health parameters degradation during the entire flight profile. The results are provided in Table 4.2. The estimation accuracy of our proposed MRKF-based FDI method is compared with the robust MM structure that utilizes the RKF as proposed in [4], where again all the sensors are healthy. Note that, the estimation accuracies are obtained corresponding to higher compressor health degradations as opposed to the degradation for which the robust filters are designed. The higher levels of degradations occur due to either special environmental conditions or that the compressor washing process was not performed on-time.

According to Table 4.2, for both robust estimation methods, the estimation error does increase by enhancing the health degradation level, however our proposed robust method is still more accurate than the robust filter that is designed in [4]. The higher estimation error may lead to false alarms generation if either the process and measurement noise levels or the health degradation levels is increased.

To investigate the false alarms rates corresponding to both robust methods, confusion matrices are obtained through increasing the level of noise and parameter uncertainty associated with 50 Monte Carlo simulation runs. The results are shown

Table 4.2: Comparison of the WMAPE% by using the MM-based FDI schemes using our proposed RKF (PRKF) and RKF in [4] in presence of different compressor health degradation levels for the engine healthy sensors scenario.

Degradation	Weighted Mean Absolute Percentage Error %											
	P_C					T_T					P_T	
	PRKF	RKF [4]	PRKF	RKF [4]	PRKF	RKF [4]	PRKF	RKF [4]	PRKF	RKF [4]	PRKF	RKF [4]
$\alpha_{\dot{m}_C} = 0.93$	0.2933	1.0252	0.6545	8.0703	0.0512	0.7053	0.2868	10.0313	3.9724	5.3669		
$\alpha_{\dot{m}_C} = 0.95$	0.1033	0.4497	1.4096	5.7001	0.0228	0.6229	0.2023	6.2245	3.2935	4.7835		
$\alpha_{\dot{m}_C} = 0.97$	0.0697	0.1450	0.6545	3.4631	0.0218	0.4538	0.1465	4.2309	1.4499	4.2429		
$\alpha_{\dot{m}_C} = 1$	0.0520	0.1003	0.1214	2.6204	0.0207	0.2126	0.1186	2.5873	0.3002	1.5217		

Table 4.3: True positive (TP), false positive (FP) and false alarm rate (FAR) that are obtained for both robust methods if either the SD_w for the process noise is multiplied by a factor of 5 and degradations of 7% and 3.5% applied to the compressor mass flow rate and the efficiency, respectively.

Scenario	TP		FP		FAR	
	PRKF	RKF [4]	PRKF	RKF [4]	PRKF	RKF [4]
$SD_w \times 5$	48	42	2	8	0.04	0.16
$\alpha_{\dot{m}_C} = 0.93 \quad \alpha_{\eta_C} = 0.965$	48	44	2	6	0.04	0.12

in Table 4.3. It must be noted that true positive (TP) is associated to cases where the healthy sensors are diagnosed healthy and false positive (FP) is associated to healthy cases in which a false alarm is generated due to non-fault related factors. Therefore, false alarm rate (FAR) can be computed according to: $FAR = \frac{FP}{TP+FP}$.

It follows from Table 4.3 that our proposed robust FDI method generates less false alarm rates as compared to the robust method that is developed in [4].

4.5.2 Case 2: Sensor FDI Using Single Layer of Multiple Models

In this case study simulation, only the first layer of multiple models that are designed for a pre-determined 3% sensor bias fault is used to detect and isolate the sensor faults having different severities that are limited within the detection range of the first layer. To compare the effectiveness of our proposed robust MM-based FDI method with the one that uses the RKF as proposed in [4], a single sensor bias fault that is similar to the a priori pre-determined sensor fault for which the multiple models are constructed for is now injected into our engine model. The mode probabilities that are generated by the single-layer MM-based structure using our proposed RKF and the RKF as developed in [4] are depicted in Figures 4.5 to 4.9 corresponding to five faulty sensor scenarios having the severity of 3% during the cruise condition that are applied at $k_{fs} = 250$ sec.

According to Figures 4.5 to 4.9 all sensor faults are accurately detected and

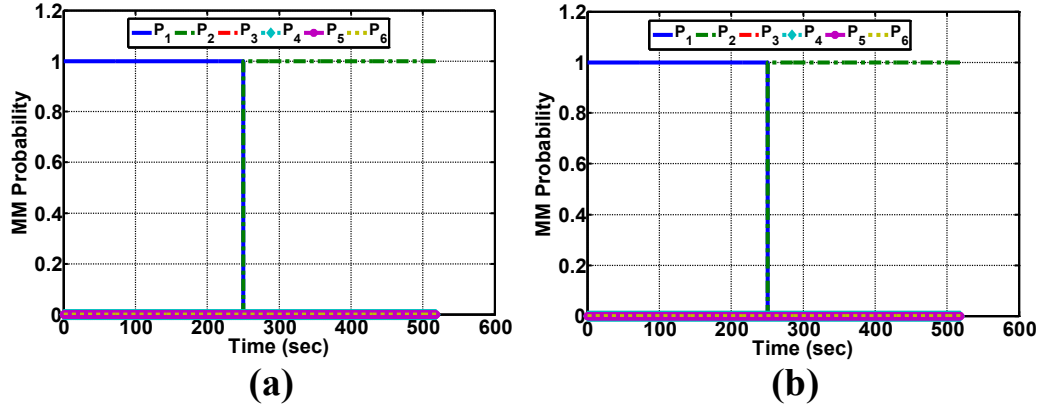


Figure 4.5: Mode probabilities by the first layer of MM-based FDI scheme for a single 3% bias fault when applied to the compressor exit temperature sensor using (a) our proposed RKF and (b) the RKF as proposed in [4] with degradations of 5% and 2.5% applied to the compressor mass flow rate and the efficiency, respectively.

isolated by utilizing our proposed robust method in shorter duration of times as compared to the FDI scheme that utilizes the RKF that is proposed in [4]. Moreover, the method in [4] cannot detect and isolate the fault that is applied to the turbine temperature sensor. Moreover, in all the above simulation studies, the MM-based structure that utilizes the LKF generates numerous false alarms before the occurrence of a fault and also detects an incorrect fault when a sensor is faulty. Therefore, our proposed method is sufficiently robust as far as the engine health parameter degradations are concerned and can correctly and reliably detect and isolate various sensor faults more accurately and promptly than all the other examined methods.

To investigate the robustness of our proposed robust MRKF-based FDI method, two confusion matrices are provided in Tables 4.4 and 4.5. These represent the results of 50 Monte Carlo simulation runs for faulty and healthy scenarios corresponding to performing two experiments, namely: (1) the SD_w is multiplied by a factor of 5 and degradations of 5% and 2.5% applied to the compressor mass flow rate and the efficiency, respectively, and (2) 7% and 3.5% degradations are applied to the

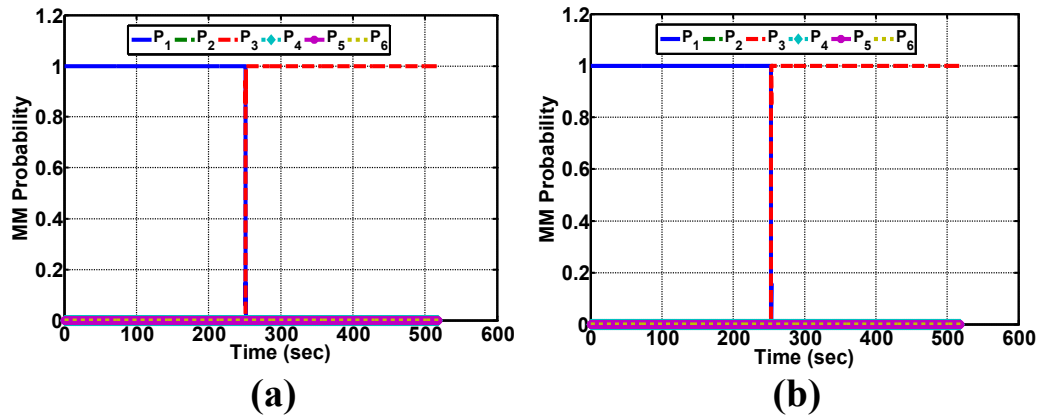


Figure 4.6: Mode probabilities by the first layer of MM-based FDI scheme for a single 3% bias fault when applied to the compressor exit pressure sensor using (a) our proposed RKF and (b) the RKF as proposed in [4] with degradations of 5% and 2.5% applied to the compressor mass flow rate and the efficiency, respectively.

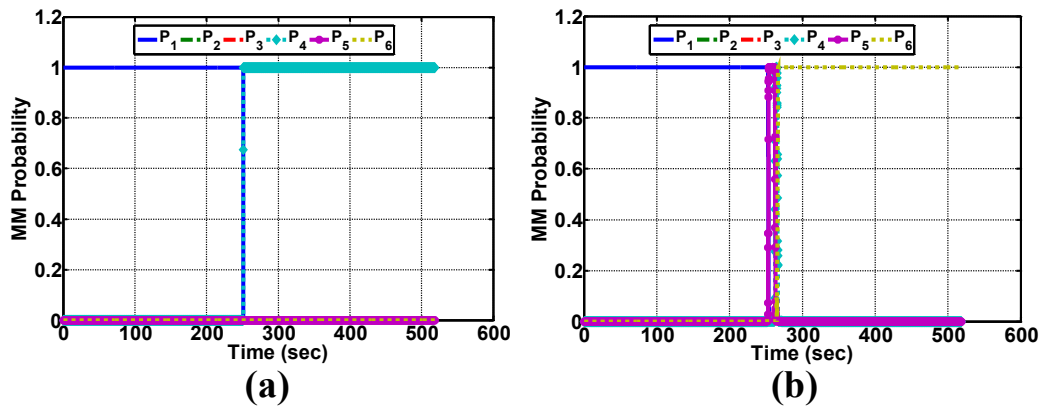


Figure 4.7: Mode probabilities by the first layer of MM-based FDI scheme for a single 3% bias fault when applied to the shaft rotational speed sensor using (a) our proposed RKF and (b) the RKF as proposed in [4] with degradations of 5% and 2.5% applied to the compressor mass flow rate and the efficiency, respectively.

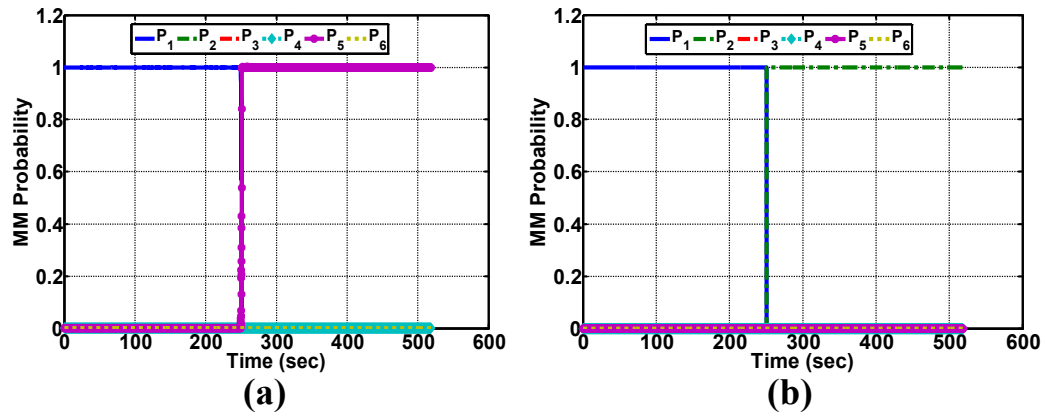


Figure 4.8: Mode probabilities by the first layer of MM-based FDI scheme for a single 3% bias fault when applied to the turbine exit temperature sensor using (a) our proposed RKF and (b) the RKF as proposed in [4] with degradations of 5% and 2.5% applied to the compressor mass flow rate and the efficiency, respectively.

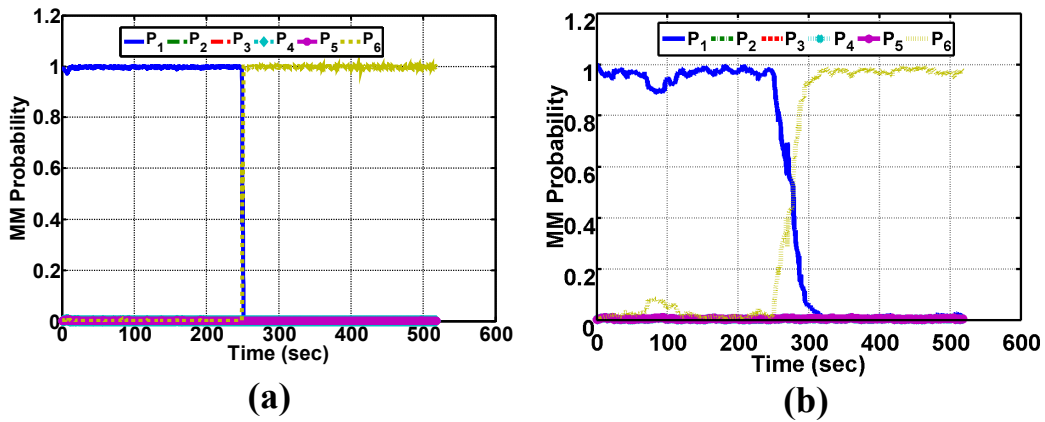


Figure 4.9: Mode probabilities by the first layer of MM-based FDI scheme for a single 3% bias fault when applied to the turbine exit pressure sensor using (a) our proposed RKF and (b) the RKF as proposed in [4] with degradations of 5% and 2.5% applied to the compressor mass flow rate and the efficiency, respectively.

Table 4.4: The confusion matrix when the process noise standard deviations are multiplied by a factor of 5.

	T_C	P_C	N	T_T	P_T	No Fault
T_C	50	0	0	0	0	0
P_C	2	48	0	0	0	0
N	2	0	46	0	0	2
T_T	0	0	0	46	2	1
P_T	0	0	0	0	48	2
No Fault	2	0	0	0	0	48

Table 4.5: The confusion matrix when degradations of 7% and 3.5% are applied to the compressor mass flow rate and the efficiency, respectively.

	T_C	P_C	N	T_T	P_T	No Fault
T_C	50	0	0	0	0	0
P_C	3	46	0	0	0	1
N	2	1	45	0	0	2
T_T	3	0	0	45	2	0
P_T	2	0	0	0	47	1
No Fault	2	0	0	0	0	48

compressor mass flow rate and the efficiency, respectively, but the SD_w is fixed at $[1, 0.1, 0.1]$.

Based on our simulation results, the first consequence of increasing either the standard deviation of the process noise or the compressor health parameters degradation would be to delay the fault detection times. Moreover, false alarms and incorrect fault detections do occur as a consequence of increase in the above uncertainty sources. Various performance metrics and indices have been defined now to formally quantify and measure the robustness of our proposed sensor FDI algorithm as a function of the levels of uncertainties, namely:

$$ACC = \frac{\sum_{i=1}^6 CM_{ii}}{\sum_{j=1}^6 \sum_{i=1}^6 CM_{ij}}, \quad IFDR = \frac{\sum_{j=1}^5 \sum_{i=1}^5 CM_{ij}(i \neq j)}{\sum_{j=1}^6 \sum_{i=1}^5 CM_{ij}}, \quad (4.47)$$

where CM_{ij} , ACC and IFDR denote the element that is placed in the i^{th} row and j^{th} column of the confusion matrix, the accuracy, and the incorrect fault detection rate, respectively. Based on the obtained results from Tables 4.4 and 4.5, the performance

Table 4.6: Our proposed robust sensor FDI scheme performance indices for different uncertainty levels.

Scenario	ACC%	IFDR%
$SD_w \times 5$	95.33	2.4
$SD_w \times 7$	91	5.6
$\alpha_{\dot{m}_C} = 0.93$ $\alpha_{\eta_C} = 0.965$	93.66	5.2
$\alpha_{\dot{m}_C} = 0.91$ $\alpha_{\eta_C} = 0.955$	86.66	8.8

indices are now given in Table 4.6.

According to this table, by increasing the uncertainty levels one would result in the decrease in the ACC, although an increase in the IFDR. Notwithstanding the above observations, the sensor FDI scheme that we have developed in this chapter still yields performance that is acceptably robust against high level uncertainty sources.

In practical applications, one cannot guarantee that a given sensor bias fault severity always exactly matches the 3% pre-determined fault for which the MM-based filters are constructed. Consequently, it is imperative that we investigate the performance of the proposed MRKF-based FDI scheme corresponding to sensor bias faults that have other severity levels starting from the minimum detectable bias. Table 4.7 depicts the resulting detection times corresponding to all the faulty modes as a function of the fault severity, when the injected faults occur at $k_{fs} = 250$ sec during the cruise condition. The results are indicated for both robust methods when 5% and 2.5% degradations are injected to the compressor mass flow rate and the efficiency, respectively.

According to Table 4.7, our proposed robust method successfully detects and isolates sensor faults having different severities in presence of the engine compressor health parameters degradations with a shorter delay time and with smaller incorrect fault detection rates. It can also be observed that higher fault severities yield larger detection time delays. This is due to the fact that the actual fault severity becomes further away from the pre-determined 3% bias fault. It should be pointed out that

Table 4.7: Fault detection delay times for all sensor fault modes as a function of the fault severity for the single-layer MM-based FDI scheme by using the proposed RKF and the one designed in [4] when degradations of 5% and 2.5% are applied to the compressor mass flow rate and the efficiency, respectively. (×) denotes incorrect fault detection cases.

Fault	Fault Detection Delay Time (sec)											
	2%		3%		4%		5%		6%		7%	
	PRKF	RKF [4]	PRKF	RKF [4]	PRKF	RKF [4]	PRKF	RKF [4]	PRKF	RKF [4]	PRKF	RKF [4]
T_C	0.2	0.9	0.1	0.7	3	4.7	5.8	8.1	7.4	11.9	10	14.1
P_C	1.5	3.1	1.3	3	0.2	1	2.1	3.7	5.4	7.9	8.1	11.1
N	2.1	×	1.3	×	0.8	2.2	0.9	2.7	2.8	5.1	5.7	8.9
T_T	1.7	×	1	×	0.3	×	0.5	×	2	×	4.7	×
P_T	7.5	18.4	0.1	10.3	1.3	41.8	4.2	87.3	11.8	116.4	18.4	148.2

Table 4.8: The maximum detectable sensor bias fault achievable in less than 10 seconds of delay by using the first layer of robust multiple models during the cruise flight condition when degradations of 5% and 2.5% are applied to the compressor mass flow rate and the efficiency, respectively.

Maximum Detectable Fault	T_C	P_C	N	T_T	P_T
		7%	8%	8%	11%

the minimum detectable sensor bias fault is 2% but one requires a larger time to detect this fault with respect to higher fault severities. Table 4.8 shows the maximum detectable faults that can be achieved in less than 10 seconds by using only the first layer of the multiple models. It can then be implied that more multiple models layers are needed to improve the fault detection range and to reduce the fault detection delay time of our proposed robust MM-based FDI method.

Consequently, a second layer of multiple models are designed to detect and isolate sensor faults with higher magnitudes under shorter detection times. Using the results in Table 4.8, the second layer of multiple models is constructed for the pre-determined sensor faults set to 8%, 9%, 9%, 12% and 6% that are associated with the sensors measuring T_C , P_C , N , T_T and P_T , respectively. These results are presented in the next subsection.

Table 4.9: Fault detection delay times for all sensor fault modes as a function of fault severity using the double-layer MM-based FDI scheme of the proposed RKF when degradations of 5% and 2.5% are injected to the compressor mass flow rate and the efficiency, respectively.

Fault Severity	Fault Detection Delay Time (sec)				
	T_C	P_C	N	T_T	P_T
2%	0.2	1.5	2.1	1.7	7.5
3%	0.1	1.3	1.3	1	0.1
4%	3	0.2	0.8	0.3	1.3
5%	5.3	2.1	0.9	0.5	4.2
6%	1.1	5.4	2.8	2	0.4
7%	0.3	7.4	4.8	4.7	0.1
8%	0.1	3	1.7	5.7	0.2
9%	0.6	0.7	0.1	4.6	0.9
10%	1.4	0.1	0.5	4.6	1.8
11%	2.5	0.1	0.9	0.6	3.3
12%	3.5	0.1	1.6	0.2	4.2
13%	4.7	0.7	2.5	0.1	6.6
14%	5.7	1.9	4	0.1	7.9
16%	7.4	4.1	7	0.2	16.1
18%	9.4	5.5	9.8	0.3	19.6

4.5.3 Case 3: Sensor FDI by Using Two Layers of Multiple Models

In this case study simulation, two layers of multiple models are used for detecting and isolating sensor faults corresponding to various severities. The faults are applied during the cruise flight condition, whereas 5% and 2.5% degradations are applied to the compressor mass flow rate and the efficiency, respectively. As compared to the previous case study simulation, our robust MM-based FDI approach is capable of detecting and isolating a wider range of faults and with less detection time delays. Table 4.9 shows the fault detection time delays for different percentages of sensor bias faults for the two layers of multiple models.

According to Table 4.9, some of the faults that were previously detected by the first layer in the case study #2, are now detectable with shorter delay times through

Table 4.10: The maximum detectable sensor bias fault achievable in less than 10 seconds of delay by using double-layer robust multiple models during the cruise flight condition when degradations of 5% and 2.5% are injected to the compressor mass flow rate and the efficiency, respectively.

Maximum Detectable Fault	T_C	P_C	N	T_T	P_T
	18%	24%	18%	44%	14%

activating the models that are included in the second layer. However, it can still be observed that the higher the fault severity with respect to the pre-determined faults that are defined for the second layer, the more delay in the detection time. Table 4.10 shows the maximum detectable faults that are achievable in less than 10 seconds of delay for various sensors using the two layers of multiple models in presence of 5% and 2.5% degradations that are injected to the compressor mass flow rate and the efficiency, respectively.

Similarly, more layers can be added to the multiple model structure to improve the fault detection range and to reduce the fault detection time delays for those faults that are limited in the detection range of the FDI algorithm. Moreover, multiple layer MM structure enables one to define the level of a fault severity through the corresponding activated layer of multiple models, given that each layer is associated with a certain range of fault severities.

Finally, to investigate the effects of the various levels of compressor health parameters degradations on the fault detection times, Figure 4.10 shows the fault detection times for three selected faulty sensors, namely T_C , N and P_T as a function of the fault severity under various degradation levels that are applied to the compressor mass flow rate and the efficiency during the cruise flight condition.

According to Figure 4.10, a sensor fault is detected and isolated sooner for lower levels of the compressor health parameters degradations. Therefore, the maximum faults that are detectable in less than 10 seconds of delay by our proposed

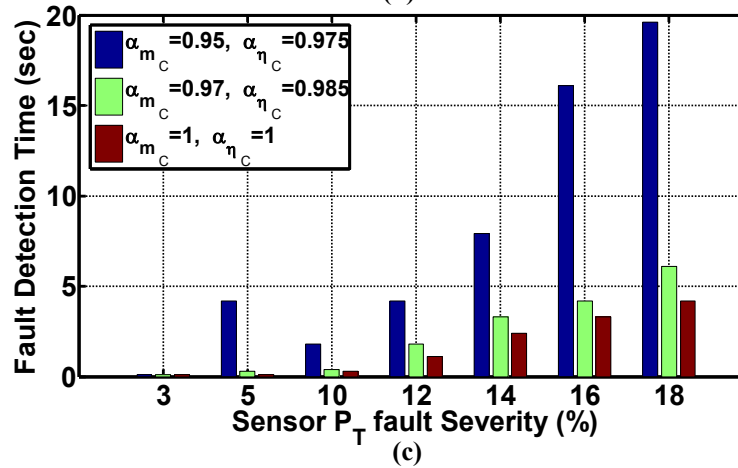
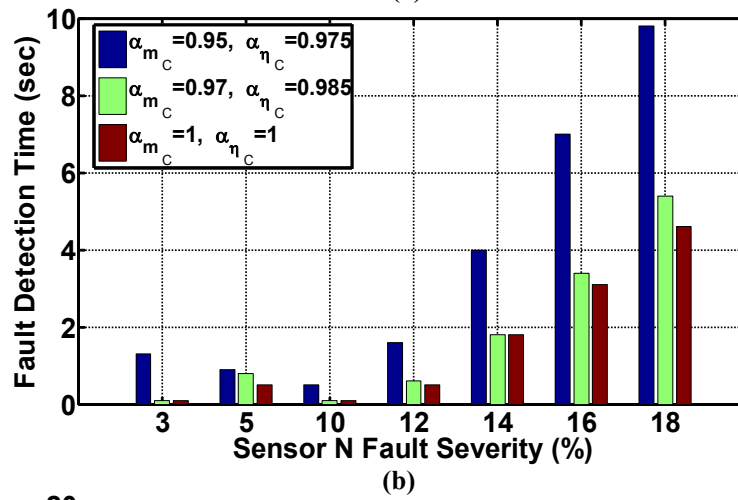
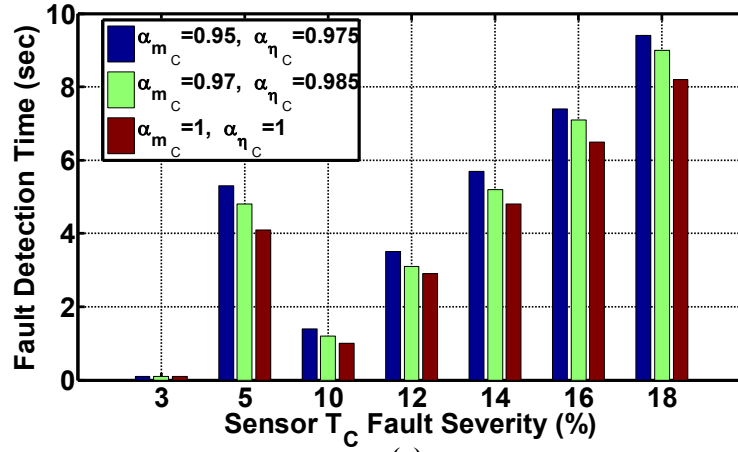


Figure 4.10: Fault detection time delays by using our proposed two layer robust MM-based FDI approach for a single bias fault when injected at $k_{fs} = 250$ sec to the sensors (a) T_C , (b) N and (c) P_T as a function of the fault severity and the compressor health parameters degradation levels.

two-layer MM-based FDI scheme will be increased subject to lower levels of compressor health parameters degradations. For instance, if 3% and 1.5% degradations are instead applied to the compressor mass flow rate and the efficiency respectively, the maximum faults that are detectable in less than 10 seconds of delay are 19%, 24% and 24% for T_C , N and P_T , respectively. However, when there is no compressor degradation, the maximum faults that are detectable in less than 10 seconds of delay are 20%, 28% and 41% for T_C , N and P_T , respectively.

Consequently, our proposed RKF outperforms the existing RKF designs in the literature in which the time-varying parameter uncertainties are only compensated for in the state and measurement matrices instead of all state space matrices. Moreover, our proposed method is capable of detecting and isolating smaller partial sensor faults as compared with the adaptive variable-structure multiple-model scheme [165] that has a limited robustness against parameter uncertainties. Unlike data-driven methods such as FDI neural networks schemes [171], our proposed method does neither need memory for collecting data nor extensive computational resources for training and designing the structure of the estimator. However, the order of the model is always a critical concern for multiple-model based schemes that can be partially rectified by integrating the FDI scheme with a proper fault identification approach for estimating the severities of fault parameters and by providing the MM-based scheme with a feedback from the fault identification module.

4.6 Summary

In this chapter, a novel robust multiple model based fault detection and isolation methodology is proposed. The proposed methodology builds on development of a robust Kalman filters that are designed for multiple piecewise linear models associated with healthy and faulty sensor scenarios in which all the state space matrices are

affected by time-varying norm bounded parameter uncertainties. The filter gain matrices are computed using two LMI feasibility conditions where the predefined state estimation error upper bounds are imposed. The proposed robust multiple model structure is then applied to solve sensor FDI problem for single spool gas turbine engine during the entire flight profile in which the compressor health parameters are degraded. To investigate the effectiveness of our proposed robust MM-based FDI approach, extensive simulation studies are conducted to compare various factors including the fault detection time, estimation accuracy, false alarm and incorrect fault detection rates among our proposed method and available work in the literature. Finally, it is observed that our proposed robust method has lower fault detection time as well as smaller false alarm and incorrect fault detection rates. It is also capable of estimating nonlinear system states more accurately as compared to the examined methods in the literature in presence of parameter uncertainties.

Chapter 5

Hybrid Fault Detection and Isolation Scheme

In this chapter, a novel hybrid scheme is proposed to solve the sensor fault detection and isolation problem for the single spool gas turbine engine. The hybrid scheme is composed of two elements: 1) the dynamic recurrent neural network (DRNN) that is utilized to approximate the engine degradation effects on sensor measurements, and 2) the bank of observers that are developed based on the engine dynamic model. The DRNN is trained off-line by using the extended Kalman filter algorithm that has a higher convergence rate and fitting accuracy as compared to the back-propagation learning (gradient descent) method [172]. The uncertainty dynamics that are approximated by our proposed DRNN is then removed from the sensor measurements and the modified sensor measurements are then applied to our proposed bank of observers for detecting and isolating the engine sensor faults. Two types of observers that have been previously proposed in preceding chapters namely the hybrid Kalman filter (HKF) and the robust Kalman filter (RKF) are used to construct the bank of observers to be integrated with the DRNN. Finally, using extensive simulation studies it is demonstrated that our proposed hybrid DRNN-HKF-based FDI

scheme is capable of reducing the fault detection time, increasing the robustness level and improving the FDI accuracy and performance outcomes as compared to our previously proposed pure model-based FDI approaches.

5.1 Proposed Hybrid Fault Detection and Isolation Structure

Robust model-based fault diagnosis strategies have restricted robustness to a particular source of uncertainty. It is not actually possible to design a completely robust strategy for all sources of uncertainties, although it is possible to improve the robustness by applying the hybrid approach. In this chapter, a hybrid gas turbine engine modeling is proposed which improves the robustness with respect to different types of modeling uncertainties when it is integrated with our proposed model-based sensor FDI approach which uses a bank of HKFs or RKF's.

In this problem, it is assumed that the discrete-time fault-free version of the actual gas turbine engine is given by,

$$\begin{aligned} X(k+1) &= \mathcal{F}(X(k), U(k), H(k), w(k)), & X(0) &= X_0, \\ Y(k) &= \mathcal{G}(X(k), U(k), H(k)) + v(k), \end{aligned} \quad (5.1)$$

where $X(k) \in \mathbb{R}^n$, $Y(k) \in \mathbb{R}^q$, $U(k) \in \mathbb{R}^p$ and $H(k) \in \mathbb{R}^r$ are the real engine state variables, sensor measurements, control inputs and health parameters, respectively. For performing simulations and implementation of our proposed online FDI scheme, it is assumed that the continuous-time actual gas turbine engine is discretized with a sufficiently small sampling period to derive the model (5.1). The engine health parameters, namely the compressor and turbine mass flow rates and efficiencies, are the state-dependent variables that are degraded from their healthy reference baselines during the engine life cycle. They depend on the engine compressor and

turbine performance maps.

Moreover, the process and measurement noise are also indicated by $w(k)$ and $v(k)$ that are assumed to be Gaussian zero mean noise signals applied to the engine ambient parameters and sensor measurements, respectively. The nominal nonlinear on-board engine model (OBEM) that is designed for the engine based on the thermodynamics laws is also defined as follows:

$$\begin{aligned} X_{\text{OBEM}}(k+1) &= f(X_{\text{OBEM}}(k), U(k), H_{\text{OBEM}}(k)), & X_{\text{OBEM}}(0) &= X_{\text{OBEM}0} \\ Y_{\text{OBEM}}(k) &= g(X_{\text{OBEM}}(k), H_{\text{OBEM}}(k)), \end{aligned} \quad (5.2)$$

where $X_{\text{OBEM}}(k) \in \mathbb{R}^n$, $Y_{\text{OBEM}}(k) \in \mathbb{R}^q$ and $H_{\text{OBEM}}(k) \in \mathbb{R}^r$ denote the OBEM state variables, system outputs and health parameters, respectively that are not exactly the same as the actual engine variables due to different uncertainty sources and neglected dynamics. In fact, the uncertainty affects the engine modeling process and so it is desirable to approximate the severity of uncertainty to be compensated in actual engine sensor measurements for further uses in our FDI scheme.

In this chapter, to approximate the uncertainty, a novel hybrid engine modeling strategy is proposed to also improve the robustness of our proposed FDI scheme as compared to our previously developed pure model-based approaches in the preceding chapters. Our proposed hybrid DRNN-based FDI scheme is composed of two main components, namely the dynamic recurrent neural network (DRNN) to estimate the effects of uncertainties, and a bank of HKFs/RKFs to utilize the modified measurements for performing sensor fault detection and isolation. The DRNN is designed off-line in a fault-free situation and is used in our proposed online FDI scheme to estimate the output error due to the model uncertainty, $Y_{\text{un}}(k) = Y(k) - Y_{\text{OBEM}}(k)$. The DRNN outputs are $\hat{Y}_{\text{un}}(k)$ that are removed later from the actual engine sensor measurements to form the modified measurements as $Y_{\text{m}}(k) = Y(k) - \hat{Y}_{\text{un}}(k)$. Then, the modified sensor measurements, $Y_{\text{m}}(k)$, are used in a bank of HKFs/RKFs by using a multiple-model scheme to detect and isolate different sensor faults. The

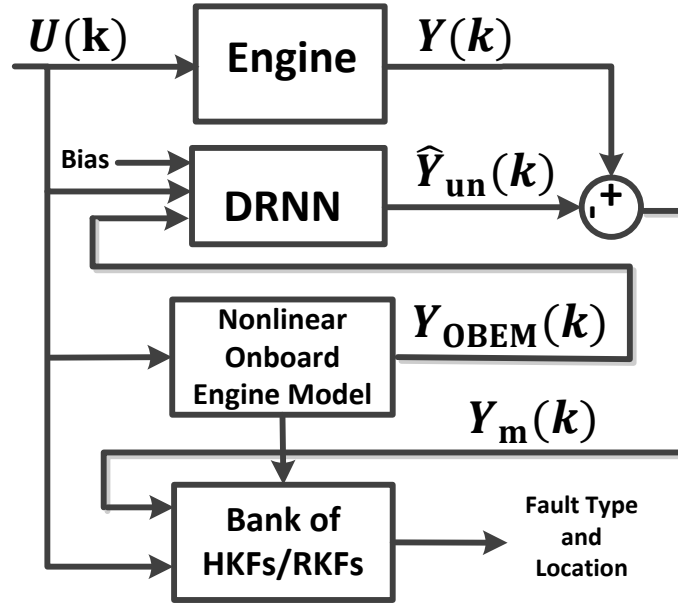


Figure 5.1: Overall structure of our proposed hybrid FDI scheme.

overall structure of our proposed on-line hybrid FDI approach is depicted in Figure 5.1. More details regarding the main components of our proposed on-line hybrid DRNN-based FDI scheme are explained in the following sections.

5.1.1 Dynamic Recurrent Neural Network (DRNN)

DRNN is a class of neural network models in which the connections among many of its neurons form a directed cycle which is defined as a recurrent. Such a recurrence or cycle is associated with the time delay operation. The time delay recurrence over temporal dimension leads to a memory structure which is defined as the internal state that enables the DRNN to represent temporal dynamic behavior. The DRNN itself can be considered as a deep structure since the temporal unfolding of DRNN generates many layers as many as the length of an input signal. The DRNN works based on the input signals and internal states to encode the past information in the

temporal sequence that is already processed by a DRNN.

Generally, the dynamic neural network (DNN) is categorized into two main groups: a) the DNN that uses the current and time-delayed inputs in which the number of delays in the tapped delay line must be set *a priori* and is correlated with the order of the original dynamic system, and b) the DRNN with internal recurrent connections to the input, hidden and output layer neurons. Training the DRNN is more complex than a static feed forward network due to the additional degrees of freedom and a more complicated error surface and also the problem of vanishing gradient.

In this chapter, the DRNN is used to approximate the engine modeling uncertainty terms due to the its health parameters degradation. To train the DRNN, the data can be collected from either a fault-free actual gas turbine engine or an engine simulator for the entire operating range. The differences between the actual engine sensor measurements and nonlinear OBEM outputs are also found to be utilized in the DRNN training process. The DRNN is designed to identify $Y_{\text{un}}(k)$ which is the output error that is generated due to different sources of uncertainties. The training process is performed offline to minimize the sum of mean squared error cost function that is defined as $\frac{1}{2} \sum_{k=1}^{\mathcal{T}} (\hat{Y}_{\text{un}}(k) - Y_{\text{un}}(k))^2$, where $\hat{Y}_{\text{un}}(k)$ is the estimated output generated by our proposed DRNN and \mathcal{T} denotes the total length of the training samples. The overall structure of our proposed offline DRNN training is shown in Figure 5.2.

In this chapter, the state-space model of the DRNN is used as an architectural framework which is a proper choice for sequential state estimation methods that are applied for DRNN training process. In the state-space model, there are certain number of states that are associated with hidden neurons as well as feedbacks from the hidden layer to the input layer. In this structure, the layer which stores the hidden neurons outputs for one time-step and then feeds them to the input layer is

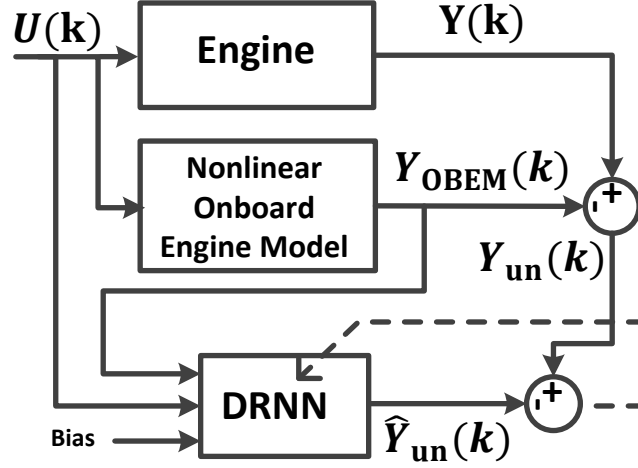


Figure 5.2: Offline training procedure of the DRNN for the hybrid engine modeling.

called the context layer. A nonlinear mapping is commonly performed by the hidden layer, but the output layer is generally linear, leading to the following equations:

$$\begin{aligned}\mathcal{X}(k+1) &= \Phi(W_{xx}\mathcal{X}(k) + W_{xu}\mathcal{U}(k)), & \mathcal{X}(0) &= \mathcal{X}_0, \\ \hat{Y}_{\text{un}}(k) &= W_{yx}\mathcal{X}(k),\end{aligned}\tag{5.3}$$

where $\mathcal{X}(k) \in \mathbb{R}^l$ and $\mathcal{U}(k) \in \mathbb{R}^{(q+p+1)}$ are the network internal state variables and inputs.

In Figure 5.2, the input signal is the augmented vector of the engine control input signal $U(k)$, OBEM outputs $Y_{\text{OBEM}}(k)$ and the bias term. The network output signals, $\hat{Y}_{\text{un}}(k) \in \mathbb{R}^q$, represent the engine output errors due to the uncertainty which are generated by the output layer of the DRNN. Moreover, W_{xx} , W_{xu} and W_{yx} represent the synaptic weights from the context layer to the hidden neurons, and from the input source neurons to the hidden neurons and from the hidden neurons to the output neurons, respectively. The activation function of the hidden neurons are denoted by Φ , that is a sigmoidal function. It typically takes the form of a hyperbolic tangent or logistic function. The feedback is also a unit-time delay from

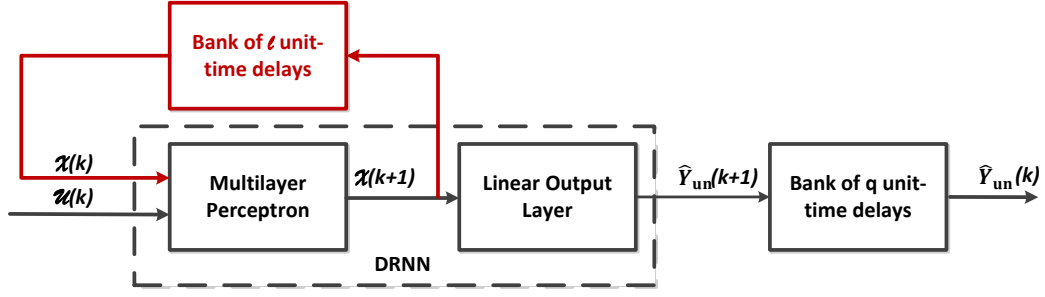


Figure 5.3: State-space model of the DRNN.

the hidden neurons to the input nodes. In case it is desired to add feedback from output neurons to the hidden neurons, the state-space equation will be changed to $\mathcal{X}(k+1) = \Phi(W_{xx}\mathcal{X}(k) + W_{xu}\mathcal{U}(k) + W_{xy}\hat{Y}_{un}(k))$, in which W_{xy} denotes the corresponding feedback weights. Figure 5.3 displays the state-space model of the DRNN with the feedback part that is shown in red and is composed of l unit-time delays as part of the context layer corresponding to the network internal state vector elements. Note that in Figure 5.3 the output feedback is not considered.

Different methods namely, the back-propagation through time (BPTT), real-time recurrent learning (RTRL), and extended Kalman filter will be introduced in the following sections as the DRNN supervised learning approaches [172, 173]. More details regarding the formulation of different supervised learning methods for the DRNN are explained in Section 5.2. When the DRNN is trained offline, all the synaptic weights are fixed and it is then applied in our proposed online FDI scheme in conjunction with a bank of HKFs/RKFs which constitutes the second element of our proposed hybrid FDI approach.

5.1.2 Bank of Hybrid/Robust Kalman Filters

The HKF and RKF are previously introduced in Chapters 3 and 4 and it was shown that the HKF is intuitively robust with respect to certain levels of engine health

parameters degradation. As compared to conventional estimation approaches in the literature, the HKF is demonstrated to be more accurate in detecting and isolating single and concurrent sensor faults in different operating modes of the engine. However, it cannot operate robustly for the higher levels of health parameters degradations, unless the OBEM health parameters reference baselines are estimated off-line and updated periodically. Therefore, there is a risk of generating false alarms or incorrect fault detections in case the health parameters reference baselines are not updated for the OBEM or their estimation error is not sufficiently small. Also, the fault detection time may increase rapidly in case of a higher mismatch between the real engine and the associated OBEM. To rectify the above problems, it is proposed to improve the HKF-based FDI robustness through being integrated with our proposed DRNN structure.

Moreover, the previously proposed RKF-based FDI framework is formally designed to be robust to certain levels of health parameter degradations, that are 2.5% degradation on the compressor efficiency and 5% degradation on the compressor mass flow rate. However, for higher percentage of degradation, the proposed RKF-based FDI framework does not operate sufficiently robust and may generate false alarms and incorrect fault detections. Therefore, it is necessary to improve the robustness of the RKF-based FDI scheme through integrating it with our proposed DRNN structure.

As demonstrated in Chapters 3 and 4, a bank of HKFs and RKFs are constructed for different healthy and faulty sensor scenarios and are utilized in the multiple-model structure to detect and isolate different sensor bias faults. Let us assume a sensor fault is injected to the actual gas turbine engine in (5.1) as,

$$\begin{aligned} X(k+1) &= \mathcal{F}(X(k), U(k), H(k), w(k)), & X(0) &= X_0, \\ Y(k) &= \mathcal{G}(X(k), U(k), H(k)) + \sum_{i=1}^q b_s z_s \delta(k - k_{fs}) + v(k), \end{aligned} \quad (5.4)$$

where q is the total number of sensors, b_s and z_s respectively represent the s^{th} sensor bias fault magnitude and a fault location vector that has a unit value for the s^{th} sensor and the other elements are zero. $\delta(k - k_{fs})$ denotes a unit step function that occurs at sample k_{fs} corresponding to the s^{th} sensor.

The bank of HKFs/RKFs receives the modified sensor measurements, $Y_m(k) = Y(k) - \hat{Y}_{un}(k)$ as well as the engine control input. Hence, it is expected to achieve lower uncertainty effects on the engine sensor measurements due to removal of the DRNN outputs from the actual engine sensor measurement. The bank of HKFs/RKFs are also expected to be more robust while receiving the modified sensor measurements.

Remark 5.1: The DRNN is trained offline by using the signals $U(k)$, $Y_{OBEM}(k)$ and $Y_{un}(k)$ for the entire operating regime of the gas turbine engine. It is assumed that the training data is collected for the fault-free engine. The reason that the DRNN uses the OBEM outputs rather than the sensor measurements is to avoid the DRNN to be adapted with the fault terms that may occur during an online operation and that can affect the engine sensor measurements. The DRNN must be specialized to solely approximate the uncertainty effects, but not an engine fault.

5.2 DRNN Structure and the Training Process

In general, there are two modes of training for different types of neural networks, namely the batch mode and the sequential mode. In the batch mode, the network parameters are adjusted for the entire training samples, however in the sequential mode the parameter adjustment is performed after the presentation of each training pattern. Similar modes are also defined in the literature for DRNN as epochwise and continuous training procedures. Based on these two modes, two gradient descent-based training algorithms that involve the propagation of derivatives are developed

for DRNN training that are back-propagation through time (BPTT) and real-time recurrent learning (RTRL). The derivative information is propagated in the backward direction for the former one and in a forward direction for the latter [172].

The BPTT is the extension of the standard back-propagation algorithm. It can be derived by unfolding the temporal operation of the DRNN into the layered feedforward topology in which the temporal behavior is represented by one layer in each time step. The BPTT training can be performed in two forms of epochwise and continuous forms. In the epochwise BPTT training algorithm, the sum of mean square errors is minimized as,

$$\mathcal{E} = \frac{1}{2} \sum_{k=1}^{\mathcal{T}} \sum_{j=1}^q (Y_{\text{un}}^j(k) - \hat{Y}_{\text{un}}^j(k))^2, \quad (5.5)$$

where \mathcal{T} and q denote the total number of training samples and the number of network outputs, respectively. The DRNN weight parameters, $w_{ji}(k)$ (the elements of W_{xx} , W_{xu} and W_{yx} weight matrices) are updated according to the following rule,

$$w_{ji}(k+1) = w_{ji}(k) - \gamma \frac{\partial \mathcal{E}}{\partial w_{ji}(k)}, \quad (5.6)$$

where γ is the learning rate and $w_{ji}(k)$ is the synaptic weight from the i^{th} neuron to the j^{th} neuron.

To compute the gradients, the error term associated with the j^{th} neuron can be defined as,

$$\delta_j(k) = -\frac{\partial \mathcal{E}}{\partial O_j(k)}, \quad (5.7)$$

where $O_j(k)$ is the j^{th} term of $O(k)$ that is the induced local field or potential of neurons. The induced local field is computed as $O(k) = W_{xx}\mathcal{X}(k) + W_{xu}\mathcal{U}(k)$ for the hidden neurons and as $O(k) = W_{yx}\mathcal{X}(k)$ for the output neurons. The j^{th} error term at $k = \mathcal{T}$ is computed as,

$$\delta_j(\mathcal{T}) = \Phi'(O_j(\mathcal{T}))(Y_{\text{un}}^j(\mathcal{T}) - \hat{Y}_{\text{un}}^j(\mathcal{T})), \quad (5.8)$$

where $\Phi'(\cdot)$ is the derivative of an activation function. For all the other time steps in the time frame, $k = \mathcal{T} - 1, \mathcal{T} - 2, \dots, 1$, the error term is recursively computed as,

$$\delta_j(k) = \Phi'(O_j(k)) \left[(Y_{\text{un}}^j(k) - \hat{Y}_{\text{un}}^j(k)) + \sum_i w_{ji} \delta_i(k+1) \right], \quad (5.9)$$

where the error term associated with the output neurons are propagated back from the output layer at time k , and the error term associated with the hidden neurons are propagated back at time $k+1$. Once the computation of the back propagation has been performed, the synaptic weight w_{ji} is adjusted as,

$$\Delta w_{ji} = -\gamma \frac{\partial \mathcal{E}}{\partial w_{ji}} = \gamma \sum_{k=1}^{\mathcal{T}} \delta_j(k) \mathcal{I}_i(k-1), \quad (5.10)$$

where $\mathcal{I}_i(k-1)$ is the input applied to the i th synapse of neuron j at time $k-1$.

The computational complexity of the BPTT is $O(M^2)$ per time step, where M is the total number of weight parameters. Compared to the standard BP, the BPTT converges more slowly due to dependencies between time frames and it is more likely to be stuck in a poor local minimum due to exploding and vanishing gradient effects. Different techniques, such as the echo-state property that is used in primal-dual learning algorithm as a constrained optimization problem, are introduced in the literature to avoid the exploding and vanishing gradient effects [174].

The BPTT has also a continuous version in which the cost function is computed at each time step and the weights are individually adjusted for each training pattern. For this purpose, a relevant history of inputs and internal states are saved for a time called truncation depth. Only the history over a truncation depth is restored. This property can control the computational complexity and improve the practicality of the learning process. It must be noted that the truncation depth must be sufficiently large to keep the convergence of derivatives and small enough to control the computational complexity.

To use the truncated BPTT algorithm the instantaneous value of the cost function is used as,

$$\mathcal{E}(k) = \frac{1}{2} \sum_{j=1}^q (Y_{\text{un}}^j(k) - \hat{Y}_{\text{un}}^j(k))^2. \quad (5.11)$$

If h indicates the truncation depth, the error term associated with the j th neuron is given by,

$$\delta_j(t) = -\frac{\partial \mathcal{E}(t)}{\partial O_j(t)}, \quad k - h < t \leq k \quad (5.12)$$

which ends in the following error terms associated with the k th sample and the preceding samples with the depth of h , $k - h < t \leq k$, that is

$$\delta_j(t) = \begin{cases} \Phi'(O_j(k)(Y_{\text{un}}(k) - \hat{Y}_{\text{un}}(k))), & t = k \\ \Phi'(O_j(t)) \sum_i w_{ji}(t) \delta_i(t+1), & k - h < t < k. \end{cases} \quad (5.13)$$

Similarly, once the back propagation computation has been performed the weights are updated as,

$$\Delta w_{ji}(k) = \gamma \sum_{t=k-h+1}^k \delta_j(t) \mathcal{I}_i(t-1), \quad (5.14)$$

where γ should be sufficiently small to avoid the weight values change significantly.

Moreover, the real-time recurrent learning (RTRL) method is another learning method that is more suitable for online learning, although the corresponding computational cost is $O(l+q)^4$, and therefore it is recommended to be utilized for small size networks. The details regarding this learning method are explained further in [172].

One of the remedies for solving the vanishing gradient problem is to use the second-order training algorithm such as the quasi-Newton, Levenberg-Marquardt and conjugate gradient methods, however they are sometimes trapped in a local solution. The nonlinear sequential state estimation methods are capable of not only evolving the weight parameters of a network in a sequential manner, but also provide

one with the second-order information of data by means of calculating the prediction-error covariance matrix that is also evolved sequentially. The Kalman filter (KF)-based training is a popular method for nonlinear sequential state estimation that is developed to train a neural network in the late 1980s [175].

The KF-based training methods have better fitting accuracy, faster convergence speed and use second-order derivative information unlike the gradient descent methods. They are also less likely to converge to a local optimum due to their stochastic training process and do not also need any regularization to avoid over fitting.

In this chapter, the DRNN training is considered as a state estimation problem of an unknown ideal network that provides zero residual. The states are the neural network weight parameters $W(k)$ in which the $W_{xu}(k)$, $W_{xx}(k)$ and $W_{yx}(k)$ elements are included in an orderly fashion such that the weights associated to the first neuron in the first layer are followed by those of the second neuron, carrying on in this manner until all the neurons are accounted for in $W(k)$. The residual vector is also the current training error $Y_{\text{un}}(k) - \hat{Y}_{\text{un}}(k)$.

Let us assume that the ideal state-space model of the network is given by:

$$\begin{aligned} W(k+1) &= W(k) + \varsigma_w(k), \quad W(0) = W_0, \\ Y_{\text{un}}(k) &= \mathcal{F}(W(k), U(k), \mathcal{X}(k)) + \varsigma_v(k), \end{aligned} \tag{5.15}$$

where $\varsigma_w(k)$ and $\varsigma_v(k)$ are assumed to be the zero mean Gaussian process and measurement noise, respectively. The corresponding fixed diagonal noise covariance matrices that are used for the Kalman filter-based training process are Q and R , respectively. Note that the covariance matrices can also be considered time-varying particularly for adjusting the network convergence speed. Moreover, \mathcal{F} is a nonlinear function which defines an ideal network structure to generate the output $Y_{\text{un}}(k)$ and indicates the overall nonlinearity of the network from the input to the output layer, and $\mathcal{X}(k)$ denotes the network internal states. It must be noted that $Y_{\text{un}}(k)$

is the desired output of the DRNN that is perfectly matched with the engine sensor measurements difference, $Y(k) - Y_{\text{OBEM}}(k)$, however their corresponding predicted value is indicated as $\hat{Y}_{\text{un}}(k)$, that is used to measure the residual or innovation process. Moreover, \mathcal{F} has a known structure but with unknown parameters.

The training data set includes the pairs of $\{\mathcal{U}(k), Y_{\text{un}}(k)\}_{k=1}^T$ samples. The relevant formulations associated with the EKF-based DRNN training algorithm is as follows,

$$\begin{aligned}
K(k) &= P(k|k-1)\mathcal{H}^T(k) [\mathcal{H}(k)P(k|k-1)\mathcal{H}^T(k) + R]^{-1}, \\
r(k) &= Y_{\text{un}}(k) - \mathcal{F}(\hat{W}(k|k-1), \mathcal{X}(k), \mathcal{U}(k)), \\
\hat{W}(k|k) &= \hat{W}(k|k-1) + K(k)r(k), \\
\hat{W}(k+1|k) &= \hat{W}(k|k), \\
P(k|k) &= P(k|k-1) - K(k)\mathcal{H}(k)P(k|k-1), \\
P(k+1|k) &= P(k|k) + Q,
\end{aligned} \tag{5.16}$$

where $K(k)$, $P(k)$ and $\mathcal{H}(k)$ denote the Kalman gain matrix, the prediction-error covariance matrix (carries the second-order derivative information) and the measurement matrix, respectively. The predicted network output $\hat{Y}_{\text{un}}(k|k-1)$ is calculated by the use of predicted weight parameters $\hat{W}(k|k-1)$, network inputs $U(k)$ and internal state vector $\mathcal{X}(k)$ as indicated in (5.3). Thus, the DRNN supplies the EKF with $\hat{Y}_{\text{un}}(k|k-1)$ as the predicted estimate of the observable $Y_{\text{un}}(k)$ in order to compute the residual vector.

The measurement matrix of the linearized model is also obtained by calculating the partial derivatives of the actual network outputs with respect to the network

weight parameters vector as,

$$\mathcal{H}(k) = \begin{bmatrix} \frac{\partial \mathcal{F}_1}{\partial W_1(k)} & \frac{\partial \mathcal{F}_1}{\partial W_2(k)} & \cdots & \frac{\partial \mathcal{F}_1}{\partial W_M(k)} \\ \frac{\partial \mathcal{F}_2}{\partial W_1(k)} & \frac{\partial \mathcal{F}_2}{\partial W_2(k)} & \cdots & \frac{\partial \mathcal{F}_2}{\partial W_M(k)} \\ \vdots & \vdots & \vdots & \vdots \\ \frac{\partial \mathcal{F}_q}{\partial W_1(k)} & \frac{\partial \mathcal{F}_q}{\partial W_2(k)} & \cdots & \frac{\partial \mathcal{F}_q}{\partial W_M(k)} \end{bmatrix}, \quad (5.17)$$

where M is the total number of weight parameters and $\mathcal{H}(k) \in \mathbb{R}^{q \times M}$. In this thesis, the above partial derivatives are calculated by using the truncated BPTT algorithm. The computational complexity of the EKF-based training process is $O(qM^2)$. To compute the measurement matrix, the partial derivatives in (5.17) are evaluated at $W(k) = \hat{W}(k|k-1)$.

In the EKF-based supervised learning process, the DRNN utilizes $\hat{W}(k|k-1)$ to compute $\hat{Y}_{\text{un}}(k|k-1)$ in response to the input vector $\mathcal{U}(k)$. Then, $\hat{Y}_{\text{un}}(k|k-1)$ is supplied to the EKF algorithm and is taken as $\mathcal{F}(\hat{W}(k|k-1), \mathcal{U}(k), \mathcal{X}(k))$ according to the second line in (5.16). As per the following lines of the equations in (5.16) and using the innovation process, the EKF updates the old estimate of the weight vector and computes $\hat{W}(k|k)$. Finally, the updated weight vector is supplied to the DRNN by EKF via a bank of unit-time delays. Therefore, according to Figure 5.4 the DRNN performs the role of the predictor and the EKF learning process provides the supervision and performs the role of the corrector.

5.3 Hybrid DRNN-based FDI Scheme

The hybrid DRNN-based FDI scheme is constructed using multiple hybrid Kalman filters or robust Kalman filters as proposed in Chapters 3 and 4. As per explanations in Sections 3.2 and 4.3, the piecewise linear (PWL) models are derived at multiple operating points to cover the entire flight profile.

In the DRNN-HKF-based scheme, the PWL models are used to compute the

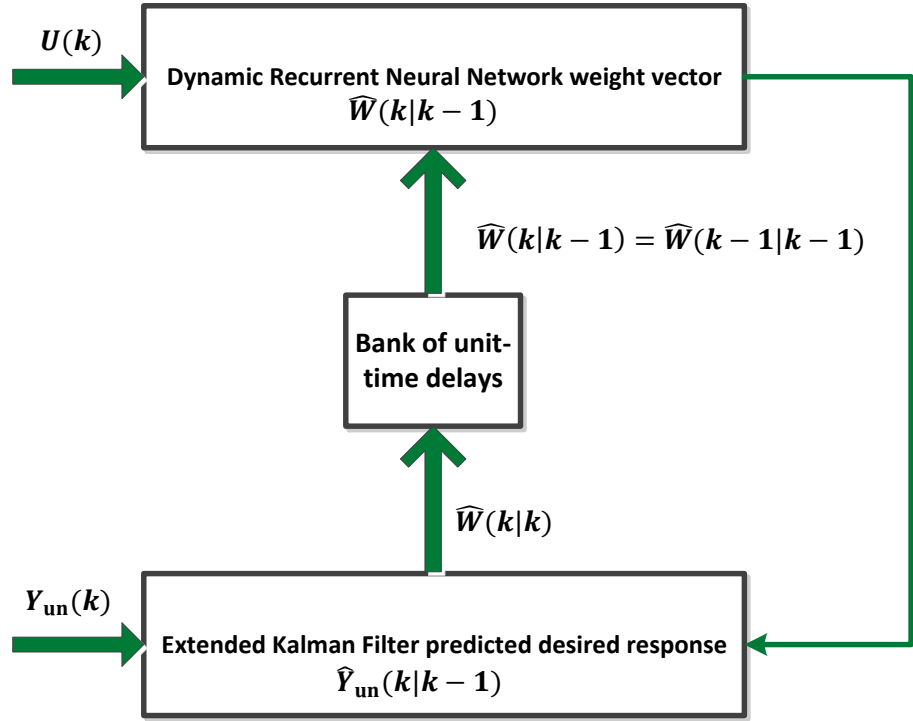


Figure 5.4: EKF-based training of the DRNN weights.

corresponding steady-state Kalman gain matrices for various sensor modes in (5.4). Therefore, the HKF for the j^{th} sensor mode at the i^{th} operating point is designed as follows:

$$\begin{aligned} \hat{X}^{(i,j)}(k+1) - X_{\text{OBEM}}(k+1) &= A^i(\hat{X}^{(i,j)}(k) - X_{\text{OBEM}}(k)) + K_{\text{ss}}^i(Y_m(k) - \hat{Y}^{(i,j)}(k)), \\ \hat{Y}^{(i,j)}(k) &= C^i(\hat{X}^{(i,j)}(k) - X_{\text{OBEM}}(k)) + Y_{\text{OBEM}}(k) + b_{dj}a_j\delta_j(k), \end{aligned} \quad (5.18)$$

which is similar to (3.17) with its defined variables in Section 3.2. Note that unlike our proposed HKF methodology in Chapter 3, in this chapter the OBEM health parameters are fixed at their corresponding healthy reference baselines and the HKF receives the modified measurements rather than the real ones.

In DRNN-RKF-based scheme, using the uncertain PWL models state-space matrices the RKF for the j^{th} sensor mode at the i^{th} operating point is designed as

follows:

$$\begin{aligned}\Delta\hat{X}^{(i,j)}(k+1) &= G^i\Delta\hat{X}^{(i,j)}(k) + K^i\Delta Y_m^i(k), \\ \Delta\hat{Y}^{(i,j)}(k) &= \bar{C}^i\Delta\hat{X}^{(i,j)}(k) + b_{dj}a_j\delta_j(k),\end{aligned}\tag{5.19}$$

which is similar to (4.39) with its defined variables in Section 4.3. Note that $\Delta Y_m(k) = Y(k) - Y_{ss} - \hat{Y}_{un}(k)$ denotes the perturbation of the modified measurements from their corresponding steady-state operating points.

Following the design of multiple HKFs and RKF, their corresponding residuals, covariance matrices and likelihood functions are respectively given by:

$$\begin{aligned}\gamma^{(i,j)}(k) &= Y_m(k) - \hat{Y}^{(i,j)}(k), \\ S^{(i,j)}(k) &= \text{cov}(\gamma^{(i,j)}(k)), \\ f^{(i,j)}(\gamma^{(i,j)}(k)) &= \frac{1}{(2\pi)^{q/2}\sqrt{|S^{(i,j)}(k)|}} \times \exp\left[\frac{-1}{2}(\gamma^{(i,j)}(k))^T(S^{(i,j)}(k))^{(-1)}(\gamma^{(i,j)}(k))\right],\end{aligned}\tag{5.20}$$

The normalized weights are also computed as follows:

$$\mu^{(i,j)}(k) = \frac{f^{(i,j)}(\gamma^{(i,j)}(k))\mu^{(i,j)}(k-1)}{\sum_{i=1}^L f^{(i,j)}(\gamma^{(i,j)}(k))\mu^{(i,j)}(k-1)}.\tag{5.21}$$

Corresponding to each sensor mode, the weighted residual and the covariance matrices are computed as follows:

$$\begin{aligned}\gamma_c^j(k) &= \sum_{i=1}^L \mu^{(i,j)}(k)\gamma^{(i,j)}(k), \\ S_c^j(k) &= \sum_{i=1}^L (\mu^{(i,j)}(k))^2 S^{(i,j)}(k),\end{aligned}\tag{5.22}$$

Finally, to detect and isolate sensor fault by using our proposed DRNN-HKF or DRNN-RKF based frameworks, the hypothesis conditional probability $P_j(k)$ is defined as (3.23) or (4.44) and is computed recursively. Hence, the condition of the system and the location of a single faulty sensor can be detected and isolated based on evaluating $P_j(k)$ and determining its maximum value. In other words, a similar sensor FDI logic is utilized in both DRNN-HKF and DRNN-RKF based schemes.

5.4 Convergence Analysis

In this section, the convergence of our proposed dynamic recurrent neural network that is trained by the EKF algorithm is investigated. The analysis is performed for a more general DRNN that is called the modified Elman neural network [176]. In this network, in addition to the unit-time delay feedback connections from the hidden neurons to input neurons, the auto-feedback connections with fixed gains exist from the context layer to the hidden layer. Note that the context layer includes the nodes receiving the feedback connections from the hidden neurons. It must be noted that the following analysis is completely valid for our proposed DRNN which has an Elman structure without the above auto-feedback connections.

Let us consider the following unknown discrete-time nonlinear system:

$$X(k+1) = \mathcal{F}(X(k), U(k)), \quad (5.23)$$

where $U(k) \in \mathbb{R}^p$ is the input vector, $X(k) \in \mathbb{R}^n$ is the state vector. $U(k)$ and $X(k)$ are known and \mathcal{F} is an unknown general nonlinear smooth function. To identify the nonlinear system, the state-space model of the modified Elman DRNN is given by:

$$\hat{X}(k+1) = A\hat{X}(k) + W^y(k)\Phi(W^x(k)\hat{X}(k) + W^uU(k)), \quad (5.24)$$

where $\hat{X}(k) \in \mathbb{R}^n$ represents the internal state of the modified Elman DRNN. The matrix $A \in \mathbb{R}^{n \times n}$ is a stable fixed and known matrix with the elements showing the auto-feedback connection gains. $W^x(k) \in \mathbb{R}^{n \times n}$, $W^u(k) \in \mathbb{R}^{n \times p}$ and $W^y(k) \in \mathbb{R}^{n \times n}$ represent the synaptic weights from the context layer to the hidden layer, from the input layer to hidden layer and from the hidden layer to the output layer, respectively. Also, Φ is an n-dimensional sigmoidal vector function $\Phi = [\Phi_1, \Phi_2, \dots, \Phi_n]^T$

that is given by:

$$\begin{aligned} \Phi(W^x(k)\hat{X}(k) + W^u(k)U(k)) = & [\Phi_1(\sum_{j=1}^n w_{1j}^x(k)\hat{x}_j(k) + \sum_{h=1}^p w_{1h}^u(k)u_h(k)), \\ & \Phi_2(\sum_{j=1}^n w_{2j}^x(k)\hat{x}_j(k) + \sum_{h=1}^p w_{2h}^u(k)u_h(k)), \dots, \\ & \Phi_n(\sum_{j=1}^n w_{nj}^x(k)\hat{x}_j(k) + \sum_{h=1}^p w_{nh}^u(k)u_h(k))]^T, \end{aligned} \quad (5.25)$$

where $\hat{x}_j(k)$ and $u_h(k)$ are the j^{th} and h^{th} elements of state and input vectors, respectively. The unknown nonlinear system in (5.23) can be written as follows:

$$X(k+1) = AX(k) + W^y(k)\Phi(W^x(k)X(k) + W^u(k)U(k)) + \eta(k), \quad (5.26)$$

where $\eta(k) = \mathcal{F}(X(k), U(k)) - AX(k) - W^y(k)\Phi(W^x(k)X(k) + W^u(k)U(k))$ is the modeling error with respect to the weights. The identification error $\eta(k)$ can be made sufficiently small by locating appropriate number of neurons in the hidden layer. The state-space model in (5.3) is similar to (5.23), in which the auto-feedback connections are removed.

Using the Taylor series approximation, the nonlinear term of (5.26) can be expressed around the equilibrium points $\bar{W}^x = W^x(0)$, $\bar{W}^u = W^u(0)$ and $\bar{W}^y = W^y(0)$. The weights deviations are also denoted as $\Delta W^y(k) = W^y(k) - \bar{W}^y$, $\Delta W^x(k) = W^x(k) - \bar{W}^x$ and $\Delta W^u(k) = W^u(k) - \bar{W}^u$. Specifically, we have

$$W^y(k)\Phi(W^x(k)X(k) + W^u(k)U(k)) = W^y(k)[\Phi_1, \Phi_2, \dots, \Phi_n]^T \quad (5.27)$$

where the Φ vector function elements are given by (5.25) in which the $\hat{x}_j(k)$ is replaced by $x_j(k)$. Using the following set of equations, it can easily be shown that the Taylor series can be expressed as:

$$\begin{aligned} W^y(k)\Phi(W^x(k)X(k) + W^u(k)U(k)) = & \bar{W}^y\Phi(\bar{W}^x X(k) \\ & + \bar{W}^u U(k)) + B^T(k)W(k) + \epsilon(k), \end{aligned} \quad (5.28)$$

where $B(k) = \begin{bmatrix} B^u(k) \\ B^x(k) \\ B^y(k) \end{bmatrix} \in \mathbb{R}^{(pn^2+n^3+n^2) \times n}$ and $W(k) = \begin{bmatrix} \theta^u(k) \\ \theta^x(k) \\ \theta^y(k) \end{bmatrix} \in \mathbb{R}^{(pn^2+n^3+n^2) \times 1}$

and $\epsilon(k)$ represents the higher order terms of the Taylor series. $B(k)$ is the scaling matrix of $W(k)$ as the parameter matrix showing the deviations of the network synaptic weights as follows:

$$\begin{aligned} \theta^u(k) &= [\mathcal{W}^u(k), \mathcal{W}^u(k), \dots, \mathcal{W}^u(k)]^T, \\ \theta^x(k) &= [\mathcal{W}^x(k), \mathcal{W}^x(k), \dots, \mathcal{W}^x(k)]^T, \\ \theta^y(k) &= [\Delta W_1^y(k), \Delta W_2^y(k), \dots, \Delta W_n^y(k)]^T, \end{aligned} \quad (5.29)$$

where $\mathcal{W}^u(k) = [\Delta W_1^u(k), \Delta W_2^u(k), \dots, \Delta W_i^u(k), \dots, \Delta W_n^u(k)]$, $\mathcal{W}^x(k) = [\Delta W_1^x(k), \Delta W_2^x(k), \dots, \Delta W_i^x(k), \dots, \Delta W_x^u(k)]$ in which $\Delta W_i^u(k)$, $\Delta W_i^x(k)$ and $\Delta W_i^y(k)$ are the i^{th} rows of the matrices $\Delta W^u(k)$, $\Delta W^x(k)$ and $\Delta W^y(k)$, respectively. Moreover, $\theta^u(k) \in \mathbb{R}^{pn^2 \times 1}$, $\theta^x(k) \in \mathbb{R}^{n^3 \times 1}$ and $\theta^y(k) \in \mathbb{R}^{n^2 \times 1}$. Note that the blocks of $B(k)$ are also given as follows:

$$\begin{aligned} B^u(k) &= \begin{bmatrix} B_1^u(k) & 0 & \dots & 0 \\ 0 & B_2^u(k) & \dots & 0 \\ \vdots & \vdots & \ddots & \vdots \\ 0 & 0 & \dots & B_n^u(k) \end{bmatrix}^T & B^x(k) &= \begin{bmatrix} B_1^x(k) & 0 & \dots & 0 \\ 0 & B_2^x(k) & \dots & 0 \\ \vdots & \vdots & \ddots & \vdots \\ 0 & 0 & \dots & B_n^x(k) \end{bmatrix}^T \\ B^y(k) &= \begin{bmatrix} B_1^y(k) & 0 & \dots & 0 \\ 0 & B_2^y(k) & \dots & 0 \\ \vdots & \vdots & \ddots & \vdots \\ 0 & 0 & \dots & B_n^y(k) \end{bmatrix}^T \end{aligned} \quad (5.30)$$

where $B^u(k) \in \mathbb{R}^{pn^2 \times n}$, $B^x(k) \in \mathbb{R}^{n^3 \times n}$ and $B^y(k) \in \mathbb{R}^{n^2 \times n}$. Also, their corresponding blocks are displayed as follows in which the sample time k is removed for

simplicity,

$$\begin{aligned}
B_i^u &= \left[\bar{w}_{i1}^y \Phi'_{\bar{W}_1^u} \text{diag}(U), \bar{w}_{i2}^y \Phi'_{\bar{W}_2^u} \text{diag}(U), \dots, \bar{w}_{ij}^y \Phi'_{\bar{W}_j^u} \text{diag}(U), \dots, \bar{w}_{in}^y \Phi'_{\bar{W}_n^u} \text{diag}(U) \right], \\
B_i^x &= \left[\bar{w}_{i1}^y \Phi'_{\bar{W}_1^x} \text{diag}(X), \bar{w}_{i2}^y \Phi'_{\bar{W}_2^x} \text{diag}(X), \dots, \bar{w}_{ij}^y \Phi'_{\bar{W}_j^x} \text{diag}(X), \dots, \bar{w}_{in}^y \Phi'_{\bar{W}_n^x} \text{diag}(X) \right], \\
B_i^y &= \left[\Phi_1(0), \Phi_2(0), \dots, \Phi_i(0), \dots, \Phi_n(0) \right]
\end{aligned} \tag{5.31}$$

where $i = 1, 2, \dots, n$. The $\text{diag}(X) \in \mathbb{R}^{n \times n}$ and $\text{diag}(U) \in \mathbb{R}^{p \times p}$ are diagonal matrices in which the diagonal elements are constructed by using X and U vector elements, respectively. Also, $\Phi'_{\bar{W}_j^u}$ and $\Phi'_{\bar{W}_j^x}$ are n and p -dimensional row vectors representing the partial derivatives of Φ with respect to the j^{th} rows of W^x and W^u matrices that are evaluated at their corresponding equilibrium points \bar{W}_j^u and \bar{W}_j^x , respectively. And \bar{w}_{ij}^y is the i^{th} row and j^{th} element of W^y that is evaluated at its corresponding equilibrium point. Moreover, $\Phi_i(0)$ denotes the i^{th} element of the matrix Φ in which all the weight matrices elements are replaced by their corresponding equilibrium points.

The Taylor series approximation is given in (5.28), where the unknown non-linear system (5.26) can be rewritten as follows:

$$\begin{aligned}
X(k+1) &= AX(k) + \bar{W}^y \Phi(\bar{W}^x X(k) + \bar{W}^u U(k)) \\
&\quad + B^T(k)W(k) + \epsilon(k) + \eta(k),
\end{aligned} \tag{5.32}$$

where $\varsigma_v(k) = \epsilon(k) + \eta(k)$ is the updated definition of the modeling error. Let us consider

$$Y(k) = B^T(k)W(k) + \varsigma_v(k), \tag{5.33}$$

where

$$Y(k) = X(k+1) - AX(k) - \bar{W}^y \Phi(\bar{W}^x X(k) + \bar{W}^u U(k)). \tag{5.34}$$

Now, we use the EKF to train the modified Elman DRNN weight parameters such that the identification error $e_x(k) = \hat{X}(k) - X(k)$ remains bounded.

The parameter matrix $W(k)$ is also modeled as $W(k+1) = W(k) + \varsigma_w(k)$, where $\varsigma_w(k) = [\varsigma_{w1}(k), \varsigma_{w2}(k), \dots, \varsigma_{wn}(k)]^T$ represents the process noise. Therefore, the weight parameters dynamic equations are given as follows:

$$\begin{aligned} W(k+1) &= W(k) + \varsigma_w(k), \\ Y(k) &= B^T(k)W(k) + \varsigma_v(k), \end{aligned} \quad (5.35)$$

$\varsigma_w(k)$ and $\varsigma_v(k)$ denote the process and measurement noise, respectively. It is assumed that the process and measurement noise are uncorrelated and their corresponding covariance matrices are Q and R , respectively. The equation (5.35) is the random walk model for the weight parameters in which the parameters are assumed to be unknown with a small random walk component to provide the adaptive estimation. The EKF which updates the weight parameters can be designed as follows:

$$\begin{aligned} \hat{W}(k+1) &= \hat{W}(k) + K(k)e_y(k), \\ \hat{Y}(k) &= B^T(k)\hat{W}(k), \\ e_y(k) &= Y(k) - \hat{Y}(k), \end{aligned} \quad (5.36)$$

where $\hat{Y}(k)$ is the estimated Kalman output and $K(k)$ is the Kalman gain. The parameter estimation error is defined as:

$$\tilde{W}(k) = W(k) - \hat{W}(k). \quad (5.37)$$

Using (5.35) and (5.37), the parameter estimation error dynamic can be expressed as:

$$\tilde{W}(k+1) = [I - K(k)B^T(k)]\tilde{W}(k) + \varsigma_w(k) - K(k)\varsigma_v(k). \quad (5.38)$$

The parameter estimation error covariance matrix is $P(k) \in \mathbb{R}^{(pn^2+n^3+n^2) \times (pn^2+n^3+n^2)}$ that can easily be defined as:

$$P(k) = E\{\tilde{W}(k)\tilde{W}^T(k)\} \quad (5.39)$$

Substituting (5.38) into (5.39) yields

$$\begin{aligned}
P(k+1) &= E\{\tilde{W}(k+1)\tilde{W}^T(k+1)\} \\
&= E\{[(I - K(k)B^T(k))\tilde{W}(k) + \varsigma_w(k) - K(k)\varsigma_v(k)] \\
&\quad \times [(I - K(k)B^T(k))\tilde{W}(k) + \varsigma_w(k) - K(k)\varsigma_v(k)]^T\} \\
&= (I - K(k)B^T(k))E\{\tilde{W}\tilde{W}^T(k)\}(I - K(k)B^T(k))^T + E\{\varsigma_w(k)\varsigma_w^T(k)\} \\
&\quad + K(k)E\{\varsigma_v(k)\varsigma_v^T(k)\}K^T(k) \\
&\quad + \text{cross-terms}(\tilde{W}(k), \varsigma_w(k), \varsigma_v(k)). \tag{5.40}
\end{aligned}$$

The cross-terms of $(\tilde{W}(k), \varsigma_w(k), \varsigma_v(k))$ are zero since they are independent. Therefore, $P(k+1)$ can be rewritten as follows:

$$\begin{aligned}
P(k+1) &= P(k) + Q - P(k)B(k)(R + B^T(k)P(k)B(k))^{-1}B^T(k)P(k) \\
&\quad + [K(k) - P(k)B(k)(R + B^T(k)P(k)B(k))^{-1}](R + B^T(k)P(k)B(k)) \\
&\quad [K(k) - P(k)B(k)(R + B^T(k)P(k)B(k))^{-1}]^T, \tag{5.41}
\end{aligned}$$

The $[\cdot](R + B^T(k)P(k)B(k))[\cdot]^T$, $P(k)$ and Q are positive semi-definite matrices. Therefore, to minimize $P(k+1)$, the term $K(k) - P(k)B(k)(R + B^T(k)P(k)B(k))^{-1}$ should be made equal to zero. Consequently, the Kalman filter gain is obtained as:

$$K(k) = P(k)B(k)(R + B^T(k)P(k)B(k))^{-1}. \tag{5.42}$$

Therefore, $P(k+1)$ becomes

$$\begin{aligned}
P(k+1) &= P(k) + Q - P(k)B(k)(R + B^T(k)P(k)B(k))^{-1}B^T(k)P(k) \\
&= Q + [I - K(k)B^T(k)]P(k) \tag{5.43}
\end{aligned}$$

The network parameters are trained by using the EKF algorithm that is developed in (5.36), (5.42) and (5.43). The Kalman error $e_y(k) = Y(k) - \hat{Y}(k)$ is not the same as the identification error $\hat{X}(k) - X(k)$, however they are minimized at the same time. It can easily be shown that

$$e_x(k+1) = Ae_x(k) + e_y(k). \tag{5.44}$$

Hence, it can be shown that for $k \geq 1$, $e_x(k) = A^k e_x(0) + \sum_{j=0}^{k-1} A^{k-j-1} e_y(j)$. Since $e_x(0)$ is constant and A is a stable matrix, the minimization of the Kalman error $e_y(j)$ implies that the upper bound of the identification error $e_x(k)$ is minimized as follows:

$$|e_x(k)| \leq |e_x(0)| + \sum_{j=0}^{k-1} |e_y(j)|. \quad (5.45)$$

It must be noted that in the EKF-based training algorithm, the learning rate is adjusted by $K(k)$ that is not always positive definite matrix and is also changed through the time. This is the main reason why the EKF-based training method has a faster convergence rate than the back propagation method. The speed of convergence can be increased by means of the Q adaptation law using the maximum likelihood method [90]. Moreover, note that the above convergence analysis can be applied to the standard Elman DRNN without auto-feedback connections with only slight modifications.

5.5 Simulation Results

In this section, different simulation cases are presented to investigate the efficiency and performance of our proposed hybrid FDI approach. For this purpose, the DRNN that is proposed in Section 5.2 is integrated with the bank of HKFs, as designed in Chapter 3, and the RKFs as designed in Chapter 4. In each experiment, different factors, namely the fault detection time, false alarm rate, accuracy and incorrect fault detection rate are investigated.

To perform simulations, two complete flight profiles are considered. The first flight profile (FP1) is used to simulate the hybrid scheme constituting the DRNN and a bank of HKFs and the second flight profile (FP2) is used to simulate the hybrid scheme constituting DRNN and a bank of RKF. The FP1 and FP2 that are respectively used in Chapters 3 and 4 are displayed in Figure 5.5. For each flight

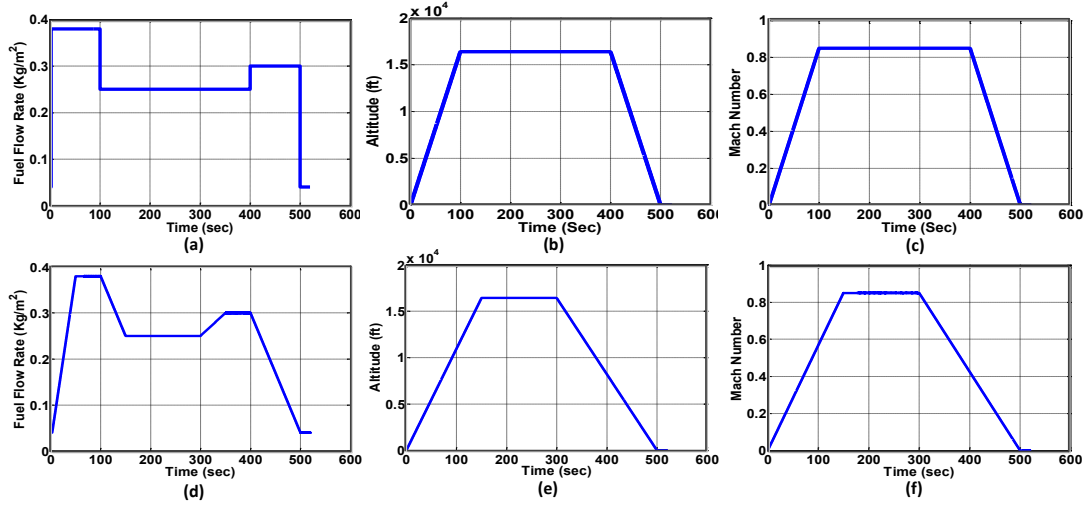


Figure 5.5: (a-c) FP1 fuel flow rate, altitude and Mach number, (d-f) FP2 fuel flow rate, altitude and Mach number.

profile the changes of the fuel flow rate, altitude and Mach number are displayed.

5.5.1 DRNN Training Process

To construct the online hybrid DRNN-HKF-based (HNNHKF) FDI scheme, first the DRNN has to be trained offline for the gas turbine engine with healthy sensors and different values of the health parameters degradations. During the training process, the network parameters are specified through the cost function minimization. The number of hidden neurons, number of epochs, the initial values for covariance matrices P , Q and R as well as the window size (truncation depth) constitute the set of parameters that have to be defined through the learning process. The overall structure of the proposed DRNN is displayed in Figure 5.6 including the input, context, hidden and output layers. The input and output nodes are set to 7 and 5, respectively. The input vector is constructed by augmenting the engine input (fuel mass flow rate), OBEM outputs as well as the bias term. The output vector also represents the estimated uncertainty effects associated with five sensor measurements.

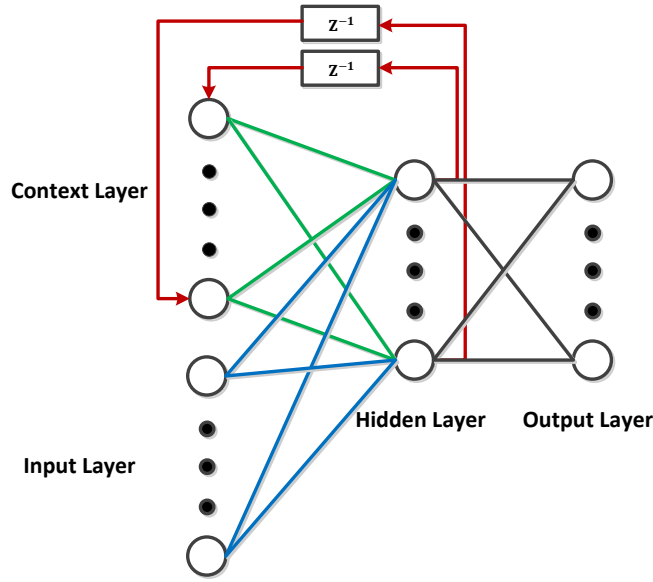


Figure 5.6: DRNN structure

As per explanations given in Section 5.2, the engine control input, OBEM outputs and actual engine sensor measurements construct the training data set that are assumed to be collected during the entire flight profile. The same set of nonlinear state space equations as used in (2.3) are used for both the actual engine and the OBEM. The actual engine and the OBEM are simulated for the flight profiles that are displayed in Figure 5.5. For more details regarding the engine dynamic equations, environmental parameters and ambient condition, refer to the descriptions in (2.3).

For our simulations, the OBEM operates at the healthy reference baselines of the engine health parameters, however the actual engine is degraded gradually due to the aging process during a set of flights. The process and measurement noise are respectively applied on ambient parameters and engine sensor measurements. Similar noise standard deviations as defined in Chapter 2 are used in this chapter. The associated process and measurement noise factors are $K_w = 0.2$ and $K_v = 1$. The DRNN is designed to approximate the corresponding differences between the actual engine sensor measurements and the OBEM outputs.

The learning process is performed by collecting the training and validation data and using the 5-fold cross-validation method. For this purpose, the FP1 and FP2 are simulated five times with respectively $\alpha_{\dot{m}_C} = 0.93$ and $\alpha_{\eta_C} = 0.965$ as well as $\alpha_{\dot{m}_C} = 0.82$ and $\alpha_{\eta_C} = 0.91$. The engine control input, OBEM outputs and the engine sensor measurements are recorded to construct the training and the validation data sets. The data is generated for different values of the health parameters degradations. Note that the health parameters degradations are the ones for which the previously HKF and RKF based FDI schemes generate many false alarms. The initial values of the other parameters are also set as: $\text{Diag}(P) = 100$, $\text{Diag}(Q) = 0.000001$, $\text{Diag}(R) = 10$ and $h = 10$.

The first step of the learning process is to define the number of hidden neurons. As per (5.5), the mean square error (MSE) is computed for the DRNN with various number of hidden neurons. Figure 5.7 displays the trends of the mean square errors corresponding to the training and validation data in terms of the hidden neurons number for both FP1 and FP2. To obtain these errors, four flights data are considered as the training set and the last one is used as the validation data. The 5-fold cross-validation is used and finally the average of MSEs associated to five clusters of training and validation data are measured. The simulations are performed for 10 epochs.

Using Figure 5.7, the proper number of hidden neurons are determined for both FP1 and FP2. The neurons are set to the number for which the training and validation errors are started to be almost fixed or increased, otherwise the DRNN will be over-trained and the network generalization ability will be diminished. In our simulation studies, the proper number of hidden neurons that are determined for FP1 and FP2 are 6 and 5, respectively.

The second step is to determine the number of epochs. An epoch is a single

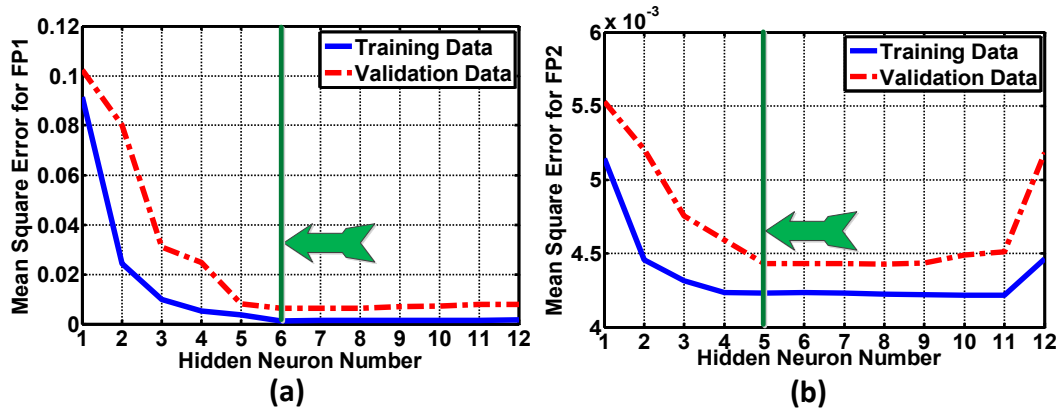


Figure 5.7: (a) Average of MSEs for five clusters of training and validation data, for (a) FP1 under $\alpha_{m_C} = 0.93$ and $\alpha_{\eta_C} = 0.965$, and (b) FP2, under $\alpha_{m_C} = 0.82$ and $\alpha_{\eta_C} = 0.91$, versus the number of hidden neurons.

pass through the entire training set, followed by testing of the validation set. Figure 5.8 displays the trends of the mean square errors corresponding to the training and validation data in terms of the number of epochs for both the FP1 and FP2. Similarly, the 5-fold cross-validation method is used and finally the average of MSEs associated to five clusters of training and validation data are measured. The corresponding DRNNs are simulated with the best number of hidden neurons that are obtained in Figure 5.7.

Using Figure 5.8, the proper number of epochs are determined for both FP1 and FP2, that are equal to 9 and 11, respectively. The higher number of epochs does not necessarily improve the DRNNs performance.

In the last step, similar simulations are also performed to determine the other DRNN parameters. The same 5-fold cross-validation is used to determine the proper sets of parameters that lead to minimum MSE values associated to FP1 and FP2. Table 5.1 displays the other parameters for the two DRNNs that are trained for FP1 and FP2.

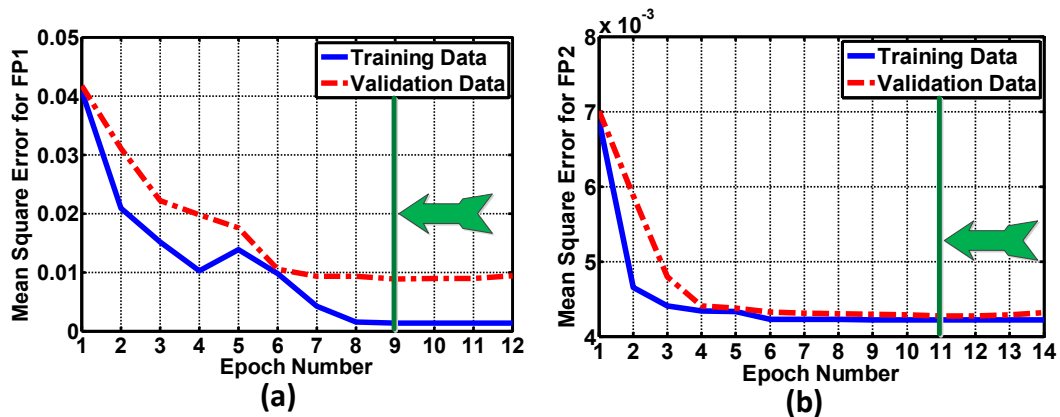


Figure 5.8: (a) Average of MSEs for five clusters of training and validation data, for (a) FP1 under $\alpha_{m_C} = 0.93$ and $\alpha_{\eta_C} = 0.965$, and (b) FP2 under $\alpha_{m_C} = 0.82$ and $\alpha_{\eta_C} = 0.91$ versus the number of epochs.

Table 5.1: The network parameters that are determined during the DRNNs trainings associated with FP1 and FP2, respectively.

Flight Profile	Diag(P)	Diag(Q)	Diag(R)	h
FP1	160	0.000001	10	6
FP2	140	0.000001	10	10

5.5.2 DRNN Integration with Bank of Hybrid Kalman Filters

In this section, the DRNN that is trained for FP1 in the preceding section is integrated with a bank of HKFs to construct the hybrid DRNN-HKF-based FDI scheme. The bank of HKFs are previously developed in Chapter 3 for different healthy and faulty sensor scenarios. As per the simulation studies in Chapter 3, the bank of HKFs are intuitively robust with respect to certain limited engine health parameters degradation. However, for higher values of the degradation, false alarms will occur. In this chapter, it is expected to improve the robustness by integrating the DRNN with the bank of HKFs as displayed in Figure 5.1.

In the following subsections, various case studies are simulated to investigate and demonstrate the advantages of our proposed hybrid DRNN-HKF-based

(HNNHKF) FDI scheme performance as compared to multiple HKF-based FDI scheme that is designed in Chapter 3 in terms of fault promptness detection, fault estimation accuracy, false alarms and incorrect fault detection rates. It must also be noted that, similar to the previous chapters, the multiple-model scheme is utilized to detect and isolate sensor faults. Three simulation case studies are conducted in this section as summarized below:

- **Case (a.1):** To evaluate the robustness of our proposed hybrid MM-based FDI method, the engine model in (5.4) is simulated without a sensor fault but with compressor health degradations as well as the process and measurement noise during the entire FP1. Our objective is to compare the false alarm rates and estimation accuracy between our proposed hybrid DRNN-HKF-based FDI scheme and the multiple HKF-based FDI scheme that is proposed in Chapter 3. For this purpose, different levels of degradation as well as the disturbance noise are applied to the actual engine.
- **Case(b.1):** To evaluate the effectiveness of our proposed hybrid DRNN-HKF-based FDI scheme, the engine model in (5.4) is simulated with a 3% single sensor bias fault that occurs at different stages of the flight profile namely at climbing, cruise and landing. The multiple-model structure is developed for 3% pre-determined sensor bias fault. The compressor health parameters degradations are set to $\alpha_{m_c} = 0.93$ and $\alpha_{\eta_c} = 0.965$. Our objective is to compare the fault detection time, FDI accuracy and incorrect fault detection rates for 3% single sensor fault that may occur at different states of FP1.
- **Case (c.1):** To evaluate the effectiveness of our proposed hybrid DRNN-HKF-based FDI scheme, the engine model in (5.4) is simulated with a single sensor bias fault with various severities that occur at different stages of FP1. Our objective is to investigate the fault detection times in terms of sensor fault

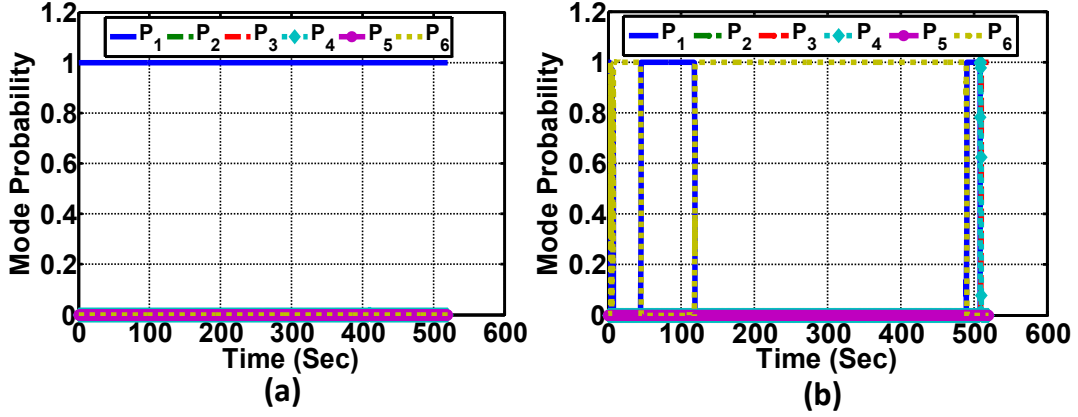


Figure 5.9: Mode probabilities for healthy sensors for the engine with $\alpha_{m_C} = 0.93$ and $\alpha_{\eta_C} = 0.965$ during FP1 using the (a) hybrid DRNN-HKF-based FDI scheme, and (b) multiple HKF-based FDI scheme.

severities as well as to obtain the maximum bias fault than can be detected in less than 20 seconds using the same MM structure that is constructed for 3% pre-determined fault and the DRNN that is previously trained for FP1.

Case (a.1): False Alarm and Estimation Accuracy Evaluation

In this case study simulation, no fault is applied to the actual engine sensors, hence the mode probability corresponding to the healthy sensor should be approximately close to one and other probabilities associated with the faulty sensor modes should be all almost close to zero. Figure 5.9 provides a comparison between the mode probabilities for healthy sensors that are generated by our proposed hybrid DRNN-HKF-based FDI scheme and the multiple HKF-based FDI scheme that is designed in Chapter 3.

Figure 5.9 demonstrates the robustness of our proposed hybrid FDI approach as compared to the multiple HKF-based FDI scheme. The latter one generates many false alarms for the healthy engine due to effects of compressor health degradation. In another experiment, the metric known as the weighted mean absolute percentage error (WMAPE) is calculated for all the engine outputs during the entire FP1 as

defined in (4.46).

To compare the estimation accuracy of our proposed hybrid DRNN-HKF-based FDI method with that of multiple HKF-based FDI scheme, the WMAPE% is calculated for the engine healthy sensor measurements in presence of various percentages of the compressor health parameters degradation during the entire FP1. Moreover, the effects of different noise factors, associated with the process and measurement noise, on WMAPE% are investigated. The results are provided in Table 5.2.

According to Table 5.2, for both FDI schemes, the estimation error does increase by enhancing either the health degradation level or process and measurement noise factors, however our proposed hybrid DRNN-HKF-based FDI scheme is still more accurate than the multiple HKF-based FDI scheme that is proposed in Chapter 3. The higher estimation error may lead to false alarms generation if either the process and measurement noise levels or the health degradation levels are increased.

To investigate the false alarms rates corresponding to hybrid and multiple HKF-based FDI schemes, confusion matrices are obtained through increasing the level of noise and parameter uncertainty associated with 50 Monte Carlo simulation runs. The results are shown in Table 5.3. It must be noted that true positive (TP) is associated to cases where the healthy sensors are diagnosed healthy and false positive (FP) is associated to healthy cases in which a false alarm is generated due to non-fault related factors. Therefore, false alarm rate (FAR) can be computed according to $FAR = \frac{FP}{TP+FP}$.

The process and measurement noise factors are changed in the first three rows of Table 5.3, and the compressor health degradation level is only changed in the last three rows. It follows from Table 5.3 that our proposed hybrid DRNN-HKF-based FDI method generates significantly lower false alarm rates as compared to the multiple HKF-based method. Note that although the DRNN is trained for

Table 5.2: Comparison of the WMAPE% by using the HNNHKF and MHKF based FDI schemes in presence of different compressor health degradation levels and process and measurement noise factors for the engine healthy sensors scenario during the entire FPI.

Scenarios	Weighted Mean Absolute Percentage Error %															
	T_T				P_C				N				T_T			
	HNNHKF	MHKF	HNNHKF	MHKF	HNNHKF	MHKF	HNNHKF	MHKF	HNNHKF	MHKF	HNNHKF	MHKF	HNNHKF	MHKF		
$K_w = 0.2$	0.9369	1.5421	0.5948	0.6444	0.6939	7.7578	0.3382	0.4519	0.0287	0.1459	0.0287	0.0287	0.0287			
$K_v = 1$	0.6600	1.5968	0.5468	1.4205	0.6958	8.0781	0.4276	0.938	0.0302	0.5596	0.0302	0.0302	0.0302			
$K_v = 1.5$	0.9202	1.6333	0.5335	1.7277	0.6947	7.9205	0.4181	1.1245	0.0341	0.7674	0.0341	0.0341	0.0341			
$K_v = 2$	0.9401	1.7690	0.6568	0.6969	0.7551	6.5461	0.3724	0.5162	0.0235	0.1827	0.0235	0.0235	0.0235			
$\alpha_{\eta_C} = 0.96$	1.0285	2.2232	0.7852	0.8021	0.8846	7.2863	0.4407	0.6497	0.0276	0.2549	0.0276	0.0276	0.0276			
$\alpha_{\eta_C} = 0.95$	1.2063	2.9750	0.9963	1.0109	1.0966	7.6064	0.5651	0.8861	0.0283	0.4112	0.0283	0.0283	0.0283			
$\alpha_{\eta_C} = 0.935$																

Table 5.3: True positives (TP), false positives (FP) and false alarm rates (FAR) that are obtained for HNNHKF and MHKF based FDI methods if either the K_w and K_v for the process and measurement noise or the compressor health degradation is increased.

Scenario	TP		FP		FAR	
	HNNHKF	MHKF	HNNHKF	MHKF	HNNHKF	MHKF
$K_w = 0.2 \quad K_v = 1$	50	3	0	47	0	0.94
$K_w = 0.5 \quad K_v = 1.5$	50	1	0	49	0	0.98
$K_w = 1 \quad K_v = 2$	48	0	2	50	0.04	1.00
$\alpha_{\dot{m}_C} = 0.92 \quad \alpha_{\eta_C} = 0.96$	50	2	0	48	0	0.96
$\alpha_{\dot{m}_C} = 0.90 \quad \alpha_{\eta_C} = 0.95$	48	0	2	50	0.04	1.00
$\alpha_{\dot{m}_C} = 0.87 \quad \alpha_{\eta_C} = 0.935$	47	0	3	50	0.06	1.00

$\alpha_{\dot{m}_C} = 0.93$ and $\alpha_{\eta_C} = 0.965$, the FAR is still sufficiently low for higher health degradation magnitudes.

Case (b.1): A 3% Sensor Bias Fault Detection and Isolation

In this section, the fault detection time (FDT) is measured for the 3% single sensor bias fault that occurs in different modes of FP1 including the climbing, cruise and landing. Similar to Chapter 3, the MM scheme is used to calculate the probabilities associated with the derived healthy and faulty models to evaluate the maximum probability and to detect and isolate the single sensor fault. The MM scheme is constructed for the pre-determined bias faults with the severity of 3% of the engine steady-state output values under cruise condition.

Table 5.4 shows the fault detection times for different 3% single sensor fault scenarios at different stages of the flight profile. It also compares the FDTs that are obtained by using our proposed hybrid DRNN-HKF-based FDI scheme with that generated by the multiple HKF-based FDI scheme. To show the capability of our proposed hybrid FDI schemes, the sensor fault is injected at $k_f = 50$ sec during the climbing mode, at $k_f = 250$ sec during the cruise mode and at $k_f = 450$ sec during the landing mode. Note that the degradation factors associated with the compressor health parameters are set to $\alpha_{\dot{m}_C} = 0.93$ and $\alpha_{\eta_C} = 0.965$.

Table 5.4: Comparison of FDTs between the HNNHKF and MHKF based FDI schemes associated with a single 3% sensor bias fault that occurs at different stages of FP1 with $\alpha_{m_C} = 0.93$ and $\alpha_{\eta_C} = 0.965$. (\times) denotes incorrect fault detection cases and ($*$) denotes false alarms and/or incorrect fault detections besides the correctly detected fault.

Faulty Scenario	FDI Method	Sensor FDT (sec)		
		$k_f = 50$	$k_f = 250$	$k_f = 450$
Fault on T_C	HNNHKF	63.3	5.2	49.7
	MHKF	405.9	10*	36.8
Fault on P_C	HNNHKF	38.2	3.9	16.8
	MHKF	437.6	251.9*	23.4*
Fault on N	HNNHKF	43	3.6	17.5
	MHKF	454.5*	254.5*	52*
Fault on T_T	HNNHKF	51.1	8.7	32.8
	MHKF	\times	\times	\times
Fault on P_T	HNNHKF	49.8	3.3	19.2
	MHKF	57.8	39.2	25.1*

By comparing the results in Table 5.4, it can be concluded that the sensor fault detection times during the cruise mode are much less than that of the other flight modes since there are fewer variations of thrust and ambient conditions. In spite of a large input and ambient condition variations during the climbing and the landing modes, it is still possible to detect a sensor fault by applying our proposed hybrid DRNN-HKF-based FDI scheme.

In addition, Figures 5.10, 5.11 and 5.12 depict the mode probabilities for three selected fault scenarios when the bias fault occurs at different instants of the flight profile. The value of the injected fault is set to 3% of the engine steady-state output value, while the degradation factors associated with the compressor health parameters are set to $\alpha_{m_C} = 0.93$ and $\alpha_{\eta_C} = 0.965$. As per Figures 5.10, 5.11 and 5.12, our proposed DRNN-HKF-based FDI scheme is capable of detecting and isolating different sensor faults that occur during the entire flight mode within a certain limited time delay, however the multiple HKF-based FDI scheme generates many false alarms before the occurrence of a fault and detects various incorrect faults instead of the one that occurs.

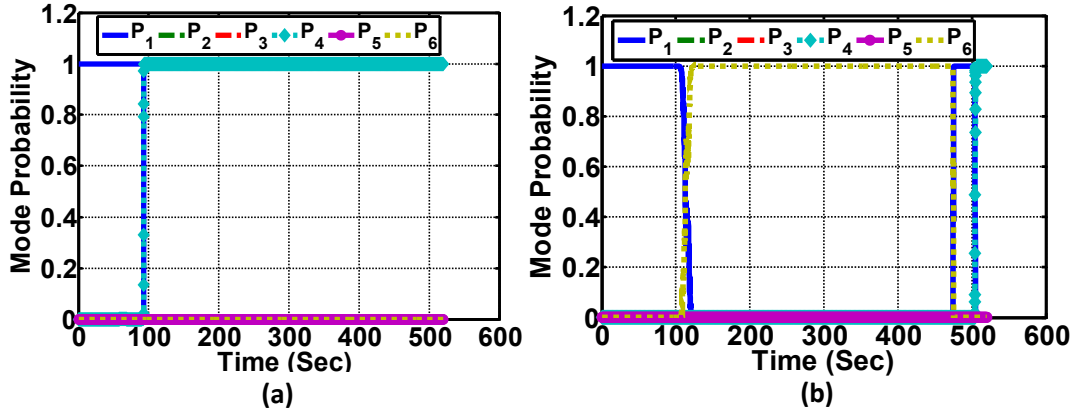


Figure 5.10: Mode probabilities generated by (a) our proposed hybrid DRNN-HKF-based FDI scheme and (b) multiple HKF-based FDI scheme, for 3% bias fault applied at $k_f = 50$ sec to the N sensor with $\alpha_{m_C} = 0.93$ and $\alpha_{\eta_C} = 0.965$.

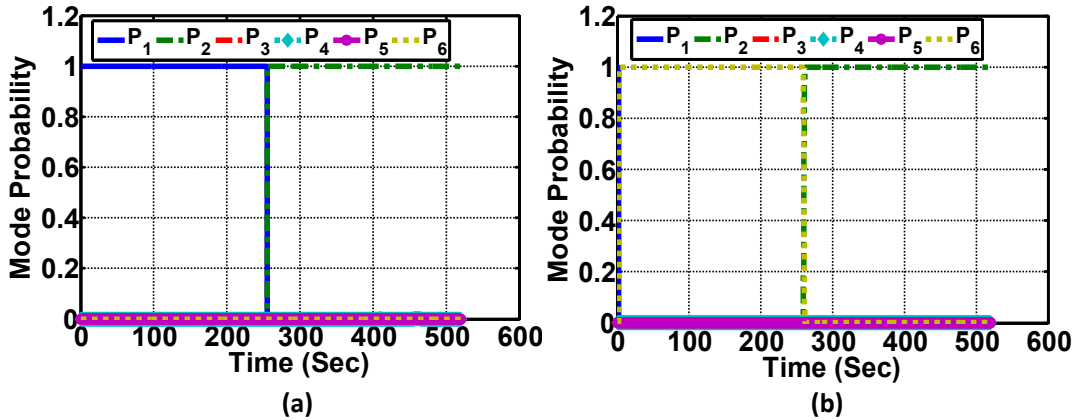


Figure 5.11: Mode probabilities generated by (a) our proposed hybrid DRNN-HKF-based FDI scheme and (b) multiple HKF-based FDI scheme, for 3% bias fault applied at $k_f = 250$ sec to the T_C sensor with $\alpha_{m_C} = 0.93$ and $\alpha_{\eta_C} = 0.965$.

To quantify the effectiveness and reliability of our proposed hybrid DRNN-HKF-based FDI scheme, two confusion matrices (CM) are obtained in which either the compressor health degradation magnitude or disturbance noise factor is increased. For this purpose, 50 Monte Carlo simulations are performed. The first confusion matrix corresponding to $\alpha_{m_C} = 0.90$ and $\alpha_{\eta_C} = 0.95$ is displayed in Table 5.5. The second one is corresponding to $K_w = 0.5$ and $K_v = 1.5$ that is displayed in Table 5.6.

Table 5.5: The confusion matrix that is obtained for hybrid DRNN-HKF-based FDI scheme for 3% single sensor bias fault that is applied to the engine under $\alpha_{r_{m_C}} = 0.90$ and $\alpha_{\eta_C} = 0.95$.

CM1	T_C	P_C	N	T_T	P_T	No Fault
T_C	50	0	0	0	0	0
P_C	0	50	0	0	0	0
N	0	0	50	0	0	0
T_T	5	0	3	40	2	0
P_T	5	0	0	0	45	0
No Fault	2	0	0	0	0	48

Table 5.6: The confusion matrix that is obtained for hybrid DRNN-HKF-based FDI scheme for 3% single sensor bias fault that is applied to the engine under $K_w = 0.5$ and $K_v = 1.5$.

CM2	T_C	P_C	N	T_T	P_T	No Fault
T_C	50	0	0	0	0	0
P_C	0	50	0	0	0	0
N	0	0	50	0	0	0
T_T	2	0	0	43	5	0
P_T	3	0	0	0	47	0
No Fault	0	0	0	0	0	50

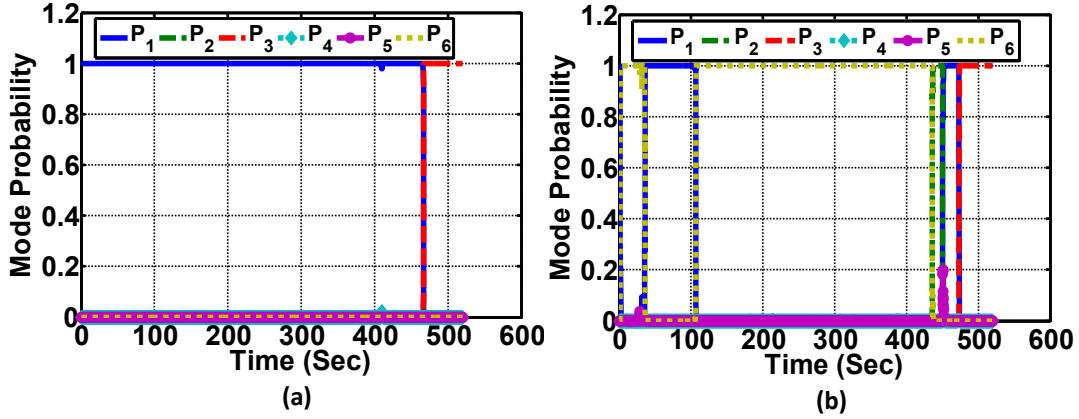


Figure 5.12: Mode probabilities generated by (a) our proposed hybrid DRNN-HKF-based FDI scheme and (b) multiple HKF-based FDI scheme, for 3% bias fault applied at $k_f = 450$ sec to the P_C sensor with $\alpha_{m_c} = 0.93$ and $\alpha_{\eta_c} = 0.965$.

Table 5.7: Hybrid DRNN-HKF-based Sensor FDI algorithm performance indices corresponding to different levels of uncertainties.

Scenarios	FPR	ACC	IFDR
$K_w = 0.2 \quad K_v = 1$	0	1	0
$K_w = 0.5 \quad K_v = 1.5$	0	0.967	0.04
$\alpha_{m_c} = 0.93 \quad \alpha_{\eta_c} = 0.965$	0	1	0
$\alpha_{m_c} = 0.90 \quad \alpha_{\eta_c} = 0.943$	0.04	0.95	0.06

According to our simulations, the initial impact of any increase in either the noise factors or the engine health degradation magnitudes is to delay the fault detection time. Moreover, the occurrence of false alarms and incorrect fault detections are the other consequences due to increases in the above uncertainty sources. Different performance indices can be defined to quantify the robustness of our proposed hybrid DRNN-HKF-based sensor FDI algorithm with respect to the levels of uncertainty sources. False positive (false alarm) rate (FPR), accuracy (ACC) and incorrect fault detection rate (IFDR) are the indices defined in (3.31) and are computed in Table 5.7 for our proposed hybrid DRNN-HKF-based FDI scheme to investigate the effects of various uncertainty sources.

According to Table 5.7, increasing the levels of uncertainty sources results in

decrease of ACC, but increase in FPR and IFDR. Notwithstanding these observations, our proposed hybrid DRNN-HKF-based FDI scheme still works sufficiently robust with respect to engine health degradation as well as the process and measurement noise, particularly as compared to the previously developed MHKF-based FDI scheme which is a totally model-based structure.

Case (c.1): Sensor Fault Detection and Isolation for Different Fault Severities

In real applications, there is no guarantee that the sensor bias fault severity always matches the 3% pre-determined fault for which the MM structure is designed. Therefore, it is essential to investigate the performance of our proposed hybrid DRNN-HKF-based FDI scheme for an applied sensor bias fault having different severities starting from the minimum detectable bias. Table 5.8 shows the detection times for all faulty modes as a function of the fault severities, when the applied faults occur during the cruise mode of FP1 with also $\alpha_{\dot{m}_C} = 0.93$ and $\alpha_{\eta_C} = 0.965$.

It can be observed from Table 5.8 that the higher the fault severity with respect to the pre-determined 3% fault, the later the detection time, given that the actual fault becomes further different from the pre-determined bias fault. Note that the minimum detectable sensor bias fault is 2% that requires larger time to be detected as compared to the higher fault severities.

Table 5.8: The sensor fault detection times for all fault modes as a function of the fault severity during the cruise of FP1, with $\alpha_{\dot{m}_C} = 0.93$ and $\alpha_{\eta_C} = 0.965$.

Fault Time	2%	3%	4%	5%	6%
T_C	5.3	5.2	5.3	7.4	9.2
P_C	27.4	3.9	7.7	15.8	33.1
N	31.6	3.6	2.5	6	13.1
T_T	40.9	8.7	12.5	19.8	45.6
P_T	11.3	3.3	3.6	3.9	4.7

It should be pointed out that our proposed hybrid DRNN-HKF-based structure

Table 5.9: The maximum sensor bias fault (as percentage of the engine steady-state outputs) that can be detected in less than 20 seconds during the cruise mode of FP1 by using our proposed hybrid DRNN-HKF-based FDI scheme under $\alpha_{\dot{m}_C} = 0.93$ and $\alpha_{\eta_C} = 0.965$.

Sensor Fault	T_C	P_C	N	T_T	P_T
Maximum Detectable Fault%	37	5.8	10	5	20

is designed for a 3% sensor bias fault and is not capable of detecting and isolating sensor bias faults that have far greater severities. For this purpose, Table 5.9 shows the maximum sensor bias faults that are detectable in less than 20 seconds by using our proposed hybrid DRNN-HKF-based FDI scheme under $\alpha_{\dot{m}_C} = 0.93$ and $\alpha_{\eta_C} = 0.965$. The reported fault severities in Table 5.9 are obtained for the cruise mode of FP1. However, if an applied sensor bias fault increases far beyond the corresponding maximum detectable fault as indicated in Table 5.9, an incorrect fault may be detected. Therefore, it is recommended that one incorporates more models within the MM-based structure corresponding to higher pre-determined sensor faults to become capable of detecting and isolating faults with higher magnitudes in shorter durations of time.

5.5.3 DRNN Integration with a Bank of Robust Kalman Filters

In this section, the DRNN that is trained for FP2 in Section 5.5.1 is integrated with a bank of RKFs to construct the hybrid DRNN-RKF-based FDI scheme. The bank of RKFs are previously developed in Chapter 4 for different healthy and faulty sensor scenarios. As per the derivations in Chapter 4, the RKF is formally designed to be robust with respect to compressor health degradation with $\alpha_{\dot{m}_C} = 0.95$ and $\alpha_{\eta_C} = 0.975$. However, a risk of a false alarm is increased for higher engine degradation magnitudes. In this section, the DRNN is combined with the previously designed bank of RKFs to investigate the robustness with respect to engine health parameters

degradations.

In the following subsection, various case studies similar to those in the preceding section are performed to investigate the pros and cons of our proposed hybrid DRNN-RKF-based (HNNRKF) FDI scheme as compared to multiple RKF-based FDI scheme that is designed in Chapter 4 in terms of fault promptness detection, fault estimation accuracy, false alarms and incorrect fault detection rates. The single-layer multiple-model approach is also utilized as explained in Chapter 4. Three simulation case studies are conducted in this section as summarized below:

- **Case (a.2):** To evaluate the robustness of our proposed hybrid DRNN-RKF-based FDI method, the engine model in (5.4) is simulated without a sensor fault but with compressor health degradations as well as the process and measurement noise during the entire FP2. Our objective is to compare the false alarm rates and estimation accuracy between our proposed hybrid DRNN-RKF-based FDI scheme and the multiple RKF-based FDI scheme that is proposed in Chapter 4. For this purpose, different levels of degradation as well as the disturbance noise are applied to the actual engine.
- **Case(b.2):** To evaluate the effectiveness of our proposed hybrid DRNN-RKF-based FDI scheme, the engine model in (5.4) is simulated with a 3% single sensor bias fault that occurs at different stages of the flight profile namely at climbing, cruise and landing. The multiple-model structure is developed for 3% pre-determined sensor bias fault. The compressor health parameters degradation are set to $\alpha_{m_C} = 0.82$ and $\alpha_{\eta_C} = 0.91$. Our objective is to compare the fault detection time, hybrid FDI accuracy and incorrect fault detection rates for 3% single sensor fault that may occur at different stages of FP2.

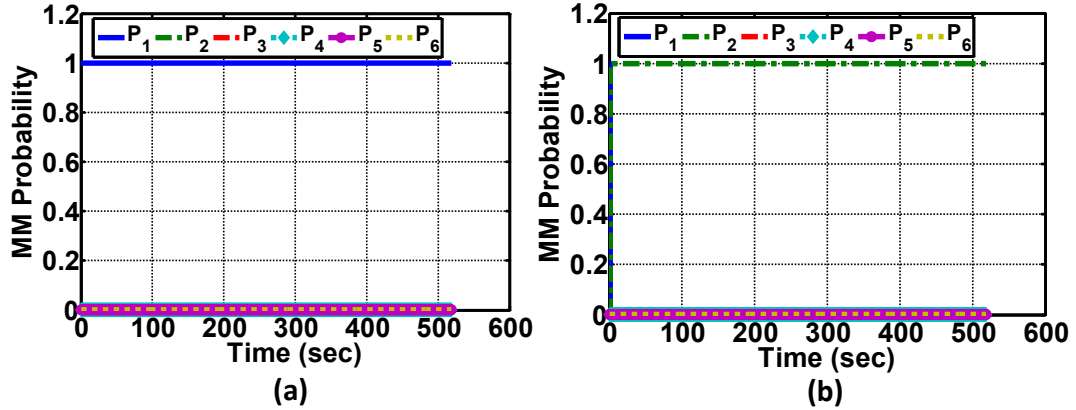


Figure 5.13: Mode probabilities for healthy sensors for the engine with $\alpha_{m_C} = 0.82$ and $\alpha_{\eta_C} = 0.91$ during FP2 using the (a) hybrid DRNN-RKF-based FDI scheme, and (b) multiple RKF-based FDI scheme.

- **Case (c.2):** To evaluate the effectiveness of our proposed hybrid DRNN-RKF-based FDI scheme, the engine model in (5.4) is simulated with a single sensor bias fault with various severities that occur at different stages of FP2. Our objective is to investigate the fault detection times in terms of sensor fault severities as well as to obtain the maximum bias fault than can be detected in less than 20 seconds using the same single-layer MM structure that is constructed for 3% pre-determined fault and the DRNN that is previously trained for FP2.

Case (a.2): False Alarm and Estimation Accuracy Evaluation

In this case study simulation, no fault is applied to the actual engine sensors. Figure 5.13 provides a comparison between the mode probabilities for healthy sensors that are generated by our proposed hybrid DRNN-RKF-based FDI scheme and the multiple RKF-based FDI scheme that is designed in Chapter 4.

The Figure 5.13 demonstrates the robustness of our proposed hybrid FDI approach as compared to the multiple RKF-based FDI scheme. The latter one generates a false alarm for the healthy engine due to the effects of compressor health

degradation. In another experiment, the WMAPE is calculated for all the engine outputs during the entire FP2 as defined in (4.46).

To compare the estimation accuracy of our proposed hybrid DRNN-RKF-based FDI method with that of multiple RKF-based FDI scheme, the WMAPE% is calculated for the engine healthy sensor measurements in presence of various percentages of the compressor health parameters degradation during the entire FP2. Moreover, the effects of different noise factors on WMAPE%, associated to the process and measurement noise are investigated. The results are provided in Table 5.10.

According to Table 5.10, for both FDI schemes, the estimation error does increase by enhancing either the health degradation level or the process and measurement noise factors, however our proposed hybrid DRNN-RKF-based FDI scheme is still more accurate than the multiple RKF-based FDI scheme.

To investigate the false alarm rates corresponding to hybrid and multiple RKF-based FDI schemes, confusion matrices are obtained through increasing the level of noise and parameter uncertainty associated with 50 Monte Carlo simulation runs. The results are shown in Table 5.11.

The process and measurement noise factors are changed in the first three rows of Table 5.11, and the compressor health degradation level is only changed in the last three rows. It follows from Table 5.11 that our proposed hybrid DRNN-RKF-based FDI method generates significantly lower false alarm rates as compared to the multiple HKF-based method. Note that although the DRNN is trained for $\alpha_{\dot{m}_C} = 0.82$ and $\alpha_{\eta_C} = 0.91$, the FAR is still sufficiently low for higher health degradation magnitudes.

Table 5.10: Comparison of the WMAPE% by using the HNNRKF and MRKF based FDI schemes in presence of different compressor health degradation levels and process and measurement noise factors for the engine healthy sensors scenario.

Scenarios	Weighted Mean Absolute Percentage Error %													
	T_T			P_C			N			T_T			P_T	
	HNNRKF	MRKF	HNNRKF	HNNRKF	MRKF	MRKF	HNNRKF	MRKF	HNNRKF	MRKF	HNNRKF	MRKF	HNNRKF	MRKF
$K_w = 0.2$	2.0411	4.8896	2.4226	3.7330	0.0019	0.0255	0.3545	0.4544	3.3010	3.9648	3.3010	3.3010	3.3010	3.9648
$K_w = 0.5$	2.2491	4.9085	3.0236	3.7495	0.0033	0.0256	0.4598	0.5216	3.3121	5.5069	3.3121	3.3121	3.3121	5.5069
$K_w = 1$	2.3523	4.9457	3.4034	3.7950	0.0078	0.0257	0.4718	0.5962	3.3226	7.3145	3.3226	3.3226	3.3226	7.3145
$\alpha_{\eta_C} = 0.81$	2.4950	5.1938	3.6646	3.8672	0.0011	0.0249	0.4170	0.6386	3.6828	3.9779	3.6828	3.6828	3.6828	3.9779
$\alpha_{\eta_C} = 0.8$	2.6362	5.5037	3.9257	3.9998	0.0015	0.0253	0.4374	0.6805	3.9949	4.0825	0.6805	0.6805	3.9949	4.0825
$\alpha_{\eta_C} = 0.78$	2.9480	6.1431	4.2717	4.4980	0.0017	0.0255	0.4467	0.7736	4.0405	4.9282	0.7736	0.7736	4.0405	4.9282

Table 5.11: TP, FP and FAR that are obtained for HNNRKF and MRKF based FDI methods if either the K_w and K_v for the process and measurement noise or the compressor health degradation is increased.

Scenario	TP		FP		FAR	
	HNNRKF	MRKF	HNNRKF	MRKF	HNNRKF	MRKF
$K_w = 0.2$ $K_v = 1$	50	1	0	49	0	0.98
$K_w = 0.5$ $K_v = 1.5$	48	0	2	50	0.04	1.00
$K_w = 1$ $K_v = 2$	45	0	5	50	0.1	1.00
$\alpha_{\dot{m}_C} = 0.81$ $\alpha_{\eta_C} = 0.905$	50	0	0	50	0	1.00
$\alpha_{\dot{m}_C} = 0.8$ $\alpha_{\eta_C} = 0.9$	45	0	5	50	0.1	1.00
$\alpha_{\dot{m}_C} = 0.78$ $\alpha_{\eta_C} = 0.989$	43	0	7	50	0.14	1.00

Case (b.2): A 3% Sensor Bias Fault Detection and Isolation

In this section, the FDT is measured for the 3% single sensor bias fault that occurs in different modes of FP2 including the climbing, cruise and landing. The MM scheme is constructed for the pre-determined bias faults with the severity of 3% of the engine steady-state output values under cruise condition.

Table 5.12 shows the fault detection times for each 3% single sensor fault scenario at different stages of the flight profile. It also compares the FDTs that are obtained by using our proposed hybrid DRNN-RKF-based FDI scheme with that generated by the multiple RKF-based FDI scheme. To show the capability of our proposed FDI schemes, the sensor fault is injected at $k_f = 50$ sec during the climbing mode, at $k_f = 250$ sec during the cruise mode and at $k_f = 450$ sec during the landing mode. Note that the degradation factors associated to the compressor health parameters are set to $\alpha_{\dot{m}_C} = 0.82$ and $\alpha_{\eta_C} = 0.91$.

By comparing the results in Table 5.12, it can be concluded that the sensor fault detection times during the cruise mode are much less than that of the other flight modes since there is less variation of thrust and ambient conditions. In spite of a large input and ambient condition variations during the climbing and the landing modes, it is still possible to detect a sensor fault by applying our proposed hybrid DRNN-RKF-based FDI scheme.

Table 5.12: Comparison of FDTs between the HNNRKF and MRKF based FDI schemes associated with a single 3% sensor bias fault that occurs at different stages of FP2 with $\alpha_{m_C} = 0.82$ and $\alpha_{\eta_C} = 0.91$. (\times) denotes not detectable fault and (*) denotes false alarms and/or incorrect fault detections besides the correct fault detection.

Faulty Scenario	FDI Method	Sensor FDT (sec)		
		$k_f = 50$	$k_f = 250$	$k_f = 450$
Fault on T_C	HNNRKF	89.2	6.1	53.7
	MRKF	368.4*	21.1*	24.9
Fault on P_C	HNNRKF	47.5	5.3	23
	MRKF	\times	\times	\times
Fault on N	HNNRKF	\times	\times	\times
	MRKF	\times	69.8*	\times
Fault on T_T	HNNRKF	300.5	51*	9.3*
	MRKF	7.2*	2.8*	3.3*
Fault on P_T	HNNRKF	63.1	5.7	27.6
	MRKF	\times	\times	\times

In addition, Figures 5.14, 5.15 and 5.16 depict the mode probabilities for three selected fault scenarios when the bias fault occurs at different instants of the flight profile. The value of the injected fault is set to 3% of the engine steady-state output values, while the degradation factors associated with the compressor health parameters are set to $\alpha_{m_C} = 0.82$ and $\alpha_{\eta_C} = 0.91$. As per Figures 5.14, 5.15 and 5.16, our proposed DRNN-RKF-based FDI scheme is more capable of detecting and isolating different sensor faults occur during the entire flight mode in a certain limited time delay as compared to the multiple RKF-based FDI scheme that generates many false alarms before the occurrence of a fault and detects various incorrect faults instead of the one that occurs. Nevertheless, our proposed hybrid DRNN-RKF-based FDI scheme is not capable of detecting a sensor fault with N sensor.

To quantify the effectiveness and reliability of our proposed hybrid DRNN-RKF-based FDI scheme, two confusion matrices (CM) are obtained in which either the compressor health degradation magnitude or the disturbance noise factor is increased. For this purpose, 50 Monte Carlo simulations are performed. The first confusion matrix corresponding to $\alpha_{m_C} = 0.80$ and $\alpha_{\eta_C} = 0.90$ is displayed in Table

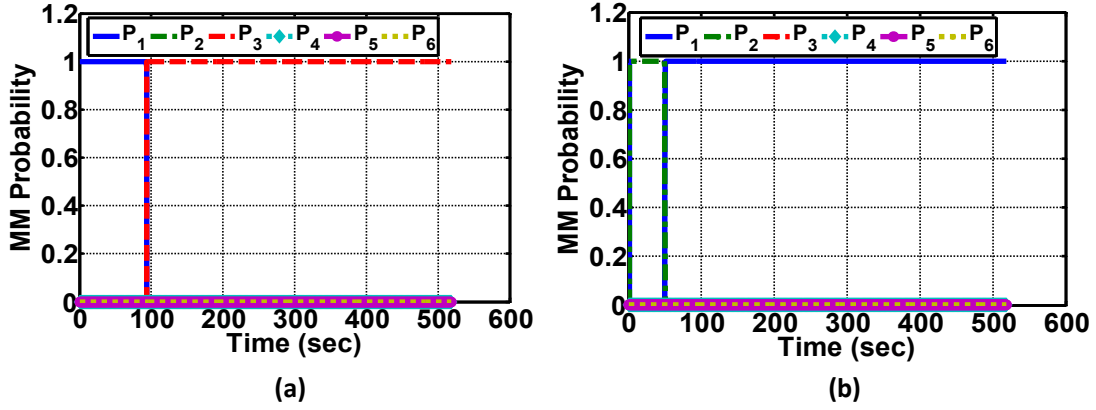


Figure 5.14: Mode probabilities generated by (a) our proposed hybrid DRNN-RKF-based FDI scheme and (b) multiple RKF-based FDI scheme, for 3% bias fault applied at $k_f = 50$ sec to the P_C sensor with $\alpha_{m_C} = 0.82$ and $\alpha_{\eta_C} = 0.91$.

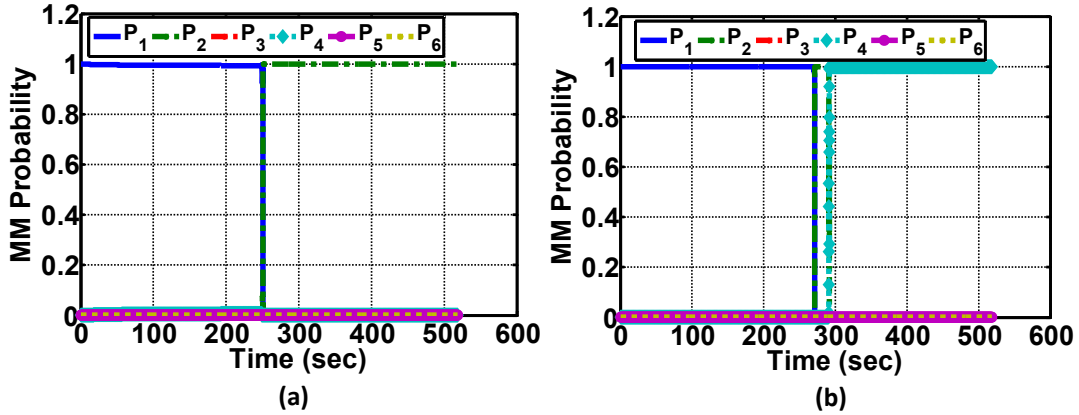


Figure 5.15: Mode probabilities generated by (a) our proposed hybrid DRNN-RKF-based FDI scheme and (b) multiple RKF-based FDI scheme, for 3% bias fault applied at $k_f = 250$ sec to the T_C sensor with $\alpha_{m_C} = 0.82$ and $\alpha_{\eta_C} = 0.91$.

5.13. The second one is corresponding to $K_w = 0.5$ and $K_v = 1.5$ that is displayed in Table 5.14.

Using the simulation results, different performance indices can be defined to quantify the robustness of our proposed hybrid DRNN-RKF-based sensor FDI algorithm with respect to the levels of uncertainty sources. The FPR, ACC and IFDR are computed in Table 5.15 for our proposed hybrid DRNN-RKF-based FDI scheme to investigate the effects of various uncertainty sources. According to Table 5.15,

Table 5.13: The confusion matrix that is obtained for hybrid DRNN-RKF-based FDI scheme for 3% single sensor bias fault that is applied to the engine under $\alpha_{\dot{m}_C} = 0.80$ and $\alpha_{\eta_C} = 0.90$.

CM1	T_C	P_C	N	T_T	P_T	No Fault
T_C	50	0	0	0	0	0
P_C	0	50	0	0	0	0
N	39	0	0	0	11	0
T_T	2	0	0	40	8	0
P_T	5	0	0	0	45	0
No Fault	5	0	0	0	0	45

Table 5.14: The confusion matrix that is obtained for hybrid DRNN-RKF-based FDI scheme for 3% single sensor bias fault that is applied to the engine under $K_w = 0.5$ and $K_v = 1.5$.

CM2	T_C	P_C	N	T_T	P_T	No Fault
T_C	50	0	0	0	0	0
P_C	0	50	0	0	0	0
N	37	0	0	0	13	0
T_T	4	0	0	32	14	0
P_T	0	0	0	0	50	0
No Fault	2	0	0	0	0	48

Table 5.15: Hybrid DRNN-RKF-based Sensor FDI algorithm performance indices corresponding to different levels of uncertainties.

Scenarios	FPR	ACC	IFDR
$K_w = 0.2$ $K_v = 1$	0	0.78	0.264
$K_w = 0.5$ $K_v = 1.5$	0.04	0.767	0.272
$\alpha_{\dot{m}_C} = 0.82$ $\alpha_{\eta_C} = 0.91$	0	0.783	0.24
$\alpha_{\dot{m}_C} = 0.80$ $\alpha_{\eta_C} = 0.90$	0.1	0.767	0.26

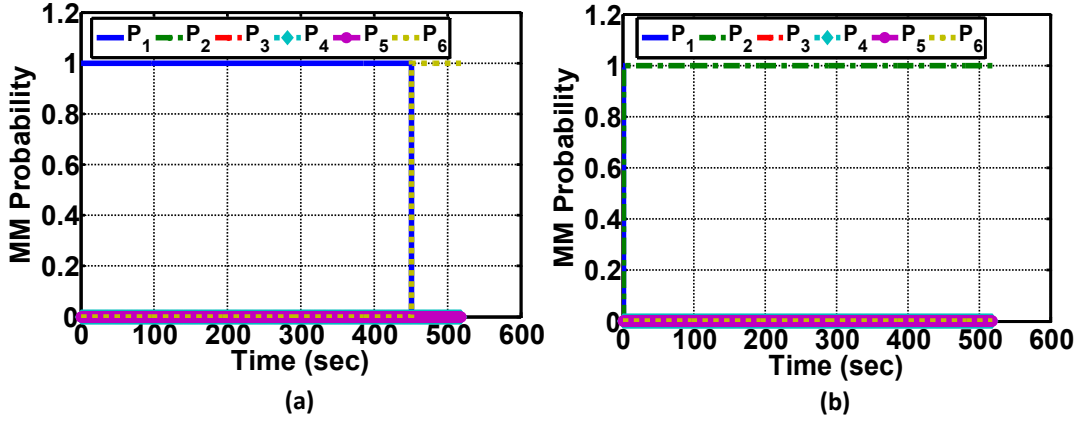


Figure 5.16: Mode probabilities generated by (a) our proposed hybrid DRNN-RKF-based FDI scheme and (b) multiple RKF-based FDI scheme, for 3% bias fault applied at $k_f = 450$ sec to the P_T sensor with $\alpha_{m_c} = 0.82$ and $\alpha_{\eta_c} = 0.91$.

increasing the levels of uncertainty sources results in decrease of ACC, but increase in FPR and IFDR.

Case (c.2): Sensor Fault Detection and Isolation for Different Fault Severities

In this section, the performance of our proposed hybrid DRNN-RKF-based FDI scheme is investigated for an applied sensor bias fault having different severities starting from the minimum detectable bias. Table 5.16 shows the detection times for all faulty modes as a function of the fault severities, when the applied faults occur during the cruise of FP2 with also $\alpha_{m_c} = 0.82$ and $\alpha_{\eta_c} = 0.91$.

It can be observed from Table 5.16 that the higher the fault severity with respect to the pre-determined 3% fault, the later the detection time, given that the actual fault becomes further different from the pre-determined bias fault. Note that the minimum detectable sensor bias fault is 2% that requires larger time to be detected as compared to the higher fault severities.

Moreover, Table 5.9 shows the maximum sensor bias faults that are detectable in less than 20 seconds by using our proposed hybrid DRNN-RKF-based FDI scheme

Table 5.16: The sensor fault detection times for all fault modes as a function of the fault severity during the cruise of FP2, with $\alpha_{\dot{m}_C} = 0.82$ and $\alpha_{\eta_C} = 0.91$. (\times) denotes a non-detectable fault, and ($*$) denotes the incorrect fault detection besides the correctly detected fault.

Fault Time	2%	3%	4%	5%	6%
T_C	14.9	6.1	7.4	10.3	12.1
P_C	37.4	5.3	8.7	19.2	34.7
N	\times	\times	\times	\times	\times
T_T	100.1*	51*	59.1*	61.3*	68.9*
P_T	15.7	5.7	6.4	7.1	7.8

Table 5.17: The maximum sensor bias fault (as percentage of the engine steady-state outputs) that are detected in less than 20 seconds during the cruise mode of FP2 by using our proposed hybrid DRNN-RKF-based FDI scheme under $\alpha_{\dot{m}_C} = 0.82$ and $\alpha_{\eta_C} = 0.91$. (\times) denotes non-detectable fault.

Sensor Fault	T_C	P_C	N	T_T	P_T
Maximum Detectable Fault%	32	5.1	\times	N/A	16.7

under $\alpha_{\dot{m}_C} = 0.82$ and $\alpha_{\eta_C} = 0.91$. The reported fault severities in Table 5.17 are obtained for the cruise mode of FP2. However, if an applied sensor bias fault increases far beyond the corresponding maximum detectable fault as indicated in Table 5.17, an incorrect fault may be detected. Therefore, it is recommended that one incorporates more models within the MM-based structure corresponding to higher pre-determined sensor faults to become capable of detecting and isolating faults with higher magnitudes in shorter durations of time.

5.5.4 Comparison

In this chapter, two hybrid FDI schemes using the previously designed HKF and RKF are developed to address the sensor fault detection and isolation problem for the single spool gas turbine engine. Different factors including the fault detection times, estimation accuracy, false alarm rates, incorrect fault detection rates and the ranges of detectable faults corresponding to different engine sensors are obtained in preceding sections. As per the above observations, the hybrid DRNN-HKF-based

FDI scheme is a more reliable and applicable method as compared to the hybrid DRNN-RKF-based FDI scheme. Table 5.18 displays the comparison results among the two proposed hybrid FDI schemes.

The comparison results that are provided in Table 5.18 confirm that the hybrid DRNN-HKF-based FDI scheme is more accurate and reliable than the hybrid DRNN-RKF-based FDI scheme. It detects different sensor faults in less delay time and has a wider range of detectable faults using the single-layer multiple-model structure. It also provides one with smaller FAR, IDFR and WMAPE values as compared to the hybrid DRNN-RKF-based FDI scheme. Unlike the hybrid DRNN-HKF, the hybrid DRNN-RKF is not sufficiently reliable for detecting and isolating all faulty sensors, particularly N and T_T sensors for which the FDI scheme cannot detect a fault or detects an incorrect one. The reason for insufficient accuracy and reliability of DRNN-RKF-based FDI scheme is the compensation that is made towards the applied uncertainty using two simultaneous tools as the DRNN and RKF. According to results in Chapter 4, the RKF is designed for $\alpha_{m_C} = 0.95$ and $\alpha_{\eta_C} = 0.975$. Hence, part of uncertainty is compensated twice using the RKF as well as the DRNN that is designed to approximate the uncertain terms that are removed later from the engine measurements. This leads to the defective operation of hybrid DRNN-RKF methods in specific faulty scenarios.

It must be noted that that there is no limitation to apply the proposed hybrid DRNN-HKF-based FDI scheme in real-time applications since the DRNN is trained offline and most of the simulation time is dedicated to the OBEM simulation, but not the HKF and DRNN structures since the Kalman gains and network parameters are already obtained in an offline mode.

Table 5.18: Comparison of FDT for 3% sensor faults during the cruise mode, maximum detectable faults in less than 20 seconds, WMAPE, FAR, ACC, and IDFR corresponding to hybrid DRNN-HKR and DRNN-RKF based FDI schemes, under $\alpha_{mic} = 0.93$ and $\alpha_{\eta_C} = 0.965$ for FP1 that is used for DRNN-HKF and $\alpha_{mic} = 0.82$ and $\alpha_{\eta_C} = 0.91$ for FP2 that is used for DRNN-RKF methods. (\times) denotes the non-detected fault, and (*) denotes incorrect fault detection cases besides the correctly detected fault.

Indices	Hybrid DRNN-HKF-based FDI					Hybrid DRNN-RKF-based FDI				
	T_C	P_C	N	T_T	P_T	T_C	P_C	N	T_T	P_T
FDT (sec)	5.2	3.9	3.6	8.7	3.3	6.1	5.3	\times	51*	5.7
MaxFault (%)	37	5.8	10	5	20	32	5.5	\times	N/A	16.7
WMAPE (%)	0.8971	0.5323	0.6104	0.214	0.0212	2.3143	3.2712	0.001	0.3908	3.4592
FAR	0					0				
ACC	1					0.783				
IDFR	0					0.24				

5.6 Summary

In this chapter, two hybrid DRNN-based FDI schemes are proposed using the previously designed HKF and RKF methods that are designed in Chapters 3 and 4, respectively. The DRNN is trained offline by the use of the EKF approach to minimize the error and to determine network parameters. The convergence of EKF-based training of an Elman DRNN is also shown in this chapter. Finally, the trained network is then used in an online FDI algorithm to approximate the uncertain terms associated with the engine sensor measurements. The network outputs are removed from the actual engine measurements to obtain the modified measurements that are finally applied to the bank of filters for sensor FDI purposes. This allows one to improve the robustness with respect to the engine uncertainty and modeling errors as compared to the pure model-based approaches that are previously developed either in this thesis or in the literature.

Using extensive simulation case studies and computing different performance indices, it is demonstrated that the hybrid DRNN-HKF-based FDI scheme is more accurate and reliable to be applied in real-time applications as compared to the hybrid DRNN-RKF-based FDI scheme. It generates less FAR and IFDR as well as more estimation accuracy. The fault detection delay time is sufficiently low for different faulty scenarios and a large range of sensor faults can be detected using only one layer of the multiple-model structure.

Chapter 6

Conclusions and Future Directions of Research

This dissertation was mainly concerned with the robust sensor fault detection and isolation of single spool gas turbine engine using different model-based and hybrid structures. We developed pure model-based FDI algorithms by constructing two particular filters namely, hybrid Kalman filter and robust Kalman filter, where in the former approach an online onboard engine model is used to follow the actual engine during the entire flight profile and in the latter one a quadratically stable robust filter is designed for a linear uncertain system with time-varying norm bounded uncertainties that affect all the system state equation matrices. The proposed filters are utilized in multiple-model structure in which different models are constructed corresponding to healthy and faulty sensors scenarios. In another part of this dissertation, a hybrid structure in which a dynamic recurrent neural network is integrated with a bank of hybrid/robust Kalman filters is proposed to improve the robustness with respect to the engine health degradation. Extensive simulation studies are conducted to investigate the effectiveness of our proposed FDI methods. Below, we provide the thesis summary based on the results that were provided in Chapters 3

to 5.

6.1 Multiple HKF-based Fault Detection, Isolation and Identification

In Chapter 3, a novel approach for both single and concurrent sensor fault detection, isolation and identification/estimation (FDII) for single spool gas turbine engine is proposed. Our methodology is based on the developed *Hybrid Kalman Filter (HKF)* as the detection filter of a *hierarchical multiple-model* based structure. Despite the use of linear Kalman filters, the HKF is capable of capturing the nonlinearities of the system by integrating a nonlinear on-board engine model (OBEM) with piecewise linear (PWL) models to cover the entire operating range of the engine. Compared to the multiple linear Kalman filter (MLKF), our proposed approach requires fewer number of operating points although each corresponds to a larger operating range.

Another important contribution of this work is in the inclusion of the effects of health parameter degradations in our proposed sensor FDII scheme through updating the OBEM health parameters reference baselines that enables one to prevent false alarms and incorrect fault detections. Therefore, unlike most of the previous work in the literature that have not considered the influence of health parameters variations on the performance of the developed FDII approaches, our proposed sensor FDII scheme is sufficiently more effective for use in the entire flight profile. It is furthermore suitable during the engine life cycle by updating the OBEM health parameters reference baselines, and by replacing the steady-state values with the OBEM states and outputs and integration of the designed PWL models. Moreover, our proposed MM-based sensor FDI scheme is integrated with the modified GLR method to estimate a sensor fault severity.

Finally, it is demonstrated through extensive simulation studies that the accuracy and robustness of our proposed MHKF-based FDI approach against the engine health parameter degradations are significantly superior to that of those generated by other investigated methods such as the MLKF, EKF, UKF, and CKF.

The future directions for research can be summarized as follows:

- As mentioned in Chapter 3, the OBEM uses the same dynamic equations as the actual engine, but with different compressor and turbine health parameters. Therefore, one may consider the situation in which there is a dynamic mismatch between the OBEM and the actual engine.
- As per the last experiment in Chapter 3, the number of required operating points covering the entire flight profile is determined by computing mean of the combined residual signals in presence of health parameters degradations for the MLKF and MHKF methods. Based on these results, it was concluded that the mean of the combined residual signal associated with the healthy mode can be reduced by increasing the number of the operating points. Nevertheless, one may propose a technical approach to determine the number of required operating points using the residual signal, operating range of the given nonlinear system and the system state dynamics.
- A formal approach can also be presented to investigate the stability property of a soft switching mechanism among the PWL models.

6.2 Multiple RKF-based Fault Detection and Isolation

In Chapter 4, a novel *robust multiple-model* based fault detection and isolation methodology is proposed and developed. Our methodology builds on development

of a *Robust Kalman Filter* as the detection filter. Multiple robust filters are designed for the piecewise linear models that are associated with various faulty and healthy sensor modes in which all the state space matrices are affected by time-varying parameter uncertainties. The filter gain matrices are obtained by reformulating two algebraic Riccati equations into linear matrix inequality (LMI) feasibility conditions where predefined upper bounds on the state estimation errors are imposed. This is done to avoid restricting the degrees of freedom in optimizing the error covariance matrix upper bound when one is not critical. The robust filters can be applied to the entire operating range of a nonlinear system by means of integrating the PWL models based on their associated normalized weights. The multiple RKF-based FDI strategy is then applied to solve and address the sensor FDI problem in a single spool gas turbine engine during its entire flight profile in which the engine health parameter degradations are considered as a source of uncertainty in addition to the external process and measurement noise.

We have further demonstrated and illustrated through extensive simulation studies that the estimation accuracy and its robustness with respect to the engine health degradation of our proposed robust FDI scheme are superior to those that are developed by standard MM-based structures utilizing the linear Kalman filter (LKF) as well as the one which uses the robust filter that is designed in [4]. Moreover, the robust MM-based FDI scheme we have proposed has lower fault detection delay times and lower rates of false alarms and incorrect fault detections as compared to the above methods. We have also shown that our proposed robust sensor FDI strategy was extended to detect and isolate multiple concurrent faults corresponding to the full flight profile by utilizing a hierarchical MM-based structure.

The future directions of research in this area can be summarized below:

- In Chapter 4, the RKF is designed for the linear uncertain system with time-varying norm bounded parameter uncertainties that affect system states and

noise signature matrices. In this problem, it is assumed that the input is the state-feedback control signal whose uncertainty is included as part of A and C matrices in the closed-loop system. However, one may extend our proposed RKF design to work for an open-loop system with an already known input signal that has an uncertain signature matrix.

- In Chapter 4, it is assumed that the process and measurement noise are independent Gaussian noise which is a common assumption in the literature. However, our proposed RKF can be extended for the linear uncertain system in which the noise elements are auto-correlated and cross-correlated. The distributed weighted robust Kalman filter fusion technique is a potential method to address this problem.
- A formal study is also proposed to be performed to verify whether the filtering process is quadratically stable and does satisfy the performance requirements when the corresponding PWL models are combined for the entire operating regime.

6.3 Hybrid DRNN-based Fault Detection and Isolation

In Chapter 5, two hybrid DRNN-based FDI schemes are proposed using the previously designed HKF and RKF methods that are developed in Chapters 3 and 4, respectively. The DRNN is trained offline by using the EKF approach to minimize the mean square error to determine network parameters including the number of hidden neurons and epochs, the diagonal elements of P , Q and R matrices as well as the truncation depth. The actual engine input and output signals as well as the OBEM outputs are used to construct the training and validation data sets. A 5-fold

cross-validation process is also used to determine network parameters. To perform training, the network parameters are modeled as state variables that are predicted by DRNN and are corrected by EKF. The measurement matrix is computed using the truncated back propagation method. Finally, the trained network is used in an online FDI algorithm to approximate the uncertain terms associated with the engine sensor measurements. The network outputs are removed from the actual engine measurements to obtain the modified measurements that are finally applied to the bank of filters for sensor FDI purposes. This allows one to improve the robustness with respect to the engine uncertainty and modeling errors as compared to the pure model-based approaches that are previously developed either in this thesis or in the literature.

Different simulation case studies are conducted to investigate the robustness of our proposed hybrid FDI approach with respect to various levels of uncertainty, the promptness of the fault detection, the estimation accuracy, the false alarm and incorrect fault detection rates as well as the range of detectable faults. Using extensive simulation case studies and computing different performance indices, it is clearly demonstrated that the hybrid DRNN-HKF-based FDI scheme is more accurate and reliable to be applied in real-time applications as compared to the hybrid DRNN-RKF-based FDI scheme. It generates lower FAR and IFDR as well as higher estimation accuracy. The fault detection delay time is sufficiently low for different faulty scenarios and a wider range of sensor faults can be detected by using only one layer of the multiple models structure.

The future directions of research in this area can be summarized below:

- In this thesis, an EKF algorithm is used to train the DRNN parameters. The trained network is used to address the sensor FDI problem for the single spool gas turbine engine whose model order is equal to four. However, a vanishing gradient may happen for a more complex system during the measurement

matrix computation. Therefore, it is proposed to utilize the gradient-free observer-based algorithms namely, the unscented and cubature Kalman filters to train the network parameters.

- In this chapter, the DRNN is used to approximate the engine health degradation terms associated with sensor measurements. Since the engine degradation is a slow and gradual process, the network is trained offline and then it is combined with the bank of filter in an online FDI scheme. However, one may design a DRNN to approximate engine modeling error or neglected dynamics that is not necessarily changed slowly. Therefore, in this case it is recommended to train the network online while it is combined with the model-based part of the FDI scheme. This is a challenging problem in which the network training should be sufficiently robust with respect to any engine sudden fault that may affect the network training output.

Finally, as per the results that are presented in this thesis, the hybrid structure in which a bank of HKFs are used is the recommended approach over the other proposed methodologies. It is capable of detecting and isolating sensor faults in shorter durations of time, estimating the engine state variables with higher accuracy, generating lower rates of false alarms and incorrect fault detections. It is also sufficiently robust with respect to health parameter degradation at different levels. Unlike the pure robust model-based filters that are designed for the particular form of modeling uncertainty, the hybrid structure is the more general approach that is designed to be robust against different sources of modeling uncertainties. Although the hybrid FDI strategy is the more reliable and accurate approach as compared to the other proposed methodologies, it is still recommended to compute the complexity order associated with our proposed techniques to select the best approach for real-time applications. One may select the proper FDI strategy for a nonlinear system based on the available processing resource as well as the required level of reliability and

accuracy.

Bibliography

- [1] J. L. Kerrebrock, *Aircraft engines and gas turbines*, vol. 22. MIT press Cambridge, MA, 1992.
- [2] J. S. Litt, D. L. Simon, S. Garg, T.-H. Guo, C. Mercer, R. Millar, A. Behbahani, A. Bajwa, and D. T. Jensen, “A survey of intelligent control and health management technologies for aircraft propulsion systems,” *Journal of Aerospace Computing, Information, and Communication*, vol. 1, no. 12, pp. 543–563, 2004.
- [3] E. Naderi, N. Meskin, and K. Khorasani, “Nonlinear fault diagnosis of jet engines by using a multiple model-based approach,” *J. of Eng. for Gas Turbines and Power*, vol. 134, no. 1, p. 011602, 2012.
- [4] Z. Wang and B. Huang, “Robust H_2/H_∞ filtering for linear systems with error variance constraints,” *IEEE Transaction on Signal Processing*, vol. 48, no. 8, pp. 2463–2467, 2000.
- [5] R. Isermann and P. Balle, “Trends in the application of model-based fault detection and diagnosis of technical processes,” *Control Engineering Practice*, vol. 5, no. 5, pp. 709–719, 1997.
- [6] P. M. Frank, “Fault diagnosis in dynamic systems using analytical and knowledge-based redundancy: A survey and some new results,” *Automatica*, vol. 26, no. 3, pp. 459–474, 1990.

- [7] Z. Gao, C. Cecati, and S. X. Ding, “A survey of fault diagnosis and fault-tolerant techniquespart i: Fault diagnosis with model-based and signal-based approaches,” *IEEE Transactions on Industrial Electronics*, vol. 62, no. 6, pp. 3757–3767, 2015.
- [8] A. S. Willsky and H. L. Jones, “A generalized likelihood ratio approach to the detection and estimation of jumps in linear systems,” *IEEE Transactions on Automatic Control*, vol. 21, no. 1, pp. 108–112, 1976.
- [9] J. J. Gertler, “Survey of model-based failure detection and isolation in complex plants,” *IEEE Control systems magazine*, vol. 8, no. 6, pp. 3–11, 1988.
- [10] I. Hwang, S. Kim, Y. Kim, and C. E. Seah, “A survey of fault detection, isolation, and reconfiguration methods,” *IEEE Transaction on Control Systems Technology*, vol. 18, no. 3, pp. 636–653, 2010.
- [11] X. Dai and Z. Gao, “From model, signal to knowledge: A data-driven perspective of fault detection and diagnosis,” *IEEE Transactions on Industrial Informatics*, vol. 9, no. 4, pp. 2226–2238, 2013.
- [12] Z. Gao, C. Cecati, and S. X. Ding, “A survey of fault diagnosis and fault-tolerant techniquespart ii: Fault diagnosis with knowledge-based and hybrid/active approaches,” *IEEE Transactions on Industrial Electronics*, vol. 62, no. 6, pp. 3768–3774, 2015.
- [13] Z. Gao, S. X. Ding, and C. Cecati, “Real-time fault diagnosis and fault-tolerant control,” *IEEE Transactions on Industrial Electronics*, vol. 62, no. 6, pp. 3752–3756, 2015.
- [14] L. A. Urban, “Gas path analysis applied to turbine engine condition monitoring,” in *American Institute of Aeronautics and Astronautics and Society of*

Automotive Engineers, Joint Propulsion Specialist Conference, pp. 1972–1082, 1972.

- [15] A. Volponi, H. DePold, R. Ganguli, and C. Daguang, “The use of Kalman filter and neural network methodologies in gas turbine performance diagnostics: a comparative study,” *Journal of engineering for gas turbines and power*, vol. 125, no. 4, pp. 917–924, 2003.
- [16] V. Venkatasubramanian, R. Rengaswamy, K. Yin, and S. N. Kavuri, “A review of process fault detection and diagnosis: Part i: Quantitative model-based methods,” *Journal of Computers & chemical engineering*, vol. 27, no. 3, pp. 293–311, 2003.
- [17] J. C. d. Silva, A. Saxena, E. Balaban, and K. Goebel, “A knowledge-based system approach for sensor fault modeling, detection and mitigation,” *Expert Systems with Applications*, vol. 39, no. 12, pp. 10977–10989, 2012.
- [18] R. K. Mehra and J. Peschon, “An innovations approach to fault detection and diagnosis in dynamic systems,” *Automatica*, vol. 7, no. 5, pp. 637–640, 1971.
- [19] J. Gertler, “Fault detection and isolation using parity relations,” *Control engineering practice*, vol. 5, no. 5, pp. 653–661, 1997.
- [20] R. J. Patton and J. Chen, “Review of parity space approaches to fault diagnosis for aerospace systems,” *Journal of Guidance, Control, and Dynamics*, vol. 17, no. 2, pp. 278–285, 1994.
- [21] J. Stoustrup and H. H Niemann, “Fault estimationa standard problem approach,” *International Journal of Robust and Nonlinear Control*, vol. 12, no. 8, pp. 649–673, 2002.
- [22] R. Isermann, “Process fault detection based on modeling and estimation methodsa survey,” *Automatica*, vol. 20, no. 4, pp. 387–404, 1984.

- [23] A. Baniamerian and K. Khorasani, "Fault detection and isolation of dissipative parabolic pdes: Finite-dimensional geometric approach," in *American Control Conference (ACC)*, pp. 5894–5899, IEEE, 2012.
- [24] A. Baniamerian, N. Meskin, and K. Khorasani, "A geometric approach to fault detection and isolation of multi-dimensional (nd) systems," *Multidimensional Systems and Signal Processing*, pp. 1–26, 2016.
- [25] T. E. Menke and P. S. Maybeck, "Sensor/actuator failure detection in the vista f-16 by multiple model adaptive estimation," *IEEE Transactions on Aerospace and Electronic Systems*, vol. 31, no. 4, pp. 1218–1229, 1995.
- [26] P. S. Maybeck, "Multiple model adaptive algorithms for detecting and compensating sensor and actuator/surface failures in aircraft flight control systems," *Int. J. of Robust and Nonlinear Control*, vol. 9, no. 14, pp. 1051–1070, 1999.
- [27] N. Meskin, E. Naderi, and K. Khorasani, "Fault diagnosis of jet engines by using a multiple model-based approach," *ASME Turbo Expo*, no. GT2010-23442, pp. 319–329, 2010.
- [28] N. Meskin, E. Naderi, and K. Khorasani, "A multiple model-based approach for fault diagnosis of jet engines," *IEEE Transactions on Control System Technology*, pp. 254–262, 2013.
- [29] R. J. Patton, P. M. Frank, and R. N. Clarke, *Fault diagnosis in dynamic systems: theory and application*. Prentice-Hall, Inc., 1989.
- [30] R. N. Clark, "A simplified instrument failure detection scheme," *IEEE Transactions on Aerospace and Elec. Sys.*, no. 4, pp. 558–563, 1978.
- [31] R. V. Beard, *Failure accommodation in linear systems through self-reorganization*. PhD thesis, MIT, 1971.

- [32] E. Chow and A. Willsky, "Analytical redundancy and the design of robust failure detection systems," *IEEE Transactions on Automatic Control*, vol. 29, no. 7, pp. 603–614, 1984.
- [33] X. Ding and L. Guo, "An approach to time domain optimization of observer-based fault detection systems," *International Journal of Control*, vol. 69, no. 3, pp. 419–442, 1998.
- [34] R. J. Patton and J. Chen, "Robust fault detection using eigenstructure assignment: A tutorial consideration and some new results," in *30th IEEE Conf. on Decision and Control*, pp. 2242–2247, 1991.
- [35] R. Patton and J. Chen, "Observer-based fault detection and isolation: robustness and applications," *Control Engineering Practice*, vol. 5, no. 5, pp. 671–682, 1997.
- [36] P. M. Frank and X. Ding, "Frequency domain approach to optimally robust residual generation and evaluation for model-based fault diagnosis," *Automatica*, vol. 30, no. 5, pp. 789–804, 1994.
- [37] S. Bhattacharyya, "Observer design for linear systems with unknown inputs," *IEEE Transactions on Automatic Control*, vol. 23, no. 3, pp. 483–484, 1978.
- [38] K. Watanabe and D. M. Himmelblau, "Instrument fault detection in systems with uncertainties," *International Journal of Systems Science*, vol. 13, no. 2, pp. 137–158, 1982.
- [39] R. Seliger and P. Frank, "Fault-diagnosis by disturbance decoupled nonlinear observers," in *30th IEEE Conference on Decision and Control*, pp. 2248–2253, 1991.

- [40] J. Gertler, “All linear methods are equal and extendible to (some) nonlinearities,” *International Journal of Robust and Nonlinear Control*, vol. 12, no. 8, pp. 629–648, 2002.
- [41] P. M. Frank and X. Ding, “Survey of robust residual generation and evaluation methods in observer-based fault detection systems,” *Journal of process control*, vol. 7, no. 6, pp. 403–424, 1997.
- [42] M. Witczak, “Unknown input observers and filters,” in *Fault Diagnosis and Fault-Tolerant Control Strategies for Non-Linear Systems*, pp. 19–56, Springer, 2014.
- [43] M. A. Demetriou, “Using unknown input observers for robust adaptive fault detection in vector second-order systems,” *Mechanical systems and signal processing*, vol. 19, no. 2, pp. 291–309, 2005.
- [44] P. Kudva, N. Viswanadham, and A. Ramakrishna, “Observers for linear systems with unknown inputs,” *IEEE Transactions on Automatic Control*, vol. 25, pp. 113–115, 1980.
- [45] P. Lu, E.-J. van Kampen, C. C. de Visser, and Q. Chu, “Framework for state and unknown input estimation of linear time-varying systems,” *Automatica*, vol. 73, pp. 145–154, 2016.
- [46] M. Hou and P. Muller, “Disturbance decoupled observer design: A unified viewpoint,” *IEEE Transactions on Automatic Control*, vol. 39, no. 6, pp. 1338–1341, 1994.
- [47] M. Rodrigues, D. Theilliol, and D. Sauter, “Design of an active fault tolerant control and polytopic unknown input observer for systems described by a multi-model representation,” in *44th IEEE Conference on Decision and Control, and European Control Conference. CDC-ECC’05*, pp. 3815–3820, 2005.

- [48] M. Aldeen and R. Sharma, “Estimation of states, faults and unknown disturbances in non-linear systems,” *International Journal of Control*, vol. 81, no. 8, pp. 1195–1201, 2008.
- [49] J. Chen and R. J. Patton, *Robust model-based fault diagnosis for dynamic systems*. Kluwer academic publishers, 1999.
- [50] J. George, “Robust Kalman-Bucy filter,” *IEEE Transaction on Automatic Control*, vol. 58, no. 1, pp. 174–180, 2013.
- [51] D. H. Lee, Y. H. Joo, and M. H. Tak, “A convex optimization approach to adaptive stabilization of discrete-time LTI systems with polytopic uncertainties,” *International Journal of Adaptive Control and Signal Processing*, 2014, DOI: 10.1002/acs.2525.
- [52] W. Qi, P. Zhang, and Z. Deng, “Robust weighted fusion Kalman filters for multisensor time-varying systems with uncertain noise variances,” *Signal Processing*, vol. 99, pp. 185–200, 2014.
- [53] J. Zhang, Y. Xia, and P. Shi, “Parameter-dependent robust H_∞ filtering for uncertain discrete-time systems,” *Automatica*, vol. 45, no. 2, pp. 560–565, 2009.
- [54] S. Aouaouda, M. Chadli, P. Shi, and H. Karimi, “Discrete-time H_-/H_∞ sensor fault detection observer design for nonlinear systems with parameter uncertainty,” *International Journal of Robust and Nonlinear Control*, vol. 25, no. 3, pp. 339–361, 2015.
- [55] D. Henry, J. Cieslak, A. Zolghadri, and D. Efimov, “A non-conservative H_-/H_∞ solution for early and robust fault diagnosis in aircraft control surface servo-loops,” *Control Engineering Practice*, vol. 31, pp. 183–199, 2014.

- [56] I. R. Petersen and A. V. Savkin, *Robust Kalman filtering for signals and systems with large uncertainties*. Springer Science & Business Media, 1999.
- [57] R. Babuska and H. B. Verbruggen, “Fuzzy set methods for local modeling and identification,” 1997.
- [58] X. C. Zhang, A. Visala, A. Halme, and P. Linko, “Functional state modelling approach for bioprocesses: local models for aerobic yeast growth processes,” *Journal of Process Control*, vol. 4, no. 3, pp. 127–134, 1994.
- [59] M. Meila and M. I. Jordan, “Markov mixtures of experts,” *Multiple Model Approaches to Modeling and Control*, pp. 145–166, 1997.
- [60] L. Ljung, “Asymptotic behavior of the extended kalman filter as a parameter estimator for linear systems,” *IEEE Transactions on Automatic Control*, vol. 24, no. 1, pp. 36–50, 1979.
- [61] S. Julier and J. Uhlmann, “New extension of the Kalman filter to nonlinear systems,” in *AeroSense’97*, pp. 182–193, International Society for Optics and Photonics, 1997.
- [62] I. Arasaratnam and S. Haykin, “Cubature Kalman filters,” *IEEE Transactions on Automatic Control*, vol. 54, no. 6, pp. 1254–1269, 2009.
- [63] F. Alrowaie, R. Gopaluni, and K. Kwok, “Fault detection and isolation in stochastic non-linear state-space models using particle filters,” *Control Engineering Practice*, vol. 20, no. 10, pp. 1016–1032, 2012.
- [64] S. Yin and X. Zhu, “Intelligent particle filter and its application to fault detection of nonlinear system,” *IEEE Transactions on Industrial Electronics*, vol. 62, no. 6, pp. 3852–3861, 2015.

- [65] N. Scenna, "Some aspects of fault diagnosis in batch processes," *Journal of Reliability Engineering and System Safety*, vol. 70, no. 1, pp. 95–110, 2000.
- [66] R. Rengaswamy and V. Venkatasubramanian, "A syntactic pattern-recognition approach for process monitoring and fault diagnosis," *Engineering Applications of Artificial Intelligence*, vol. 8, no. 1, pp. 35–51, 1995.
- [67] S. Wang and J. Cui, "Sensor-fault detection, diagnosis and estimation for centrifugal chiller systems using principal-component analysis method," *Applied Energy*, vol. 82, no. 3, pp. 197–213, 2005.
- [68] X. Wang, U. Kruger, G. W. Irwin, G. McCullough, and N. McDowell, "Non-linear pca with the local approach for diesel engine fault detection and diagnosis," *IEEE Transactions on Control Systems Technology*, vol. 16, no. 1, pp. 122–129, 2008.
- [69] G. Li, S. J. Qin, and D. Zhou, "Geometric properties of partial least squares for process monitoring," *Automatica*, vol. 46, no. 1, pp. 204–210, 2010.
- [70] S. J. Qin, "Survey on data-driven industrial process monitoring and diagnosis," *Annual Reviews in Control*, 2012.
- [71] A. Widodo and B.-S. Yang, "Support vector machine in machine condition monitoring and fault diagnosis," *Mechanical systems and signal processing*, vol. 21, no. 6, pp. 2560–2574, 2007.
- [72] S. Yin, X. Gao, H. R. Karimi, and X. Zhu, "Study on support vector machine-based fault detection in tennessee eastman process," in *Abstract and Applied Analysis*, vol. 2014, Hindawi Publishing Corporation, 2014.
- [73] B. M. Ebrahimi, J. Faiz, M. Javan-Roshtkhari, and A. Z. Nejjhad, "Static eccentricity fault diagnosis in permanent magnet synchronous motor using time

- stepping finite element method,” *IEEE Transactions on Magnetics*, vol. 44, no. 11, pp. 4297–4300, 2008.
- [74] B. M. Ebrahimi, J. Faiz, and M. J. Roshtkhari, “Static-, dynamic-, and mixed-eccentricity fault diagnoses in permanent-magnet synchronous motors,” *IEEE Transactions on Industrial Electronics*, vol. 56, no. 11, pp. 4727–4739, 2009.
- [75] B. M. Ebrahimi, M. J. Roshtkhari, J. Faiz, and S. V. Khatami, “Advanced eccentricity fault recognition in permanent magnet synchronous motors using stator current signature analysis,” *IEEE Transactions on Industrial Electronics*, vol. 61, no. 4, pp. 2041–2052, 2014.
- [76] B. Pourbabaei, M. J. Roshtkhari, and K. Khorasani, “Feature learning with deep convolutional neural networks for screening patients with paroxysmal atrial fibrillation,” in *International Joint Conference on Neural Networks (IJCNN)*, pp. 5057–5064, IEEE, 2016.
- [77] D. Capriglione, C. Liguori, C. Pianese, and A. Pietrosanto, “On-line sensor fault detection, isolation, and accommodation in automotive engines,” *IEEE Transactions on Instrumentation and Measurement*, vol. 52, no. 4, pp. 1182–1189, 2003.
- [78] S. P. Zhao and K. Khorasani, “A recurrent neural network based fault diagnosis scheme for a satellite,” in *33rd Annual Conference of the IEEE Industrial Electronics Society, IECON 2007*, pp. 2660–2665, 2007.
- [79] M. Ayoubi, “Fault diagnosis with dynamic neural structure and application to a turbo-charger,” in *Proc. Int. Symp. Fault Detection Supervision and Safety for Technical Processes, SAFEPROCESS*, vol. 94, pp. 618–623, 1994.

- [80] L. Li, L. Ma, and K. Khorasani, "A dynamic recurrent neural network fault diagnosis and isolation architecture for satellites actuator/thruster failures," in *Advances in Neural Networks-ISNN 2005*, pp. 574–583, Springer, 2005.
- [81] H. A. Talebi, K. Khorasani, and S. Tafazoli, "A recurrent neural-network-based sensor and actuator fault detection and isolation for nonlinear systems with application to the satellite's attitude control subsystem," *IEEE Transactions on Neural Networks*, vol. 20, no. 1, pp. 45–60, 2009.
- [82] A. Yazdizadeh and K. Khorasani, "Adaptive time delay neural network structures for nonlinear system identification," *Neurocomputing*, vol. 47, no. 1, pp. 207–240, 2002.
- [83] A. Volponi and T. Brotherton, "A bootstrap data methodology for sequential hybrid engine model building," in *IEEE Aerospace Conference*, pp. 3463–3471, 2005.
- [84] R. Loukil, M. Chtourou, and T. Damak, "Training a neural observer using a hybrid approach," in *9th International Multi-Conference on Systems, Signals and Devices (SSD)*, pp. 1–5, IEEE, 2012.
- [85] S. Haykin *et al.*, *Kalman filtering and neural networks*. Wiley Online Library, 2001.
- [86] R. Ahmed, M. El Sayed, S. Gadsden, and S. Habibi, "Fault detection of an engine using a neural network trained by the smooth variable structure filter," in *IEEE International Conference on Control Applications (CCA)*, pp. 1190–1196, 2011.
- [87] S. Habibi, "The smooth variable structure filter," *Proceedings of the IEEE*, vol. 95, no. 5, pp. 1026–1059, 2007.

- [88] R. Ahmed, M. El Sayed, S. A. Gadsden, J. Tjong, and S. Habibi, "Automotive internal-combustion-engine fault detection and classification using artificial neural network techniques," *IEEE Transactions on Vehicular Technology*, vol. 64, no. 1, pp. 21–33, 2015.
- [89] A. Y. Alanis, E. N. Sanchez, A. G. Loukianov, and M. A. Perez, "Real-time recurrent neural state estimation," *IEEE Transactions on Neural Networks*, vol. 22, no. 3, pp. 497–505, 2011.
- [90] X. Wang and Y. Huang, "Convergence study in extended kalman filter-based training of recurrent neural networks," *IEEE Transactions on Neural Networks*, vol. 22, no. 4, pp. 588–600, 2011.
- [91] J. de Jesús Rubio and W. Yu, "Nonlinear system identification with recurrent neural networks and dead-zone kalman filter algorithm," *Neurocomputing*, vol. 70, no. 13, pp. 2460–2466, 2007.
- [92] H. C. Cho, J. Knowles, M. S. Fadali, and K. S. Lee, "Fault detection and isolation of induction motors using recurrent neural networks and dynamic bayesian modeling," *IEEE Transactions on Control Systems Technology*, vol. 18, no. 2, pp. 430–437, 2010.
- [93] O. ÖZGÖNENEL and T. Yalcin, "A complete motor protection algorithm based on pca and ann: a real time study," *Turkish Journal of Electrical Engineering & Computer Sciences*, vol. 19, no. 3, pp. 317–334, 2011.
- [94] D. He, R. Li, and J. Zhu, "Plastic bearing fault diagnosis based on a two-step data mining approach," *IEEE Transactions on Industrial Electronics*, vol. 60, no. 8, pp. 3429–3440, 2013.
- [95] X.-S. Pu, T. H. Nguyen, D.-C. Lee, K.-B. Lee, and J.-M. Kim, "Fault diagnosis of dc-link capacitors in three-phase ac/dc pwm converters by online estimation

- of equivalent series resistance,” *IEEE Transactions on Industrial Electronics*, vol. 60, no. 9, pp. 4118–4127, 2013.
- [96] N. Sheibat-Othman, N. Laouti, J.-P. Valour, and S. Othman, “Support vector machines combined to observers for fault diagnosis in chemical reactors,” *The Canadian Journal of Chemical Engineering*, vol. 92, no. 4, pp. 685–695, 2014.
- [97] V. Ferreira, R. Zanghi, M. Fortes, G. Sotelo, R. Silva, J. Souza, C. Guimarães, and S. Gomes, “A survey on intelligent system application to fault diagnosis in electric power system transmission lines,” *Electric Power Systems Research*, vol. 136, pp. 135–153, 2016.
- [98] T. Kobayashi and D. L. Simon, “Evaluation of an enhanced bank of Kalman filters for in-flight aircraft engine sensor fault diagnostics,” *Journal of Engineering for Gas Turbines and Power*, vol. 127, p. 497, 2005.
- [99] T. Kobayashi and D. L. Simon, “Application of a bank of Kalman filters for aircraft engine fault diagnostics,” *NASA/TM J*, vol. 212526, pp. 1–10, 2003.
- [100] T. Kobayashi and D. L. Simon, “Hybrid Kalman filter approach for aircraft engine in-flight diagnosis: Sensor fault detection case,” *Journal of Engineering for Gas Turbines and Power*, vol. 129, no. 3, pp. 746–754, 2007.
- [101] S. Simani, C. Fantuzzi, and S. Beghelli, “Diagnosis techniques for sensor faults of industrial processes,” *IEEE Transactions on Control Systems Technology*, vol. 8, no. 5, pp. 848–855, 2000.
- [102] A. J. Volponi, H. DePold, R. Ganguli, and C. Daguang, “The use of Kalman filter and neural network methodologies in gas turbine performance diagnostics: a comparative study,” *J. of Eng. for Gas Turbines and Power*, vol. 125, pp. 917–924, 2003.

- [103] R. Ganguli, "Application of fuzzy logic for fault isolation of jet engines," *Journal of Engineering for Gas Turbines and Power*, vol. 125, no. 3, pp. 617–623, 2003.
- [104] S. Sampath and R. Singh, "An integrated fault diagnostics model using genetic algorithm and neural networks," *Journal of Engineering for Gas Turbines and Power*, vol. 128, pp. 49–56, 2006.
- [105] S. Rahme and N. Meskin, "Adaptive sliding mode observer for sensor fault diagnosis of an industrial gas turbine," *Control Engineering Practice*, vol. 38, pp. 57–74, 2015.
- [106] E. Tsoutsanis, N. Meskin, M. Benammar, and K. Khorasani, "Transient gas turbine performance diagnostics through nonlinear adaptation of compressor and turbine maps," *J. of Engineering for Gas Turbines and Power*, vol. 137, no. 9, p. 091201, 2015.
- [107] E. Tsoutsanis, N. Meskin, M. Benammar, and K. Khorasani, "A component map tuning method for performance prediction and diagnostics of gas turbine compressors," *Applied Energy*, vol. 135, pp. 572–585, 2014.
- [108] Q. Wang, J. Huang, and F. Lu, "An improved particle filtering algorithm for aircraft engine gas-path fault diagnosis," *Advances in Mechanical Engineering*, vol. 8, no. 7, 2016.
- [109] N. Daroogheh, N. Meskin, and K. Khorasani, "Particle filtering for state and parameter estimation in gas turbine engine fault diagnostics," in *American Control Conference*, pp. 4343–4349, IEEE, 2013.
- [110] N. Daroogheh, N. Meskin, and K. Khorasani, "A novel particle filter parameter prediction scheme for failure prognosis," in *American Control Conference*, pp. 1735–1742, IEEE, 2014.

- [111] A. Salar, N. Meskin, and K. Khorasani, “A novel affine qlpv model derivation method for fault diagnosis H_∞ performance improvement,” in *American Control Conference*, pp. 823–830, IEEE, 2015.
- [112] X. Zhang, L. Tang, and J. Decastro, “Robust fault diagnosis of aircraft engines: A nonlinear adaptive estimation-based approach,” *IEEE Transactions on Control Systems Technology*, vol. 21, no. 3, pp. 861–868, 2013.
- [113] L. Shang and G. Liu, “Sensor and actuator fault detection and isolation for a high performance aircraft engine bleed air temperature control system,” *IEEE Transactions on Control Systems Technology*, vol. 19, no. 5, pp. 1260–1268, 2011.
- [114] D. Doel, “An assessment of weighted-least-squares-based gas path analysis,” *Journal of Engineering for Gas Turbines and Power*, vol. 116, no. 2, 1994.
- [115] H. DePold and F. Gass, “The application of expert systems and neural networks to gas turbine prognostics and diagnostics,” *Journal of Engineering for Gas Turbines and Power*, vol. 121, no. 4, pp. 607–612, 1999.
- [116] D. Simon and D. Simon, “Aircraft turbofan engine health estimation using constrained Kalman filtering,” tech. rep., DTIC Document, 2003.
- [117] D. Simon and D. Simon, “Constrained Kalman filtering via density function truncation for turbofan engine health estimation,” *International Journal of Systems Science*, vol. 41, no. 2, pp. 159–171, 2010.
- [118] A. J. Volponi, H. DePold, R. Ganguli, and C. Daguang, “The use of Kalman filter and neural network methodologies in gas turbine performance diagnostics: a comparative study,” *Journal of Engineering for Gas Turbines and Power*, vol. 125, pp. 917–924, 2003.

- [119] T. Kobayashi and D. Simon, “Hybrid neural-network genetic-algorithm technique for aircraft engine performance diagnostics,” *Journal of propulsion and power*, vol. 21, no. 4, pp. 751–758, 2005.
- [120] M. VanDyke, J. Schwartz, and C. Hall, “Unscented Kalman filtering for spacecraft attitude state and parameter estimation,” *Department of Aerospace and Ocean Engineering, Virginia Polytechnic Institute & State University, Blacksburg, Virginia*, 2004.
- [121] D. L. Simon and A. W. Rinehart, “Sensor selection for aircraft engine performance estimation and gas path fault diagnostics,” *Journal of Engineering for Gas Turbines and Power*, vol. 138, no. 7, p. 071201, 2016.
- [122] H. A. Nozari, M. A. Shoorehdeli, S. Simani, and H. D. Banadaki, “Model-based robust fault detection and isolation of an industrial gas turbine prototype using soft computing techniques,” *Neurocomputing*, vol. 91, pp. 29–47, 2012.
- [123] X. Liu and Z. Gao, “Novel unknown input observer for fault estimation of gas turbine dynamic systems,” in *13th International IEEE Conference on Industrial Informatics (INDIN)*, pp. 562–567, 2015.
- [124] P. Dewallef and O. Leonard, “On-line performance monitoring and engine diagnostic using robust kalman filtering techniques,” *ASME Turbo Expo*, no. GT2003-38379, pp. 395–403, 2003.
- [125] K. Kanelopoulos, A. Stamatis, and K. Mathioudakis, “Incorporating neural networks into gas turbine performance diagnostics,” *ASME 97-GT-35, International Gas Turbine and & Aero Engine Congress and Exhibition, Orlando, Florida*, 1997.
- [126] S. Ogaji, “Advanced gas-path fault diagnostics for stationary gas turbines,” 2003.

- [127] C. Romessis, A. Stamatias, and K. Mathioudakis, "A parametric investigation of the diagnostic ability of probabilistic neural networks on turbofan engines," in *ASME TURBOEXPO*, 2001.
- [128] M. Amozegar and K. Khorasani, "An ensemble of dynamic neural network identifiers for fault detection and isolation of gas turbine engines," *Neural Networks*, vol. 76, pp. 106–121, 2016.
- [129] Z. S. Vanini, K. Khorasani, and N. Meskin, "Fault detection and isolation of a dual spool gas turbine engine using dynamic neural networks and multiple model approach," *Information Sciences*, vol. 259, pp. 234–251, 2014.
- [130] Z. S. Vanini, N. Meskin, and K. Khorasani, "Multiple-model sensor and components fault diagnosis in gas turbine engines using autoassociative neural networks," *Journal of Engineering for Gas Turbines and Power*, vol. 136, no. 9, p. 091603, 2014.
- [131] P. Tamilselvan and P. Wang, "Failure diagnosis using deep belief learning based health state classification," *Reliability Engineering & System Safety*, vol. 115, pp. 124–135, 2013.
- [132] R. Yedavalli, "Robust estimation and fault diagnostics for aircraft engines with uncertain model data," in *American Control Conference*, pp. 2822–2827, IEEE, 2007.
- [133] R. Yedavalli and W. Li, "Aircraft engine fault detection using dynamic/adaptive threshold approach," in *ASME Turbo Expo: Power for Land, Sea and Air*, 2007.

- [134] P. Shankar and R. Yedavalli, “Neural-network-based observer for turbine engine parameter estimation,” *Proceedings of the Institution of Mechanical Engineers, Part I: Journal of Systems and Control Engineering*, vol. 223, no. 6, pp. 821–832, 2009.
- [135] T. Brotherton, A. Volponi, R. Luppold, and D. Simon, “estorm: enhanced self tuning on-board real-time engine model,” in *IEEE Aerospace Conferences, Big Sky MT*, 2003.
- [136] A. Volponi, “Use of hybrid engine modeling for on-board module performance tracking,” in *ASME Turbo Expo: Powers for Land, Sea and Air*, 2005.
- [137] G. Feng, “Stability analysis of piecewise discrete time linear systems. submitted to,” *IEEE Transactions on Automatic Control*, vol. 47, no. 7, pp. 1108–1112, 2002.
- [138] M. Johansson, A. Rantzer, *et al.*, “Computation of piecewise quadratic lyapunov functions for hybrid systems,” *IEEE transactions on automatic control*, vol. 43, no. 4, pp. 555–559, 1998.
- [139] A. Hassibi and S. Boyd, “Quadratic stabilization and control of piecewise-linear systems,” in *American Control Conference*, vol. 6, pp. 3659–3664, IEEE, 1998.
- [140] L. Rodrigues, A. Hassibi, and J. P. How, “Output feedback controller synthesis for piecewise-affine systems with multiple equilibria,” in *American Control Conference*, vol. 3, pp. 1784–1789, IEEE, 2000.
- [141] A. Bemporad, G. Ferrari-Trecate, M. Morari, *et al.*, “Observability and controllability of piecewise affine and hybrid systems,” *IEEE transactions on automatic control*, vol. 45, no. 10, pp. 1864–1876, 2000.

- [142] L. Rodrigues and J. P. How, “Observer-based control of piecewise-affine systems,” *International Journal of Control*, vol. 76, no. 5, pp. 459–477, 2003.
- [143] R. E. Kalman, “A new approach to linear filtering and prediction problems,” *Journal of basic Engineering*, vol. 82, no. 1, pp. 35–45, 1960.
- [144] R. Royce, *The jet engine*. John Wiley & Sons, 2015.
- [145] R. D. Flack, *Fundamentals of jet propulsion with applications*, vol. 17. Cambridge University Press, 2005.
- [146] J. D. Mattingly and H. Von Ohain, *Elements of propulsion: gas turbines and rockets*. American Institute of Aeronautics and Astronautics Reston, Va, USA, 2006.
- [147] H. Cohen, G. F. C. Rogers, H. I. H. Saravanamuttoo, and H. (r.) Saravanamuttoo, “Gas turbine theory,” 1987.
- [148] R. Kurz and K. Brun, “Degradation in gas turbine systems,” *Journal of Engineering for Gas Turbines and Power*, vol. 123, no. 1, pp. 70–77, 2001.
- [149] C. S. Byington, M. Watson, M. J. Roemer, T. R. Galie, J. J. McGroarty, and C. Savage, “Prognostic enhancements to gas turbine diagnostic systems,” tech. rep., DTIC Document, 2003.
- [150] R. Salamat, *Gas path diagnostics for compressors*. Cranfield University, 2012.
- [151] N. L. R. Group, “GSP software,” <http://www.gspteam.com>, 2011.
- [152] S. Camporeale, B. Fortunato, and M. Mastrovito, “A modular code for real time dynamic simulation of gas turbines in simulink,” *Journal of Engineering for Gas Turbines and Power*, vol. 128, no. 3, pp. 506–517, 2006.

- [153] V. Panov, “Gasturbolib: Simulink library for gas turbine engine modelling,” in *ASME Turbo Expo 2009: Power for Land, Sea, and Air*, pp. 555–565, American Society of Mechanical Engineers, 2009.
- [154] J. H. Wilkinson and J. H. Wilkinson, *The algebraic eigenvalue problem*, vol. 87. Clarendon Press Oxford, 1965.
- [155] B. Pourbabaee, N. Meskin, and K. Khorasani, “Multiple-model based sensor fault diagnosis using hybrid kalman filter approach for nonlinear gas turbine engines,” in *American Control Conference*, pp. 4717–4723, IEEE, 2013.
- [156] B. Pourbabaee, N. Meskin, and K. Khorasani, “Sensor fault detection, isolation, and identification using multiple-model-based hybrid kalman filter for gas turbine engines,” *IEEE Transactions on Control Systems Technology*, vol. 24, no. 4, pp. 1184–1200, 2016.
- [157] R. Murray-Smith and T. Johansen, *Multiple Model Approaches to Nonlinear Modelling and Control*. CRC press, 1997.
- [158] X. R. Li and Y. Zhang, “Numerically robust implementation of multiple-model algorithms,” *IEEE Transactions on Aerospace and Electronic Systems*, vol. 36, no. 1, pp. 266–278, 2000.
- [159] J. Prakash, S. C. Patwardhan, and S. Narasimhan, “A supervisory approach to fault-tolerant control of linear multivariable systems,” *Industrial & Engineering Chemistry Research*, vol. 41, no. 9, pp. 2270–2281, 2002.
- [160] J. Prakash, S. Narasimhan, and S. C. Patwardhan, “Integrating model based fault diagnosis with model predictive control,” *Industrial & Engineering Chemistry Research*, vol. 44, no. 12, pp. 4344–4360, 2005.
- [161] S. C. Patwardhan, S. Manuja, S. Narasimhan, and S. L. Shah, “From data to diagnosis and control using generalized orthonormal basis filters. part II:

- Model predictive and fault tolerant control,” *J. of Process Control*, vol. 16, no. 2, pp. 157–175, 2006.
- [162] A. P. Deshpande and S. C. Patwardhan, “Online fault diagnosis in nonlinear systems using the multiple operating approach,” *Ind. Eng. Chem. Res.*, vol. 47, no. 17, pp. 6711–6726, 2008.
- [163] T. Fawcett, “An introduction to ROC analysis,” *Pattern recognition letters*, vol. 27, no. 8, pp. 861–874, 2006.
- [164] Y. Zhan and J. Jiang, “An interacting multiple-model based fault detection, diagnosis and fault-tolerant control approach,” in *Proceedings of the 38th IEEE Conf. on Decision and Control*, vol. 4, pp. 3593–3598, 1999.
- [165] J. Ru and X. R. Li, “Variable-structure multiple-model approach to fault detection, identification, and estimation,” *IEEE Transactions on Control Systems Technology*, vol. 16, no. 5, pp. 1029–1038, 2008.
- [166] B. Pourbabaee, N. Meskin, and K. Khorasani, “Sensor fault detection and isolation using multiple robust filters for linear systems with time-varying parameter uncertainty and error variance constraints,” in *IEEE Conf. on Control Applications (CCA)*, pp. 382–389, 2014.
- [167] B. Pourbabaee, N. Meskin, and K. Khorasani, “Robust sensor fault detection and isolation of gas turbine engines subjected to time-varying parameter uncertainties,” *Mechanical Systems and Signal Processing*, vol. 76, pp. 136–156, 2016.
- [168] G. Garcia, D. Arzelier, *et al.*, “Robust stabilization of discrete-time linear systems with norm-bounded time-varying uncertainty,” *Systems & Control Letters*, vol. 22, no. 5, pp. 327–339, 1994.

- [169] Z. Wang, “Robust filter design with time-varying parameter uncertainty and error variance constraints,” *International Journal of Control*, vol. 72, no. 1, pp. 30–38, 1999.
- [170] J. Lofberg, “Yalmip: A toolbox for modeling and optimization in matlab,” in *IEEE International Symposium on Computer Aided Control Systems Design*, pp. 284–289, 2004.
- [171] S. G. Barad, P. Ramaiah, R. Giridhar, and G. Krishnaiah, “Neural network approach for a combined performance and mechanical health monitoring of a gas turbine engine,” *Mechanical Systems and Signal Processing*, vol. 27, pp. 729–742, 2012.
- [172] S. S. Haykin, *Neural networks and learning machines*, vol. 3. Pearson Education Upper Saddle River, 2009.
- [173] A. Chernodub, “Training dynamic neural networks using the extended kalman filter for multi-step-ahead predictions,” in *Artificial Neural Networks*, pp. 221–243, Springer, 2015.
- [174] D. Yu and L. Deng, “Recurrent neural networks and related models,” in *Automatic Speech Recognition*, pp. 237–266, Springer, 2015.
- [175] S. Singhal and L. Wu, “Training multilayer perceptrons with the extended kalman algorithm.” in *NIPS*, pp. 133–140, 1988.
- [176] Y.-c. Cheng, W.-M. Qi, and W.-Y. Cai, “Dynamic properties of elman and modified elman neural network,” in *Machine Learning and Cybernetics, 2002. Proceedings. 2002 International Conference on*, vol. 2, pp. 637–640, IEEE, 2002.